



Terms and Conditions of Use of Digitised Theses from Trinity College Library Dublin

Copyright statement

All material supplied by Trinity College Library is protected by copyright (under the Copyright and Related Rights Act, 2000 as amended) and other relevant Intellectual Property Rights. By accessing and using a Digitised Thesis from Trinity College Library you acknowledge that all Intellectual Property Rights in any Works supplied are the sole and exclusive property of the copyright and/or other IPR holder. Specific copyright holders may not be explicitly identified. Use of materials from other sources within a thesis should not be construed as a claim over them.

A non-exclusive, non-transferable licence is hereby granted to those using or reproducing, in whole or in part, the material for valid purposes, providing the copyright owners are acknowledged using the normal conventions. Where specific permission to use material is required, this is identified and such permission must be sought from the copyright holder or agency cited.

Liability statement

By using a Digitised Thesis, I accept that Trinity College Dublin bears no legal responsibility for the accuracy, legality or comprehensiveness of materials contained within the thesis, and that Trinity College Dublin accepts no liability for indirect, consequential, or incidental, damages or losses arising from use of the thesis for whatever reason. Information located in a thesis may be subject to specific use constraints, details of which may not be explicitly described. It is the responsibility of potential and actual users to be aware of such constraints and to abide by them. By making use of material from a digitised thesis, you accept these copyright and disclaimer provisions. Where it is brought to the attention of Trinity College Library that there may be a breach of copyright or other restraint, it is the policy to withdraw or take down access to a thesis while the issue is being resolved.

Access Agreement

By using a Digitised Thesis from Trinity College Library you are bound by the following Terms & Conditions. Please read them carefully.

I have read and I understand the following statement: All material supplied via a Digitised Thesis from Trinity College Library is protected by copyright and other intellectual property rights, and duplication or sale of all or part of any of a thesis is not permitted, except that material may be duplicated by you for your research use or for educational purposes in electronic or print form providing the copyright owners are acknowledged using the normal conventions. You must obtain permission for any other use. Electronic or print copies may not be offered, whether for sale or otherwise to anyone. This copy has been supplied on the understanding that it is copyright material and that no quotation from the thesis may be published without proper acknowledgement.

**RECOGNITION OF ABNORMAL THERMAL HISTORIES OF JURASSIC
SOURCE ROCKS FROM INTEGRATED ANALYSES OF VITRINITE
REFLECTANCE AND ORGANIC MATTER COLOUR/FLUORESCENCE**

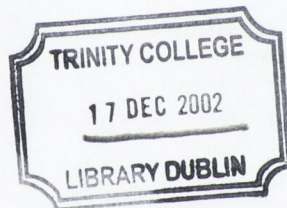
by

GERARD A. McCAUGHAN

A thesis submitted in partial fulfilment of the regulations for the degree of Doctor of
Philosophy

Department of Geology, University of Dublin, Trinity College.

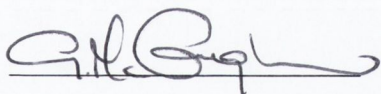
August 2002



THES
7071

DECLARATION

This thesis is entirely my own work, except where otherwise stated. All references are duly acknowledged. It has not been previously submitted as an exercise for a degree at this or any other university. Reproduction in whole or part of this work is authorised, provided that the source is acknowledged, at the discretion of the depository library of the University of Dublin.

A handwritten signature in black ink, appearing to read 'Gerard McCaughan', with a horizontal line underneath the text.

Gerard McCaughan

To my parents

SUMMARY

By investigating three sedimentary horizons through the aureole of a Tertiary dyke intruding a Middle Jurassic sedimentary section in NE Skye, the thermal response rates of the various organic maturity indicators to short-term high temperature heating events were evaluated. A detailed assessment was conducted, of the reaction of vitrinite reflectance (VR), kerogen colour and fluorescence, to the short-lived high temperatures associated with the dyke.

Image analysis (IA) techniques were applied to develop a new system for vitrinite reflectance measurement at Trinity College Dublin. Vitrinite reflectance shows a marked reaction to the high temperatures close to the dyke. Within a zone equivalent to *ca.* 50% dyke thickness (d.t.), rank changes from the high-volatile bituminous (0.72–0.79% R_r) through medium volatile bituminous, low volatile bituminous, semi-anthracite to anthracite (3.1–3.6% R_r) are observed. Reflectance reversals, previously reported adjacent to igneous intrusions, were not observed in any of the sample horizons. Peak palaeotemperatures in excess of 300°C, computed from the measured VR data, are indicated in the host rocks adjacent to the dyke contact.

Colour image analysis techniques were used to 'quantitatively' determine kerogen colour, through the measurement of red, green and blue (RGB) pixel intensities. In the absence of adequate numbers of suitable palynomorphs, a colour evaluation of amorphous organic matter (AOM) proved to be an acceptable alternative for kerogen colour evaluation. Within a zone equivalent to *ca.* 50% d.t., mean RGB colour intensities decrease sharply towards the dyke. The position of the break in slope of mean RGB intensities correlates well with that of the R_r data. A good correlation of mean red and green intensities with vitrinite reflectance exists up to *ca.* 1.6% R_r . Analysis of variance (ANOVA) of the RGB intensity mean values identified green as the most sensitive parameter in relation to thermal maturation. Plots of the relative percentages of red, green and blue against % R_r reveal a unique maturation pathway for each of the three colour parameters, and suggest a close relationship with fluorescence intensity.

Cessation of organic matter fluorescence was delayed relative to VR in two of the three sample horizons. Slight differences in fluorescence properties between sample horizons may reflect varying diagenetic degradation, or compositional differences in the AOM.

A simple one-dimensional model of transient conductive heat flow, the *Schmidt Plot*, was used to model the temperature change produced in the host rocks by heat transfer from the dyke. Using a simple 'divided-bar' apparatus, thermal conductivity (k) measurements of

selected rock samples were completed. Experimentally determined k values from this study fall within the range of published k values for the measured lithologies. Good agreement between measured k values for the dyke and host lithologies justified the use of a single thermal diffusivity (κ) value in the model for both dyke and host rocks.

The model shows that significant cooling of the dyke occurs within days and weeks of its emplacement. The rate of dyke cooling indicated by the model decreases markedly after 1 year, as the heat from the intrusion is dissipated further away into the host rocks. The thickness of the dyke and the duration of magma flow were found to have the most significant effect on the width of the contact aureole indicated by the model. The effect of thermal conductivity on T_{\max} was found to be greatest during the early stages of cooling, but its overall influence is limited. Increasing the value of T_{magma} or T_{host} increased T_{contact} , and the width of the contact aureole indicated by the model. However, as magma flow duration only controls T_{magma} , and is independent of T_{host} , the effect of T_{host} on T_{\max} values close to the dyke is considered relatively minor.

Good agreement between numerically modelled and VR derived peak palaeotemperatures was observed at distances greater than 3m from the dyke, suggesting that the apparent 'background' maturity level was achieved in part by heat associated with the intrusion. Close to the dyke, peak palaeotemperatures calculated from measured VR data considerably underestimate those predicted by the model. A number of reasons for this disparity between observed and modelled palaeotemperatures are considered likely:

1. It is likely that the heating episode *at* peak temperature was too brief for vitrinite in the host rocks adjacent to the dyke to stabilise and record the maximum temperatures achieved.
2. The *rate* of heating in the host rocks adjacent to the dyke may have been too rapid to facilitate equilibration of complex vitrinite maturation reactions.
3. Standard empirical burial and geothermal calibrations used to translate % R_r data to peak palaeotemperatures are likely to be inappropriate for contact metamorphic systems. Furthermore, the application of R_r as a high temperature geothermometer is limited, due to the anomalous behaviour of R_{\min} above the ~meta-anthracite stage of coal rank.
4. Convection and/or advection may have partly contributed as alternative mechanisms of heat transfer during the cooling of the dyke.

ACKNOWLEDGEMENTS

I would like to thank the following:

Prof. Phillip Allen and Dr. John Graham for use of the departmental facilities.

Prof. Geoff Clayton for his supervision of this project, his encouragement, advice and friendship.

Statoil for funding the project.

Trinity Trust for travel assistance.

The incomparable technical staff of the Geology Department, Neil, Declan, Maura, and especially Frank.

Our librarian, Dr. Patrick Wyse Jackson.

The departmental secretary, Joann Layng.

The academic staff of the Geology Department for teaching me all that I was willing to learn, and for engaging with me in various discussions on different aspects of this project.

Dr. James Killen of the Geography Department for his assistance on all aspects statistical.

Professor Iggy McGovern of the Physics Department, Geoff, Neil, John and Robbie for lending their help and various parts of equipment during the thermal conductivity determination experiments.

Geoff, Niall and Robbie for their assistance during the collection of samples over a cold, scampi munching weekend on the Isle of Skye.

Dr. Mike Cunningham for his time and help with Visual Basic programming.

Dr. Robbie Goodhue for many valuable discussions on various aspects of the project, and for keeping my spirits up during the final phase.

My postgraduate colleagues, past and present, a number of whom have become, and will remain, close friends. Special thanks must go to Jacqui for putting up with me in a small space for too long.

My family for their support over the years. Dave and Nigel for the same.

Jules for your endless encouragement, support and patience.

CONTENTS

SUMMARY

ACKNOWLEDGEMENTS

CHAPTER 1: INTRODUCTION	1
1.1 Aims of this project	1
1.2 Requirements of sampling locality	3
1.3 Sampling focus	3
1.4 Northeast Ireland	4
1.5 Isle of Skye.....	8
1.5.1 Mesozoic sedimentation history	8
1.5.2 Tertiary igneous history	12
1.5.3 Carn Dearg, Loch Eishort	15
1.5.4 Broadford Bay (Waterloo)	17
1.5.5 Bearreraig Bay	19
1.5.5.2 Dyke petrography.....	21
1.5.5.2 Dyke geochemistry	25
CHAPTER 2: VITRINITE REFLECTANCE, MATERIALS AND METHODS	28
2.1 Vitrinite reflectance	28
2.1.1 Coalification, rank and maturation	28
2.1.2 Origin and classification of vitrinite	29
2.1.3 Evolution of vitrinite during coalification.....	30
2.1.4 Optical properties of vitrinite	30
2.1.5 Benefits of the vitrinite reflectance method	34
2.2 Preparations of samples for vitrinite reflectance.....	35
2.2.1 Sample preparation	35
2.2.2 Mounting and polishing	38
2.3 Measurement of vitrinite reflectance	40
2.3.1 System setup.....	40
2.3.2 System calibration	40
2.3.3 Reflectance measurement.....	43
2.3.4 Accuracy of vitrinite reflectance results	44

CHAPTER 3: QUANTITATIVE AOM COLOUR, MATERIALS AND METHODS	48
3.1 Organic matter colour	48
3.1.1 Organic matter colour	48
3.1.2 Visual colour scales	51
3.1.3 Quantitative organic matter colour	53
3.1.4 Quantitative colour measurement using image analysis	54
3.2 Preparation of samples for AOM colour determination	55
3.2.1 Sample preparation	55
3.2.2 Mounting	55
3.3 Colour measurement	56
3.3.1 System setup	56
3.3.2 System calibration	57
3.3.3 Colour measurement	61
3.3.4 Accuracy of colour measurements	62
3.4 Organic matter fluorescence	66
3.4.1 Basis of fluorescence	66
3.4.2 Application of fluorescence microscopy	68
3.4.3 Sample preparation	69
3.4.3 Fluorescence measurement	70
CHAPTER 4: VITRINITE REFLECTANCE RESULTS.....	71
4.1 Introduction	71
4.2 Vitrinite reflectance results	71
4.2.1 Vitrinite reflectance of BBN sample horizon.....	71
4.2.2 Vitrinite reflectance of BGSNH sample horizon.....	76
4.2.3 Vitrinite reflectance of the BGSN sample horizon.....	76
4.3 Discussion	76
4.4 Thermal modelling	79
4.4.1 Models that consider temperature and time	79
4.4.2 Models that consider temperature only	84
4.5 Translation of R_r data to palaeotemperature	90
4.6 Summary	97
CHAPTER 5: AOM COLOUR AND FLUORESCENCE RESULTS.....	99
5.1 Introduction	99
5.2 Description of AOM used in colour investigations.....	99
5.2.1 Description of AOM from the BBN sample horizon.....	100

5.2.2 Description of AOM from the BGSHN sample horizon	101
5.2.3 Description of AOM from the BGSN sample horizon	101
5.3 Organic matter fluorescence results	102
5.3.1 AOM fluorescence in BBN samples.....	105
5.3.2 AOM fluorescence in BGSHN samples.....	105
5.3.3 AOM fluorescence in BGSN samples	106
5.3.4 Discussion	107
5.4 AOM colour results	110
5.4.1 BBN sample horizon.....	114
5.4.2 BGSHN sample horizon.....	114
5.4.3 BGSN sample horizon	114
5.5 Analysis of RGB results	117
5.5.1 Analysis of raw RGB data.....	117
5.5.2 Statistical analysis of RGB parameters.....	117
5.5.3 Comparison with vitrinite reflectance.....	120
5.5.4 Relative RGB intensity of samples.....	123
5.5.5 Conversion of RGB to HSB	126
5.6 Discussion	128
5.7 Summary	131
CHAPTER 6: NUMERICAL MODELLING OF HEAT FLOW.....	132
6.1 Introduction.....	132
6.2 Basis for the Schmidt Method: heat flow theory.....	132
6.3 Validity of the Schmidt Plot.....	136
6.4 Boundary conditions.....	139
6.5 Assessment of thermal parameters	140
6.5.1 Thermal diffusivity	140
6.5.1.1 Thermal conductivity	140
6.5.1.2 Volumetric heat capacity	150
6.5.2 Magma temperature	151
6.5.3 Host rock temperature.....	151
6.5.4 Magma flow	154
6.6 Results of heat flow modelling	155
6.6.1 Temperature distribution over time	155
6.6.2 Sensitivity of Schmidt model to thermal parameters.....	159
6.6.3 Range of T_{\max} in host rocks	163
6.7 Summary	167

CHAPTER 3: QUANTITATIVE AOM COLOUR, MATERIALS AND METHODS	48
3.1 Organic matter colour	48
3.1.1 Organic matter colour	48
3.1.2 Visual colour scales	51
3.1.3 Quantitative organic matter colour	53
3.1.4 Quantitative colour measurement using image analysis	54
3.2 Preparation of samples for AOM colour determination	55
3.2.1 Sample preparation	55
3.2.2 Mounting	55
3.3 Colour measurement	56
3.3.1 System setup	56
3.3.2 System calibration	57
3.3.3 Colour measurement	61
3.3.4 Accuracy of colour measurements	62
3.4 Organic matter fluorescence	66
3.4.1 Basis of fluorescence	66
3.4.2 Application of fluorescence microscopy	68
3.4.3 Sample preparation	69
3.4.3 Fluorescence measurement	70
CHAPTER 4: VITRINITE REFLECTANCE RESULTS	71
4.1 Introduction	71
4.2 Vitrinite reflectance results	71
4.2.1 Vitrinite reflectance of BBN sample horizon	71
4.2.2 Vitrinite reflectance of BGSN sample horizon	76
4.2.3 Vitrinite reflectance of the BGSN sample horizon	76
4.3 Discussion	76
4.4 Thermal modelling	79
4.4.1 Models that consider temperature and time	79
4.4.2 Models that consider temperature only	84
4.5 Translation of R_r data to palaeotemperature	90
4.6 Summary	97
CHAPTER 5: AOM COLOUR AND FLUORESCENCE RESULTS	99
5.1 Introduction	99
5.2 Description of AOM used in colour investigations	99
5.2.1 Description of AOM from the BBN sample horizon	100

5.2.2 Description of AOM from the BGSNH sample horizon	101
5.2.3 Description of AOM from the BGSN sample horizon	101
5.3 Organic matter fluorescence results	102
5.3.1 AOM fluorescence in BBN samples.....	105
5.3.2 AOM fluorescence in BGSNH samples.....	105
5.3.3 AOM fluorescence in BGSN samples	106
5.3.4 Discussion	107
5.4 AOM colour results	110
5.4.1 BBN sample horizon.....	114
5.4.2 BGSNH sample horizon.....	114
5.4.3 BGSN sample horizon	114
5.5 Analysis of RGB results	117
5.5.1 Analysis of raw RGB data.....	117
5.5.2 Statistical analysis of RGB parameters.....	117
5.5.3 Comparison with vitrinite reflectance.....	120
5.5.4 Relative RGB intensity of samples.....	123
5.5.5 Conversion of RGB to HSB	126
5.6 Discussion	128
5.7 Summary	131
CHAPTER 6: NUMERICAL MODELLING OF HEAT FLOW.....	132
6.1 Introduction.....	132
6.2 Basis for the Schmidt Method: heat flow theory.....	132
6.3 Validity of the Schmidt Plot.....	136
6.4 Boundary conditions.....	139
6.5 Assessment of thermal parameters	140
6.5.1 Thermal diffusivity	140
6.5.1.1 Thermal conductivity	140
6.5.1.2 Volumetric heat capacity	150
6.5.2 Magma temperature	151
6.5.3 Host rock temperature.....	151
6.5.4 Magma flow	154
6.6 Results of heat flow modelling	155
6.6.1 Temperature distribution over time	155
6.6.2 Sensitivity of Schmidt model to thermal parameters.....	159
6.6.3 Range of T_{\max} in host rocks	163
6.7 Summary	167

CHAPTER 7: COMPARISON OF MODELLED T_{\max} WITH MATURITY DATA.....	169
7.1 Comparison of modelled T_{\max} with VR-derived palaeotemperatures	169
7.2 Discussion	172
7.3 Summary	189
CHAPTER 8: SUMMARY OF CONCLUSIONS.....	191
REFERENCES.....	196-217

APPENDICES

- I. Sample catalogue
- II. R_r histograms
- III. RGB histograms
- IV. Maturity data (VR, RGB data with TAI, and fluorescence)
- V. VR-translated peak palaeotemperatures
- VI. Geochemical data
- VII. Thermal Conductivity Data
- VIII. QUIPS routines & Schmidt model VBA source code
- IX. RGB statistics: ANOVA details

PLATES

LIST OF FIGURES

Figure No.	Figure Caption	Page
1.1	Correlation of organic maturation indices. After Clayton <i>et al.</i> (1989)	2
1.2	Geological summary map of the Ulster Basin area, onshore northeast Ireland	6
1.3	Location of sampled dyke and adjacent mudstones at Island Magee, Larne, northeast Ireland.	7
1.4	Map of the Hebrides Basin, showing present distribution of Triassic and Jurassic rocks. Modified from Morton and Hudson (1987).	10
1.5	Geological map of the Isle of Skye.	11
1.6	Stratigraphic relationships on the Isle of Skye. Modified from Bell and Harris (1986).	14
1.7	Map showing location of samples collected at Carn Dearg, Loch Eishort, central Skye.	16
1.8	Map showing location of samples collected at Waterloo, Broadford Bay, central Skye.	18
1.9	Map showing location of samples collected at Berreraig, northeast Skye.	20
1.10	Palynofacies of BBN horizon 'background'.	22
1.11	Palynofacies of BGSHN horizon 'background'.	23
1.12	Palynofacies of BGSN horizon 'background'.	24
1.13	Plot of total alkalis versus silica data for the studied dyke at Berreraig, including standard nomenclature for normal volcanic rocks. Modified from Cox <i>et al.</i> (1979).	26
1.14	Comparison between total alkali/silica variation in the studied dyke at Berreraig and the basalt-benmoreite and basalt-trachyte trends of the Skye lavas (Thompson <i>et al.</i> 1972). The alkaline/subalkaline divide of Swarzer and Rogers (1974) is also shown.	26
1.15	Alkalis-iron-magnesium (AFM) ternary plot of the studied dyke at Berreraig. The shaded area represents the Trotternish sill field of northern Skye (Gibson 1990). Also shown are the fractionation trends of the Skye lavas (1) (Thompson <i>et al.</i> 1972) and the Hawaiian alkali suite (2) (Macdonald and Katsura 1964).	27
1.16	Composition of the studied dyke plotted on the Ti/Y/Zr discriminant diagram of Pearce and Cann (1973). The scaling factors used in the diagram serve to bring the points into the centre of the triangle without altering their relative position (Pearce and Cann 1973)	27
2.1	Relationship between vitrinite and different chemical parameters of rank. After Teichmüller and Teichmüller (1979).	31
2.2	Coalification stages and vitrinite evolution, including coalification jumps in vitrinite. Modified from Teichmüller (1987).	32
2.3	Plot of vitrinite reflectance versus microwave power after 30 minutes. The red data	37

CHAPTER 7: COMPARISON OF MODELLED T_{\max} WITH MATURITY DATA.....	169
7.1 Comparison of modelled T_{\max} with VR-derived palaeotemperatures	169
7.2 Discussion	172
7.3 Summary	189
CHAPTER 8: SUMMARY OF CONCLUSIONS.....	191
REFERENCES.....	196-217

APPENDICES

- I. Sample catalogue
- II. R_r histograms
- III. RGB histograms
- IV. Maturity data (VR, RGB data with TAI, and fluorescence)
- V. VR-translated peak palaeotemperatures
- VI. Geochemical data
- VII. Thermal Conductivity Data
- VIII. QUIPS routines & Schmidt model VBA source code
- IX. RGB statistics: ANOVA details

PLATES

LIST OF FIGURES

Figure No.	Figure Caption	Page
1.1	Correlation of organic maturation indices. After Clayton <i>et al.</i> (1989)	2
1.2	Geological summary map of the Ulster Basin area, onshore northeast Ireland	6
1.3	Location of sampled dyke and adjacent mudstones at Island Magee, Larne, northeast Ireland.	7
1.4	Map of the Hebrides Basin, showing present distribution of Triassic and Jurassic rocks. Modified from Morton and Hudson (1987).	10
1.5	Geological map of the Isle of Skye.	11
1.6	Stratigraphic relationships on the Isle of Skye. Modified from Bell and Harris (1986).	14
1.7	Map showing location of samples collected at Carn Dearg, Loch Eishort, central Skye.	16
1.8	Map showing location of samples collected at Waterloo, Broadford Bay, central Skye.	18
1.9	Map showing location of samples collected at Berreraig, northeast Skye.	20
1.10	Palynofacies of BBN horizon 'background'.	22
1.11	Palynofacies of BGSNH horizon 'background'.	23
1.12	Palynofacies of BGSN horizon 'background'.	24
1.13	Plot of total alkalis versus silica data for the studied dyke at Berreraig, including standard nomenclature for normal volcanic rocks. Modified from Cox <i>et al.</i> (1979).	26
1.14	Comparison between total alkali/silica variation in the studied dyke at Berreraig and the basalt-benmoreite and basalt-trachyte trends of the Skye lavas (Thompson <i>et al.</i> 1972). The alkaline/subalkaline divide of Swarzer and Rogers (1974) is also shown.	26
1.15	Alkalis-iron-magnesium (AFM) ternary plot of the studied dyke at Berreraig. The shaded area represents the Trotternish sill field of northern Skye (Gibson 1990). Also shown are the fractionation trends of the Skye lavas (1) (Thompson <i>et al.</i> 1972) and the Hawaiian alkali suite (2) (Macdonald and Katsura 1964).	27
1.16	Composition of the studied dyke plotted on the Ti/Y/Zr discriminant diagram of Pearce and Cann (1973). The scaling factors used in the diagram serve to bring the points into the centre of the triangle without altering their relative position (Pearce and Cann 1973)	27
2.1	Relationship between vitrinite and different chemical parameters of rank. After Teichmüller and Teichmüller (1979).	31
2.2	Coalification stages and vitrinite evolution, including coalification jumps in vitrinite. Modified from Teichmüller (1987).	32
2.3	Plot of vitrinite reflectance versus microwave power after 30 minutes. The red data	37

	point represents the unheated standard.	
2.4	Plot of vitrinite reflectance versus microwave heating time at 50% power. The red data point represents the unheated standard.	37
2.5	Schematic of the image analysis system for organic petrology at Trinity College Dublin.	40
2.6	Characterisation of the illumination disparity observed using the TCD vitrinite reflectance measurement system.	47
3.1	Correlation of some published amorphous kerogen terminology, also indicating biological precursor material and kerogen type. Modified from Tyson (1995).	50
3.2	Reproduction of Pearson's amended colour standard (version #2, 1984) used for visual AOM colour determinations in this study.	52
3.3	Plot showing RGB intensity of background illumination versus lamp voltage. The area enclosed by the dashed lines indicates the optimum voltage estimated for RGB colour work.	58
3.4	Microscope set-up used for AOM colour determination in this study.	59
3.5	JVC TK-C1380 video camera software set-up used in this study. The camera set-up screen operation buttons are located at the top of the camera.	59
3.6(a)	Camera white balance adjustment versus RGB intensity of background illumination. The dashed lines mark out a zone, within which the RGB values of the background illumination remain unchanged with changing camera white balance.	60
3.6(b)	Camera white balance adjustment versus RGB intensity of reference spore used for calibration in this study. The dashed lines mark out a zone, within which the RGB values of the background illumination remain unchanged with changing camera white balance.	60
3.6(c)	Background illumination used for this study (R = 232 G = 233 B = 231).	60
3.6(d)	Background illumination used by Yule <i>et al.</i> (1998) (R = 137 G = 170 B = 147).	60
3.6(e)	Reference spore used for calibration in this study (R = 213 G = 88 B = 43).	60
3.7	<i>EasyColour.Q5R</i> , <i>Image Setup</i> Dialog. The video and offset are set to "Standard Settings".	63
3.8	<i>EasyColour.Q5R</i> , <i>Colour Detect</i> Dialog. Regions of interest are detected by setting the RGB threshold values with the mouse button (note that the "Accumulate" checkbox is checked).	63
3.9	<i>EasyColour.Q5R</i> , <i>Binary Edit</i> Dialog. Using the mouse, the operator identifies regions of the binary image to measure (note that the "Accept" bullet box is checked).	64
3.10	<i>EasyColour.Q5R</i> , <i>Measure Feature</i> Dialog. An RGB measurement of the binary image will be completed when the <u>M</u> EASURE button is depressed.	64
3.11	Inconsistent Binary Detection during RGB measurement (a) Multiple determinations made on one spore (b) Multiple determinations made on one AOM particle. Note that the calculated mean RGB value for the AOM particle	65

	does not match the colour observed visually.	
3.12	Basis of fluorescence: the excitation of a substance by heat or light causes it to fluoresce. The fluorescent radiation is of lower energy (longer wavelength) than the excitation radiation.	67
4.1	Plot of mean random vitrinite reflectance (R_r) for the BBN sample horizon versus perpendicular distance from the dyke contact. The R_r values have \pm one standard deviation about the mean.	72
4.2	Plot of mean random vitrinite reflectance (R_r) for the BGSHN sample horizon versus perpendicular distance from the dyke contact. The R_r values have \pm one standard deviation about the mean.	73
4.3	Plot of mean random vitrinite reflectance (R_r) for the BGSN sample horizon versus perpendicular distance from the dyke contact. The R_r values have \pm one standard deviation about the mean.	74
4.4	Cumulative plot of mean random vitrinite reflectance for the BBN, BGSHN and BGSN sample horizons versus perpendicular distance from the dyke contact.	75
4.5	The temperature-rank nomogram. Determination of rank from (maximum) temperature and duration of reaction (i.e., geological time). The intersection of the time curve (in My) and of the temperature gives, on the abscissa a value for Z (rank) expressed above in % VR ₀ and % VM (after Karweil 1955, Teichmüller 1968 and Bostick 1971).	81
4.6	Hood <i>et al.</i> 's Level of Organic Metamorphism (LOM) diagram. The straight lines essentially represent a doubling of reaction rate with every 10°C temperature increase. After Hood <i>et al.</i> (1975).	81
4.7	Plot of vitrinite reflectance versus burial temperature. After Price (1983).	86
4.8	Plot of vitrinite reflectance versus burial time since attainment of 80% of present day (maximal) temperature for two temperature intervals, 60 - 75°C (lower, dots) and 100 - 120°C (upper, crosses). After Price (1983).	86
4.9	Peak temperature (T_{peak}) from reequilibrated fluid inclusions versus mean random vitrinite reflectance ($R_v = R_r$) for burial heating and hydrothermal metamorphism, based on data from Barker and Goldstein (1990), Aizawa (1989) and unpublished data. After Barker and Pawlewicz (1994).	89
4.10	Plot of peak palaeotemperatures, computed using Barker and Pawlewicz's (1994) geothermal VR-geothermometer, against perpendicular distance from the dyke contact for the BBN, BGSHN and BGSN sample horizons.	91
4.11	Plot of peak palaeotemperatures, computed using Barker's (1988) algorithm, against perpendicular distance from the dyke contact for the BBN, BGSHN and BGSN sample horizons.	92
4.12	Plot of peak palaeotemperatures, computed using Barker and Goldstein's (1990) algorithm, against perpendicular distance from the dyke contact for the BBN, BGSHN and BGSN sample horizons.	93
5.1	Comparison of AOM fluorescence colour against distance from the dyke contact for the BBN, BGSHN and BGSN sample horizons.	103

	point represents the unheated standard.	
2.4	Plot of vitrinite reflectance versus microwave heating time at 50% power. The red data point represents the unheated standard.	37
2.5	Schematic of the image analysis system for organic petrology at Trinity College Dublin.	40
2.6	Characterisation of the illumination disparity observed using the TCD vitrinite reflectance measurement system.	47
3.1	Correlation of some published amorphous kerogen terminology, also indicating biological precursor material and kerogen type. Modified from Tyson (1995).	50
3.2	Reproduction of Pearson's amended colour standard (version #2, 1984) used for visual AOM colour determinations in this study.	52
3.3	Plot showing RGB intensity of background illumination versus lamp voltage. The area enclosed by the dashed lines indicates the optimum voltage estimated for RGB colour work.	58
3.4	Microscope set-up used for AOM colour determination in this study.	59
3.5	JVC TK-C1380 video camera software set-up used in this study. The camera set-up screen operation buttons are located at the top of the camera.	59
3.6(a)	Camera white balance adjustment versus RGB intensity of background illumination. The dashed lines mark out a zone, within which the RGB values of the background illumination remain unchanged with changing camera white balance.	60
3.6(b)	Camera white balance adjustment versus RGB intensity of reference spore used for calibration in this study. The dashed lines mark out a zone, within which the RGB values of the background illumination remain unchanged with changing camera white balance.	60
3.6(c)	Background illumination used for this study (R = 232 G = 233 B = 231).	60
3.6(d)	Background illumination used by Yule <i>et al.</i> (1998) (R = 137 G = 170 B = 147).	60
3.6(e)	Reference spore used for calibration in this study (R = 213 G = 88 B = 43).	60
3.7	<i>EasyColour.Q5R</i> , <i>Image Setup</i> Dialog. The video and offset are set to "Standard Settings".	63
3.8	<i>EasyColour.Q5R</i> , <i>Colour Detect</i> Dialog. Regions of interest are detected by setting the RGB threshold values with the mouse button (note that the "Accumulate" checkbox is checked).	63
3.9	<i>EasyColour.Q5R</i> , <i>Binary Edit</i> Dialog. Using the mouse, the operator identifies regions of the binary image to measure (note that the "Accept" bullet box is checked).	64
3.10	<i>EasyColour.Q5R</i> , <i>Measure Feature</i> Dialog. An RGB measurement of the binary image will be completed when the <u>M</u> EASURE button is depressed.	64
3.11	Inconsistent Binary Detection during RGB measurement (a) Multiple determinations made on one spore (b) Multiple determinations made on one AOM particle. Note that the calculated mean RGB value for the AOM particle	65

	does not match the colour observed visually.	
3.12	Basis of fluorescence: the excitation of a substance by heat or light causes it to fluoresce. The fluorescent radiation is of lower energy (longer wavelength) than the excitation radiation.	67
4.1	Plot of mean random vitrinite reflectance (R_r) for the BBN sample horizon versus perpendicular distance from the dyke contact. The R_r values have \pm one standard deviation about the mean.	72
4.2	Plot of mean random vitrinite reflectance (R_r) for the BGSHN sample horizon versus perpendicular distance from the dyke contact. The R_r values have \pm one standard deviation about the mean.	73
4.3	Plot of mean random vitrinite reflectance (R_r) for the BGSN sample horizon versus perpendicular distance from the dyke contact. The R_r values have \pm one standard deviation about the mean.	74
4.4	Cumulative plot of mean random vitrinite reflectance for the BBN, BGSHN and BGSN sample horizons versus perpendicular distance from the dyke contact.	75
4.5	The temperature-rank nomogram. Determination of rank from (maximum) temperature and duration of reaction (i.e., geological time). The intersection of the time curve (in My) and of the temperature gives, on the abscissa a value for Z (rank) expressed above in % VR ₀ and % VM (after Karweil 1955, Teichmüller 1968 and Bostick 1971).	81
4.6	Hood <i>et al.</i> 's Level of Organic Metamorphism (LOM) diagram. The straight lines essentially represent a doubling of reaction rate with every 10°C temperature increase. After Hood <i>et al.</i> (1975).	81
4.7	Plot of vitrinite reflectance versus burial temperature. After Price (1983).	86
4.8	Plot of vitrinite reflectance versus burial time since attainment of 80% of present day (maximal) temperature for two temperature intervals, 60 - 75°C (lower, dots) and 100 - 120°C (upper, crosses). After Price (1983).	86
4.9	Peak temperature (T_{peak}) from reequilibrated fluid inclusions versus mean random vitrinite reflectance ($R_v = R_r$) for burial heating and hydrothermal metamorphism, based on data from Barker and Goldstein (1990), Aizawa (1989) and unpublished data. After Barker and Pawlewicz (1994).	89
4.10	Plot of peak palaeotemperatures, computed using Barker and Pawlewicz's (1994) geothermal VR-geothermometer, against perpendicular distance from the dyke contact for the BBN, BGSHN and BGSN sample horizons.	91
4.11	Plot of peak palaeotemperatures, computed using Barker's (1988) algorithm, against perpendicular distance from the dyke contact for the BBN, BGSHN and BGSN sample horizons.	92
4.12	Plot of peak palaeotemperatures, computed using Barker and Goldstein's (1990) algorithm, against perpendicular distance from the dyke contact for the BBN, BGSHN and BGSN sample horizons.	93
5.1	Comparison of AOM fluorescence colour against distance from the dyke contact for the BBN, BGSHN and BGSN sample horizons.	103

5.2	Comparison of AOM fluorescence colours against vitrinite reflectance (R_r) in the BBN, BGSHN and BGSN sample horizons.	104
5.3	(a) Plot of all RGB intensity data against distance from dyke contact for the BBN sample horizon. (b) Plot of mean RGB intensities against distance from dyke contact for the BBN sample horizon. An inverted vitrinite reflectance profile is included on a secondary axis for comparison.	111
5.4	(a) Plot of all RGB intensity data against distance from dyke contact for the BGSHN sample horizon. (b) Plot of mean RGB intensities against distance from dyke contact for the BGSHN sample horizon. An inverted vitrinite reflectance profile is included on a secondary axis for comparison.	112
5.5	(a) Plot of all RGB intensity data against distance from dyke contact for the BGSN sample horizon. (b) Plot of mean RGB intensities against distance from dyke contact for the BGSN sample horizon. An inverted vitrinite reflectance profile is included on a secondary axis for comparison.	113
5.6	(a) Plot of red intensity against green intensity for BBN, BGSHN and BGSN sample sets. (b) Plot of green intensity against blue intensity for BBN, BGSHN and BGSN sample sets. (c) Plot of red intensity against blue intensity for BBN, BGSHN and BGSN sample sets.	116
5.7	Plots of mean RGB intensity versus mean random vitrinite reflectance (% R_r) for the Bearerraig Bay samples: (a) BBN samples, (b) BGSHN samples, and (c) BGSN samples.	121
5.8	Plot showing relative mean RGB intensities of AOM against vitrinite reflectance for the BBN, BGSHN and BGSN sample horizons.	125
5.9	Plot of hue (H) against brightness (B) colour parameters for AOM from the BBN, BGSHN and BGSN sample horizons. TAI values for the BBN samples are included adjacent to the BBN H/B data points. The dashed lines enclose the H/B maturation pathway followed by the AOM. The HSB values are derived from measured RGB intensities.	127
6.1	Nomenclature for numerical solution of one-dimensional unsteady-state conduction.	135
6.2	The Schmidt Plot: graphical construction for one-dimensional unsteady-state conduction.	135
6.3	Input and output display examples of the Excel Visual Basic for Applications (VBA) simulation of the Schmidt Plot.	137
6.4	Apparatus used in this study for determination of thermal conductivity of rock. Inset: dimensions of solid brass cylinders used as part of the apparatus for the thermal conductivity experiments.	143
6.5	Thermal conductivity measurement: plots showing temperature gradients across the dyke lithology sample (BBD01).	144-145
6.6	Thermal conductivity measurement: plots showing temperature gradients across a sample of the BGSHN shale lithology (BGSH02N).	146
6.7	Thermal conductivity measurement: plots showing temperature gradients across a	147

	sample of the BGSN sandy limestone lithology (BGS04N).	
6.8	Mean range of thermal conductivity for abundant rock types. After Schön (1996).	149
6.9	Silicate liquidus temperatures at liquidus temperatures at 1 atm versus iron/magnesium ratios for selected Skye lavas. The dashed lines indicate the iron/magnesium ratios of two dyke samples from this study and their corresponding silicate liquidus temperature correlation on this diagram. Modified from Thompson <i>et al.</i> (1972).	153
6.10	(a) Modelled temperature as a function of distance from the dyke centre and time for 1 month after emplacement of the 1.3m thick dyke at Berreraig. (b) Modelled maximum temperature after 1 month as a function of distance from the dyke centre.	157
6.11	(a) Modelled temperature as a function of distance from the dyke centre and time for 5 years after emplacement of the 1.3m thick dyke at Berreraig. (b) Modelled maximum temperature after 5 years as a function of distance from the dyke centre.	158
6.12	Variation of T_{\max} with dyke thickness: maximum temperature (T_{\max}) after 2 years as a function of distance from the dyke margin for different thickness of dyke.	160
6.13	Variation of T_{\max} with magma flow time: maximum temperature (T_{\max}) after 5 years as a function of distance from the dyke margin for different durations of magma flow.	160
6.14	Variation of T_{\max} with thermal conductivity, k . (a) Maximum temperature (T_{\max}) after 1 month as a function of distance from the centre of a 1.3m thick dyke for 3 different k values. (b) Maximum temperature after 1 year as a function of distance from the centre of a 1.3m thick dyke for the same k values.	162
6.15	Variation of T_{\max} with T_{host} . Maximum temperature (T_{\max}) after 5 years as a function of distance from the centre of a 1.3m thick dyke for different initial host rock temperatures (T_{host}).	164
6.16	Variation of T_{\max} with T_{magma} . Maximum temperature (T_{\max}) after 5 years as a function of distance from the centre of a 1.3m thick dyke for different initial magma temperatures (T_{magma}).	164
6.17	Modelled range of T_{\max} after 5 years, as a function of distance from the centre of the 1.3m thick dyke at Berreraig. The lines on the plot represent the modelled maximum temperature (T_{\max}) for the upper and lower temperature scenarios described above.	166
7.1	Comparison of T_{\max} range predicted by the Schmidt conductive cooling model and measured VR-derived peak palaeotemperature (T_p) data, computed using the algorithms of (a) Barker (1988), (b) Barker and Goldstein (1990), (c) Barker and Pawlewicz (1994, geothermal), versus distance from the dyke contact.	170
7.2	Comparison of model T_{\max} and VR-derived peak temperatures (T_p) versus distance from the dyke contact. The model-derived maximum temperature profile is computed, based on the adjusted thermal parameters described in the text. VR-derived peak palaeotemperatures (T_p) are computed using the geothermal VRG of Barker and Pawlewicz (1994).	171

7.3	Modelled temperatures at various distances from the dyke contact as a function of time, based on the thermal parameters listed in Table 6.3.	174
7.4	Modelled heating time above vitrinite T_p (from Barker and Pawlewicz's (1994) geothermal VRG) versus observed disparity between modelled and VR-derived temperatures.	175
7.5	Modelled heating time within 15°C above vitrinite T_p (from Barker and Pawlewicz's (1994) geothermal VRG) versus observed disparity between modelled and VR-derived temperatures.	175
7.6	Plot of reaction extent (kerogen weight loss in %) versus heating time for kerogen at various temperatures. After Ishiwatari <i>et al.</i> (1977).	177
7.7	Schematic flow diagram to illustrate the control exerted by the capacity of the vitrinite microporous network. After Carr (2000).	177
7.8	(a) Translated peak temperatures and associated error range, based on standard deviations of measured VR data, as a function of distance from the dyke contact. (b) Variation of standard deviation on measured VR data with distance from the dyke contact. (c) Error range of translated temperatures, based on standard deviations on measured VR data, versus distance from the dyke contact. Translated temperatures after Barker and Goldstein (1990).	179
7.9	Construction of error bars on VR-translated temperatures.	180
7.10	Increase of coalification between the stages of bituminous coal and graphite, on the basis of hydrogen content and of optical reflectance of vitrinite (R_{max} , R_r , R_{min}). After Ragot (1977).	180
7.11	Experimentally derived VR-temperature calibration of Bostick (1970, 1971) and Bostick and Pawlewicz (1984). Reflectance of 'low-gray fragments' from 'hydrothermal bomb' samples – shown as approximate plots of frequency of readings with a particular reflectance value. The mean value is marked by an "x". After Bostick (1970).	182
7.12	Comparison of temperatures, estimated using Bostick's (1970, 1971) experimentally derived calibration curve, and T_{max} range predicted by the Schmidt conductive cooling model, versus distance from the dyke contact.	183
7.13	Four models of cooling in a host rock after intrusion of an igneous dyke, as described by Barker <i>et al.</i> (1998).	185
7.14	(a) Plot of VR-derived temperatures from each of the sample horizons, translated using the calibration of Barker and Pawlewicz (1986), as a function of normalised distance from the dyke contact (X/D). (b) Plot of R_r and mean AOM RGB intensity data from the BBN sample horizon as a function of X/D .	187
7.15	Major element oxide abundances (Wt. %) for selected samples from the BBN shale horizon plotted as a function of distance from the dyke contact (X/D). For comparison, % R_r data for the same samples are also plotted on the right hand axis.	188
8.1	Relationships of maturation indices from the studied sample horizons	194

LIST OF TABLES

Table No.	Table Caption	Page
1.1	Maturity of the Waterloo Mudstone Formation at Island Magee, Larne.	8
1.2	Background maturity of Pabay Shales at Carn Dearg, Loch Eishort, central Skye.	17
1.3	Maturity of Pabay Shales at Waterloo, Broadford Bay, central Skye.	19
1.4	Sample details from Berreraig Bay locality, northeast Skye.	21
2.1	Stages of oil maturation in relation to vitrinite reflectance (after Taylor <i>et al.</i> 1998). The limiting values of vitrinite reflectance may vary depending on thermal history and kerogen type.	28
2.2	Subdivision of the vitrinite maceral group according to the ICCP System 1994 (ICCP 1998)	29
2.3	Time/power programs, operator codes and vitrinite reflectance results for samples used in <i>Microdigest</i> experiment.	38
2.4	Reflectance standards used for calibration in this study. R_o indicates reflectance under oil and R_a indicates reflectance in air, i.e., without any medium between the sample and the microscope objective.	42
2.5	QUIPS routines used for vitrinite reflectance work in this study and the reflectance standards used for calibration.	42
2.6	% R_o and standard deviation data within calibration frame, full measure frame and limiting frame for reflectance standards used in <i>LowReflectance.Q5R</i> and <i>MedReflectance.Q5R</i> .	46
4.1	Maximum and minimum values of T_{peak} for the three sample horizons, computed via the VR-temperature models of Barker and Pawlewicz (1994, geothermal), Barker (1988) and Barker and Goldstein (1990).	94
5.1	% R_r , TAI and mean RGB intensity levels of samples used in single factor ANOVA.	118
5.2	ANOVA table, demonstrating the sources of variances for Red Green and Blue parameters.	119
6.1	Measured thermal conductivity values of rocks from Berreraig Bay.	148
6.2	Geochemical analyses data of Berreraig dyke samples. Normalised data calculated using PETRO.CALC.PLOT (Sidder 1994).	152
6.3	Thermal parameters used to model temperature distribution in the studied dyke and host rocks at Berreraig, and methods used to estimate same.	156
6.4	Effect of thermal conductivity on cooling rate.	161
6.5	Variation of $T_{contact}$ with T_{magma} and duration of magma flow.	163
6.6	Thermal parameters used to model the range of Tmax for the Berreraig Bay dyke and host	165

CHAPTER 1

INTRODUCTION

1.1 AIMS OF THIS PROJECT

The main objective of this research was to devise methods of distinguishing between Jurassic hydrocarbon source rocks which have undergone 'normal' burial maturation and rocks which have attained the same maturation level partly due to their proximity to igneous intrusions. Vitrinite reflectance, palynomorph colour and palynomorph fluorescence are widely used as parameters of organic maturation. Correlations between these organic maturity parameters are well established for 'normal' burial systems (Epstein *et al.* 1977; Héroux *et al.* 1979; Teichmüller 1987; Clayton *et al.* 1989, and others) (Figure 1.1). These correlations extend to stages of hydrocarbon generation and peak palaeotemperature (T_{peak}), through calibration of vitrinite reflectance. However, a number of workers have reported marked deviations from the established maturity correlations in areas of enhanced heat flow, such as the contact zones of igneous intrusions (Fitzgerald 1994; Goodhue 1996; McCormack *et al.* 1997). This can have some important implications for sediments at or just below the oil window (e.g., much of the Jurassic in NW Europe).

By investigating Jurassic sections adjacent to Tertiary igneous dykes, the thermal response rates of the various organic maturity indicators to short-term high temperature heating events are appraised. As part of this project, image analysis methods were used to establish a new system for vitrinite reflectance measurement at Trinity College. Colour image analysis (CIA) techniques were used to 'quantitatively' determine kerogen colour. Due to a paucity of suitable palynomorphs in the sampled rocks, a colour evaluation of amorphous organic matter (AOM) was completed. AOM, the dominant component of oil-prone kerogen, proved to be an acceptable alternative to palynomorphs for kerogen colour evaluation. Visual colour estimates of AOM were also made and compared with results obtained from the quantitative colour determinations.

Vitrinite Reflectance Rm %	Conodont Alteration Index CAI	Thermal Alteration Index TAI	Spore Fluorescence	Maturation Zone	Hydrocarbon Generation
0.6	1				
	1.5	2	+ ve	ZONE 1	
1.2	2				
2.0	3	3		ZONE 2	O
	3.5				C
3.0	4	4		ZONE 3	D
4.0	4.5				
	5	5		ZONE 4	
5.0	6 - 7				

Figure 1.1. Correlation of maturation indices. **O** = oil, **C** = condensate and wet gas, **D** = dry gas. After Clayton *et al.* (1989).

Using a computer simulation of conductive heat transfer, the thermal history of the rocks adjacent to the dyke was mathematically modelled and compared with measured maturity data from the aureole.

1.2 REQUIREMENTS OF SAMPLING LOCALITY

The aureoles of thin igneous dykes provide ideal study material for investigating the maturation effects of short-term heating events on sedimentary rocks. The selection of a suitable sampling locality was problematic. Material was required from a locality with readily accessible, organic-rich Jurassic sediments, cut by minor intrusions. Since this study was primarily concerned with the effects of maturation, the extent of burial, both before and after intrusion, needed to be as low as possible, so that changes related to the dyke intrusion were not overprinted by later thermal events. A low background maturity level also offers a more complete picture of any thermally dependent sedimentary organic process. The dyke needed to be of sufficient thickness to provide a zone of thermal alteration wide enough to allow the collection of an adequate amount of study material, yet thin enough for irregularities in the surrounding outcrop not to interfere with sampling. The geometry of the intrusion needed to be as simple as possible for modelling purposes. In this respect, the simplest scenario envisaged would be a vertical dyke intruded into horizontal strata, to give an even distribution of heat into the adjacent country rock.

Every effort was made to ensure samples were collected along a single sedimentary horizon in the hope that any observed compositional variation in sedimentary organic content would be due to differences in the extent of thermal alteration, rather than differences in depositional environment or organic matter type.

1.3 SAMPLING FOCUS

The UK North Atlantic margin contains numerous sedimentary basins of Permian to Tertiary age, and is characterised by extensive igneous activity, mostly of Early Tertiary

age. This igneous activity was related to Late Cretaceous-Early Tertiary rifting, which led to the separation of Europe from Greenland, and ultimately to the present day continental margin. As a result, both intrusive and extrusive volcanic rocks are widespread in this region. Many of these Tertiary intrusions invade Jurassic sedimentary rocks, which form part of the infill of these basins.

During the course of this study, sampling was focused on two broad onshore areas: Northern Ireland and the Isle of Skye. Both of these areas contain Jurassic, organic-rich strata intruded by numerous Tertiary intrusions associated with the opening of the North Atlantic Ocean. A number of localities were sampled and run for 'background' maturity analysis. While all the localities sampled are detailed here, only the Bearreraig Bay locality on the Isle of Skye provided study material of adequate quality to warrant further investigation.

1.4 NORTHEAST IRELAND

Jurassic sedimentary rocks exposed onshore in northeast Ireland constitute part of the Ulster Basin (Figure 1.2). The Ulster Basin comprises the Rathlin Trough and Lough Neagh-Larne Basin, together with the offshore North Channel Basin. The basin contains rocks ranging from Permian to Tertiary in age. Mesozoic sediments seen at outcrop range in age from Upper Triassic to Lower Liassic, overlain unconformably by Upper Cretaceous strata. These have been protected from erosion by the cover of Early Tertiary plateau basalts, but their preservation is probably also due to the existence of thicker sequences in this region than elsewhere (Naylor 1992). Jurassic rocks younger than Lower Liassic age are not preserved onshore in northeast Ireland due to pre-Cretaceous erosion. Consequently, the thickness of the Lower Lias sediments in the Ulster Basin is greatly variable. The thickest sequence is found in the Rathlin Trough, where almost 250m of Sinemurian to Lower Pliensbachian rocks are recorded from the Port More borehole (Naylor 1992). Generally, however, only the Hettangian to lowest Sinemurian are preserved. A major erosional unconformity exists between the Lower Lias and Upper Cretaceous Greensand and Chalk, and derived Middle and Upper Liassic fossils have been

recorded in basal Cretaceous conglomerates in north Antrim (Wilson 1972). The Chalk or Ulster White Limestone Formation reaches a maximum thickness in the Ballycastle area, where more than 120m is preserved. Over 500m of plateau basalts of the Tertiary Antrim Lava Group (Palaeocene) form a cover of variable thickness on the Upper Cretaceous White Limestone. A number of sills, dykes and small volcanic necks are associated with these flows, several of which penetrate the Lower Lias succession. The onshore stratigraphy of northeast Ireland has been summarised by a number of authors (Wilson 1972; Naylor and Shannon 1982; McCann 1990, 1991; Naylor 1992).

There are a number of localities in northeast Ireland where Liassic strata are intruded by Tertiary igneous intrusions. In north Antrim Lower Liassic strata of the Rathlin Trough are exposed at Portrush, near Ballintoy at White Park Bay, and at Portnakillew (Wilson 1972). However, only at the Portrush and Ballintoy areas have they been intruded by Tertiary igneous intrusions.

At Portrush they have been metamorphosed by the Portrush Sill to produce a hard hornfels. This 'Portrush Rock', has an igneous appearance but contains recognisable fossils including ammonites. It was once cited by the Neptunists as proof that igneous rocks were formed by sedimentary processes. Accordingly, it is now a site of special scientific interest (S.S.S.I.) and sampling is not permitted. At White Park Bay near Ballintoy, Lower Liassic mudstones are intruded by two Tertiary dykes. However, poor exposure of the Lias on the sandy beach precluded any sampling here.

Further south around Larne, basal Liassic strata of the Waterloo Mudstone Formation (Hettangian) are exposed. These are intruded by thin Tertiary dykes immediately north of Larne Lough at Waterloo, and on the western side of Island Magee (Figure 1.3). A couple of reconnaissance samples were collected from the Island Magee locality and these were investigated for vitrinite reflectance and organic matter fluorescence. These initial analyses indicate that the maturity of the samples was too high for modelling purposes and further sampling was abandoned (Table 1.1).

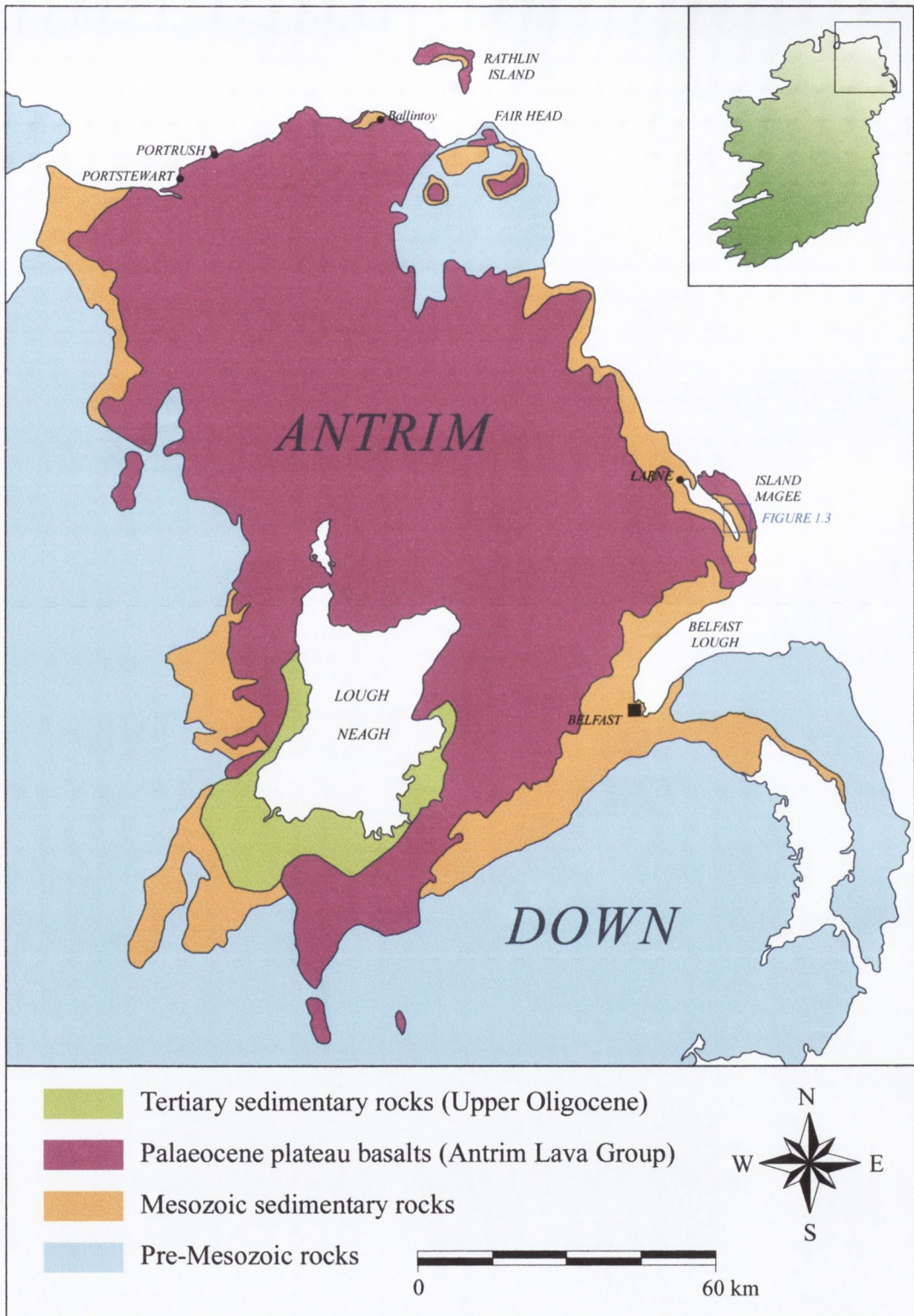


Figure 1.2. Geological summary map of the Ulster Basin area, onshore northeast Ireland.

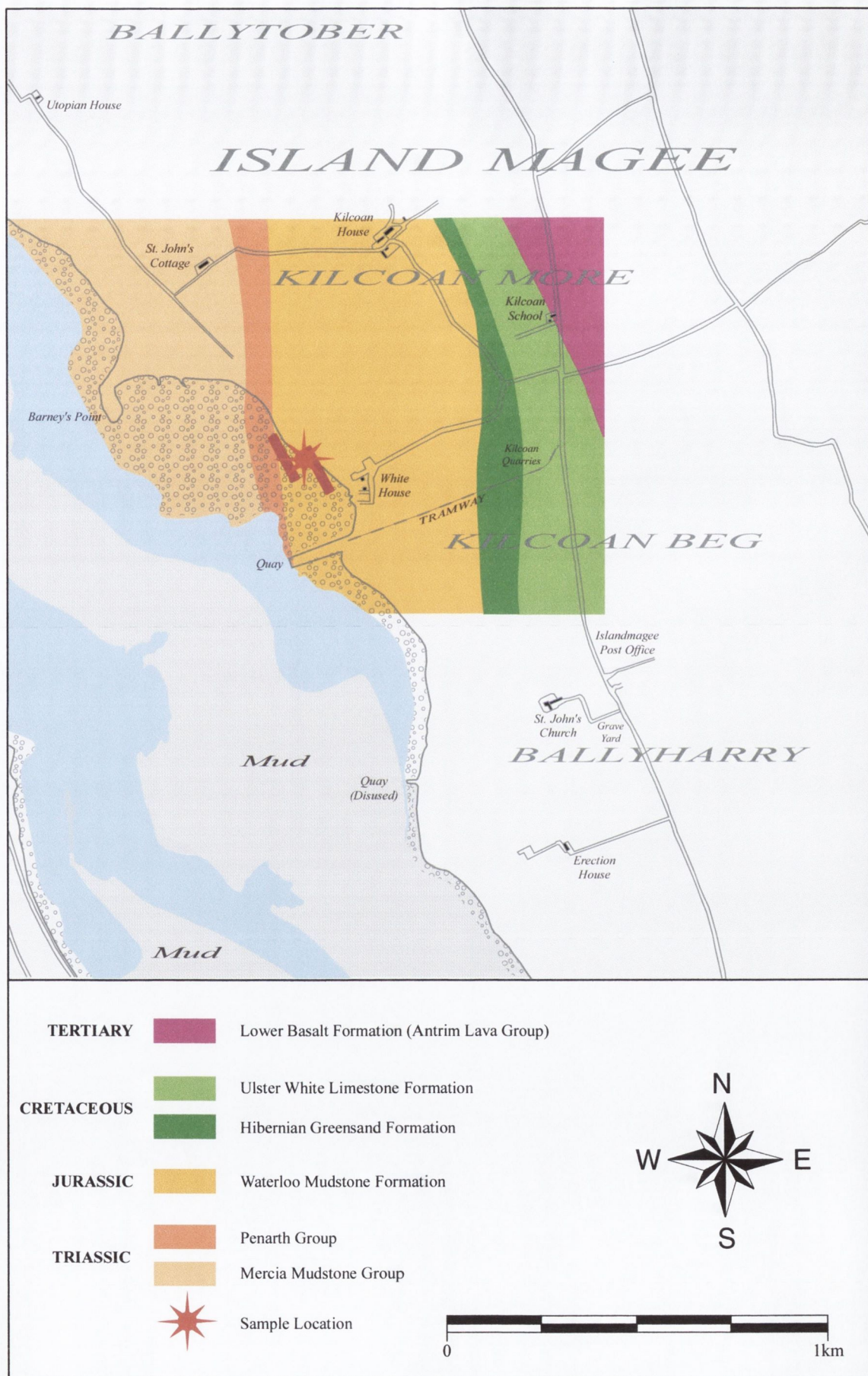


Figure 1.3. Location of sampled dyke and adjacent mudstones at Island Magee, Lame, northeast Ireland.

Sample	Details	R_r (%)	OM Fluorescence
WH03	Island Magee, 4m from dyke	1.23	No fluorescence

Table 1.1 Maturity of the Waterloo Mudstone Formation at Island Magee, Larne.

1.5 ISLE OF SKYE

Jurassic sedimentary rocks crop out on a number of the islands of the Inner Hebrides and adjacent parts of the Western Highlands of Scotland (Morton and Hudson 1995). They constitute part of the Sea of the Hebrides Basin, which subsided throughout the Triassic and Jurassic. During Early Tertiary rifting stages, the Hebrides area was the site of intense igneous activity resulting in the intrusion of numerous dykes into the Jurassic strata. On the Isle of Skye, Jurassic rocks crop out mainly along the east coast, at the margins of the overlying Tertiary plateau basalt lavas that cover wide areas of the Inner Hebrides.

Samples were collected on the Isle of Skye in two phases: April 1999 and December 1999. In April 1999 samples were collected from Eishort, central Skye and from Berreraig Bay, northeast Skye. During the second phase of sampling in December, samples were collected from Broadford Bay, central Skye and the Berreraig Bay locality was re-sampled.

1.5.1 MESOZOIC SEDIMENTATION HISTORY

Mesozoic sediments seen at outcrop in the Hebridean area range in age from Upper Triassic to Lower Kimmeridgian, overlain unconformably by Upper Cretaceous (Morton and Hudson 1995). These sediments rest unconformably on basement, ranging in age from Proterozoic Torridonian sediments (Applecross, Raasay, Skye) and Moine Schists (Ardnamurchan), to Cambro-Ordovician Durness Limestone (central Skye), Devonian Old Red Sandstone (Mull) and Carboniferous (Morvern) (Morton and Hudson 1995) (Figures 1.5 and 1.6). Mesozoic sedimentation in the Hebridean area occurred within a complex half-graben, between tectonically positive areas to the west (Outer Hebrides Platform) and

to the east (Scottish Highlands landmass) (Hudson 1983; Morton 1987; Searl 1994; Morton and Hudson 1995) (Figure 1.4). The Jurassic seas of the Hebrides Basin formed part of a network of narrow waterways that connected the Tethys in the south to the Boreal ocean in the north (Ziegler 1990). Deposition throughout occurred mainly under shallow marine conditions.

Mesozoic sedimentation in the Hebridean area accompanied three phases of rapid subsidence, each of which was followed by subsequent phases of much slower subsidence rates (Morton 1987). The Lower Jurassic strata are mostly of shallow marine origin and have a varied lithology, dominated by sandstones, limestones and shales. The lithostratigraphic nomenclature for the mid-Sinemurian part of the succession is unsettled, and the scheme used here is after Hesselbo *et al.* (1998). The earliest Jurassic deposits in the Skye area comprise the shallow water mixed carbonates and siliciclastics of the Broadford Formation (Hettangian to earliest Sinemurian). An abrupt transition to deeper water argillaceous facies at the base of the overlying Pabay Shale Formation is the local expression of a major regional deepening that occurred in the early Sinemurian (Hesselbo *et al.* 1998). With this major relative sea level rise, the dominant siliciclastic character of the basin was established, and it persisted for the remainder of the Jurassic (Hesselbo and Coe 2000). The Pabay Shale is terminated abruptly with the deposition of the Scalpa Sandstone, which marks a regional shallowing during the Late Pliensbachian. The initial Late Triassic to early Toarcian phase of rapid subsidence, was followed by slower subsidence during most of the Toarcian. This may be explained by regional sediment starvation at this time (Hesselbo and Coe 2000). The Toarcian succession comprises organic-rich shale of the Portree Shales, oolitic ironstone of the Raasay Ironstone, and mudstone of the Dun Caan Shale (Uppermost Toarcian – Aalenian).

A more rapid phase of subsidence occurred during the Middle Jurassic, beginning in the latest Toarcian and continuing until sometime in late Bathonian (~161 Ma) (Morton 1987). The Middle Jurassic of the Inner Hebrides is around 500m thick and consists of three major divisions: the Bearreraig Sandstone Formation, the Great Estuarine Group, and the Staffin Bay Formation. The Bearreraig Sandstone Formation is between 150 and 180m thick in north Skye, and comprises medium to coarse-grained, tidally generated, cross-bedded sandstones, and subordinate shales.

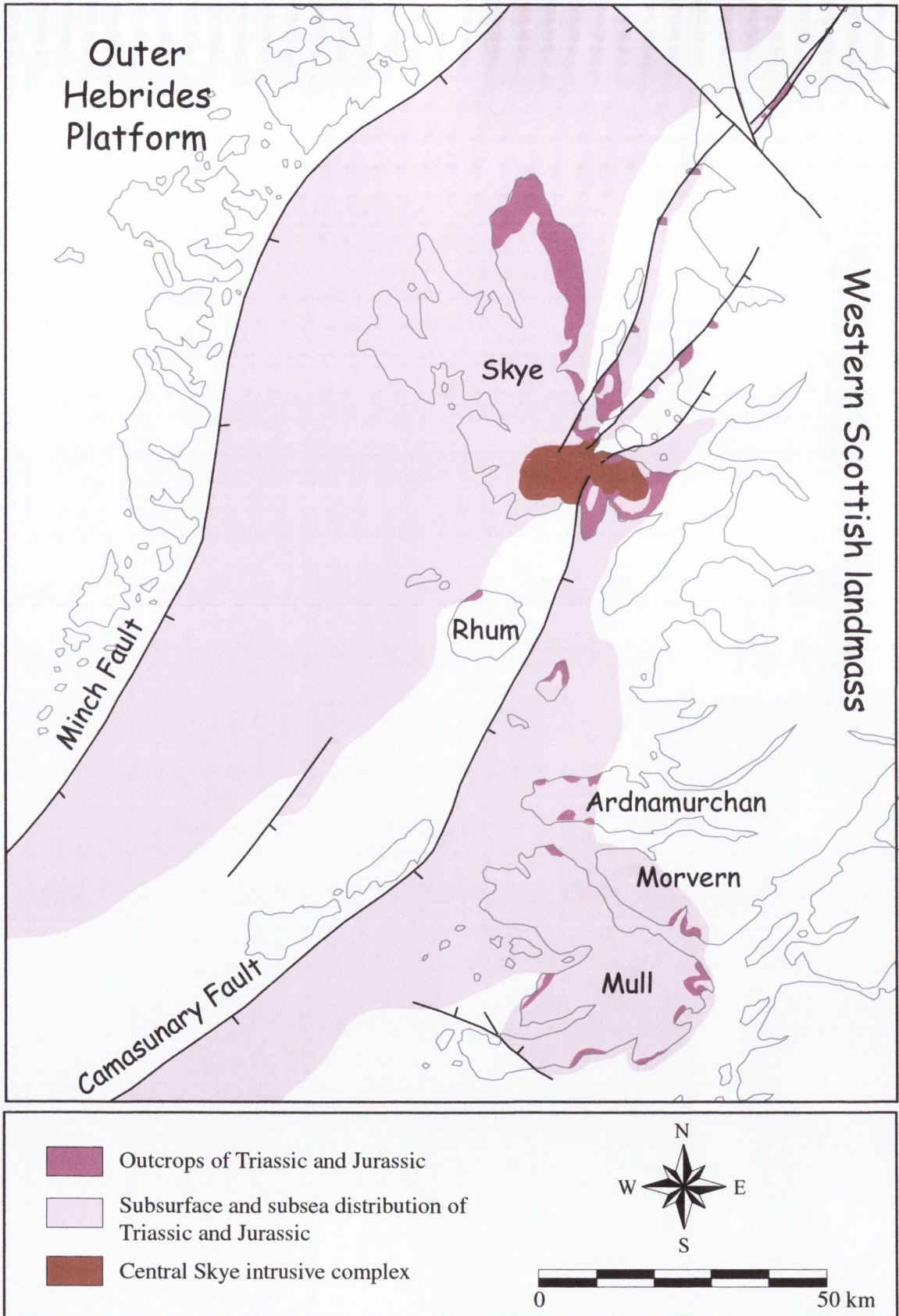


Figure 1.4. Map of the Hebrides Basin, showing present distribution of Triassic and Jurassic rocks. Modified from Morton & Hudson (1987).

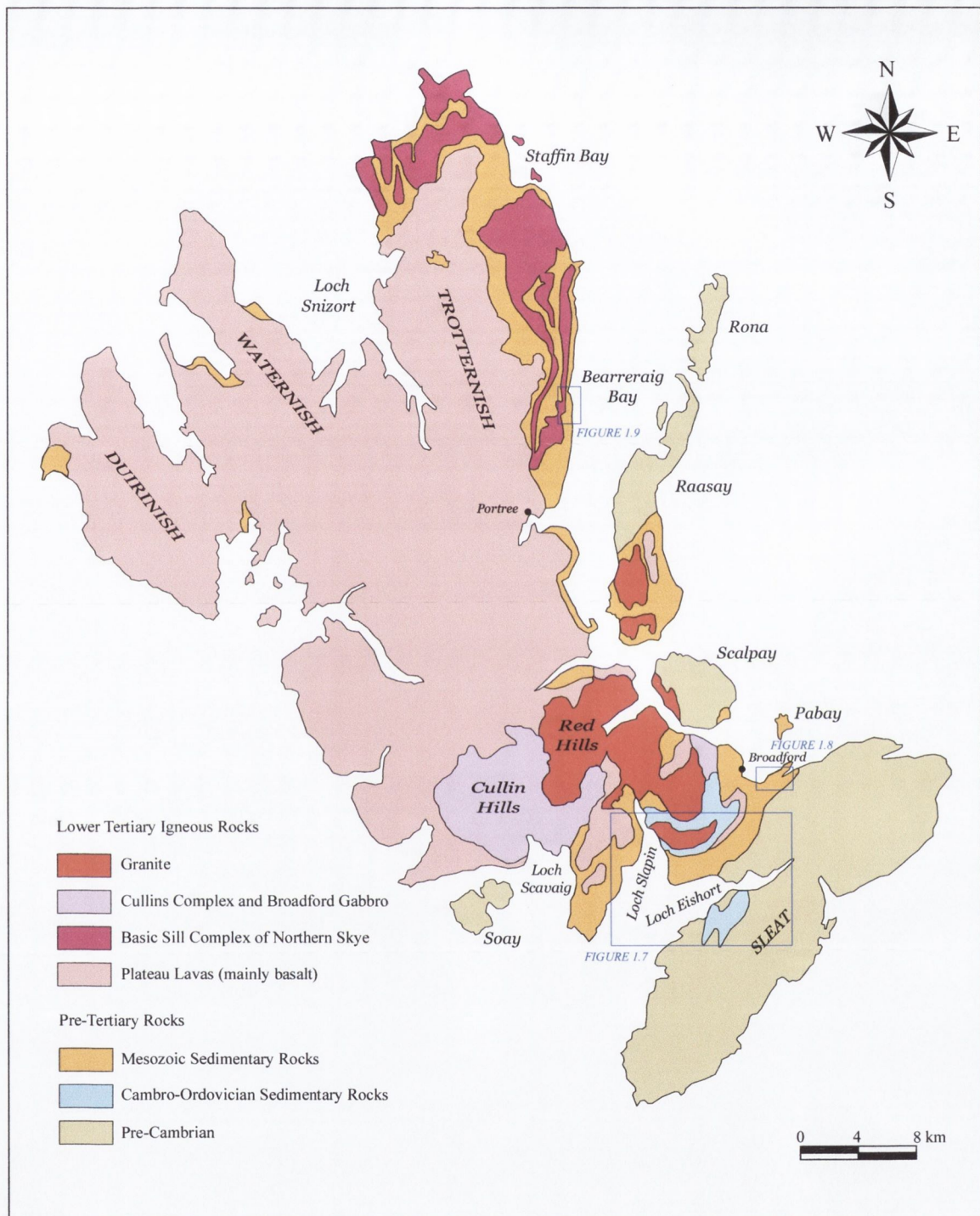


Figure 1.5. Geological summary map of the Isle of Skye

The sandstones sharply overlie the basal Dun Caan Shale Member and are abruptly blanketed by the Garantiana Clay Member. The succession is interpreted to have been deposited largely at the mouth of a macrotidal estuary (Mellere and Steel 1996). Whilst the Bearreraig Sandstone Formation is largely of marine origin and well dated by ammonites, the mostly Bathonian Great Estuarine Group represents a complex of lagoonal, deltaic and fluvial environments of quite varied salinity and lithology (Morton and Hudson 1995). The base of overlying Staffin Bay Formation marks an important marine transgression in the Middle Jurassic succession and has been dated as essentially lower Callovian in age (Sykes 1975). It consists of a coarsening upward succession and has been interpreted as a transgressive lagoon-barrier bar complex (Hudson 1983).

Following this, there was a third phase of rapid subsidence beginning in the early Oxfordian (~154 Ma). The limited evidence available suggests that on Skye, this phase of subsidence continued at least until the early Kimmeridgian. Later parts of this phase (above early Kimmeridgian, 143 Ma) are not preserved in the Hebrides region, but may have continued until basin inversion took place sometime in the Latest Jurassic to Early Cretaceous. Some limited reburial may have followed, before renewed uplift and erosion in the latest Cretaceous (Bell and Harris 1986; Morton 1987; Searl 1994).

1.5.2 TERTIARY IGNEOUS HISTORY

During early Tertiary rifting stages, between 63 and 52 Ma (Mussett *et al.* 1988), the Hebrides area was the site of intense igneous activity. Igneous activity on Skye spanned about 6 My, beginning around 59 Ma, with the development of thick plateau basalts over much of central and northern Skye (Anderson and Dunham 1966; Emeleus 1983; Bell and Harris 1986; Mussett *et al.* 1988). On Skye, the earliest activity was of an explosive nature resulting in deposits of basaltic ash up to 30m thick in north Skye (Bell and Harris 1986). The initial lavas erupted onto an irregular surface of rocks of varying age. If the observed lava sequence on Skye had been built up by the vertical emplacement of flows, the total thickness of the lava field would have exceeded 2130m (7000 ft) (Anderson and Dunham 1966). However, the distribution of lava types on Skye suggests that they were extruded over a considerable period of time from several fissures related to a central volcano. Thus,

the lava pile in north Skye is thought to have been built up by overlapping flows from several fissures opening at different times and in different places, forming an interleaved series which in any one place need not have exceeded 1200m (4000 ft) in thickness (Anderson and Dunham 1966). Rapid erosion of the lava pile occurred soon after the cessation of igneous activity and any burial resulting from the igneous extrusion is thought to have been on a geologically short timescale (Thrasher 1992).

Lava extrusion was followed by the development of several high-level central intrusive complexes in central and southern Skye. The earliest of these is the dominantly mafic, Cuillin centre, which is some 15 x 10km in extent and intrudes the earlier Tertiary lavas, and Mesozoic and Torridonian sediments. This was followed successively by the groups of granitic intrusions forming the Western Red Hills and Eastern Red Hills centres. Numerous dyke intrusions are often temporally and spatially associated with the central intrusive complexes (Emeleus 1982). These complexes have caused intense baking, reconstitution and melting of the host sediments into which they intruded. Stable isotope evidence suggests that large hydrothermal systems, associated with these intrusive centres, developed at this time (Taylor and Forester 1977). Apatite fission track analysis (AFTA) of the Jurassic sediments from Berreraig Bay suggests that the geothermal effects related to the intrusions extend to approximately a 10km radius around the centres (Lewis *et al.* 1992). Using biomarker methods, Thrasher (1992) suggested that the hydrothermal effects of the Cuillin igneous intrusive complex extended to as much as 15km from the complex margin.

Some time after the extrusion of the lavas, a major sill complex, the Trotternish Sill Complex, intruded the sedimentary rocks of north Skye. The complex, which is thought to have a focal point locally at depth (Anderson and Dunham 1966), is intruded mainly into Jurassic strata, below the lava plateau. The complex has a total thickness of 250m, with individual sills achieving in excess of 90m (Bell and Harris 1986). This has caused local metamorphism of the sediments directly underneath, however sediments more than *ca.* 100m below the contact are unaffected (Thrasher 1992). The final phase of igneous activity was the further development of dyke swarms in a regional intrusive event. Subsequently the area was uplifted and eroded during the Late Tertiary and Pleistocene.

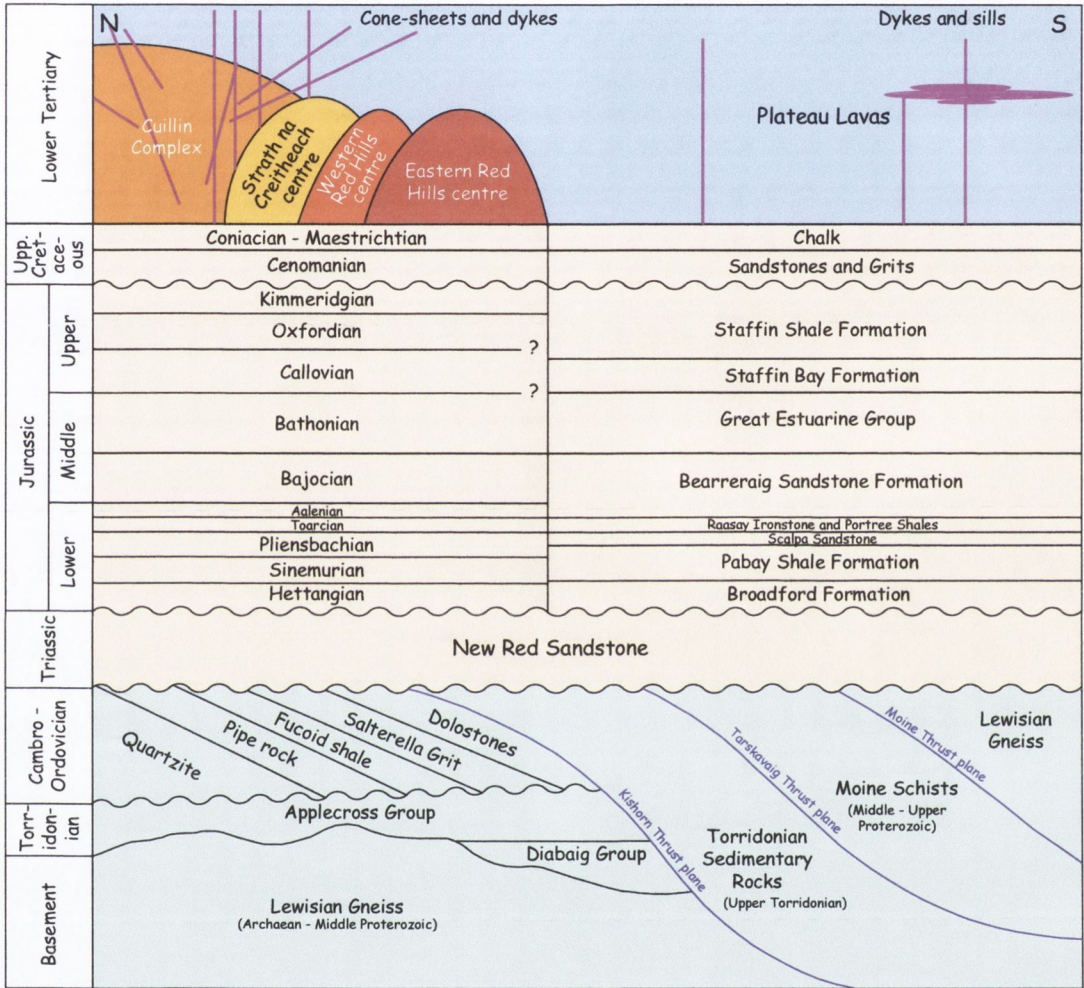


Figure 1.6. Stratigraphic relationships on the Isle of Skye. Modified from Bell & Harris (1986).

Igneous dykes of Tertiary age are present throughout the Isle of Skye and adjacent islands. Apart from those closely associated with the major intrusive centres, the dykes generally trend between NNW-SSE and NW-SE and constitute a major regional dyke swarm which extends over an area of over 4000km² from Lewis and Harris, through Skye to the Great Glen (Speight *et al.* 1982). The majority of these dykes are less than 2m wide, and are mainly either alkali olivine dolerites or tholeiites, although less common types have been identified (Bell and Harris 1986). The thickest dykes occur close to the intrusive centres, and some examples are up to 40m thick. Most of the dykes are vertical or near vertical and are discordant to the units, which they cut. Some undoubtedly represent solidified feeders to the fissure eruptions which produced the extensive plateau lavas in the area (Speight *et al.* 1982). However, they continued to be emplaced during the development of the central complexes and for some time afterwards, until igneous activity in the Hebrides finally waned between 55 and 52Ma (Mussett *et al.* 1988).

1.5.3 CARN DEARG, LOCH EISHORT

Lower Jurassic strata crop out along the northern shore of Loch Eishort, central Skye, between Boreraig and Suishnish. A low cliff section due south of Carn Dearg, exposes near horizontally bedded micaceous, silty mudstones and sandstones of the Pabay Shale Formation (Sinemurian-Pliensbachian), which are cut by a near vertical, 0.7m thick dyke (Figure 1.7). The section is best accessed by way of a narrow track off the B8083 Broadford to Elgol road. The track begins at Camas Mallag and continues southwards to Suishnish. From there, a narrow sheep trail leads eastwards down to the foreshore.

A total of 50 samples were collected from a single horizon adjacent to, and at increasing distances from, the dyke contact. The mudstones on both (east and west) sides of the dyke were sampled. A further 11 samples were collected from a thin (*ca.* 8cm thick) sandstone bed approximately 1.5m below the mudstone horizon west of the dyke, to investigate the effect of lithologically-controlled thermal conductivity variations on the transfer of heat away from the cooling dyke.

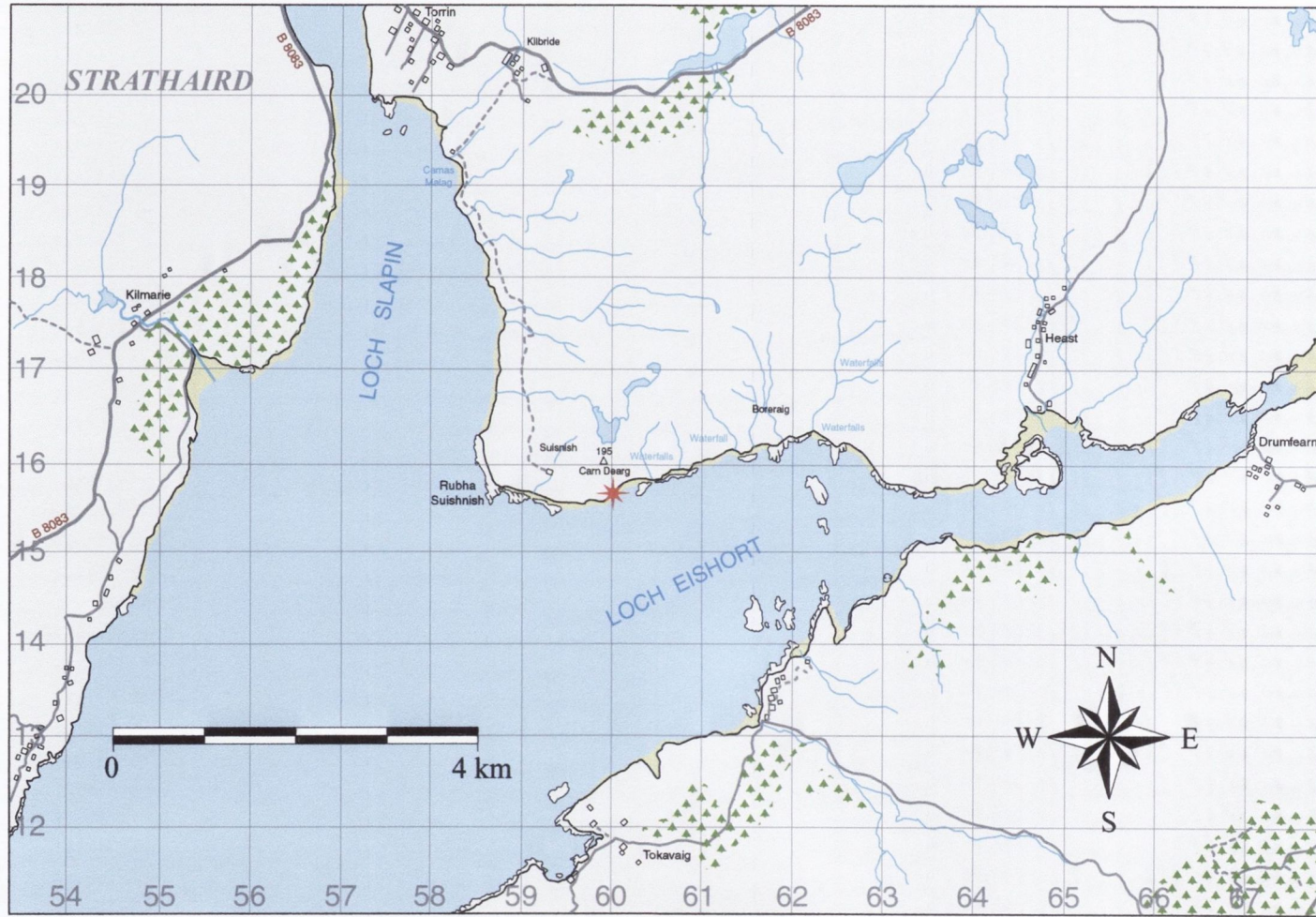


Figure 1.7. Map showing location of samples collected from Carn Dearg, Loch Eishort, central Skye

A number of 'background' samples were investigated for organic matter fluorescence and vitrinite reflectance. However, initial analysis of these samples proved them to have an elevated organic maturity relative to the regional maturity level and further analysis was abandoned. The reason for their elevated maturity is almost certainly the proximity of the sampling site to the Red Hills granite complex *ca.* 3km to the north. The maturity of the westernmost background sample is higher than its eastern counterpart. This is probably due to a large gabbro-peridotite sheet further up the hill, *ca.* 15m to the west of the dyke, which has altered the sediments below.

Sample	Formation	Lithology	R_r (%)	OM Fluorescence
CD26E	Pabay Shale	Shale, 18m from eastern dyke contact	2.17	No fluorescence
CD25W	Pabay Shale	Shale, 5.7m from western dyke contact	2.45	No fluorescence

Table 1.2 Background maturity of Pabay Shales at Carn Dearg, Loch Eishort, central Skye.

1.5.4 BROADFORD BAY (WATERLOO)

Lower Jurassic strata are extensively exposed in the low-lying area around Broadford Bay, central Skye. The best and most accessible sections are in the northeast part of the bay, where the gently dipping shales, silts and sandstones of the basal part of the Pabay Shale Formation (Uppermost Hettangian – Sinemurian) crop out. Numerous minor intrusions include several dolerite sills, dolerite and felsite dyke complexes (Morton and Hudson 1995). The beds are displaced by numerous small NW-SE trending faults.

Samples were collected from a foreshore platform at Waterloo (Figure 1.8), where a near-vertical dolerite dyke, 0.85m thick, intrudes micaceous silty shales of the basal Pabay Shale Formation. The dyke strikes 310° and both the dyke and country rocks are offset by 4m, by a small, NW-SE trending fault. Detailed sampling was conducted on both east and west sides of the dyke. A total of 47 samples were collected from a single horizon adjacent to, and at increasing distance from the dyke contacts. A number of background samples were investigated for organic matter fluorescence and vitrinite reflectance. However, initial analysis of these samples proved these also to have an elevated organic maturity level and further analysis was abandoned.

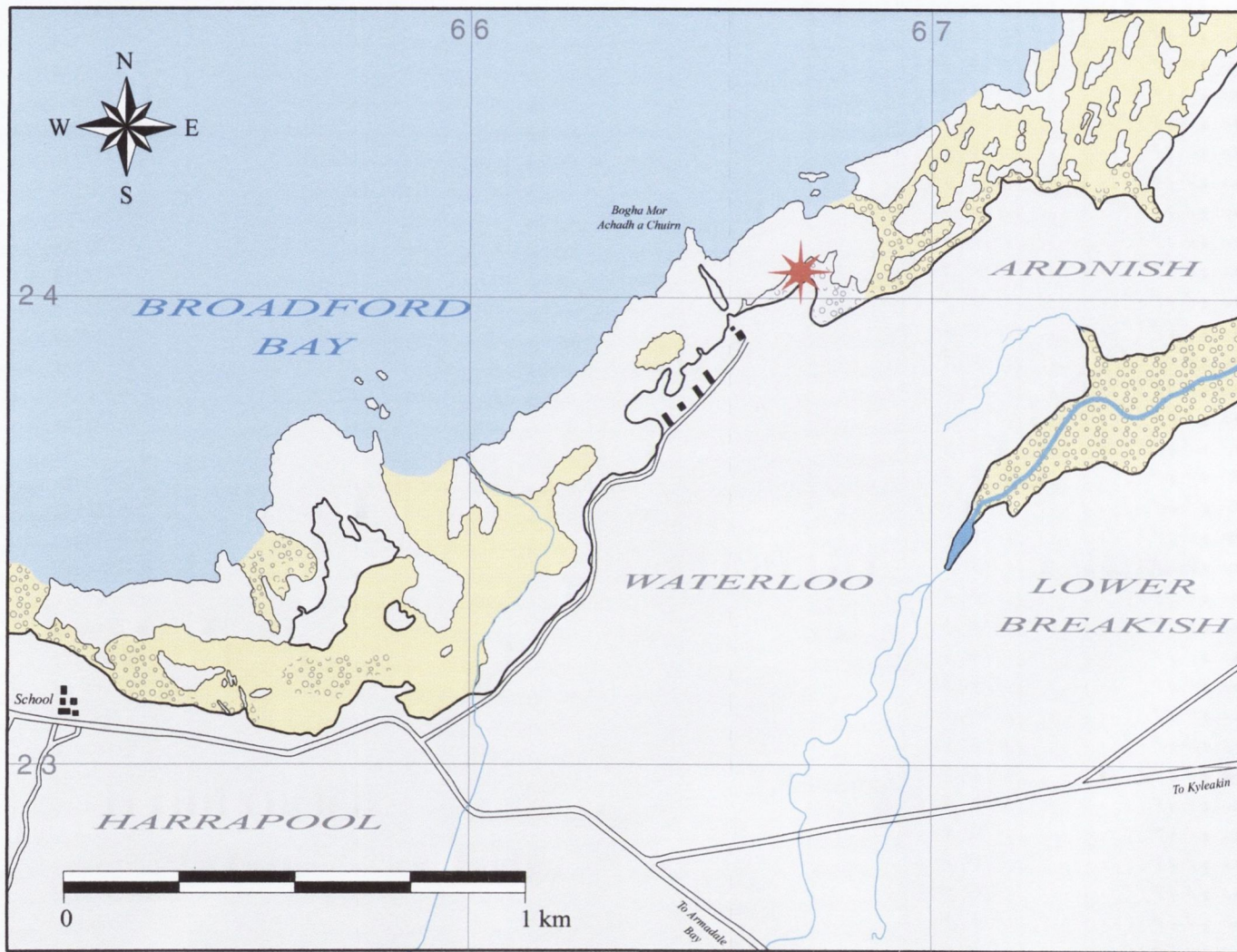


Figure 1.8. Map showing location of samples collected from Waterloo, Broadford Bay, central Skye.

Maximum burial depths of the Pabay Shales at Broadford probably exceeded 1600m before Late Jurassic-Early Cretaceous inversion (Morton 1987). However, hydrothermal convection systems associated with the nearby Skye central intrusive complexes have altered the Lower Jurassic sediments of the sampling site above regional maturity levels (Taylor and Forester 1977).

Sample	Formation	Lithology	R_r (%)	OM Fluorescence
Wo24E	Pabay Shale	Silty shale, 14.3m from eastern dyke contact	1.92	No fluorescence
Wo23W	Pabay Shale	Silty shale, 15.5m from western dyke contact	1.93	No fluorescence

Table 1.3 Maturity of Pabay Shales at Waterloo, Broadford Bay, central Skye.

1.5.5 BEARRERAIG BAY

Berreraig Bay is approached via a narrow access road from the main A855 Portree-Staffin road, to a small hydroelectric station approximately 10km north of Portree. This road is followed across a dam to a small parking area at the top of a cliff. Access to the foreshore below involves quite a steep descent down more than 600 slippery concrete steps to the generating house at sea level (Figure 1.9). The rocks in and around Berreraig Bay form the type section for the Middle Jurassic Berreraig Sandstone Formation. The entire succession is exposed here, in the cliffs and on the foreshore. The dark-grey micaceous shales and silts of the basal Dun Caan Shale Member (Aalensis Subzone, uppermost Toarcian in the lower part) are extensively exposed on the intertidal foreshore and in the low cliffs south of the bay. These shales rest non-sequentially on the Raasay Ironstone Formation, and coarsen up into the silty and sandy limestones at the base of the Ollach Sandstone Member. The sediments are cut by a number of dykes, which have caused local metamorphism of the country rock.

Using a hammer and chisel, detailed sampling was conducted from a site along the coast south of the bay (NG51375 52117). The base of a low cliff just above the foreshore exposes near horizontally bedded Dun Caan Shales, which are intruded by a near vertical 1.3m thick Tertiary basaltic dyke. The country rocks adjacent to the northern dyke contact were sampled in two phases.



Figure 1.9. Map showing location of collected samples at Bearreraig, northeast Skye.

An initial suite of 44 samples, BBN, was collected from a single horizon adjacent to the northern dyke contact. The second phase involved the collection of two more sample sets: BGSHN (14) and BGSN (7). The 'background' palynofacies for each of the sampled horizons illustrates the kerogen type (Figures 1.10, 1.11 and 1.12). All of the sample sets were collected adjacent to, and at increasing perpendicular distances from, the northern dyke contact.

Sample Suite	Samples Collected	Lithology
BBN	44	Shale horizon
BGSHN	14	Shale horizon
BGSN	7	Sandy limestone concretionary horizon

Table 1.4 Sample details from Bearreraig Bay locality, northeast Skye.

The dyke strikes at 318° and dips at 81° to 048° . This strike makes an angle of 54° with the country rocks, which strike at 012° and dip at 10° to 282° . There are no internal chilled margins evident in the dyke to suggest multiple intrusion within the dyke conduit. The dyke itself was also sampled.

1.5.5.1 DYKE PETROGRAPHY

Petrographic analysis reveals that significant alteration of the dyke has occurred. In particular, olivine and pyroxene have been extensively altered and are difficult to resolve as a result. Olivine grains have undergone complete hydrous alteration to saponite. Plagioclase is abundant in the groundmass, and is also occasionally present as discrete phenocrysts. In some cases alteration has occurred around the margins of the plagioclase phenocrysts to a clay-like mineral. The groundmass interstices between the plagioclase laths are occupied by brown-coloured (devitrified?) glass and altered pyroxenes (?). Evidence of magma flow is suggested by a vague sub-parallel arrangement of the lath-shaped plagioclases in the groundmass. This is more obvious near the margin, where alignment of the tiny needle-like plagioclase crystallites parallel to the dyke wall occurs. The presence of quartz and calcite grains and occasional sandstone lithics near the margin, suggests that contamination of the magma by the country rocks has occurred.

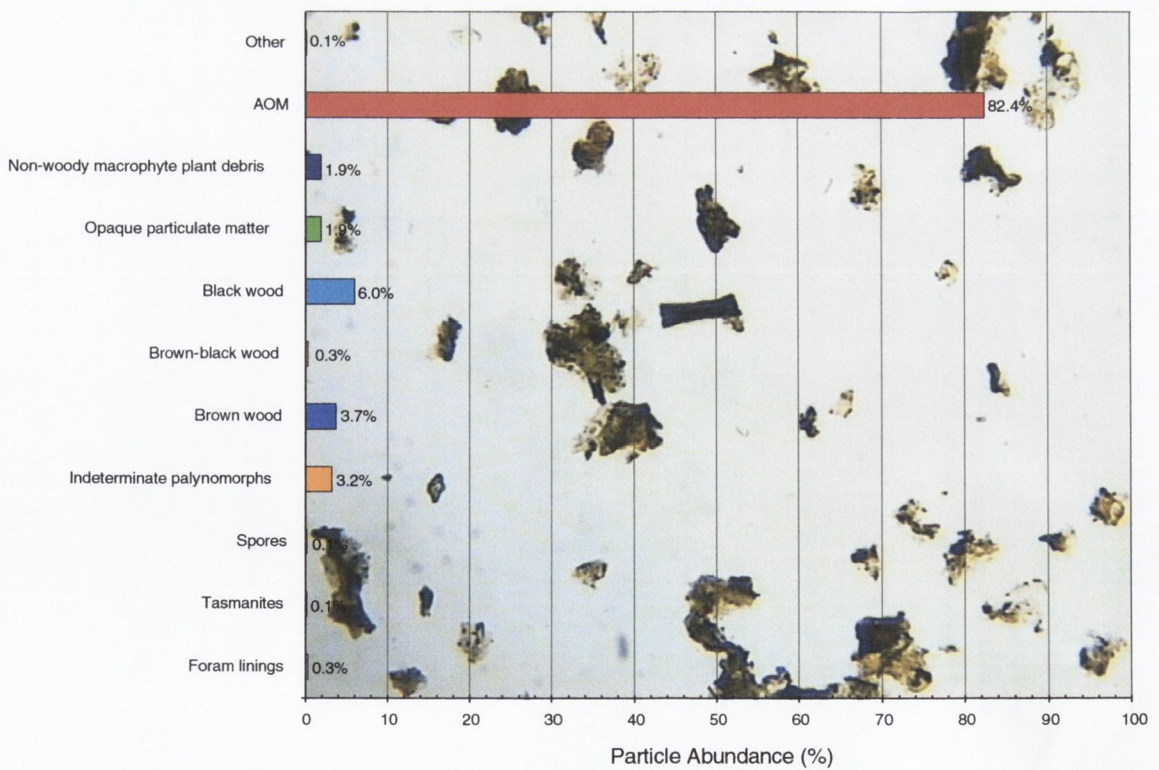
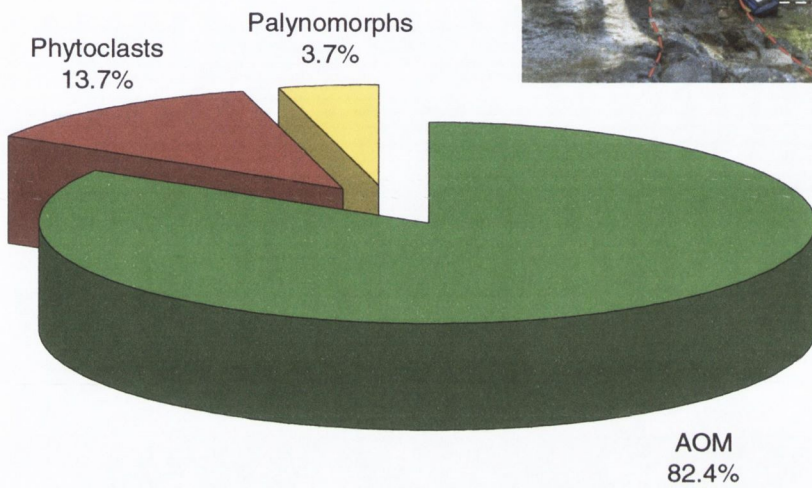


Figure 1.10. 'Background' palynofacies of the BBN sample horizon (BB44N).

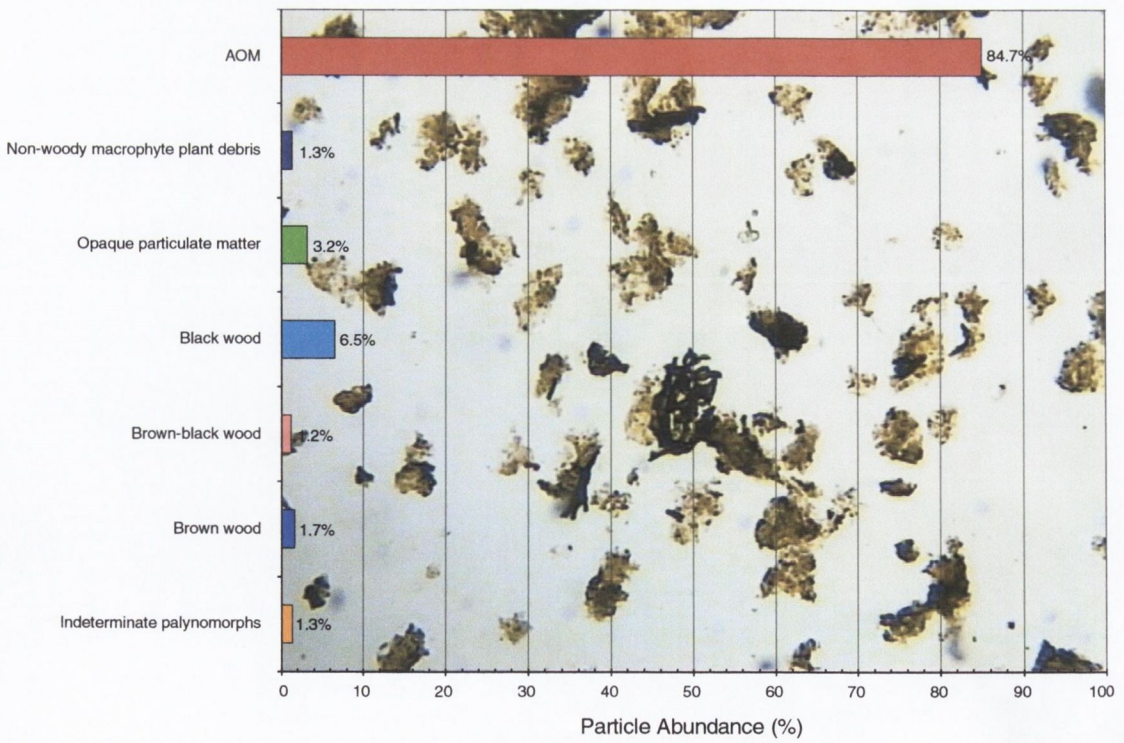
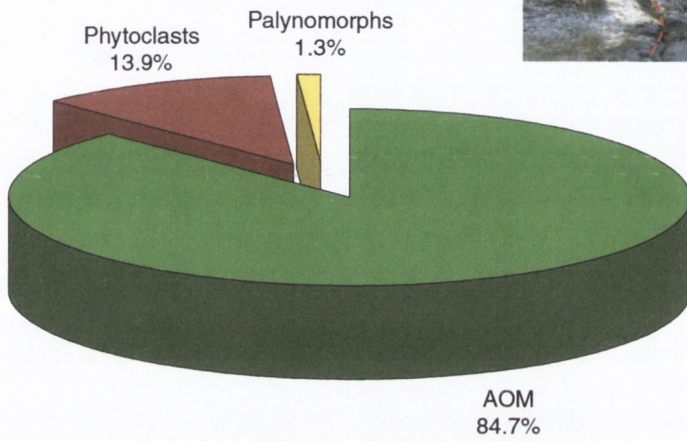


Figure 1.11. 'Background' palynofacies of the BGS HN sample horizon (BGS HN14N).

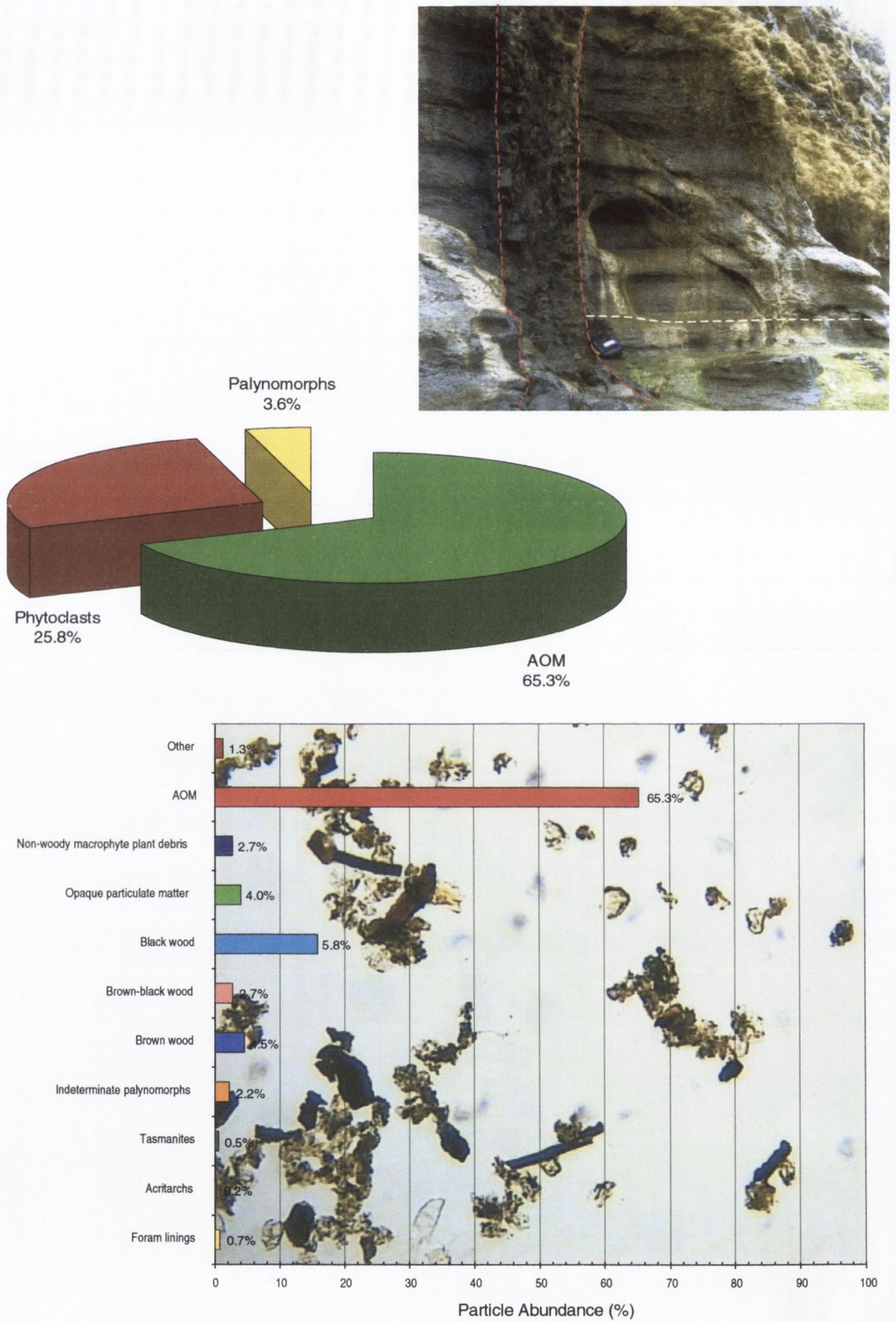


Figure 1.12. 'Background' palynofacies of the BGSN sample horizon (BGS07N).

1.5.5.2 DYKE GEOCHEMISTRY

The major element geochemistry of the studied dyke was carried out by OMAC¹ Laboratories Ltd. using Inductively Coupled Plasma – Optical Emission Spectrometry (ICP-OES). Major, minor and trace element geochemical analysis of a dyke sample was also carried out by GEOMAR² using X-ray fluorescence spectroscopy (XRF). PETRO.CALC.PLOT (Sidder 1994) was used to normalise whole rock oxide data to 100%, and to calculate the various petrologic parameters used to plot the major oxide data. All geochemical analysis data are presented in Appendix VI.

Total alkalis versus silica data for the dyke plot between the alkali olivine basalt and the hawaiite fields for normal volcanic rocks on the diagram of Cox *et al.* (1979) (Figure 1.13). Samples of the dyke margin have higher SiO₂ contents than that of the dyke centre. This perhaps reflects greater SiO₂ contamination at the dyke margin, by quartzose lithics from host rocks into which the dyke intruded. (Swarzer and Rogers 1974) have outlined differences between alkaline and subalkaline rocks based on alkali/silica variation (Figure 1.14). Analyses of the studied dyke all plot above the alkaline/subalkaline divide on Figure 1.14. Two distinct evolutionary trends have been identified within comparable igneous rocks from the Isle of Skye, namely the Skye Main Lava Series (SMLS): basalt-benmoreite and basalt-trachyte (Thompson *et al.* 1972). Total alkali/silica data for the studied dyke fall between these two evolutionary trend lines (Figure 1.14). The variation of alkalis (Na₂O + K₂O), iron (FeO + Fe₂O₃) and magnesium (MgO) data for the dyke is shown on a standard AFM diagram (Figure 1.15). The data plot within the fractionation trend presented by Gibson (1990) for the Trotternish sill field of northern Skye.

Geochemical trace element data may be used to discriminate between magma types and their associated tectonic setting. The Ti-Zr-Y discriminant diagram of Pearce and Cann (1973) reveals a within plate basalt (WPB) character for the central dyke sample (BBD01a) (Figure 1.16).

¹ OMAC Laboratories Ltd., Athenry Rd., Loughrea, Co. Galway

² Forschungszentrum GEOMAR-Wischhofstr., D-24148 Kiel, Germany

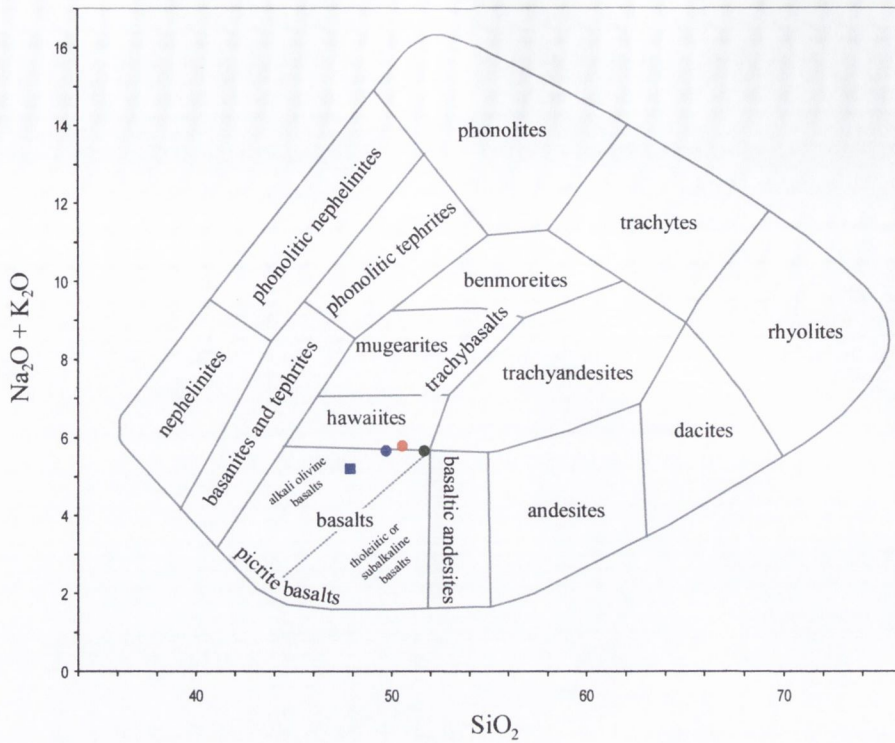


Figure 1.13. Plot of total alkalis versus silica data for the studied dyke at Berreraig, including standard nomenclature of normal volcanic rocks. The boundaries are not intended to be sharp, the fields labelled being intended only to show the approximate areas in which different types plot. Modified from Cox *et al.* (1979).

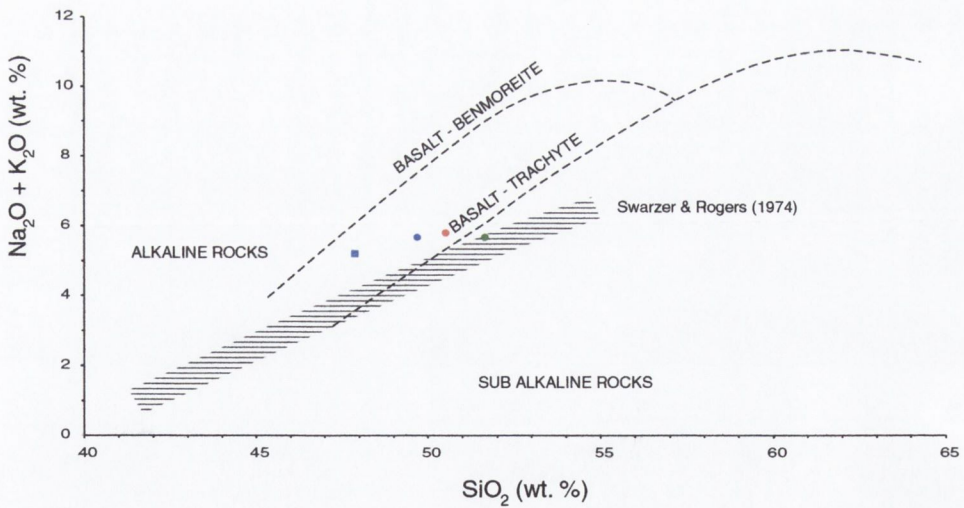


Figure 1.14 (a) Comparison between total alkali/silica variation in the studied dyke at Berreraig and the basalt-benmoreite and basalt-trachyte trends of the Skye lavas (Thompson *et al.* 1972). The alkaline/subalkaline divide of Swarzer and Rogers (1974) is also shown. Geochemical analysis by ICP-AES analysis, except *, by X-Ray fluorescence.

BBD01a	■ Dyke centre*	BBD02	● Dyke margin
BBD01b	● Dyke centre	BBD03	● Dyke margin (weathered)

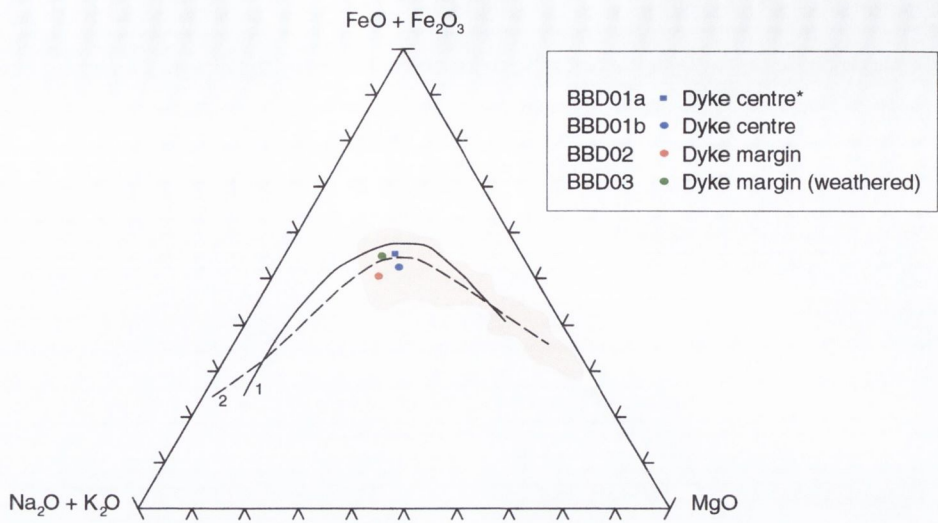


Figure 1.15. Alkalis-iron-magnesium (AFM) ternary plot of the studied dyke at Berreraig. The shaded area represents the Trotternish sill field of northern Skye (Gibson 1990). Also shown are the fractionation trends of the Skye lavas (1) (Thompson *et al.* 1972) and the Hawaiian alkali suite (2) (Macdonald and Katsura 1964). Geochemical analysis by ICP-OES analysis, except *, by X-ray fluorescence.

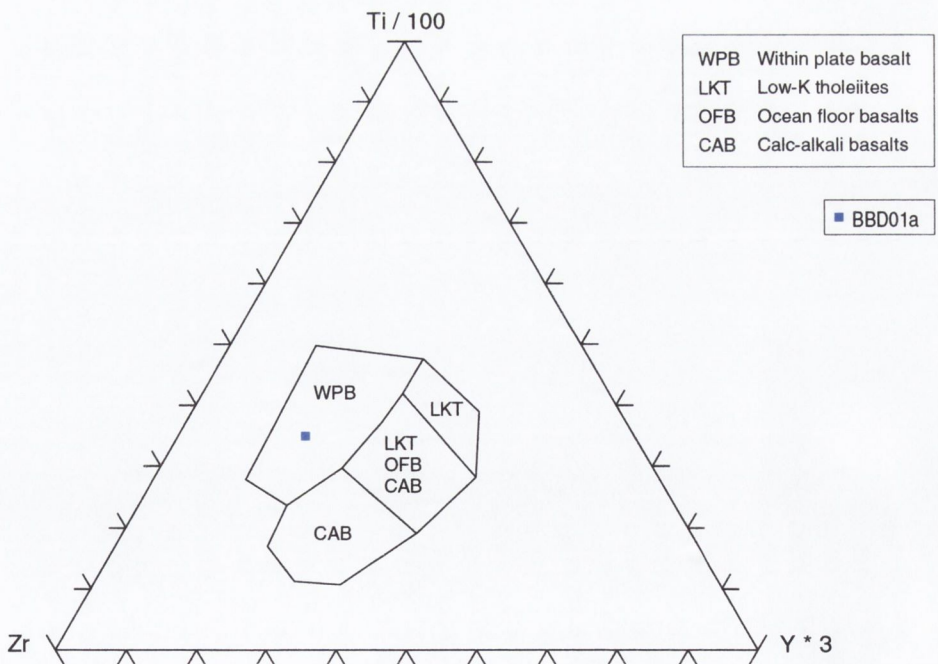


Figure 1.16. Composition of the studied dyke plotted on the Ti/Y/Zr discriminant diagram of Pearce and Cann (1973). The scaling factors used in the diagram serve to bring the points into the centre of the triangle without altering their relative position (Pearce and Cann 1973).

CHAPTER 2

VITRINITE REFLECTANCE, MATERIALS AND METHODS

2.1 VITRINITE REFLECTANCE

2.1.1 COALIFICATION, RANK AND MATURATION

The terms 'coalification', 'rank' and 'maturation' are often used loosely. Coalification and maturation both describe evolutionary processes during which organic matter undergoes two types of change: the expulsion of volatiles and the aromatisation and condensation of the residual solids. The term 'coalification' is used by coal petrologists, to describe the evolution of coal from peat (0.25% R_r) to the meta-anthracite stage (> 4.0% R_r). The term 'rank' is used to define the level of coalification (Figure 2.2). 'Maturation' is used by organic geochemists and refers to the development of organic matter that leads to oil and gas generation, and is usually applied to sedimentary rocks other than coal. Three main stages of maturation are normally identified: diagenesis, catagenesis, metagenesis (Table 2.1).

Stage of Maturation	Maturity	Vitrinite Reflectance % R_r
Diagenesis	immature	< 0.5 - 0.7
Catagenesis		
1. Main zone of oil generation	mature	> 0.5 - 0.7 to < 1.3
2. Zone of condensates and wet gas	overmature	1.3 - 2.2
Metagenesis	overmature	> 2.2 - 2.3

Table 2.1 Stages of oil maturation in relation to vitrinite reflectance (after Taylor *et al.* 1998). The limiting values of vitrinite reflectance may vary depending on thermal history and kerogen type.

Vitrinite is the main constituent of coal, and the geological processes involved in both coalification and maturation are studied mainly on the basis of its reflectance. As coalification and maturation essentially follow the same trend, namely the loss of volatiles (H, O) and increase in carbon content, both terms are used hereafter to imply the same thing.

2.3.2 ORIGIN AND CLASSIFICATION OF VITRINITE

Organic matter in sedimentary rocks is typically heterogeneous. This is due to its variable botanical origins and varying degrees of modification, both before and after deposition. The various microscopically recognisable constituents of organic matter are known as 'macerals', a term first coined by Stopes (1935) for constituents of coal isolated by maceration. Macerals vary widely in chemical composition and physical properties, and have been divided into three groups: the vitrinite group, the liptinite group (previously called 'exinite') and the inertinite group. Definition of macerals is based their appearance in reflected light, using oil immersion objectives with 25 - 50× magnification, specifically, reflectance, colour, shape and relief.

Vitrinite is the most common maceral group occurring in humic coals and is also found as a minor constituent of many sedimentary rocks. It is derived from humic substances that originate primarily from the lignin and cellulose of cell walls of higher plants. During coalification, ligno-cellulosic materials pass through a series of transformations that lead to the formation of huminite and, ultimately, vitrinite. The most recent classification of the vitrinite maceral group is presented in Table 2.2. .

Group	Subgroup	Maceral
vitrinite	telovitrinite	telinite
		collotelinite
	detrovitrinite	vitrodetrinite
		collodetrinite
	gelovitrinite	corpogelinite
		gelinite

Table 2.2 Subdivision of the vitrinite maceral group according to the ICCP System 1994 (ICCP 1998).

The reflectance of vitrinite varies more uniformly with increasing maturation than for the other maceral groups, and as such, is the most important indicator of coalification in sedimentary basins.

2.1.3 EVOLUTION OF VITRINITE DURING COALIFICATION

Vitrinite is an organic compound, whose chemical structure can be represented by several randomly dispersed stacks of polyaromatic layers 10-15Å in diameter, made up of a few fused aromatic rings (Oberlin *et al.* 1980). As coalification proceeds, these stacks reorganise themselves into larger clusters, 50-100Å in size, and these in turn fuse together to form oriented sheet structures of condensed aromatic rings. It is this increased size and orientation that is responsible for the development of reflectance anisotropy of vitrinite, which becomes progressively stronger with increasing coalification.

These organo-structural changes are accompanied by a number of chemical transformations, most notably the progressive increase in carbon content and decrease in volatiles (Figure 2.1). O is lost preferentially in CO₂ and H₂O, accompanied later by the loss of H in CH₄. Although these changes are considered gradual, four 'coalification jumps' have been recognised in vitrinite, where the changes are quite marked (Taylor *et al.* 1998). These coalification jumps and associated evolutionary changes in vitrinite are shown in Figure 2.2.

The reactions involved in coalification are irreversible. It is generally accepted that they are controlled primarily by the increase in temperature and the time available for the reactions to occur, although the relative influence of each factor has long been debated and will be discussed later. Pressure has also been suggested as a controlling factor on vitrinite maturation, suppressing vitrinite reflectance (Dalla Torre *et al.* 1997).

2.1.4 OPTICAL PROPERTIES OF VITRINITE

The reflectance of a material is defined as the ratio of the light reflected from a polished surface and the intensity of the incident light. It is expressed as a percentage of the incident light. It is a function of the refractive index and the absorptive index of the material and the media (oil or air) in which the reflectance is measured. In general, the reflectance of vitrinite progressively increases with increasing level of coalification.

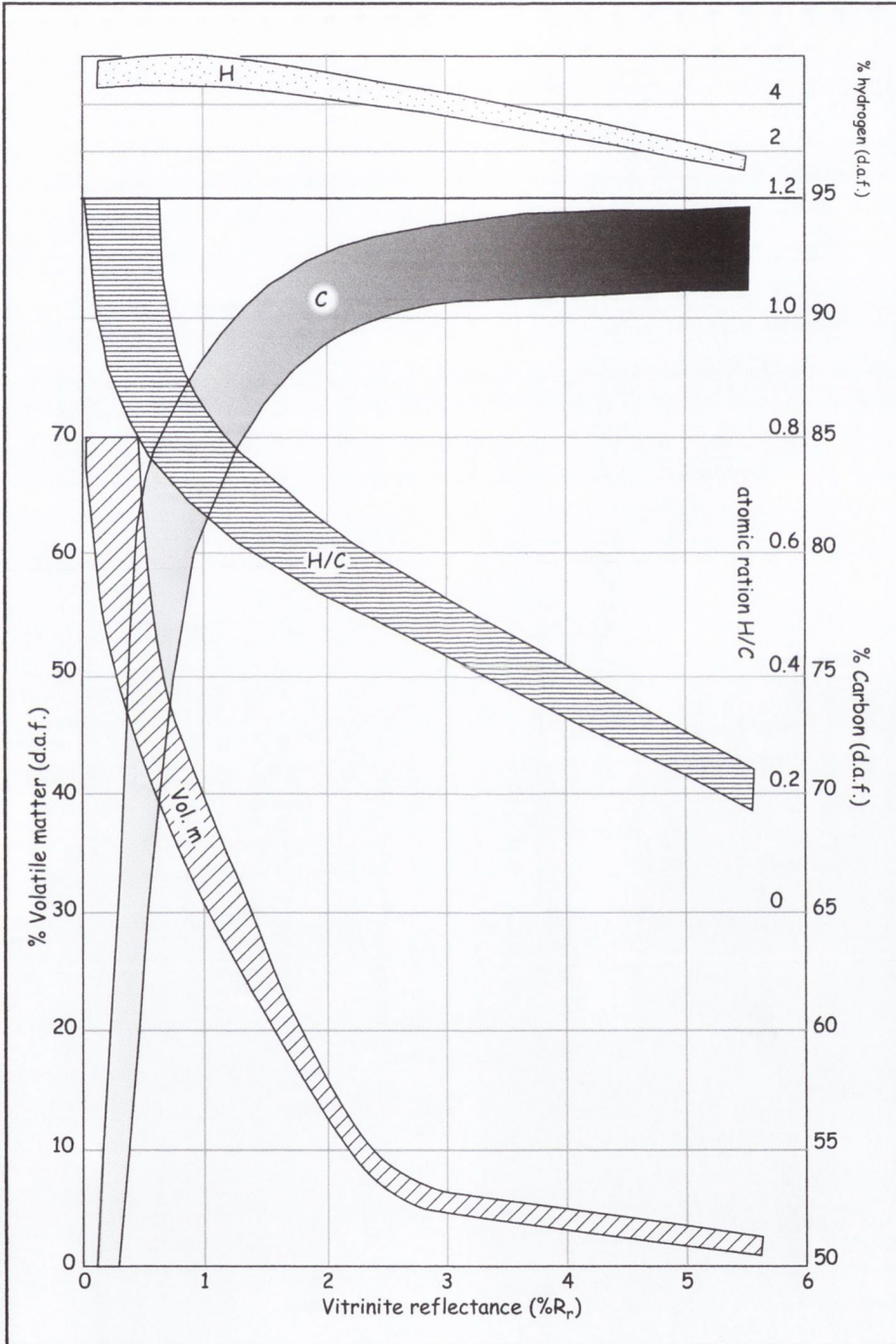


Figure 2.1. Relationship between vitrinite reflectance (% R_r) and different chemical parameters of rank (% dry, ash-free). Modified from Teichmüller & Teichmüller (1979).

Rank	R _r (%)	Vol M d.a.f. (%)	Carbon d.a.f. (%)	Vitrinite Evolution
Peat	0.2	68		Free cellulose; details of plant material often recognisable
Lignite		64	ca.60	No free cellulose; plant structures still recognisable; cell cavities frequently empty
		60		
		56		
		52		
C Sub- Bituminous	0.4	48	ca.71	Geochemical gelification takes place; vitrinite is formed
B	0.5			
A	0.6	44	ca.77	1 st Coalification jump - start of oil generation
B High volatile Bituminous	0.7	40		Randomly dispersed turbostratic stacks of 2 or 3 aromatic layers 10-15Å in diameter
	0.8			
		36		
		32		
A	1.0			
	1.2			
Medium volatile Bituminous	1.4	28	ca.87	2 nd Coalification jump - 'death line' for oil generation
Low volatile Bituminous		24		Marked loss of O Beginning of H release in CH ₄
		20		
		16		
Semi-Anthracite	2.0	12		Sudden molecular orientation in vitrinites - small aromatic stacks aggregate into clusters of 50-100Å size
		08	ca.91	3 rd Coalification jump
Anthracite	3.0			Increased loss of H in CH ₄ ; increased aromatisation
	4.0	04		
Meta-Anthracite				4 th Coalification jump
				Increased loss of H in CH ₄ ; increased aromatisation

Figure 2.2. Coalification stages and vitrinite evolution including coalification jumps in vitrinite. Modified from Teichmüller (1987).

Optically, vitrinite has the properties of a uniaxial negative material when its maximum reflectance (R_{\max}) is greater than 0.7-0.8% (Ting 1991). Below that value, vitrinite is more or less isotropic. The anisotropy of vitrinite increases proportionally with progressive orientation of its aromatic lamellae to parallel the bedding plane with increased coalification. When the reflectance of vitrinite is determined in polarised light, bands of vitrinite cut perpendicular to stratification show four characteristic positions on rotation of the object stage through 360° . These four positions are of *maximum reflectance* (R_{\max}) and *minimum reflectance* (R_{\min}) alternately. In certain circumstances however, vitrinite may have been subjected to renewed tectonic loading or re-orientation due to intergranular rotation and thus exhibit biaxial optical properties.

As rank indicators, *mean maximum reflectance* (R_{\max}) and *mean random reflectance* (R_r) of vitrinite are widely employed to determine the thermal maturation or coalification level of organic sediments. Maximum reflectance is measured in polarised light, with the polariser set at 45° , and is the preferred rank parameter in coals. The orientation of the minimum reflectance or the optic axis of vitrinite with respect to the bedding plane can be used to show the paragenetic relationship of coalification and tectonic structure. If coalification is followed by folding, the orientation of the minimum reflectance is perpendicular to bedding, regardless of bedding plane attitude. Random reflectance, which employs non-polarised light is a mean value of all reflectances of a given polished surface, and is the technique usually applied to dispersed organic matter. R_{\max} can be calculated statistically (Ting 1991) by multiplying the R_r of a large population by a conversion factor, such as expressed in the equation

$$\text{Mean } R_{\max} = 1.06 \times \text{Mean } R_r$$

The conversion factor may vary slightly depending on the nature of the vitrinite population and the overall value of vitrinite reflectance being greater or smaller than 1.0% R_{\max} . In this study *mean random reflectance* (R_r) was the parameter of vitrinite reflectance used for maturity assessment.

2.1.5 BENEFITS AND LIMITATIONS OF THE VITRINITE REFLECTANCE METHOD

Vitrinite reflectance is currently the most popular indicator of coalification level in sedimentary basins. The method is relatively cheap and can be applied to a wide range of sedimentary rocks of Devonian age or younger. Vitrinite reflectance is measured on a numerical scale and the method is standardised by the ICCP guidelines (ICCP 1971). As such, it is considered an objective technique, unlike most of the other optical maturity parameters which rely on subjective visual estimation, e.g., palynomorph colour/fluorescence, conodont colour, etc. The technique has been correlated with other maturity indicators (Teichmüller 1974; Tissot and Welte 1978; Merriman and Kemp 1997, among others) and many mathematical and geochemical models exist for the correlation of vitrinite reflectance with maximum temperature (Price 1983; Barker and Pawlewicz 1986; Burnham and Sweeney 1989; Barker and Goldstein 1990, among others). As the chemical reactions involved in the evolution of vitrinite are irreversible, vitrinite reflectance is considered to be a non-retrogressive indicator of coalification level.

Many of the drawbacks associated with the vitrinite reflectance method are related to the inherent subjectivity that exists in the correct identification of vitrinite. The individual macerals become less and less different with increased maturity, so that it becomes progressively more difficult to distinguish between them microscopically. Materials such as semifusinite and solid bitumen can look like vitrinite, but have different reflectivities at the same rank. Even properly identified vitrinite may have several sources (i.e., recycled vitrinite), but only the indigenous population may be used for maturity assessment. This is often difficult to discern. Differences in the redox conditions of the depositional environment can greatly affect the initial hydrogen content of vitrinite (Buiskool Toxopeus 1983; Durand *et al.* 1985) with hydrogen-poor, oxygen rich vitrinites maturing at an enhanced rate (Fang and Jianyu 1992). This disparity in chemical composition and reaction kinetics cannot be distinguished during R_r measurements. Poor preparation, especially inadequate polishing can result in a considerable decrease in R_r values, together with an increase in standard deviations (Buiskool Toxopeus 1983). Many samples are vitrinite-poor and may not contain sufficient particles for the recommended 100 measurements. While vitrinite reflectance is well established as a rank parameter, there is a disparity in the

established correlations with other maturity indicators in anomalous heating regimes (Fitzgerald 1994; Goodhue 1996; McCormack *et al.* 1997).

2.2 PREPARATION OF SAMPLES FOR VITRINITE REFLECTANCE

2.2.1 SAMPLE PREPARATION

The rock sample was scrubbed to remove any foreign material (e.g., algae, moss, etc.) adhering to the surface. Any weathered material was discarded. The sample was then dried and crushed to pea-sized chips. Approximately 30 - 40g of sample were placed in a labelled polythene beaker, the lid of which had a small vent hole to emit any gas that evolved during acid digestion. Any dust from the crushed rock fragments was washed off with tap water, decanting two or three times until the water was clear. Approximately 5 - 10ml of dilute (10%) hydrochloric acid (HCl) were added to test for carbonate. If carbonate was present, it was removed by digestion in 27% HCl over 24 hours. The spent HCl was decanted off and the sample jar refilled with water to progressively dilute the sample. The sample was decanted once more before the next preparation stage. To remove the silicate fraction, the sample was immersed in 40% hydrofluoric acid (HF) and placed in a water bath maintained at 60°C. The sample was stirred twice daily using a plastic rod. This served both to accelerate and to gauge the extent of digestion. Complete digestion was effected when the sample no longer felt 'gritty'. This usually took between 5 and 10 days. The spent HF was decanted off into a polythene container for safe disposal and the sample jar refilled with water. The sample was progressively diluted by allowing the organic residue to settle, decanting off the clear water and refilling with clean water. Five or six decants were usually deemed enough to sufficiently dilute most samples. The residue was then sieved through a 20µm mesh. When an adequate measure had been collected the wet residue was pipetted from the sieve to a plastic petri dish and allowed to dry overnight in an oven at 60°C before block mount preparation. Where polished slide mounts were used the residue was transferred to a glass vial and stored under water.

A number of samples were initially prepared using a PROLABO® *Microdigest 3.6* microwave digestion unit, purchased by TCD Geology Department soon after work on this project commenced. Digestion times using the *Microdigest 3.6* are of the order of 30 minutes for three rock samples (3 digestion wells). As standard acid digestion in a warm water bath can take up to three weeks, the *Microdigest 3.6* presented a much more efficient acid digestion system. A simple experiment was devised to investigate whether the high temperatures involved in microwave digestion had any maturation effect on the organic matter isolated using this technique.

A sample of low organic maturity was selected for this experiment, as it would be more susceptible to any maturity changes related to the microwave digestion process. In this case, a marl sample from the Blue Lias of Dorset was used. The rock sample was crushed, washed and divided into nine 8g aliquots. A series of nine *Microdigest* protocols were devised using various power/time combinations (Table 2.3). Microwave frequency of the *Microdigest 3.6* is 2.56GHz. A maximum power of 250W was controlled between 10% and 100% in 1% increments. Time was controlled between 00.00 and 60.00 minutes. After standard HCl treatment (as described above), each sample aliquot was transferred to a *Microdigest* well and 50ml of 40% HF was added. Each one was processed using a different *Microdigest* protocol (i.e., a different time/power program). A portion of rock sample was prepared using the 'cold' HF acid digestion method. This was used as a standard against which to compare those samples prepared using the microwave digestion unit. Vitrinite reflectance was determined for each of the ten samples. Prior to vitrinite reflectance analysis, each sample was randomly coded (G01-10) to prevent operator bias.

The results are presented in Figures 2.3 and 2.4. Although quite scattered, the results indicate that vitrinite reflectance of samples prepared using the microwave digestion unit are slightly elevated relative to samples prepared using the 'cold' digestion method. This suggests that the high temperatures produced by the microwave radiation are resetting the maximum temperature recorded by the vitrinite and precludes the use of this preparation method for vitrinite reflectance/palaeotemperature estimation.

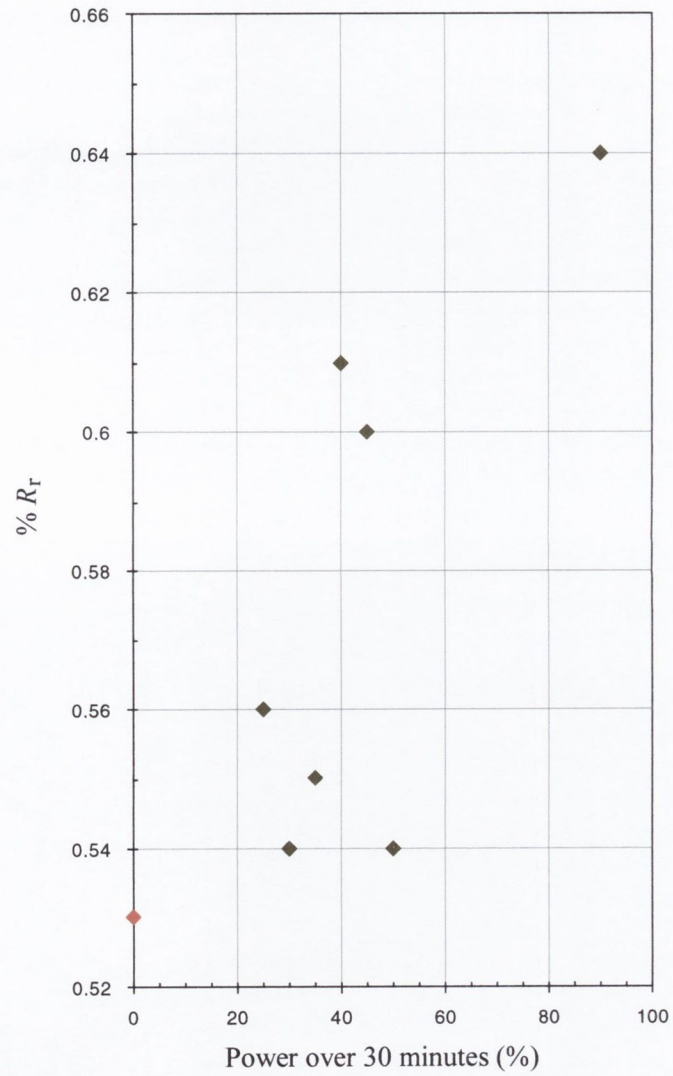


Figure 2.3. Plot of vitrinite reflectance versus microwave power after 30 minutes. The red data point represents the unheated standard.

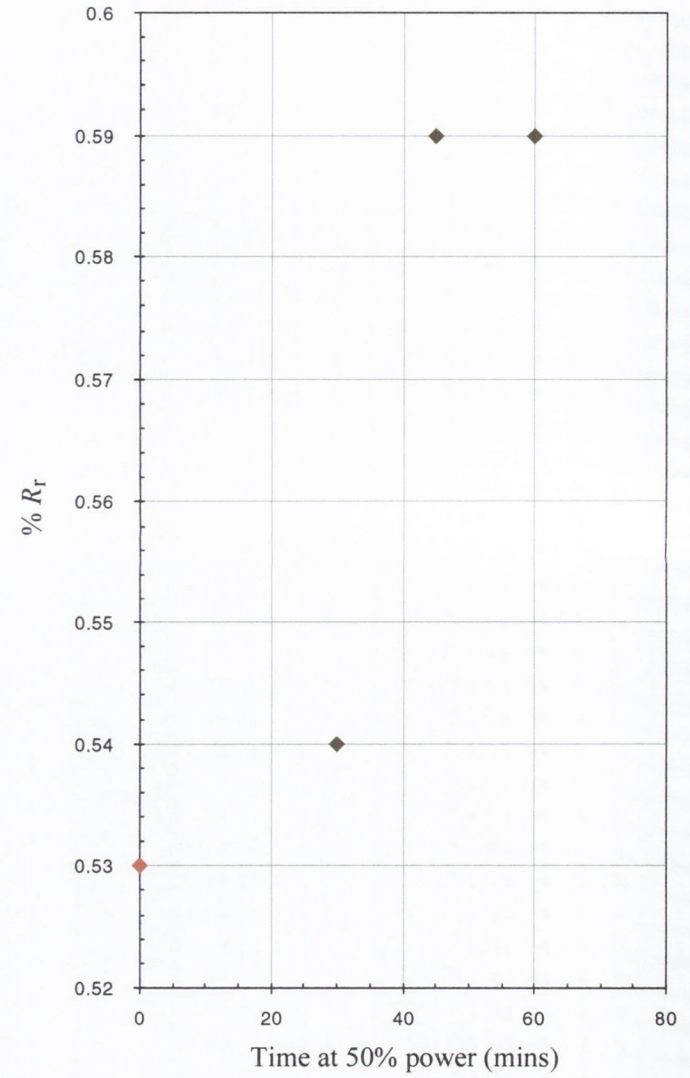


Figure 2.4. Plot of vitrinite reflectance versus microwave heating time at 50% power. The red data point represents the unheated standard.

Consequently this digestion method was abandoned for this study. Those samples that had been prepared using the *Microdigest 3.6* were reprocessed using the standard 'cold' digestion procedure.

Sample	Time/power program	Code	% R_r
MD01	30 mins @ 90%	G10	0.64
MD02	30 mins @ 50%	G01	0.54
MD03	30 mins @ 45%	G05	0.60
MD04	30 mins @ 40%	G09	0.61
MD05	30 mins @ 35%	G03	0.55
MD06	30 mins @ 30%	G08	0.54
MD07	30 mins @ 25%	G04	0.56
MD08	60 mins @ 50%	G02	0.59
MD09	45 mins @ 50%	G06	0.59
MD10	'cold' digestion	G07	0.53

Table 2.3 Time/power programs, operator codes and vitrinite reflectance results for samples used in *Microdigest* experiment.

2.2.2 MOUNTING AND POLISHING

Two methods have been used to mount the HF residues over the course of this work. Initially, a method adapted from that outlined in Hillier and Marshall (1988) was used. This method produces a polished slide mount, suitable for both reflected and transmitted light microscopy. The ability to view the various macerals in transmitted light, as well as reflected light, provided a valuable aid for maceral identification. However this method had to be abandoned some way into the project, as the supply of the resin used in this technique was discontinued. A number of resins were investigated as a possible alternative, but none proved suitable. Thereafter, samples were mounted using cold setting resin blocks. These are the most widely used type of mount for vitrinite reflectance work, but cannot be used in transmitted light due to their thickness.

Slide mounts

A 20 × 20mm square coverslip was lightly sprayed with PTFE (polytetrafluoroethylene), a dry lubricating agent. A few millilitres of the aqueous sieved residue suspension were pipetted onto the surface of the coverslip and left in a drying cabinet until completely dry.

The mounting medium for vitrinite slide mounts was a *Met-Set* resin-hardener mix. Due to its rapid cure time, this was prepared in small quantities, with 4 or 5 drops of hardener per 10ml of resin. A small measure of resin was pipetted onto a 2mm thick glass slide and the coverslip was gently placed on top, residue side down. The resin was left to cure at room temperature over 24 hours. The coverslip was then carefully removed using a blade, leaving the resin-residue mix on the glass slide.

Block mounts

The dried organic residue covering the base of the petri dish was broken up by rubbing with a blade held at an acute angle to the base of the petri dish. The organic residue was then carefully transferred to a plastic cap mould. An appropriate volume of *Epo-thin* resin (Buehler No. 20-8140-032) and hardener (Buehler No. 20-8142-016) were mixed for approximately one minute in a proportion 100:36 by weight, respectively. This was found to roughly correspond to a 10:3 ratio by volume. The mixture was allowed to stand for about a minute to allow any air bubbles to dissipate. A small measure (a few millilitres) of this resin-hardener mixture was added to the mould and mixed thoroughly with the contained organic residue. Again, the mixture was left to stand for about a minute to allow any air bubbles to dissipate, before the mould was gently topped up with the resin-hardener mixture. The mixture was left to cure at room temperature over 24 hours, after which time the block was removed from its plastic mould before the polishing stage.

Polishing

A four stage polishing procedure was employed for the block mounts. The first two stages involved grinding the block to a flat surface using water-wet silicon carbide paper of 320 and 1200 grade respectively. The final two stages involved hand-polishing the block on a polishing lap with alumina (Al_2O_3) paste of $0.5\mu\text{m}$ and $0.03\mu\text{m}$ grades respectively. Between each polishing stage, the block was sprayed with a jet of water and placed in an ultrasonic bath for 10 seconds to remove any polishing grit and avoid contamination of the next polishing stage. As the slide mount technique generally produces a flat surface, the final three polishing stages were usually adequate to produce a good polish.

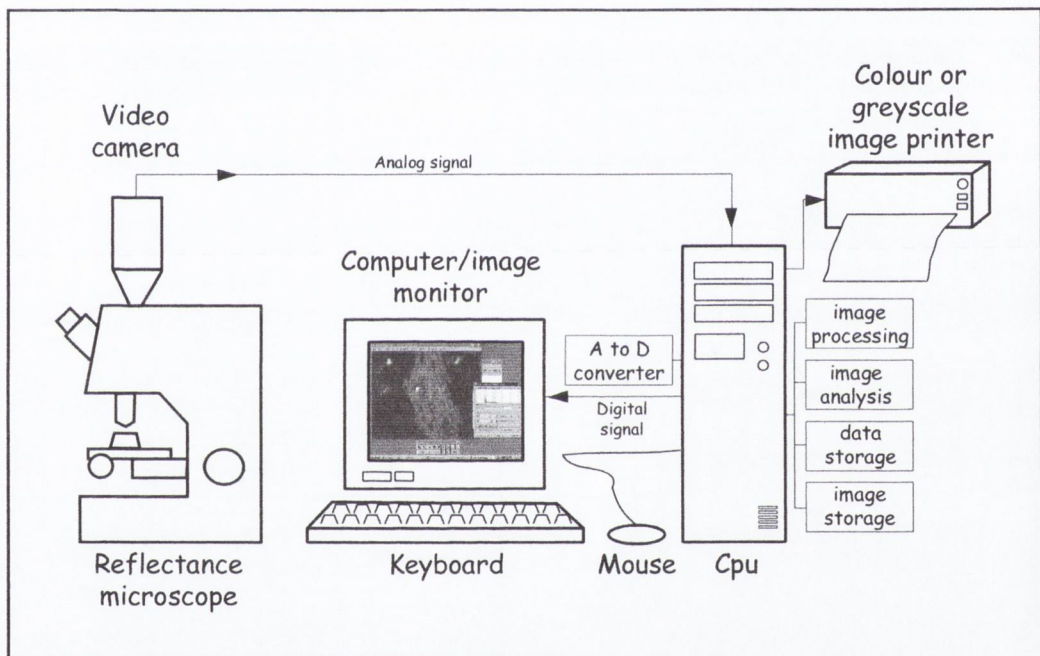


Figure 2.5. Schematic of image analysis system for organic petrology at Trinity College Dublin.

2.3 MEASUREMENT OF VITRINITE REFLECTANCE

2.3.1 SYSTEM SETUP

Vitrinite reflectance (R_r) measurements were performed using an electronic imaging system (Figure 2.5). Vitrinite was observed using a Leitz Ortholux 11 microscope equipped with a 12V/100W halogen light source with a stabilised power supply, light controlling apertures, a Berek prism-type vertical illuminator, a removable polariser and a rotating stage. A strain-free 50 \times objective lens and a pair of viewing eyepieces of 10 \times magnification were used. A SONY XC-75/75CE CCD black-and-white video camera module mounted on the microscope phototube provided the image to be processed. The analogue image was digitised, processed and analysed using a Leica Q500IW imaging workstation. The system employs the QWin application, Leica's image analysis toolkit. Essentially, image analysis consists of a sequence of operations which reduces the total information content of an image to a few pertinent measurements. These measurements are then interpreted by the user in terms of the application. Two programs (routines) were written for vitrinite reflectance work using QUIPS, an interactive macro-programming facility for Leica QWin: *LowReflectance.Q5R* and *MedReflectance.Q5R*. Both of these four-step routines have the same basic structure. The illumination settings programmed for each routine are optimised for a particular range of reflectance. The QUIPS routines employed for vitrinite reflectance are presented in Appendix VIII.

2.3.2 SYSTEM CALIBRATION

Within QWin, all grey level measurements are expressed in pixels. Pixel data was converted to % reflectance by constructing a look-up table (LUT)³, in which each grey level from 0 to 255 is related to its corresponding calibrated value of reflectance. For each grey measurement, QWin uses this table to calibrate the results before displaying them. Before QWin can calculate this table, reflectance calibration values must be input, associated with at least two different grey levels. Calibration was performed by enclosing an area (2.52 μ m

³ Look-up tables or LUTs are used to perform tasks relating to analogue-to-digital conversion, image arithmetic, and a variety of other functions. Grey LUTs are used to remap the grey levels of an image.

$\times 2.52\mu\text{m}$) on two standards of known reflectance with the measure frame. The value was then input and the mean grey level measured for that area. QWin then associates that grey level with the calibrated value specified by the user. After the standard values have been set up, QWin calculates the LUT, which provides the best fit when the 'Calibrate' button is pressed.

Reflectance standards used for calibration in this study are as follows:

Standard Type	% R_o	% R_a
Spinel (McCrone No. 307)	0.42	7.17
Glass (Leitz No. 998)	1.23	9.60
Cubic zirconia (McCrone No. 319)	3.28	13.90
Silicon carbide (McCrone No. 339)	7.56	20.70

Table 2.4 Reflectance standards used for calibration in this study. R_o indicates reflectance under oil and R_a indicates reflectance in air, i.e., without any medium between the sample and the microscope objective.

The standards, as recommended are all embedded in a matt black medium. All standards were stored in a desiccator and cleaned regularly with alcohol.

Each QUIPS reflectance routine uses a separate calibration file, which references two reflectance standards (Table 2.5). The two standards used should have reflectance values as close as possible to that of the unknown sample, so the choice of routine used depended on the reflectance level of the sample being investigated.

QUIPS Routine	Standard 1 (% R_o)	Standard 2 (% R_o)
LowReflectance.Q5R	0.42	1.23
MedReflectance.Q5R	1.23	3.28

Table 2.5 QUIPS routines used for vitrinite reflectance work in this study and the relevant reflectance standards used for calibration.

2.3.3 REFLECTANCE MEASUREMENT

Vitrinite reflectance measurements were determined in incident light of 546nm, under oil with a refractive index of 1.5193 at 20°C. The temperature of the microscope room remained constant at 20 - 21°C. The effects of any extraneous light in the microscope room, which may have interfered with the microscope system, were minimised by conducting all measurements in near-darkness behind an opaque curtain. The stage on the microscope was locked in one position and the polariser was removed. The entire system was switched on and allowed to stabilise for at least 30 minutes, prior to initial calibration. Measurement of vitrinite reflectance was carried out promptly after initial calibration was effected, and the system calibration was rechecked before studying each new sample.

Operator bias, concentration, mood and experience gained during the microscope scan, can influence the resulting reflectance histogram. To minimise operator bias, all samples were randomly coded prior to analysis. Long sittings at the microscope were avoided to maintain concentration levels. The scheme for measuring vitrinite reflectance was to first quickly scan across the polished mount in order to learn the characteristics of its contained organic matter. The sample was then scanned in a systematic fashion from left to right across the mount. Vitrinite was selected for measurement on the basis of a number of criteria:

1. Apparent colour and reflectivity deemed to be appropriate for vitrinite, i.e., mid-light grey coloured grains. High-reflecting yellow coloured grains were avoided for the most part.
2. Morphology - the grain should lack rounded edges, a feature often indicative of recycled vitrinite. Arcuate, shard-like grains (commonly seen in inertinite) were also avoided.
3. Relief - only flat, low-relief grains were selected. Grains showing differential relief, in particular around the grain edge (commonly seen in inertinite), were avoided.

4. Appearance in transmitted light (only for glass slide mounts) was a useful identification aid, as the entire grain could be observed, as opposed to the polished section only seen under reflected light.
5. High quality - Only vitrinite particles possessing a flat, polished, scratch-free surface area, large enough for reflectance measurement were selected for measurement.

2.3.4 ACCURACY OF VITRINITE REFLECTANCE RESULTS

The accuracy of vitrinite reflectance measurements is dependent on the reflectance microscope system and the number of particles measured. The total number of vitrinite reflectance measurements taken is a compromise between statistical and practical considerations (Taylor *et al.* 1998). In coal samples, published recommendations based on statistical methods suggest 100 measurements are required to estimate R_r . As the number of vitrinite particles in dispersed organic matter (DOM) samples is normally far less than in coal samples, this can often be an unrealistic target. Barker and Pawlewicz (1993) looked at reflectance distribution statistics in increments of 10 measurements and found little change in sample statistics after 50 measurements. They consider 50 measurements as an adequate estimate of R_r in DOM samples, and in samples with sparse vitrinite, advise selecting 20 - 30 high-quality particles rather than seeking a large quantity of diverse vitrinite grains to make the results more statistically significant. A similar strategy was employed in this study, as most samples were found to have comparatively sparse vitrinite. Often 2 or 3 slide preparations were required to obtain 50 measurements (blocks mounts were further ground down and re-polished).

A uniform reflectance standard was measured at different positions across the captured screen image to investigate whether results were consistent, regardless of the measure frame position on the screen. Inconsistencies in the results were observed when the measure frame was moved to different positions on the screen. In order to characterise this variation, a number of reflectance profiles across the measure area ($11,923.6\mu\text{m}^2$) were conducted for each of the reflectance standards: a left-right (L-R) horizontal, a top-bottom (T-B) vertical, a topleft-bottomright (TL-BR) diagonal and topright-bottomleft (TR-BL)

diagonal. The profiles (Appendix II) highlighted several variations that were consistent for all standards (Figure 2.6).

The horizontal profiles showed an increase in reflectance from R-L. The vertical reflectance profiles increased towards the bottom. The TL-BR diagonals showed lower reflectance towards the edges. The TR-BL diagonals consistently had the most pronounced variation, increasing from TR to BL. Furthermore, although the system had been calibrated for each of the standards prior to conducting the reflectance profiles, the average reflectance for each profile was always lower than its calibrated value. The 3.28% reflectance standard showed the most pronounced disparity, with a mean R_o of 3.21% and a standard deviation of 0.2 for the full measure screen area.

One option would have been to remove the operator's ability to adjust the shape and position of the default measure frame ($2.56\mu\text{m} \times 2.56\mu\text{m}$), locking it on a fixed on-screen position. This would have resulted in a rather tedious procedure of continually making minor adjustments to the microscope stage to find the desired measuring position on the screen. This would also have been time consuming and measurement of cracks or blemishes in the vitrinite would often have been difficult to avoid. It was decided instead, to simply compromise the operator's ability to manipulate the measure frame on screen, confining the measuring area to $791.1\mu\text{m}^2$, within an on-screen limiting frame (256x, 233y; $32.93\mu\text{m} \times 24.02\mu\text{m}$) (Figure 2.6). This was achieved by a process of trial and error, experimenting with different shapes and positions of the limiting frame until the observed disparity was reduced to an acceptable minimum. As the illumination settings are different for each reflectance routine, this limiting frame had to be tested using both routines. The standard R_o values and standard deviations for both reflectance routines for the full measure area, limiting frame and calibration frame are presented in Table 2.6. The standard R_o profiles, R_o histograms with mean and standard deviations, both within and without the limiting frame, for both *LowReflectance.Q5R* and *MedReflectance.Q5R* are shown in Appendix II. In practice, the measure frame was moved as little as possible from its default position (379x, 298y).

QUIPS Routine	Standard	Calibration frame		Full measure area		Limiting frame	
		R_o (%)	S.D.	R_o (%)	S.D.	R_o (%)	S.D.
LowReflectance.Q5R	0.42%	0.42	0.01	0.41	0.03	0.42	0.02
LowReflectance.Q5R	1.23%	1.23	0.02	1.21	0.06	1.24	0.02
MedReflectance.Q5R	1.23%	1.23	0.02	1.22	0.05	1.23	0.02
MedReflectance.Q5R	3.28%	3.28	0.02	3.23	0.14	3.29	0.04

Table 2.6. % R_o and standard deviation data within calibration frame, full measure frame and limiting frame for reflectance standards used in *LowReflectance.Q5R* and *MedReflectance.Q5R*. Examples of the calibration frame, limiting frame and full measure area are shown in Figure 2.6.

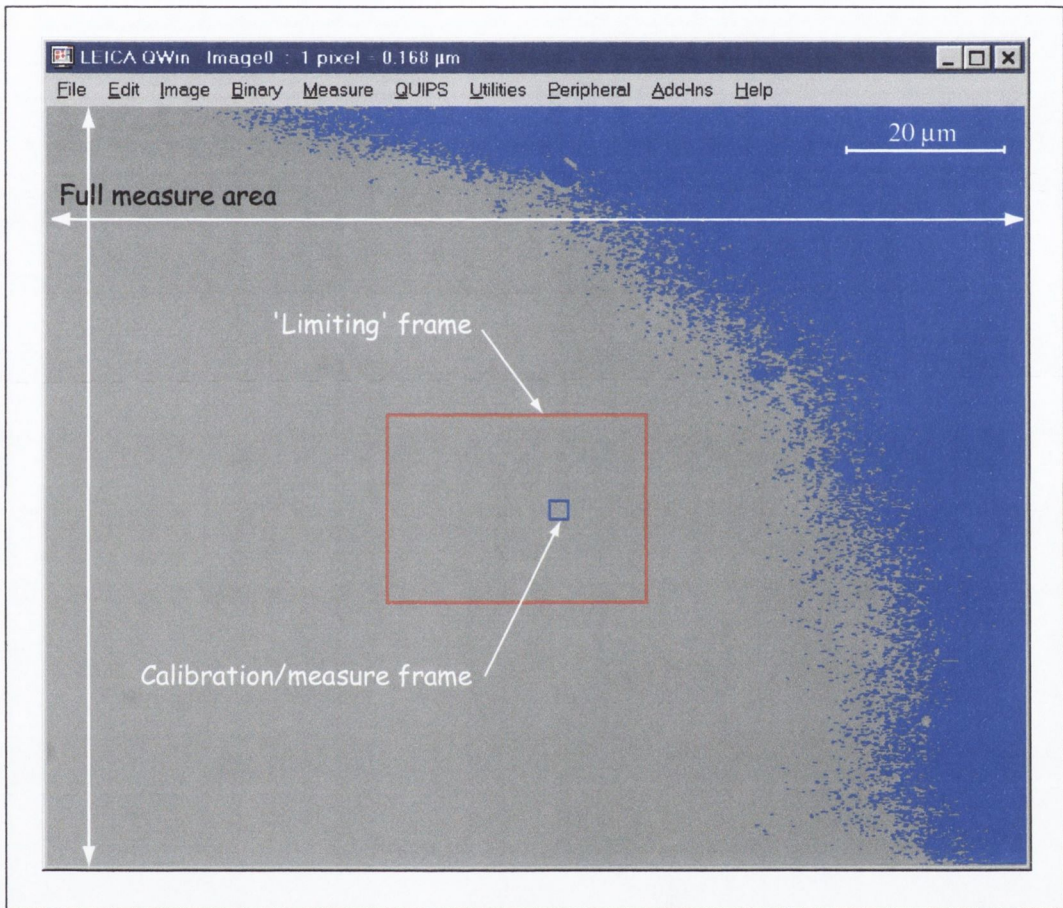


Figure 2.6. Characterisation of the illumination disparity observed using the TCD vitrinite reflectance measurement system.

CHAPTER 3

QUANTITATIVE AOM COLOUR, MATERIALS AND METHODS

3.1 ORGANIC MATTER COLOUR

3.1.1 ORGANIC MATTER COLOUR

The second most important method of maturity estimation, after vitrinite reflectance, involves the microscopic recognition of the progressive and irreversible colour changes undergone by organic matter in response to increased temperature. A continuous colour change is observed in transmitted light, depending on the organic matter type, from pale yellow, through orange, brown and finally to black in post-mature samples. The observed colour changes are a visible manifestation of the chemical changes taking place, resulting in decreased hydrogen and oxygen content relative to carbon ('carbonisation').

Because of the wide range of original colours exhibited by thermally unaltered organic material, it is necessary to restrict colour evaluation to kerogen particles that are initially yellow, yellow green, pale orange and light brown (Burgess 1974). Thus, colour designation is made on spores, pollen, cuticle, algae and amorphous organic matter (AOM), all of which are originally in the yellow to light brown part of the spectrum. To this end, spores have proved most popular, and their thermal colour changes have been well documented and linked to the various stages of petroleum generation. They show a clear and regular colour progression from various shades of yellow, through orange and brown to black, with the most dramatic colour shift (yellow orange to orange brown) occurring towards the "peak oil generation" level of maturation (Staplin 1969; Burgess 1974; Fisher *et al.* 1980; Marshall 1991; Yule *et al.* 2000). Furthermore, spores often possess large homogenous areas of uniform colour, which makes for less ambiguous colour designation.

However, spore colour is often of limited value in petroleum exploration, as spores are usually only a minor component of oil-prone kerogen, and are sometimes absent altogether. Amorphous organic matter (AOM), the dominant component of oil-prone kerogen, can

prove an acceptable alternative (and accompaniment) to spores when seeking kerogen colour evaluation. While its chemical composition is similar to that of spores, its colour changes will more closely correlate with the generation of liquid hydrocarbons. However, its variable thickness makes AOM difficult to measure consistently. Additionally, its stratigraphical anonymity (in contrast to spores) precludes easy identification of caved material, which is ubiquitous in cuttings samples from hydrocarbon wells (Marshall 1991).

At this point it is important to define what is meant by 'AOM'. Evidence from carbon isotopes suggests that all of the typical AOM in ancient marine basinal fine-grained sediments is ultimately derived from phytoplankton or bacteria (Lewan 1986). However, palynologists often use the term 'amorphous' in a purely descriptive sense without implying a precise physico-chemical condition. Thus, phytoplankton- or bacterially-derived amorphous organic matter (traditionally referred to as 'AOM'), higher plant resins, and the amorphous products of the diagenesis of macrophyte tissues would all fall into this category. During early diagenesis primary conversion of the organic matter occurs. Various physical, chemical and microbiological agents are responsible for these reactions, which occur at surface temperatures and pressures. Further degradation occurs at more advanced stages of diagenesis, when the organic debris of algal origin and the softer parts of macrophyte tissues are further broken down into a structureless amorphous mass often termed 'sapropel'. This process is often termed 'sapropelization' or 'geopolymerization' (Venkatachala 1981). Differing sources, variations in the duration of exposure to aerobic and anaerobic breakdown, and depth of burial with consequent thermal alteration are all reflected in the overall composition and source potential of the organic matter which is ultimately preserved.

There have been few attempts to sub-divide the AOM, reflecting the limited number of morphological characters available to provide a basis for the differentiation of this type of material. Nevertheless, a few schemes for the classification of amorphous material have been proposed that account for its presumed original botanical precursors and the diagenetic processes responsible for its amorphous transformation (Combaz 1980; Masran and Pocock 1981; Venkatachala 1981; Batten 1983). A number of these are presented in Figure 3.1. No one scheme has been universally adopted, reflecting the difficulties encountered when attempting to categorise amorphous organic material.

CATEGORY	SOURCE	CONSTITUENT	MACERAL GROUP	MACERAL	Masran & Pocock (1981)	Venkatachala (1981)	Batten (1983)	Combaz (1980)
Amorphous ('AOM')	Higher plant secretions	Intra-/extra-cellular resins	Liptinite or exinite	Resinite	Resins			Resineux
	Flocs	Organic aggregates and faecal pellets		Bituminite	Grey Amorphous	Biodegraded Aqueous Organic Matter Grey Amorphous Organic Matter Organic Matter of Bacterial Origin	Amorphous matter of aquatic origin	Granuleuse Grumeleuse Pelliculaire
	Phytoplankton			Liptodetrinite				
	Bacteria	Cyanobacteria/Thiobacteria		Lamalginite				
	Higher plant decomposition products	Humic cell-filling precipitates Humic extracellular precipitates	Vitrinite or Huminite	Collinite Herbamorphinite	Yellow-amber Amorphous	Amorphous Organic Matter Biodegraded Terrestrial Organic Matter	Amorphous matter of land-plant origin	Gelifee

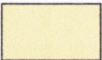
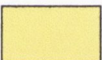
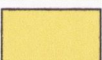

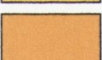

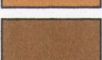
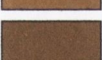

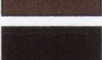
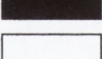
Figure 3.1. Correlation of some published amorphous kerogen terminology, also indicating biological precursor material and kerogen type. Modified from Tyson (1995).

In practice, it remains difficult and sometimes impossible to discern the original source of the amorphous kerogen. In this work, 'AOM' is used in the traditional sense, to describe presumed phytoplankton- or bacterially-derived amorphous kerogen which is oil-prone, green-yellow, orange-brown, or grey in colour, heterogeneous in nature, granular or grumose in texture and fluorescent, under blue UV radiation, at sub-mature to mature levels of maturity. A detailed physical description of the AOM used for colour investigation from each of the studied sample horizons is provided in Section 5.2.

In this study, a colour evaluation of AOM was necessitated by a paucity of palynomorphs in all sample sets (BBN, BGSHN, BGSN). Determination of AOM colour was completed using both qualitative and quantitative techniques.

3.1.2 VISUAL COLOUR SCALES

A number of scales were developed to determine thermal maturation level from visual colour estimates of kerogen, mainly spores and pollen. These have been adopted with varying degrees of success. Amongst the most popular are the TAI scale of Staplin (1969, 1977), the TAI/TAS scale of Batten (1980, 1981, 1982) and the SCI scale of Fisher *et al.* (1980). Staplin's Thermal Alteration Index (TAI) is based on 5 points and represents kerogen colour changes from fresh yellow to brownish yellow, brown, black and finally to black with additional evidence of rock metamorphism. This scale enables colour estimates to be recorded from spores, pollen, cuticles, algae and AOM. Successive scales tended to increase the number of points in order to give greater 'accuracy' over the immature to mature transition. For example, Batten's (1982) Thermal Alteration Scale (TAS) has 7 points, while the Spore Colour Index (SCI) of Fisher *et al.* (1980) has 10 points. The use of these scales was restricted due to lack of agreed standards. They are based on limited numbers of sets of selected standard palynomorphs, which are unavailable to all but the most serious of users. In order to overcome this problem, a number of colour standard charts were proposed. Pearson's (1982) index uses 10 Munsell colour standards, copies of which were freely distributed between 1981 to 1983, and later in amended form from 1984.

POLLEN/SPORE COLOR 'STANDARD'									
MUNSELL COLOR STANDARDS (MATTE FINISH)									
VERSION #2 (1984)									
ORGANIC THERMAL MATURITY	FOSSIL COLOR	APPROXIMATE CORRELATION TO OTHER SCALES		HUE	VALUE	CHROMA	DOMINANT WAVE LENGTH	EXCITATION PURITY	MUNSELL PRODUCT NO.
		TAI = 1-5	VITRINITE REFLECTANCE						
IMMATURE		1	0.5%	7.5Y	9	4	573.5	31	17,391
		1+		7.5Y	9	8	574	57.5	20,520
	* 	2-		5Y	8.5	12	576	80	19,688
* 	2	2.5Y		8	12	579	80.5	14,253	
MATURE MAIN PHASE OF LIQUID PETROLEUM GENERATION	* 	2+		10YR	7	12	582	83.5	13,800
		3-		10YR	6	10	582	80.5	12,424
		3		10YR	5	5	582	61	15,816
		3+		1.3%	10YR	4	4	582	50
DRY GAS OR BARREN		4-		10YR	3	2	582	30	15,814A
		4		10YR	2.6	1	582.5	16	19,365
		(5)							

* THESE COLORS HAVE BEEN CHANGED FROM 1981 VERSION

KEEP COLORS COVERED TO AVOID FADING.

Figure 3.2. Reproduction of Pearson's amended colour standard (version 2, 1984) used for visual AOM colour determinations in this study.

In this study, visual colour estimates of AOM were made, in order to compare with results obtained from the quantitative colour determinations. Colour designation was effected according to Pearson's amended colour standard, Version #2 (1984) (Figure 3.2). This chart includes an adaptation of Staplin's (1969) 5 point TAI scale, with intermediates, making it a 10 point scale. A visual colour estimate of AOM was made under the microscope, and compared with Pearson's colour chart. The TAI number from this chart was then attributed to the sample.

3.1.3 QUANTITATIVE ORGANIC MATTER COLOUR

The validity of visual kerogen colour estimates is often questioned, due to the subjectivity involved in the method. At best, one operator can be consistent in colour assessment, but an identical sample may be 'colour coded' quite differently by another operator, due to the differing spectral responses of the normal human eye.

There have been a number of approaches to the quantified measurement of organic matter colour. Most approaches involve spectral analysis of light transmitted through palynomorphs, mainly spores and pollen. These attempts have employed either light absorbance (Gutjahr 1966) or its reciprocal, transmittance (Grayson 1975; Smith 1983; Van Gijzel 1989; Marshall 1991; Yule *et al.* 1999; Robison *et al.* 2000) to quantify organic matter colour. Smith (1983) used microspectrophotometry to quantitatively compare and correlate the colour standards used in the indices of Staplin (1969), Batten (1980) and Fisher *et al.* (1980). She found good correlation between standards and concluded that, in general, they showed a progressive and regular series of colour increments. Marshall (1991) used the Commission Internationale de l'Eclairage (CIE) colour system to define colour in terms of its chromaticity co-ordinates (x , y) and the luminance (L). Using x and y , or x and L co-ordinates, he defined a cusp-shaped maturation pathway for spore colour, with reasonable vitrinite reflectance correlation up to 1.3% R_r . Using photometric methods, he measured a series of secondary (SCI) standards of Fisher *et al.* (1980) and found a reasonable fit on his quantitatively defined maturation pathway. Yule *et al.* (1999) used microspectrophotometry to measure the amount of light transmitted through a spore at three different wavelengths within the visible spectrum (450nm, 550nm and 650nm). Spore

colour was quantified as Spore Transmittance (% *St.*): $\%St. = 100 \times T_{550} / (T_{450} \times T_{650})$, where T is the transmission at wavelengths 450, 550 and 650nm. % *St.* values increased with increasing SCI and vitrinite reflectance.

The above methods all employ palynomorphs, mainly spores and pollen, in their quantitative assessments of colour. Another approach measures the white-light spectrum transmitted through a particle of amorphous kerogen (AOM): the dominant component of oil-prone kerogen (Van Gijzel 1989; Robison *et al.* 2000). The transmittance colour index (TCI) is obtained from rapid spectral screening of transmittance spectra in tungsten light and is based on the increased curving of these spectra with progressive thermal maturity. TCI values correlate well with mean vitrinite reflectance (R_v) and TAI. Because TCI employs amorphous kerogen, the direct thermal maturity assessment of vitrinite poor rocks can be conducted more easily (Robison *et al.* 2000).

3.1.4 QUANTITATIVE COLOUR MEASUREMENT USING IMAGE ANALYSIS

The determination of kerogen colour by microspectrophotometry involves very specialist and expensive equipment, which is beyond the reach of all but the most serious user. A cheaper, alternative approach has recently been developed for the quantification of spore colour, through the use of colour image analysis software (van de Laar and David 1998; Yule *et al.* 1998). Such image analysis outfits are widely available and have been employed for a variety of geological applications, including porosity studies (Ehrlich *et al.* 1984; Ruzyla 1986; Anselmetti *et al.* 1998), organic petrology (Chao *et al.* 1982; Goodarzi 1987; David and Fermont 1993) and palynofacies studies (Tyson 1990). Helson *et al.* (1995) used colour image analysis to quantify the Conodont Alteration Index (CAI).

A large part of colour space may be defined in terms of red, green, blue (RGB) colour coordinates. The RGB values are integers between 0 and 255 and all possible combinations of these three values give approximately 16.7 million discrete colours. The RGB colour format is used by standard display monitors, with each pixel a combination of red, green and blue. It is the measurement of these RGB pixel intensities that Yule *et al.* (1998) used

to quantify spore colour. The same approach has been applied here to quantify the colour of AOM. The method used in this study is detailed in Section 3.3.

3.2 PREPARATION OF SAMPLES FOR AOM COLOUR DETERMINATION

3.2.1 SAMPLE PREPARATION

Sample preparation for AOM colour determination is identical to the 'cold' processing procedure described in Section 2.2.1. Just as the high temperatures produced by the PROLABO® *Microdigest 3.6* precluded its use for vitrinite reflectance preparation, so too it was an unsuitable preparatory apparatus for the study of thermally induced kerogen colour alteration. Any carbonate present was first removed in HCl, followed by decant washing to remove any soluble calcium compounds. Demineralisation in HF was then completed in a warm water bath, followed by decant washing and progressive dilution with water. The residue was then divided into two unequal aliquots. The larger aliquot was sieved through a 20µm mesh, collected and stored under water in a glass vial before the mounting stage. The smaller unsieved aliquot was also stored under water in a second glass vial.

3.2.2 MOUNTING

Palynological slides were prepared from both the sieved and unsieved sample aliquots. Slides of the sieved residue were used for AOM colour, organic matter fluorescence and palynofacies investigations. Slides of the unsieved residue were kept as a reference to ensure that nothing important (e.g., small (< 20µm) palynomorphs) was lost during the sieving stage.

A few millilitres of the aqueous residue suspension were pipetted onto the surface of a coverslip using *Cellulsize* as a dispersal agent, and left to dry in a drying cabinet to prevent possible contamination by modern pollen or dust particles. A few drops of *Elavacite* mounting medium were pipetted onto a 0.8/1.0mm thick glass slide, and the coverslip was

gently placed on top, residue side down. The mounting medium was then left to cure overnight in the drying cabinet at room temperature.

3.3 COLOUR MEASUREMENT

3.3.1 SYSTEM SETUP

Image analysis systems manage live images by converting the optical image from a light microscope into an electronic signal suitable for processing. The AOM was observed using a Leitz Dialux 20 transmitted light microscope with an attached JVC TK-C1380 colour video camera. The video signal from the camera is taken and converted to a digital image by an *Analogue to Digital Converter* (ADC) within the Leica Q500IW imaging workstation. At each pixel the RGB level of the image is sampled. In this way, the entire image is broken up into a 2d array of pixels, each with a discrete RGB level. The digital image is displayed on a Mitsubishi Diamond Scan 15VX monitor and processed using the QWin software.

For colour work it is important to run the microscope lamp near its maximum voltage in order to get the whitest possible light. The power supply is also more stable at this setting. The voltage setting that was decided upon for this experiment was a compromise between using the whitest possible light (R255 G255 B255) and ensuring that the image under the microscope did not appear 'burned out'. The background illumination shows a spread in RGB values until $\sim 9V$, where Red, Green and Blue begin to converge (Figure 3.3). Above 10V the image appeared burned out. A voltage setting between 9.5 - 10V gives optimal results. A standard operating procedure was established with the microscope set-up running at 9.5V, with a 100W bulb, a Leitz NPL Fluotar L25/0.55 objective and a neutral density diffusing filter. The aperture diaphragm was fully closed (0 setting). The condenser was turned in and centred, and the field diaphragm was opened far enough for the observable field of view just to be exposed. An inconsistent condenser/field diaphragm position was found to be a major source of error when calibrating the system, so a standard procedure for positioning these needed to be established:

1. Using the 25 \times objective, focus the section with coarse and fine adjustment.

2. Fully close the field diaphragm.
3. Turn the condenser stop screw back and move the condenser into its uppermost position with the vertical adjustment.
4. Rotate the condenser stop screw to lower the condenser, so that the edge of the field diaphragm appears sharp.
5. Centre the image of the field diaphragm with the two centring screws.
6. Open the field diaphragm so that it just disappears beyond the edge of the field of view.

The microscope set-up used for colour determination in this study is detailed in Figure 3.4.

The camera setup used for colour determination in this study is detailed in Figure 3.5. The JVC TK-C1380 is a single chip Red/Green/Blue (RGB) colour video camera with a resolution of 440,000 effective picture elements. The CAMERA SETUP screen is accessed via the buttons at the top of the camera. The electronic shutter was set to 'MANUAL' and a shutter speed of 1/1000 second was used. The Automatic Gain Control (AGC) and Back Light Compensation (BLC) were disabled and the Camera White Balance was set manually. White Balance is controlled by two scales: a Red → Blue scale and a Magenta → Green scale. These scales are made up of 18 stops, with each stop comprising 16 sub-stops. The Camera White Balance setting used in this study is shown in Figure 3.5.

3.3.2 SYSTEM CALIBRATION

The RGB values are integers between 0 and 255. It is the measurement of these RGB pixel intensities which has been used to quantify the colour of the AOM. Once the system had been set up according to Section 3.3.1, the factors determining intensity levels, i.e., light source, voltage, diaphragm settings, filters, lenses, etc. were, as far as possible, kept constant during the experiment. In their study, Yule *et al.* (1998) used an RGB measurement of the background illumination to check the replicability of the set-up (Figure 3.6(d); R137 G170 B147). However, a measurement of the background illumination alone was found here to be inadequate for this purpose.

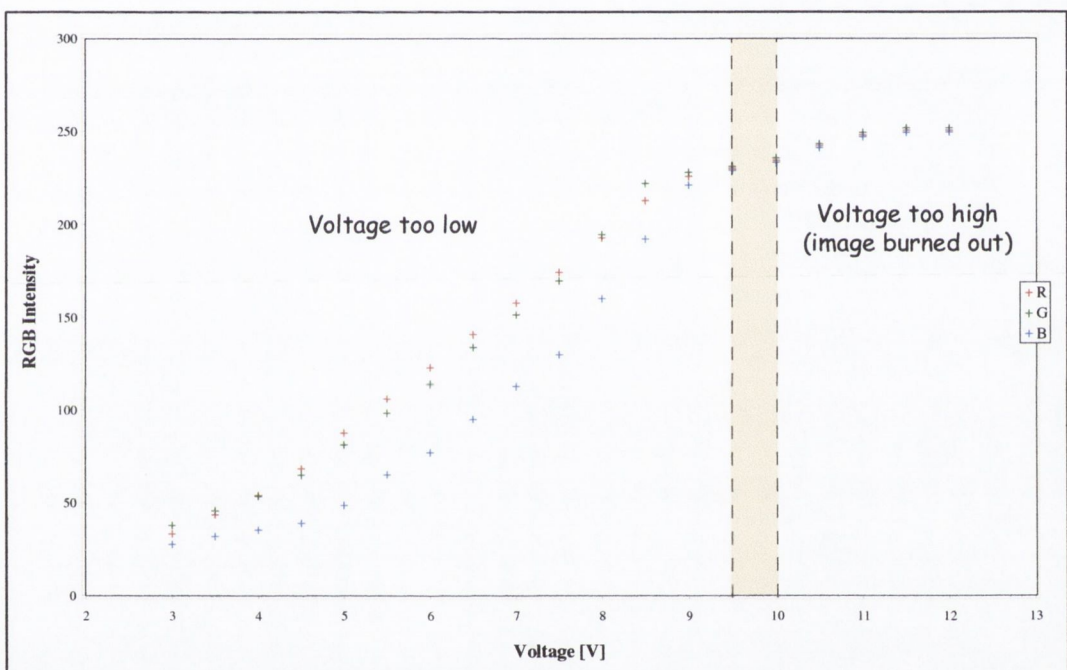


Figure 3.3. Plot showing RGB intensity of background illumination versus lamp voltage. The area enclosed by the dashed lines indicates the optimum voltage estimated for RGB colour work.

MICROSCOPE	LEITZ DIALUX 20
ILLUMINATION	9.5V, 100W
OBJECTIVE LENS	LEITZ NPL FLUOTAR L25/0.55
APERTURE DIAPHRAGM	Fully closed (0 setting)
FIELD DIAPHRAGM	Stopped just outside field of view
CONDENSER	ACHR 0.90 S1.1 (turned in)
FILTER	1 Neutral Density Diffusing Filter

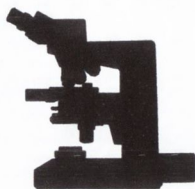


Figure 3.4. Microscope set-up used for AOM colour determination in this study

--CAMERA SETUP--

SYNC ADJUST
VIDEO ADJUST
MODE SELECT
END MEMORY

--SYNC ADJUST--

TERM.	ON
H PHASE	25
SC COARSE	1
SC FINE	128
FINE LOCK	OFF
V COARSE	1
V FINE	128
END	

--VIDEO ADJUST--

IRIS	0
COLOUR	0
PEDESTAL	0
ENHANCE	0
HUE	0
END	0

--MODE SELECT--

ID	OFF
AGC GAIN	0dB
SUPER AGC	OFF
SHUTTER	MANU(1/1000)
BLC	OFF
Av:Pk	8:2
W. BAL	MANU
HLI	OFF
END	

Figure 3.5. JVC TK-C1380 video camera software set-up used in this study. The camera set-up screen operation buttons are located at the top of the camera.

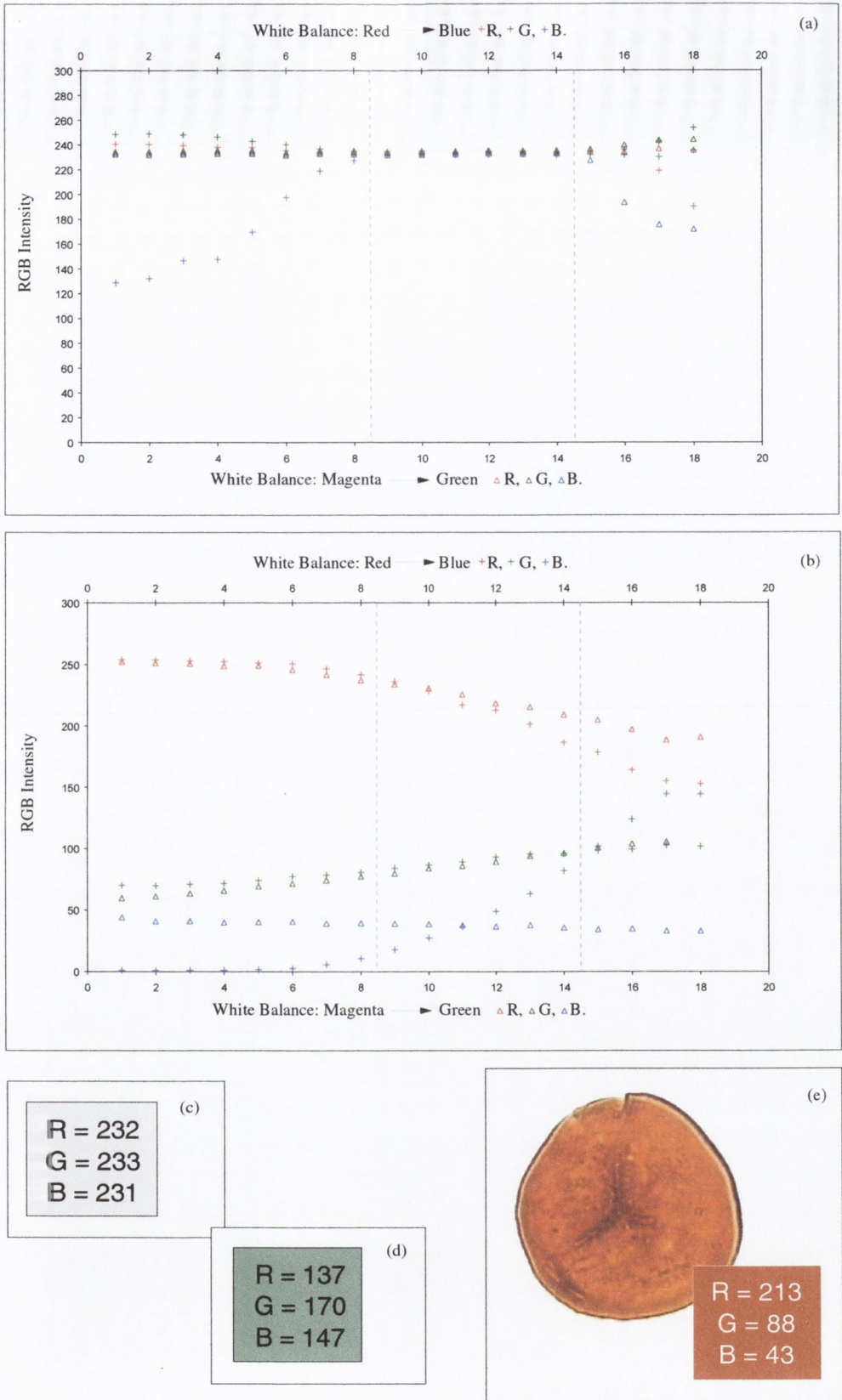


Figure 3.6. (a) Camera white balance adjustment versus RGB intensity of background illumination. The dashed lines mark out a zone within which the RGB values of the background illumination remain unchanged with changing camera white balance. (b) Camera white balance adjustment versus RGB intensity of reference spore used for calibration in this study. The dashed lines mark out a zone within which the RGB values of the background illumination remain unchanged with changing camera white balance. (c) Background illumination used in this study (R = 232 G = 233 B = 231). (d) Background illumination used in Yule *et al.* (1998) (R = 137 G = 170 B = 147). (e) Reference spore used for calibration in this study (*TCD56234*, E.F. L32/1; R = 213 G = 88 B = 43).

The colour of the background illumination proved to be insensitive to adjustments to the camera white balance, whereas the same adjustments were observed to have a major effect on the RGB values of organic material (Figures 3.6(a) and (b)). In this study, the replicability of the set-up was checked by measuring the RGB values of both the background illumination (Figure 3.6(c); R232 G233 B231) and a spore, *Punctatisporites solidus* (TCD56234, E.F. L32/1), selected as a reference standard (Figure 3.6(e); R213 G88 B43). Five RGB measurements were made on the reference spore, the mean of which was taken as the RGB value for the spore. Each time the system was set up, the colour of both the reference standard and the background illumination was determined to ensure a constant illumination between experiments. Occasionally, it was necessary to 'tweak' the voltage and/or the camera white balance by a small amount (a couple of sub-stops) in order to replicate the reference RGB values. The RGB values of the reference standards were checked before and after each sample measurement to ensure against drift.

3.3.3 COLOUR MEASUREMENT

A four step program, *EasyColour.Q5R*, was created using QUIPS, QWin's interactive macro-programming facility (Appendix VIII). It consists of *Image Setup*, *Colour Detect*, *Binary Edit* and *Measure Feature* steps:

Image Setup

This step allows the user to capture the live image from the video camera. The video gain and offset in the Image Setup dialog are set to "Standard Settings". At this stage, the AOM particle to be measured is focused and centred on the microscope cross-hairs (Figure 3.7).

Colour Detect

Detection is the process of distinguishing between wanted and unwanted regions in the field of view. The process involves a comparison between the colour image and reference RGB thresholds (i.e., upper and lower limits of the RGB intensity levels) set by the operator. The threshold RGB values are set by simply selecting regions of interest with the mouse. A number of values can be selected by checking the "Accumulate" check-box in the *Colour Detect* dialog. For each pixel within an area defined by the image frame a decision is

made by the software depending on their relative values. A binary image of the detected area is then generated (blue) (Figure 3.8).

Binary Edit

The Binary Edit step allows the operator to modify the binary image. Using the mouse, the operator can identify regions of the image that he wishes to accept (green) or reject (yellow) (Figure 3.9).

Measure Feature

This final step allows the operator to measure the mean RGB intensity level of the selected area (red) (Figure 3.10).

Care was taken to avoid AOM particles that appeared overly 'thickened' as a result of clumping. Structured particles, which had become incorporated into the AOM were also avoided. A total of 25 RGB particle measurements were recorded for each sample, the mean of which was taken as the RGB value for that sample.

3.3.4 ACCURACY OF COLOUR MEASUREMENTS

There is an inherent subjectivity involved in the selection of what areas of the spore or AOM particle are to be measured. Large errors are introduced by inconsistent selection of the area to be measured during the *Colour Detect* stage. Spores allow more consistent colour detection to be made, as they often possess large homogenous areas of uniform colour (Figure 3.11). AOM particles are essentially heterogeneous and require careful selection of the areas to be measured. Within each AOM particle, the range of RGB values is quite large, and consequently inconsistencies in measurement area selection during the *Colour Detect* stage are more likely. Multiple RGB determinations, made by the same operator, on the same AOM particle show quite a wide variation when compared with the same number of measurements made on the reference spore (Figure 3.11). Within a population of 25 AOM particles, the variation is even greater. However, the colour range observed within a sample is strongly dependent on maturation level.

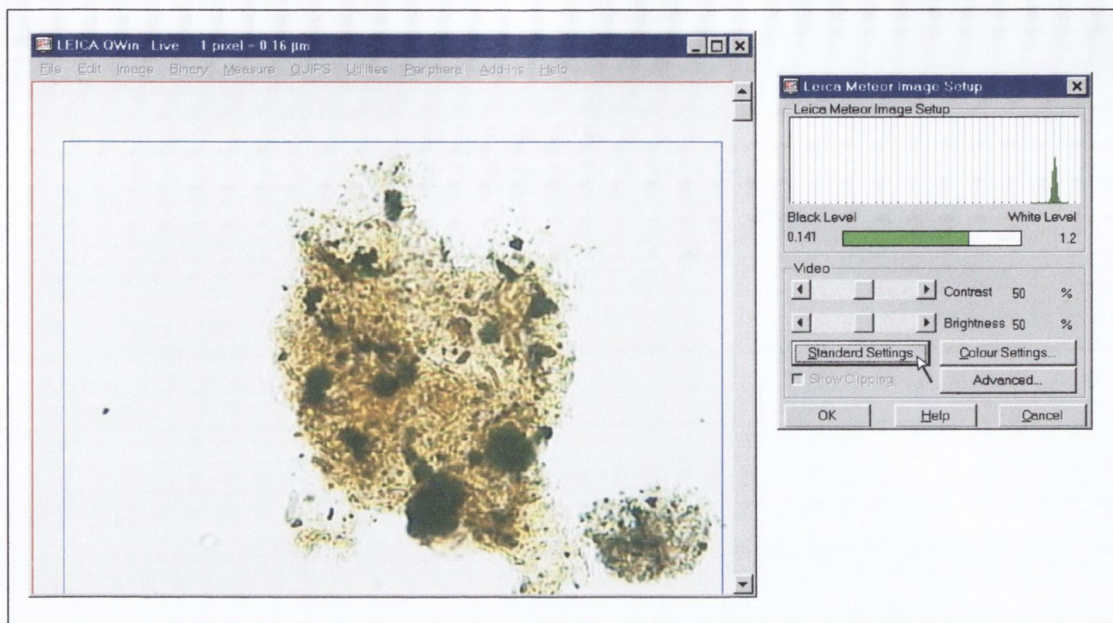


Figure 3.7. *EasyColour.Q5R*, *Image Setup* Dialog. The video gain and offset are set to "Standard Settings".

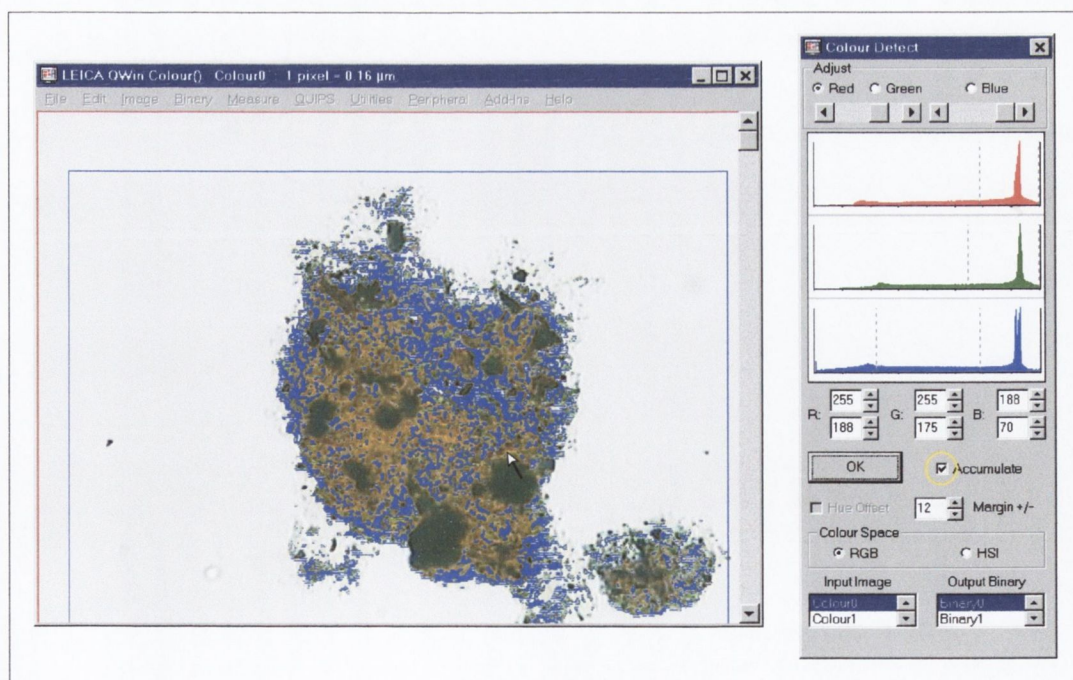


Figure 3.8. *EasyColour.Q5R*, *Colour Detect* Dialog. Regions of interest are detected by setting the RGB threshold values with the mouse button (note that the "Accumulate" checkbox is checked).

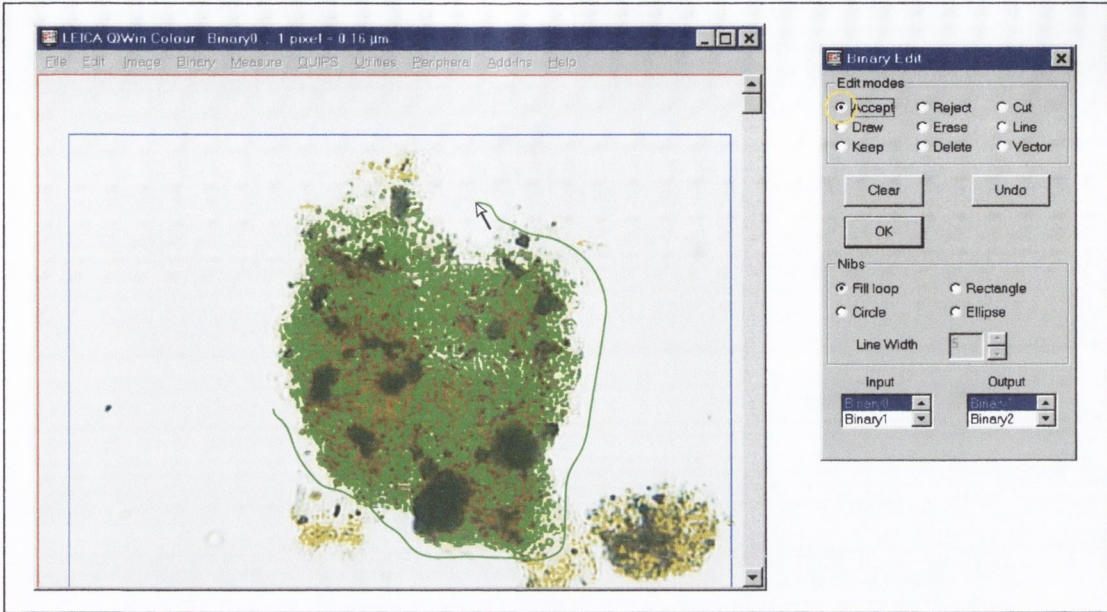


Figure 3.9. *EasyColour.Q5R*, Binary Edit dialog. Using the mouse, the operator identifies regions of the binary image to measure (note that the "Accept" bullet box is checked).

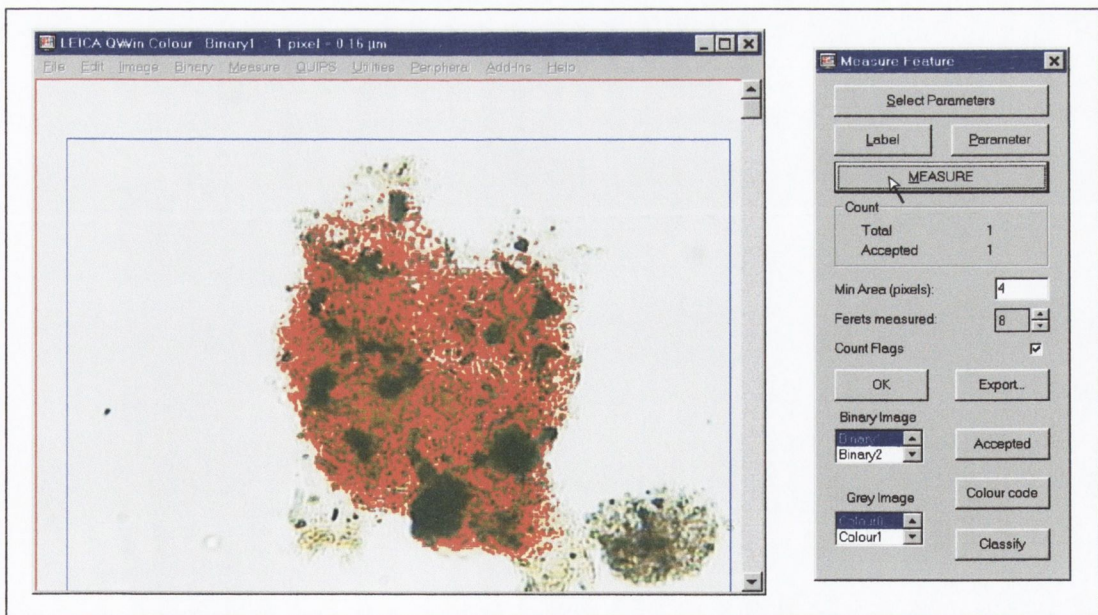


Figure 3.10. *EasyColour.Q5R*, Measure Feature dialog. An RGB measurement of the binary image will be completed when the MEASURE button is depressed.

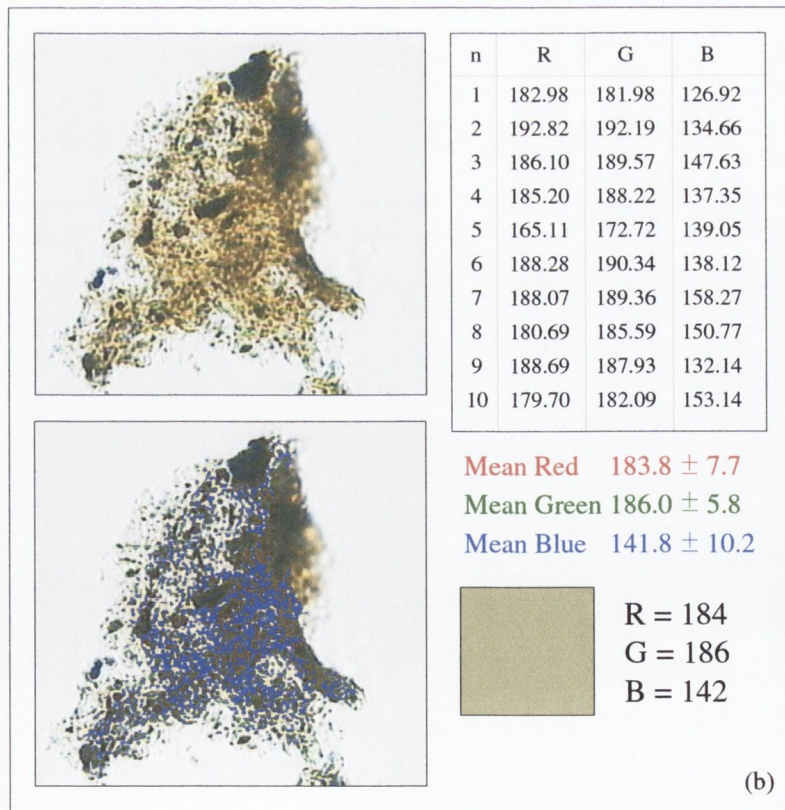
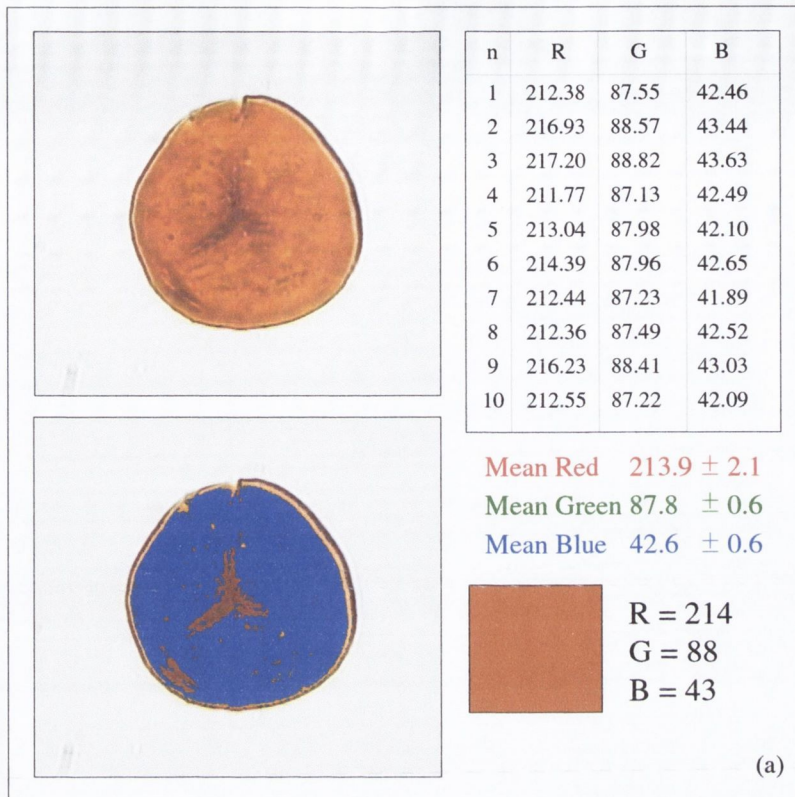


Figure 3.11. Inconsistent Binary Detection during RGB measurement (a) Multiple RGB determinations made on one spore (b) Multiple determinations made on one AOM particle. Note that the calculated mean RGB value for the AOM particle does not match the colour observed visually.

The calculated mean RGB value for the AOM particle is a composite RGB value of all the detected/accumulated areas of the particle. Another consequence of the heterogeneous nature of AOM is that the quantitatively defined RGB colour of the particle rarely matches a visual estimate of the particle colour (Figure 3.11). Spores, which are much more uniform in colour, have calculated RGB colours that correspond well to visual colour estimates.

3.4 ORGANIC MATTER FLUORESCENCE

3.4.1 BASIS OF FLUORESCENCE

Fluorescence can best be described as the short-term luminescence of a substance excited by radiation. When radiation of relatively high energy and short wavelength bombards a substance capable of fluorescing, that substance absorbs and converts a small part of that energy into heat. Most of the energy absorbed by the substance is emitted again as photons of electromagnetic radiation. The wavelength of the emitted fluorescent light is longer (lower energy) than that of the excitation radiation, falling within the visible spectrum (Figure 3.12). For visual fluorescence assessments of organic matter, blue light or (blue-UV) excitation is used. The structures which are responsible for the absorption and emission phenomena involved in the fluorescent behaviour of organic material exhibit specific types of carbon bonds (conjugated double π -bonds) which allow the electron mobility necessary for fluorescence (Taylor *et al.* 1998). These compounds, referred to as 'fluorophores', are limited to the liptinite-exinite macerals and include the carotenoids of sporinite and alginite, isoprenoids of resinite, phenols of cutinite and suberinite and some primary and secondary aromatic structures (Lin and Davis 1988). Fluorescence is apparently enhanced when these fluorophores are dispersed throughout a non-fluorescing aliphatic medium (Taylor *et al.* 1998), hence the observed correlation between fluorescence and hydrocarbon potential.

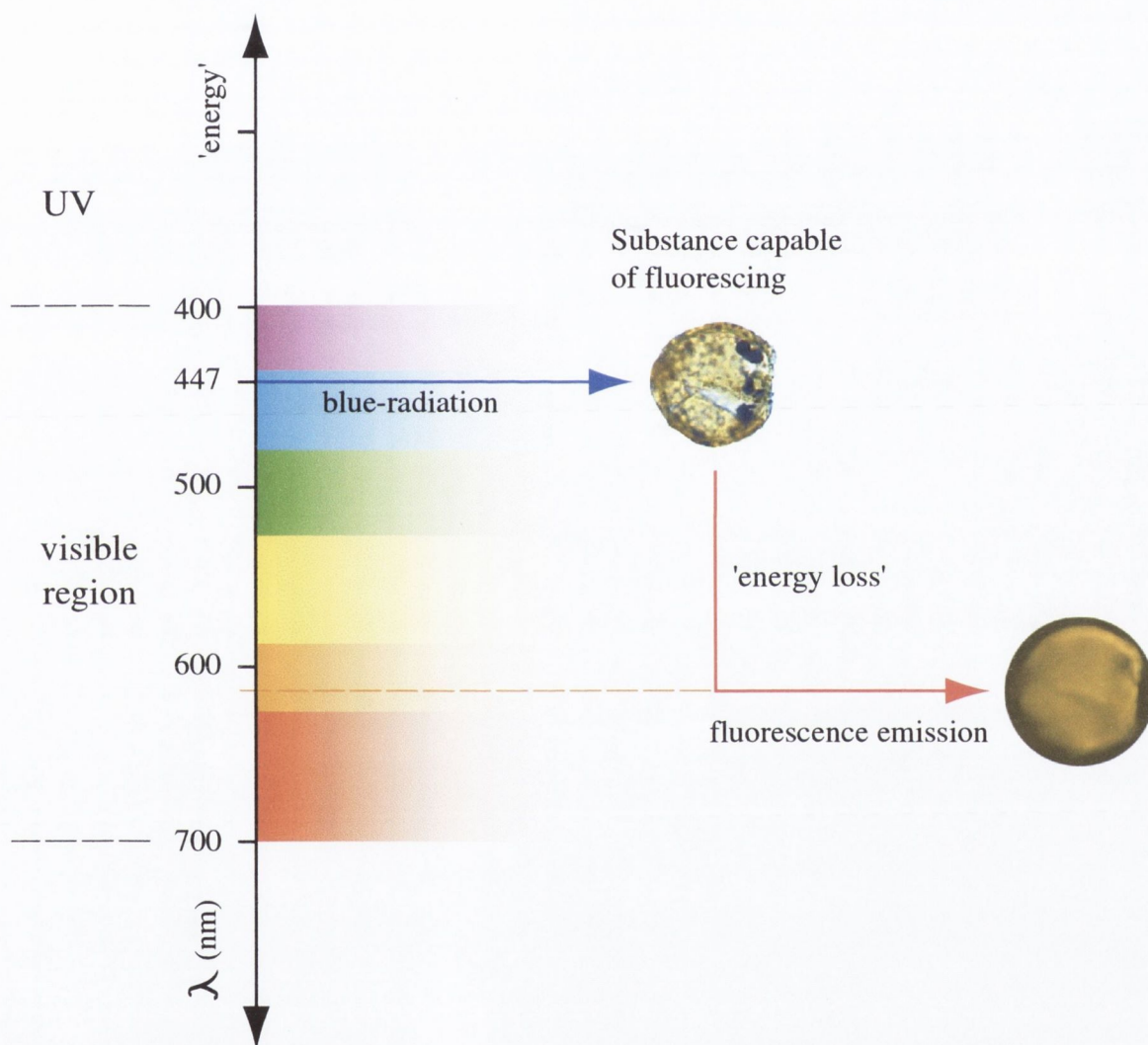


Figure 3.12. Basis of fluorescence: the excitation of a substance by heat or light causes it to fluoresce. The fluorescent radiation is of lower energy (longer wavelength) than the excitation radiation.

3.4.2 APPLICATION OF FLUORESCENCE MICROSCOPY

Fluorescence is directly related to organic matter type and level of maturity. Polymerisation, aromatisation and condensation associated with organic maturation cause a gradual shift in fluorescence colours towards the red end of the visual spectrum, i.e., from shorter to longer wavelengths. Fluorescence colours progressively decline in intensity with maturation, and shift from green through yellow, orange and finally to brown. Extinction of fluorescence in liptinites occurs at the medium-volatile bituminous coal stage, when cracking of liquid hydrocarbons into gaseous components occurs. The residual aromatic structure becomes too highly polymerised to fluoresce. This increase in size and concentration of the macromolecules together with the delocalisation of the π -electrons is responsible for the loss of fluorescence.

Sporinite exhibits the most consistent changes in fluorescence characteristics with rank and fluorescence investigations therefore traditionally favour spores and pollen. Teichmüller (1974) noted stages of marked change ('coalification jumps') in the fluorescence character of sporinites, reflecting important transformations in the liptinitic macerals. These occur at vitrinite reflectance values of 0.5% R_r , 0.8 - 0.9% R_r and 1.3% R_r , and correspond to the base, peak and top of the oil window respectively. The third 'jump' is characterised by the complete extinction of fluorescence and marks the 'death line' for oil generation.

In areas of anomalous heat flow, deviations have been recorded from the documented extinction point of spore fluorescence (1.2 to 1.35% R_r). Fitzgerald (1994) recorded premature extinction of fluorescence, at 1.1% R_r , from the Navan mine area. In siltstones adjacent to the North Star Dyke in Ballycastle, Co. Antrim, the extinction point of spore fluorescence was found to be retarded, at 1.65% R_r (Goodhue 1996).

Fluorescence colour and intensity are strongly dependent on organic matter type and species. Fresh spores and pollen have fluorescence colours ranging from blue to red depending on the species. Marine-derived palynomorphs begin fluorescing with greener colours than spores, and generally exhibit more intense fluorescence than spores of the same rank. In certain instances, acritarchs and dinoflagellates may still fluoresce slightly after the extinction of spore fluorescence. Fluorescence properties are also affected by preservation state (Tyson 1990). Diagenetic degradation can produce changes that are

similar to those due to maturation (i.e., a decrease in fluorescent intensity and a shift towards red colour) (Tyson 1995).

As primary fluorescence is limited to the liptinitic kerogen components, it is essential for assessing the proportion of highly oil-prone constituents of kerogen residues. It is especially useful for distinguishing between highly fluorescent amorphous kerogen of aquatic origin and the weakly- or non-fluorescent type, which is probably of terrestrial origin (lignin-derived). The former type is usually oil-prone, while the latter is probably gas prone or of no source potential at all. However, non-fluorescent amorphous kerogen may also represent degraded plankton-derived AOM (Tyson 1995). A weak fluorescence is sometimes observed of vitrinite particles that are present as minor constituents of oil source rocks. This is known as 'secondary fluorescence', and is attributed to the presence of migrated hydrocarbons that have become incorporated into the vitrinite structure (Teichmüller 1974).

Fluorescence microscopy is particularly useful in palynofacies investigations for detecting the presence of small, translucent palynomorphs or palynomorphs that are masked by AOM. It often indicates palynomorph abundance in AOM-rich facies is significantly underestimated by transmitted light observations (Tyson 1995). It can prove especially useful for kerogen typing through colour image analysis, where discrimination of some kerogen particles by intensity level (grey or RGB) thresholding in transmitted light is impossible (Tyson 1990).

3.4.3 SAMPLE PREPARATION

The preparation procedure for fluorescence studies is identical to that used in transmitted light analysis (Section 3.2). Consequently, the same sample slides used in the transmitted light study were used in the fluorescence analysis. For fluorescence studies, it is crucial to use an appropriate non-fluorescent mounting medium in order to maximise image contrast. The mounting medium employed here, *Elvacite*, produces a dull green-black background when viewed under the fluorescence microscope.

3.4.3 FLUORESCENCE MEASUREMENT

Organic matter fluorescence investigations were carried out using the same Leitz Dialux 20 binocular microscope that was employed in the transmitted light colour analysis. The microscope was equipped with a Leitz PLOEMOPAK 2.4 high-powered mercury vapour fluorescence illuminator, fitted with a Leitz H2 filter block (BP 390-490 excitation filter, RKP 510 dichroic mirror, LP 515 barrier filter). This lamp/filter combination produced violet and blue radiation (390-490nm). The system was allowed to stabilise for 30 minutes before any fluorescence observations were recorded.

As the actual light levels of fluorescence are quite low, fluorescence observations were carried out in a darkened room in order to facilitate easier observation. Fluorescence observations were made using a Leitz NPL Fluotar L25/0.55 objective, however critical evaluation of the extinction of fluorescence was made using the 40× objective. The organic matter was subjected to approximately one minute of excitation, after which time the fluorescence colour was recorded. Unless otherwise stated, the fluorescence colour refers to that of AOM.

CHAPTER 4

VITRINITE REFLECTANCE RESULTS

4.1 INTRODUCTION

The results of the vitrinite reflectance investigation of sediments through the aureole of the Berreraig Bay dyke are discussed in this chapter and summarised in Appendix IV and V. Vitrinite reflectance histograms for all samples analysed are presented in Appendix II. In each case, the mean random reflectance (R_r), standard deviation (S.D.) and number of measurements (N) used to calculate the mean is stated beside the histogram.

4.2 VITRINITE REFLECTANCE RESULTS

4.2.1 VITRINITE REFLECTANCE OF BBN SAMPLE HORIZON

The BBN sample suite, being the most comprehensively sampled of the three horizons, afforded the most detailed analysis. Vitrinite reflectance measurements were obtained from all 43 available samples from this horizon (sample BB39N was lost prior to the vitrinite reflectance investigation). A plot of vitrinite reflectance through the BBN sample horizon against perpendicular distance from the northern dyke contact is presented in Figure 4.1. The data indicate a local 'background' maturity level of 0.73 - 0.79% R_r at distances greater than 1.8m from the intrusion. Reflectance values initially increase gradually from 0.79% R_r to 0.97% R_r , between 1.8m and 0.5m from the dyke contact respectively. Within 0.5m of the dyke contact, the reflectance values increase sharply in the direction of the intrusion, from 0.97% R_r to 3.6% R_r at the dyke contact. The R_r data show an obvious reaction to the increased temperature close to the intrusion.

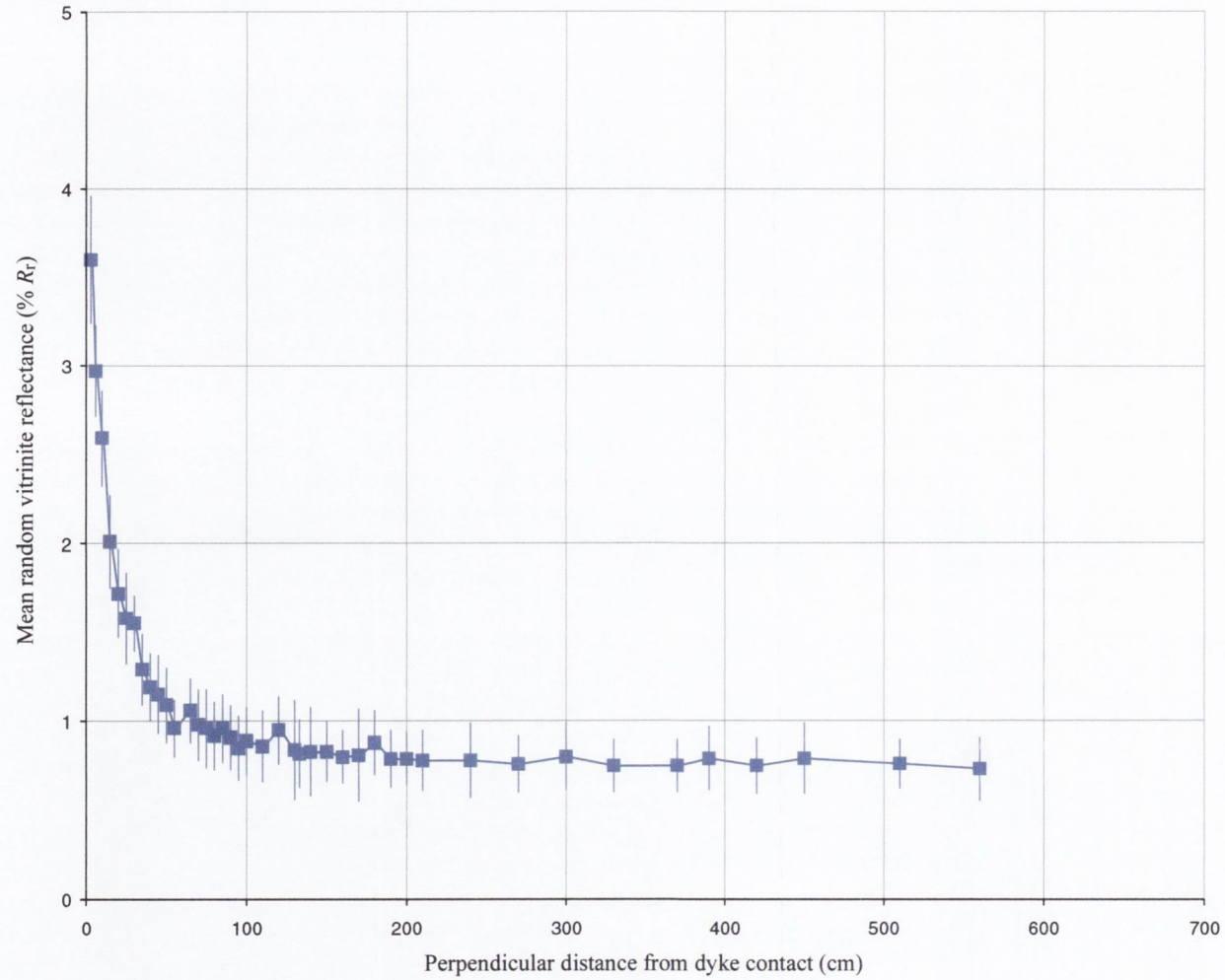


Figure 4.1 Plot of mean random vitrinite reflectance (R_r) for the BBN sample horizon versus perpendicular distance from the dyke contact. The R_r values have \pm one standard deviation about the mean.

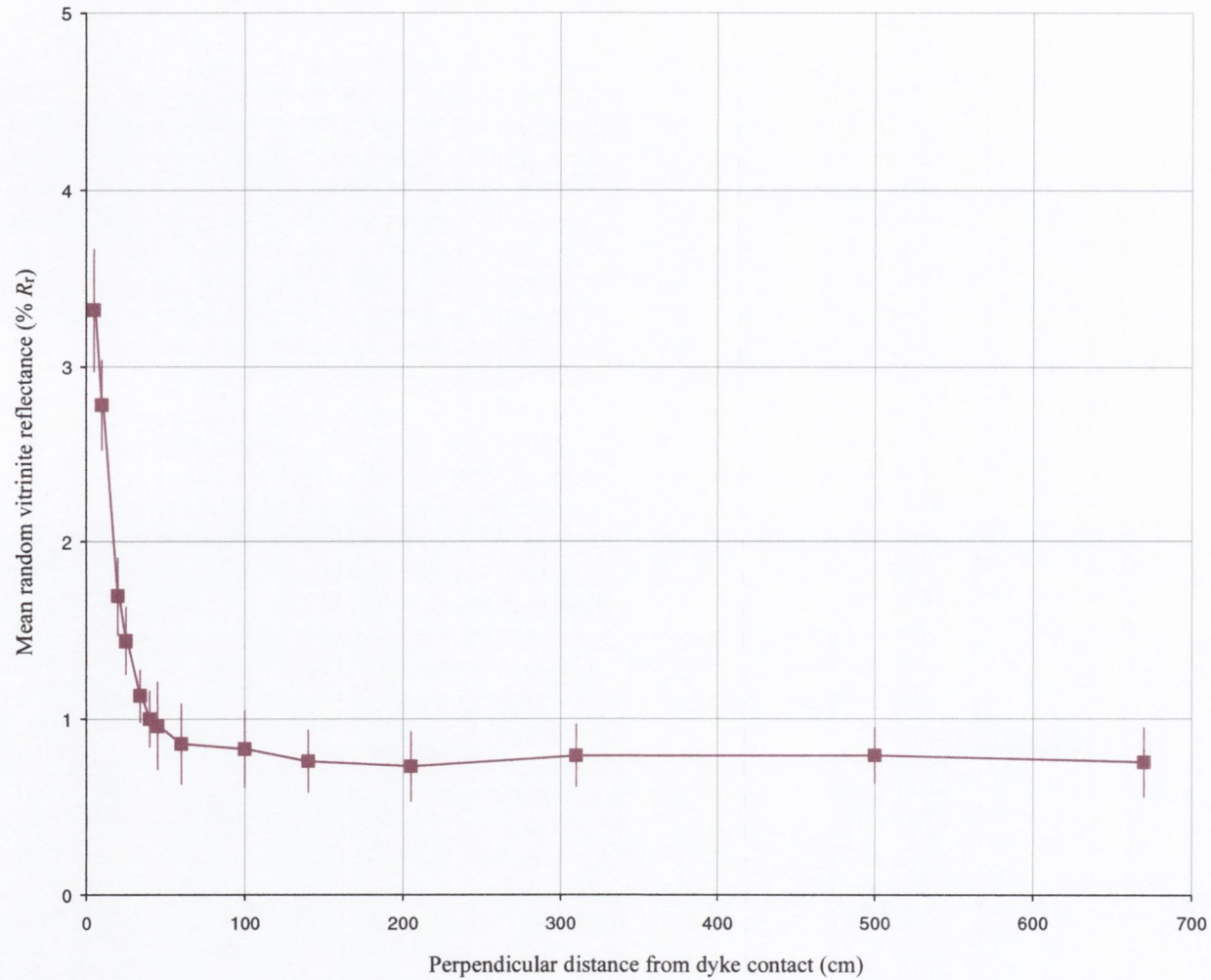


Figure 4.2. Plot of mean random vitrinite reflectance (R_r) for the BGSNH sample horizon versus perpendicular distance from the dyke contact. The R_r values have \pm one standard deviation about the mean.

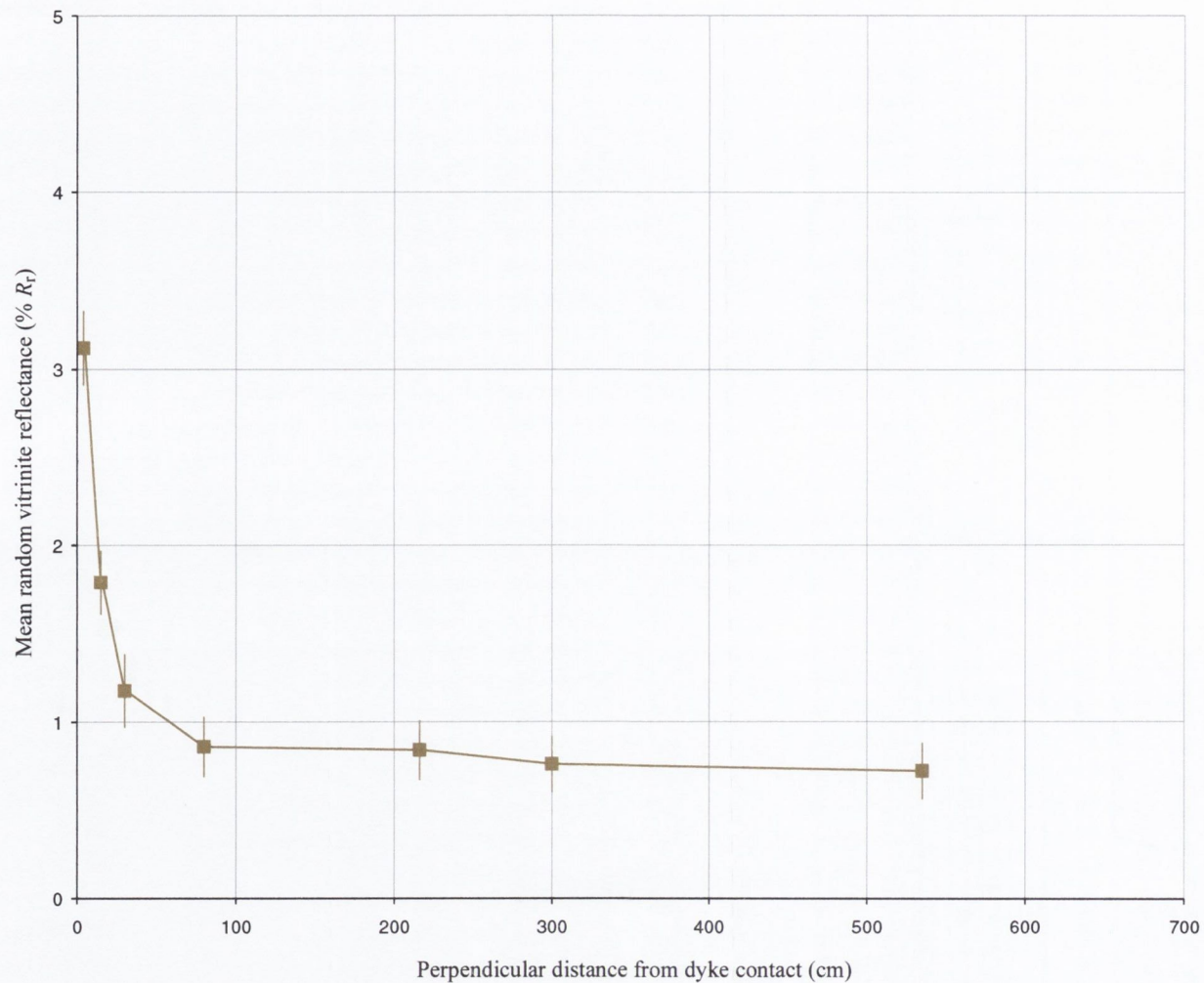


Figure 4.3. Plot of mean random vitrinite reflectance (R_T) for the BGSN sample horizon versus perpendicular distance from the dyke contact. The R_T values have \pm one standard deviation about the mean.

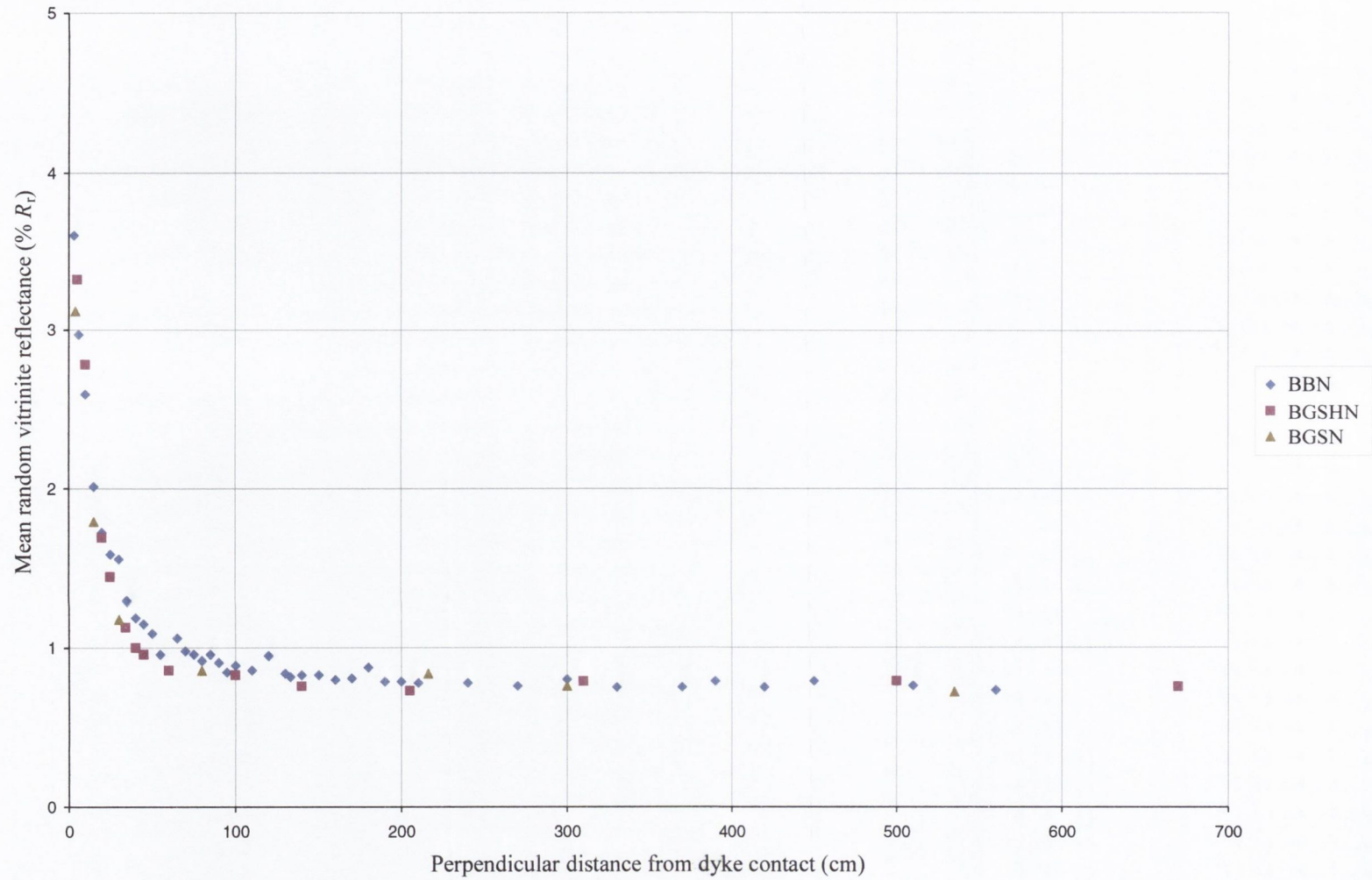


Figure 4.4. Cumulative plot of mean random vitrinite reflectance for the BBN, BGSHN and BGSN sample horizons versus perpendicular distance from the dyke contact.

4.2.2 VITRINITE REFLECTANCE OF THE BGSNH SAMPLE HORIZON

Vitrinite reflectance measurements were conducted on all 14 samples of the BGSNH sample suite. A graph of vitrinite reflectance through the BGSNH sample horizon against perpendicular distance from the northern dyke contact is presented in Figure 4.2. Local 'background' reflectance values range from 0.73% R_r to 0.79% R_r at distances greater than 1.4m from the dyke. Vitrinite reflectance values initially increase slowly, from 0.73% R_r at a distance of 1.4m from the dyke, to 0.96% R_r at 0.45m from the contact. Within 0.45m of the dyke, reflectance values increase sharply and progressively to a maximum of 3.32% R_r at the contact.

4.2.3 VITRINITE REFLECTANCE OF THE BGSN SAMPLE HORIZON

The BGSN horizon is the most sparsely sampled of the three sample suites and therefore shows the poorest resolution through the intrusion aureole. Vitrinite reflectance measurements were conducted on all 7 of the BGSN samples. A plot of vitrinite reflectance through the BGSN sample horizon against perpendicular distance from the northern dyke contact is presented in Figure 4.3. The R_r data indicate a local 'background' maturity level of between 0.72% R_r and 0.76% R_r . The position of the sharp break in slope of the R_r profile is poorly constrained due to the broad sample spacing in this horizon. Reflectance values increase progressively from 0.86% R_r at 0.7 - 0.8m from the intrusion, to a maximum of 3.12% R_r at the dyke contact.

4.3 DISCUSSION

A cumulative plot comparing the R_r profiles from each of the three sample horizons against perpendicular distance from the dyke is presented in Figure 4.4. It is possible to define a 'reflectance aureole' as the zone, within which the vitrinite shows a marked reaction to the high temperatures close to the dyke. Within this 'reflectance aureole', rank changes from the high-volatile bituminous through medium volatile bituminous, low volatile bituminous, semi-anthracite to anthracite are observed. In each case, the sharpest increase in R_r values occurs within *ca.* 0.5 - 0.6m of the dyke contact. Beyond this distance, R_r values fall

gradually to background levels. The full extent of the reflectance aureole, defined by the R_r profiles, differs slightly between each of the three sample suites. In the BBN sample horizon, the break in slope of the R_r profile is slightly more gradual compared to both the BGSHN and BGSN R_r profiles. This is perhaps partly a consequence of the fact that the BGSHN and BGSN horizons are less rigorously sampled than the BBN horizon. The position of the break in slope of R_r values is therefore less well defined in these horizons and may in fact be more gradational. However, differences in the extent of the reflectance aureole between these horizons may reflect differences in the thermal properties of the host lithologies (e.g. thermal conductivity, porosity, etc.), and/or differing mechanisms of heat transfer (e.g. convection). These are discussed in detail in Chapters 6 and 7.

The vitrinite reflectance of sediments furthest from the dyke should indicate the local background maturity level upon which the effects of contact metamorphism are apparent. Minimum average 'background' reflectance levels of 0.72 - 0.73% R_r were recorded for these sediments, although values range as high as 0.79% R_r . This local 'background' level is consistent between the three sedimentary horizons. This is at odds with the findings of Bishop and Abbott (1995), who recorded somewhat lower background reflectance values, of 0.35 - 0.45% R_r , from sediments in Bearreraig Bay. Indeed, the presence of low reflecting (< 0.4% R_r) vitrinite-like material was observed in several background samples. As many of the samples for reflectance measurement were initially mounted using the polished slide method outlined in Hillier and Marshall (1988), it was possible to observe macerals in both reflected and transmitted light. Using this technique, much of this low reflecting (< 0.4% R_r) material was identified at an early stage as solid bitumen. Inability to distinguish immature vitrinite from solid bitumen can be a major problem in organic petrography (Nuccio 1985; Taylor *et al.* 1998). Robert (1988) noted that bitumen reflectance is lower than vitrinite reflectance at low levels of maturity, but may be either lower, equal, or higher at maturity levels greater than 0.9% R_r . In transmitted light, this material is orange-brown in colour and often has a mottled texture. Particle margins frequently lack definition or have a bevelled appearance, tapering from orange to yellow towards the margin. The reflectance of such material is sometimes as low as 0.2% R_r , and its inclusion among vitrinite reflectance data would substantially lower the mean random reflectance. Once the presence of solid bitumen in the samples was recognised, care was taken not to confuse this material with vitrinite for reflectance measurement.

In the three sample horizons studied here, R_r values rise steeply to the dyke wall. Reversals of vitrinite reflectance values in sediments at the contacts of igneous bodies have been observed in a number of studies of organic metamorphism at intrusive contacts (Bostick and Pawlewicz 1984a; Raymond and Murchison 1988; Khorasani and Murchison 1990; Bishop and Abbott 1995; McCormack 1998). This phenomenon has been attributed to a combination of molecular disordering in the vitrinite at high heating rates and difficulties in attaining large uniformly polished vitrinite particles for measurement at such high temperatures (Khorasani and Murchison 1990). Because vitrinite reflectance generally increases with increasing molecular order, the decreasing molecular order near the dyke is manifested by an observed decrease in R_r values. While reflectance inversions at intrusive contacts are fairly common, they are by no means the rule and their absence should not be considered unusual. Numerous instances have also been reported where R_r values proceed steeply to maximum levels at the intrusive contact (Bostick and Pawlewicz 1984a; Raymond and Murchison 1988; Goodhue 1996). Bostick and Pawlewicz (1984b) reported reflectance reversals in two sedimentary horizons adjacent to the Walsen dyke in Colorado, while R_r values from a third horizon next to the same dyke increased steeply to the dyke wall. Barker and Lewan (1999) observed a similar retardation of R_r at high temperatures from pressurised hydrous pyrolysis experiments with supercritical water conditions ($> 374^\circ\text{C}$, 22 Mpa). The temperature and pressure conditions near dyke contacts, along with low to moderate salinity fluids are close to those required for the development of supercritical fluids. Supercritical water has the ability to readily dissolve organic compounds, including lignocellulosic material, and also seems to promote some types of chemical reactions. During thermal maturation near dykes, reaction of the condensed residual organic matter with supercritical water may occur, reducing or retarding further condensation of the OM (Barker and Lewan 1999). Barker and Lewan (1999) suggested that the atypical occurrence of retarded R_r near dyke contacts may be attributed to the limited range of physical conditions and pore-water chemistry under which supercritical water can exist in sedimentary basins. A single cause for this phenomenon is unlikely, because of "the competing influences that bear variably on the organic matter within the thermal zones of any intrusion" (Khorasani and Murchison 1990).

4.4 THERMAL MODELLING

The chemical reactions involved in the maturation of organic matter are irreversible in nature. Consequently, many attempts have been made to correlate the various organic maturity indices with maximum palaeotemperature. Of these, vitrinite reflectance is considered the most accurate and sensitive to temperature changes (Hood *et al.* 1975; Price 1983; Taylor *et al.* 1998). Nevertheless, conversion of R_r to absolute palaeotemperatures is still problematic (Johnsson *et al.* 1993). Much debate has centred on the relative influence of time and temperature on vitrinite reflectivity. Various authors have assumed that both time and temperature play important roles in determining the reflectivity of vitrinite (Karweil 1955; Teichmüller and Teichmüller 1968; Lopatin 1971; Bostick 1973; Hood *et al.* 1975). Recent chemical kinetic models of vitrinite maturation (Burnham and Sweeney 1989; Sweeney and Burnham 1990) have placed less emphasis on time. A number of field investigations where the duration of heating is well constrained (Barker 1983; Price 1983; Barker and Pawlewicz 1986; Barker 1988; Barker 1991) suggest that for burial histories characterised by uniform heating rates at the time maximum temperatures were achieved, maximum temperature largely determines vitrinite reflectance. Consequently, vitrinite reflectance may be used to estimate maximum palaeotemperatures. Several vitrinite reflectance geothermometers (VRG) have been developed for relation of vitrinite reflectance to palaeotemperature.

4.4.1 MODELS THAT CONSIDER TEMPERATURE AND TIME

The early history of maturity/coalification models saw the development of a number of empirical models for vitrinite maturation based on laboratory and field studies. The earliest attempts to model vitrinite maturation were based on the work of Karweil (1955), who first suggested that maturation was largely time controlled. By studying the thermal alteration of vitrinite in coals from the Ruhr valley in Germany, Karweil (1955) was able to calculate the activation energy required for these coals to reach their current level of maturity. He produced a nomograph for the prediction of coal rank, if both temperature and heating duration are known. Karweil (1955) assumed that the reactions required for vitrinite to mature over a given temperature and time range followed first order Arrhenius

reaction kinetics. He predicted that coal heated at high temperatures for a short period of time could achieve the same maturity as a coal heated at lower temperatures for a longer time.

Karweil's (1955) nomogram was later modified by Teichmüller and Teichmüller (1968) and Bostick (1971) (Figure 4.5). Bostick (1971) incorporated his own laboratory measurements of coal activation energies with Karweil's (1955) nomograph. Bostick's (1971) diagram included a scale for vitrinite reflectance. The work of Karweil (1955) and Bostick (1971) was utilised by Lopatin (1971) and Waples (1980) to develop the time-temperature index method (TTI). Lopatin (1971) based his TTI on empirical data from the Münsterland No. 1 borehole in NW Germany. He assumed that the reactions involved in organic maturation follow first order kinetics that are described by Arrhenius reaction rate equation, whereby the vitrinite maturation reaction rate approximately doubles with each 10°C increase in temperature. Lopatin (1971) assumed the dependence of maturity on time to be linear. Therefore, if the length of time at certain temperature is doubled, the maturity is also doubled. In his calculations, Lopatin (1971) assumed the present geothermal gradient to be constant through time. TTI was refined and correlated with vitrinite reflectance by Waples (1980). While the TTI has been widely adopted, its assumptions are oversimplified and should be considered unsatisfactory in maturity modelling (Waples *et al.* 1992a; Waples *et al.* 1992b).

Hood *et al.* (1975) considered the models of Karweil (1955) and Lopatin (1971) and developed a slightly different approach to time-temperature-maturity relationships. They considered the diagram of Karweil (1955) to overemphasise the effect of time. While previous methods were concerned with integrating the temperature effects over the entire burial history, the Level of Organic Metamorphism model (LOM) (Hood *et al.* 1975) combines maximum temperature with an 'effective heating time' (t_{eff}). They somewhat arbitrarily defined t_{eff} as the time spent within 15°C below the maximum temperature and claimed that the straight lines on their LOM diagram essentially represent a doubling of reaction rate with every 10°C temperature increase (Figure 4.6).

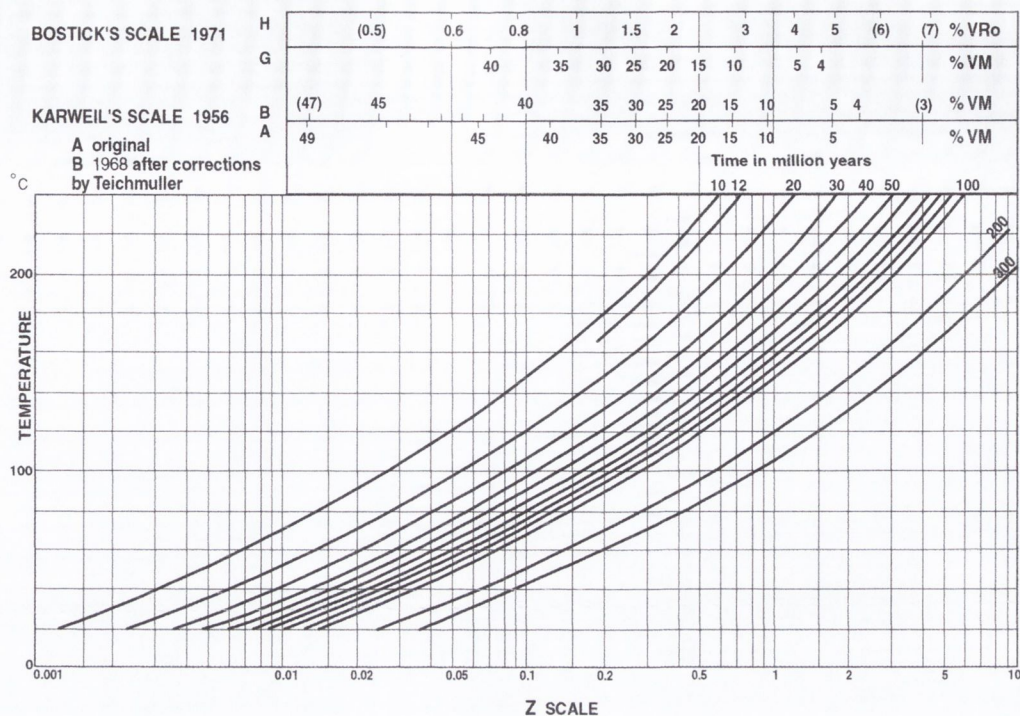


Figure 4.5. The time-temperature-rank nomogram. Determination of rank from (maximum) temperature and duration of reaction (i.e., geological time). The intersection of the time curve (in My) and of the temperature gives, on the abscissa, a value for Z (rank) expressed above in % VRo and VM % (after Karweil 1955, Teichmüller 1968, and Bostick 1971).

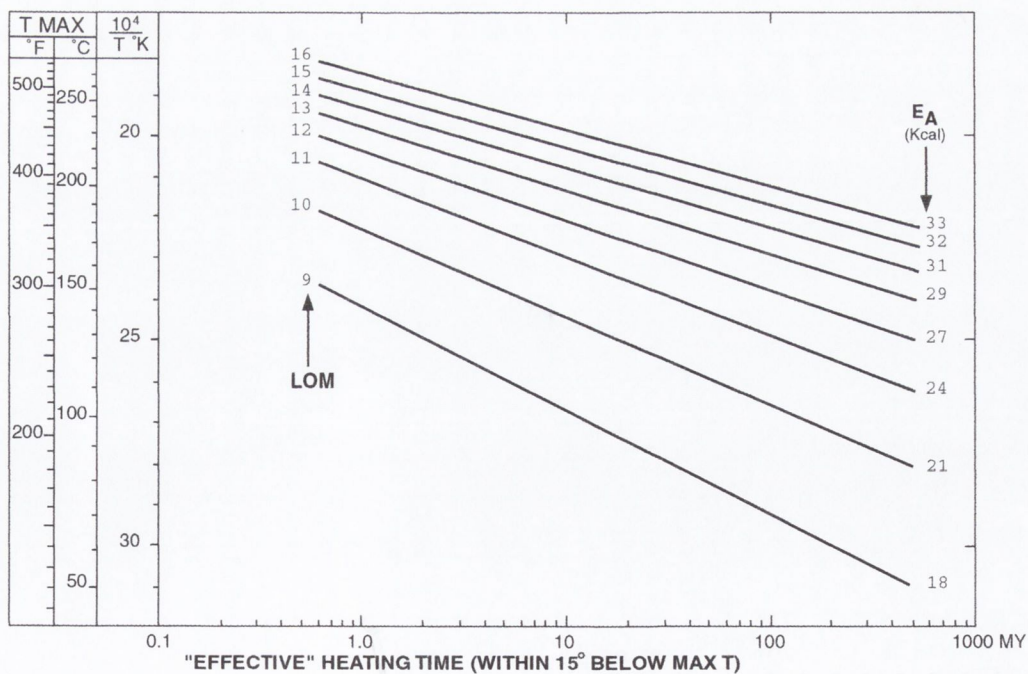


Figure 4.6. Hood *et al.*'s Level of Organic Metamorphism (LOM) diagram. The straight lines essentially represent a doubling of reaction rate with every 10° C temperature increase. After Hood *et al.* (1975).

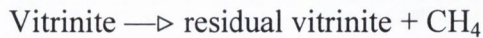
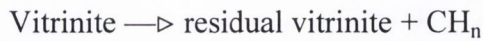
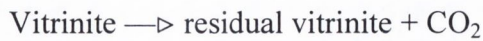
Barker and Pawlewicz (1986) argued that the functional heating duration should only consider the elapsed time while temperature *increases* within 15°C, because organic matter maturation is irreversible.

Price (1983) reviewed the models of Karweil (1955) and Lopatin (1971) and questioned the validity of some of the basic assumptions underlying these methods. Both Karweil (1955) and Lopatin (1971) assumed a constant geothermal gradient in their model calculations. Price (1983) demonstrated that the thermal history of the study areas upon which both of these model calculations are based is not as simple as had been assumed by the authors. The assumption of a constant geothermal gradient of 40°C/km in all of Karweil's calculations is not consistent with the geology of his study area in northern Germany, an area of intense igneous intrusive activity. Likewise, the Münsterland No. 1 borehole, used in Lopatin's (1971) calculations, is also situated in an area of NW Germany affected by intense regional and local igneous activity (Price 1983). Price (1983) argued that the organic geochemical changes in these authors' study areas, which were attributed to burial over long periods of geologic time at low temperatures are better explained as due to high palaeo-heat flows from various forms of magmatic or tectonothermal activity.

The use of a single first-order reaction to model the complex organic maturation reactions, which occur over a wide range of temperatures and heating rates, has also been criticised (Price 1983; Sweeney and Burnham 1990). Furthermore, Price (1983) argued that the activation energies assumed in the models of Lopatin (1971) and Hood *et al.* (1975) are unrealistically low (8.4 - 30 Kcal/mole and 33 Kcal/mole respectively), and are below experimentally determined values (> 44 Kcal/mole).

Recent chemical kinetic methods developed to model vitrinite maturity produce results which are more accurate than earlier models (Waples *et al.* 1992a; Waples *et al.* 1992b; Morrow and Issler 1993). The underlying assumption of these models is that the reflectance of vitrinite is related to its chemical composition. The most popular of these methods is the EASY%R₀ model (Sweeney and Burnham 1990), which is a modification of the earlier VITRIMAT model developed by Burnham and Sweeney (1989). EASY%R₀ is based on first-order Arrhenius reaction kinetics, and is a less time-dependent approach than the earlier vitrinite models of Karweil (1955) and Lopatin (1971). In the model, the

vitrinite maturation process is described by a series of four independent first-order parallel reactions, with a distribution of activation energies:



where CH_n represents higher hydrocarbons. The four equations can be combined as one to give the composition of the residual vitrinite as a function of the evolution of the above species over time, where the initial composition is known (determined by analytical methods). The residual vitrinite composition is then used to predict R_r . These models represent a statistical approach to average the complex processes of initiation, propagation and termination reactions that govern thermal kerogen degradation, which take place over a range of activation energies (Michelsen and Khorasani 1995).

The EASY% R_0 method may be used over a wide range of vitrinite reflectance values (0.3 - 4.5% R_r) and various heating rates (1°C/week to 1°C/My). The method has been calibrated using mean maximum reflectance (R_{max}) and optimised using random reflectance (R_r) (Sweeney and Burnham 1990). Both forms of measurement can therefore be used in the model without significant variation. Using this method, it is possible to accurately model a profile of vitrinite reflectance against time for a particular stratigraphic level, once the time-temperature history of the strata is known. The EASY% R_0 model has a much sounder theoretical base than the TTI and has the ability to incorporate the variability of the geothermal gradient through time.

Suzuki *et al.* (1993) developed a simplified adaptation of the EASY% R_0 model, SIMPLE- R_0 . Unlike the method of Burnham and Sweeney (1989) and Sweeney and Burnham (1990), this approach is based on a single activation energy, which changes as a function of R_r . This model produces very similar results to the EASY% R_0 model, but has the advantage of enabling accelerated maturity calculations (Suzuki *et al.* 1993).

Morrow and Issler (1993) compared R_r values, computed by a number of forward modelling schemes, for basinal sequences of known thermal history and constant heating rates. They concluded that, within the range of organic maturity associated with oil and gas generation, the Burnham and Sweeney's (1990) kinetic model is the most appropriate for the prediction of vitrinite reflectance. However, Barker (1991) criticised the use of the EASY% R_o model in areas of transient heat flux. He cited the example of the Cerro Prieto geothermal system in Mexico, from which apatite fission track studies indicate an age of 103 - 104 yr (Sanford and Elders 1981). Burnham and Sweeney's (1989) model requires a heating duration of 3 My to fit the observed vitrinite reflectance.

4.4.2 MODELS THAT CONSIDER TEMPERATURE ONLY

One of the cornerstone assumptions of the time dependent models of organic maturation is that the reactions involved follow Arrhenius first-order kinetics. That is to say, that when the reaction extent is plotted on logarithmic scale versus reaction time on an arithmetic scale, a straight line results. This first-order kinetic assumption is crucial, because even at slow reaction rates, given geologic time, these reactions can proceed to a high degree of completion. Price (1983) argued that there is no solid evidence from the natural system, on which to base this assumption. He pointed to conclusive evidence from laboratory studies that prove the primary organic maturation reactions to have complex higher-order reaction kinetics. Price (1983) concluded therefore that there was no basis for the time dependence which has been assumed for these reactions.

Maturity models that consider temperature alone are based on the assumption that the chemical reactions controlling the maturation of organic matter stabilise, and the maximum temperatures experienced by a sedimentary layer are sufficient to calculate vitrinite reflectance. Numerous models have been published that relate vitrinite reflectance to peak rock temperature (Barker 1983; Price and Barker 1985; Barker 1988; Barker and Goldstein 1990; Barker 1991; Tobin and Claxton 2000).

Based on data from several sedimentary basins with burial times ranging from 200,000 yr to 240 My, Price (1983) observed a strong linear correlation ($r = 0.97$) between the

logarithm of vitrinite reflectance and maximum burial temperature (Figure 4.7). This relation is described by the equation:

$$T(^{\circ}\text{C}) = 302.97 \log_{10} R_0 + 187.33$$

where $R_0 = R_r$. For any give temperature interval, Price (1983) observed that reflectance was invariant with increasing burial time (Figure 4.8). He concluded that full organic maturation is achieved after, at most, one million years, and that vitrinite reflectance can be used as an absolute palaeogeothermometer.

There is general agreement that the time at peak temperature necessary for organic matter to attain stability is important (Suggate 1982; Barker 1983; Price 1983; Barker and Pawlewicz 1986). Suggate (1982) suggested that once maximum temperature is achieved, organic matter maturation reactions are complete within 10^6 yr. This contention was supported by Price (1983). Barker (1983, 1991) demonstrated that in geothermal systems, stabilisation of vitrinite reflectance occurs within 10^4 yr. Barker's (1983) and (1991) observations were based on geologically young geothermal systems in North America that are at near-maximum temperatures. Barker (1991) found that R_r values set by a heating event lasting only 10^1 yr, closely approached the level found at comparable peak temperatures, where heating began 10^4 yr ago. From these studies, Barker concluded that vitrinite reflectance is very sensitive to maximum temperature and that it adjusts rapidly to increases in temperature (even after 10^1 yr).

Based on data from over 35 systems with functional heating durations ranging from 10^4 to 10^8 years, and spanning a maximum temperature interval of 25 to 235°C and 0.2 to 4.0% R_r , Barker and Pawlewicz (1986) found a statistical linear relationship between the logarithm of reflectance and temperature (in $^{\circ}\text{C}$):

$$\ln R_r = 0.0078(T_{\max}) - 1.2$$

or

$$T_{\max} = (\ln R_r + 1.2)/0.0078$$

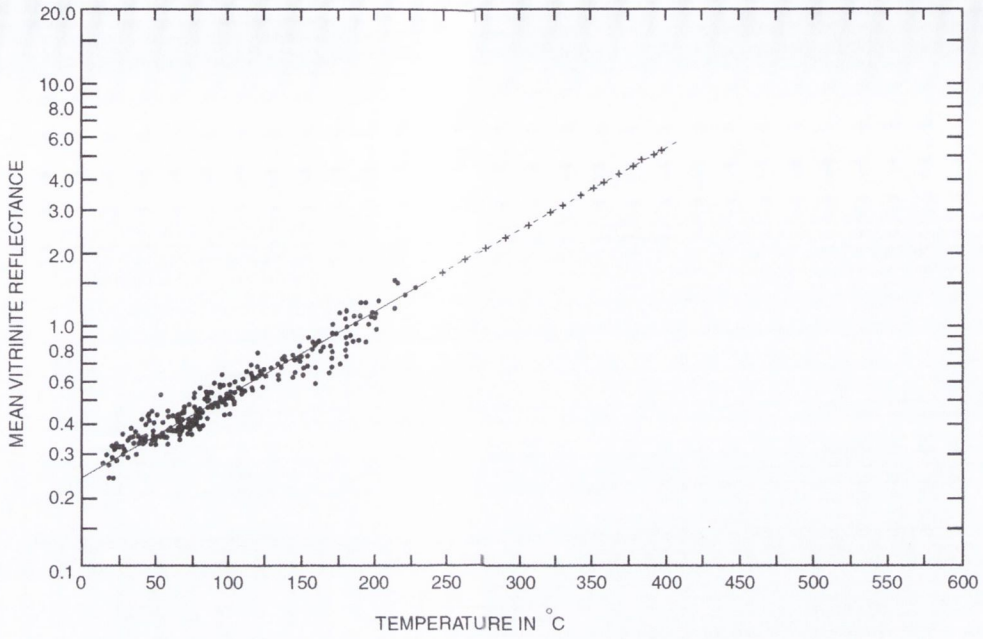


Figure 4.7. Plot of vitrinite reflectance versus burial temperature. Solid line is from linear regression analysis of data from various sedimentary basins. Burial times (times since attainment of 80% of present-day, maximal, temperatures) for sediments in these basins range from 200,000-240 million years. Dashed line is an extrapolation from projected palaeogeothermal gradients based on vitrinite reflectance versus depth plots for five different areas. Equation for the line is $T = 302.97 \log_{10} R_0 + 187.33$, where T is temperature in °C, and R_0 is mean vitrinite reflectance. This equation can only be applied to coals or rocks with type I organic matter. After Price (1983).

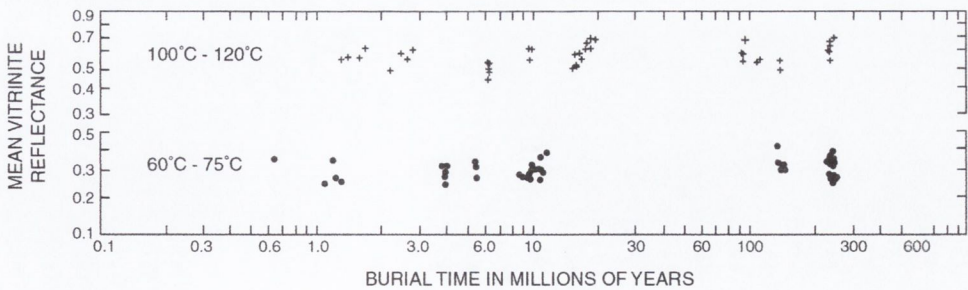


Figure 4.8. Plot of vitrinite reflectance versus burial time since attainment of 80% of present-day (maximal) temperature for two temperature intervals, 60 - 75°C (lower, dots) and 100 - 120°C (upper, crosses). After Price (1983).

where T_{\max} is the maximum temperature attained. From the strong correlation of T_{\max} with R_r , they concluded that additional heating duration once T_{\max} has been reached has no significant effect on the thermal maturation of organic matter.

Barker (1988) published a time independent vitrinite reflectance geothermometer, based on an observed linear regression correlation of T_{peak} and R_r :

$$T(^{\circ}\text{C}) = 104(\ln R_r) + 148$$

This regression correlation was a modification of the earlier Barker and Pawlewicz (1986) calibration, based on the same broad dataset.

Several attempts have been made to correlate vitrinite reflectance with homogenisation temperatures (T_h) of aqueous fluid inclusions (Bone and Russell 1988; Aizawa 1989; Barker and Goldstein 1990; Tobin and Claxton 2000). These models are based on the observation that many aqueous fluid inclusions in calcite re-equilibrate when heated to temperatures higher than those of initial entrapment. They therefore provide a useful approximation of maximum temperature reached in sedimentary basins. Of these, the most widely cited is the calibration of Barker and Goldstein (1990). Based on data from 46 diverse geologic systems, that have been at T_{peak} from 10^4 to 10^6 yr, and R_r data ranging from 0.4% to 4.6% R_r , Barker and Goldstein (1990) observed a strong correlation between homogenisation temperatures (T_h) of calcite fluid-inclusions and R_r , described by the equation:

$$\ln R_r = 0.00811(T_h) - 1.26$$

The homogenisation temperature then equates to maximum temperature attained according to the relationship:

$$T_{\text{peak}}(^{\circ}\text{C}) = 12.1 + 0.965(T_h)$$

Tobin and Claxton (2000) criticised the amount of data scatter in Barker and Goldstein's (1990) correlation and attempted to improve the T_h /VR calibration through selective sampling and measurement criteria. Only data from well constrained burial systems, without any geothermal or igneous intrusive influence, were used in their calibration. Based

on fluid inclusion and equivalent vitrinite reflectance data from 46 samples a strong correlation ($r^2 = 0.805$) was observed between T_h and R_r :

$$\%R_r = (2.1113)\log T_h - 3.2640$$

The amount of data scatter (absolute deviation of measured R_r) from the logarithmic correlation line is minimal (generally less than $\pm 0.12\%$ R_r , maximum deviation of $\pm 0.32\%$ R_r) compared to that of Barker and Goldstein (1990) ($\pm 0.5 - 0.6\%$ R_r). However, the maturity range of the dataset used by Tobin and Claxton (2000) to produce their calibration is quite restricted (0.5 - 1.6% R_r), compared to that used by Barker and Goldstein (1990) (0.4 - 4.6% R_r). They noted that the prediction error was more significant at lower levels of thermal maturity than at higher maturity levels. They also observed that median T_h data underestimated T_{peak} , computed using EASY% R_0 (Sweeney and Burnham 1990), by 15 - 24°C (average 19°C), and should not be considered an absolute equivalent for T_{peak} .

Barker and Pawlewicz (1994) asserted that the amount of scatter in the datasets used to calibrate vitrinite reflectance geothermometers, is mainly attributable to the practice of grouping datasets from both burial and hydrothermal metamorphism environments together. They suggested that the scatter in their previous calibration (Barker and Pawlewicz 1986) masked different maturation paths for burial heating and hydrothermal metamorphism systems (Figure 4.9). Based on a compilation of published (Barker 1983; Aizawa 1989; Barker and Goldstein 1990) and unpublished data, Barker and Pawlewicz (1994) published separate reduced major axis regression calibrations for burial heating and hydrothermal metamorphism paths:

$$T_{peak} = (\ln(R_r) + 1.68) / 0.0124 \text{ for burial heating } (r^2 = 0.7; n = 51)$$

and

$$T_{peak} = (\ln(R_r) + 1.19) / 0.00782 \text{ for hydrothermal metamorphism } (r^2 = 0.7; n = 72)$$

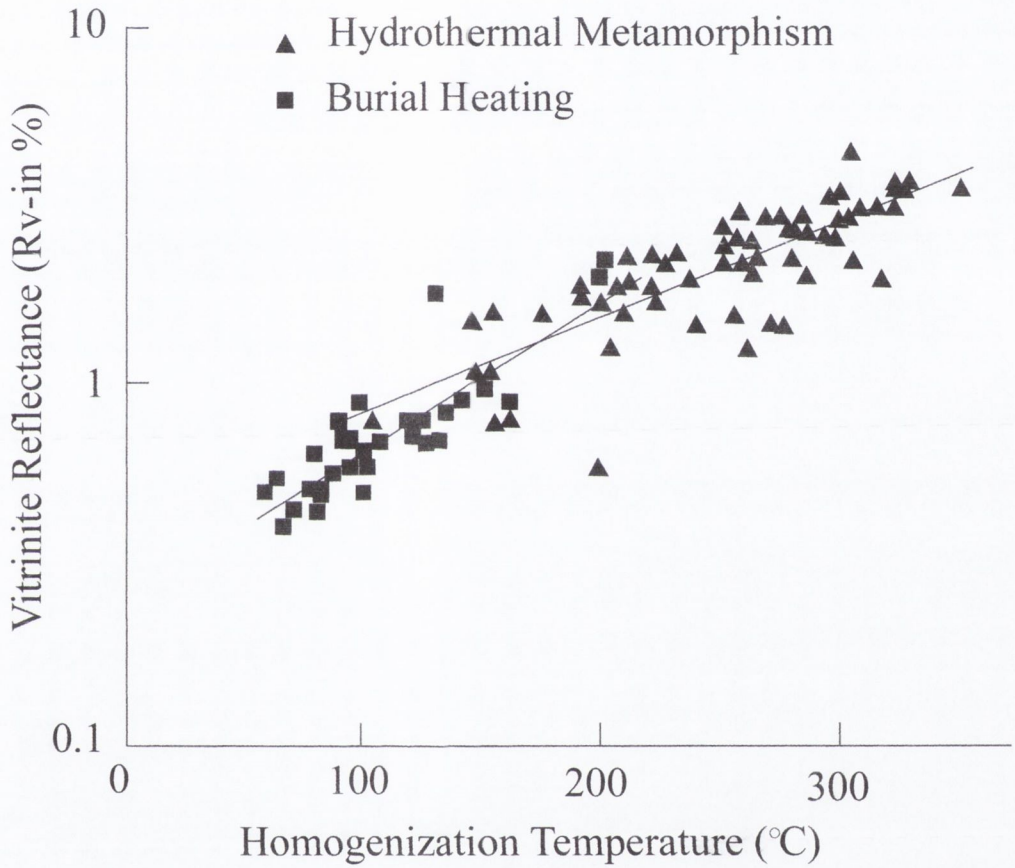


Figure 4.9. Peak temperature (T_{peak}) from reequilibrated fluid inclusions versus mean random vitrinite reflectance ($R_v = R_r$) for burial heating and hydrothermal metamorphism, based on data from Barker and Goldstein (1990), Aizawa (1989) and unpublished data. After Barker and Pawlewicz (1994).

The results of this exercise showed that for burial heating systems, previous geothermometers, derived by including hydrothermal metamorphism data, can significantly overestimate temperatures in the upper temperature ranges (Barker and Pawlewicz 1994).

Johnsson *et al.* (1993) examined the temperature dependent models of Price (1983), Barker and Pawlewicz (1986) and Barker (1988), and concluded that the correlation of Barker (1988) most closely matches the results predicted by the kinetic models (Burnham and Sweeney 1989; Sweeney and Burnham 1990). Corcoran and Clayton (2001) recently compared the empirical time independent schemes of Barker and Pawlewicz (1986), Barker (1988) and Barker and Goldstein (1990) to the kinetic scheme of Burnham and Sweeney (1989). Palaeotemperatures and palaeogeothermal gradients derived via the empirical scheme of Barker (1988) were found to most closely approximate those predicted via the kinetic Burnham and Sweeney (1989) model. This is consistent with the conclusions reached by Johnsson *et al.* (1993). Below 0.9% R_r , the Barker (1988) model predicts lower palaeotemperatures than the Burnham and Sweeney (1989) kinetic model. Between 0.9 and 1.3% R_r , palaeotemperatures predicted by the Barker (1988) model are higher than those computed by Burnham and Sweeney's (1989) scheme (Corcoran and Clayton 2001).

4.5 TRANSLATION OF R_r DATA TO PALAEOTEMPERATURE

Time-temperature modelling of the sediments in Berreraig Bay has not been attempted in this study due to the large number of uncertainties concerning the geological history of the area. In particular, precise knowledge is lacking of the post inversion burial by Tertiary basalts, the numerous Tertiary intrusions and the associated variation in geothermal gradient at that time.

Peak palaeotemperatures, computed from the measured R_r data for each sample horizon, using several temperature dependent models (Barker and Pawlewicz 1986; Barker 1988; Barker and Goldstein 1990; Barker and Pawlewicz 1994) are presented in Appendix V.

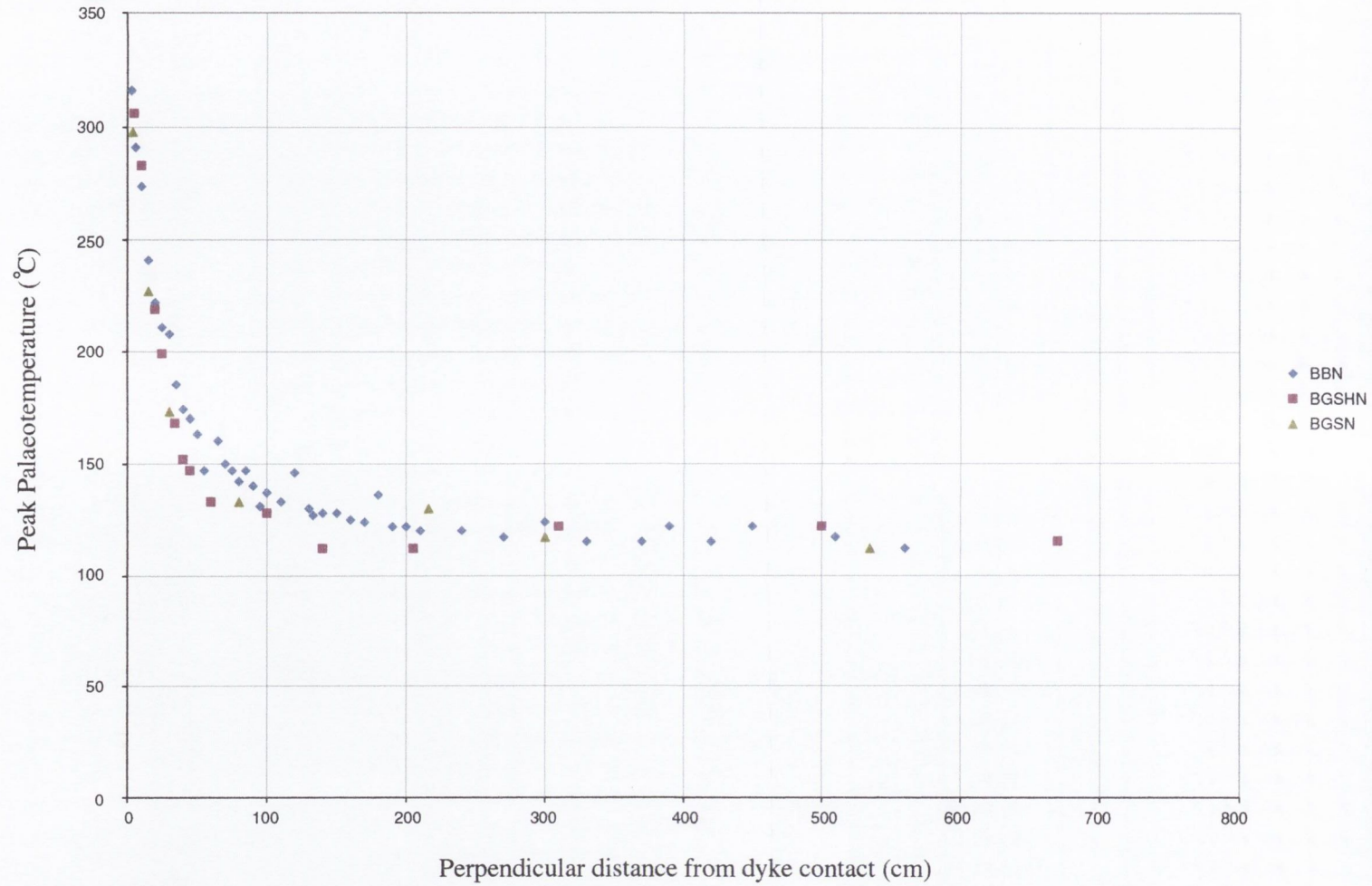


Figure 4.10. Plot of peak palaeotemperatures computed using Barker and Pawlewicz's (1994) geothermal VR-geothermometer against perpendicular distance from the dyke contact for the BBN, BGSHN and BGSN sample horizons.

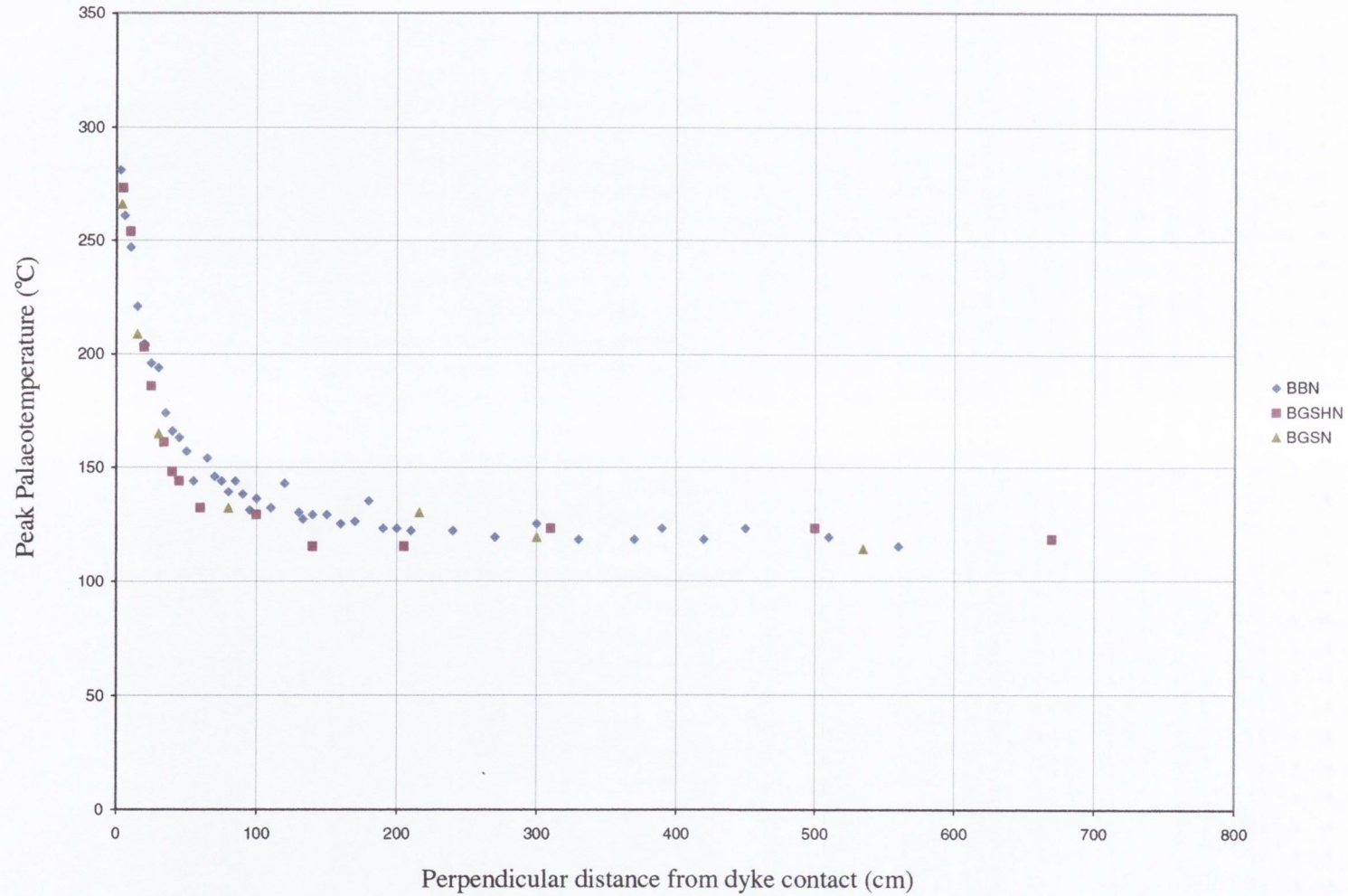


Figure 4.11. Plot of peak palaeotemperatures computed using Barker's (1988) algorithm against perpendicular distance from the dyke contact for the BBN, BGSHN and BGSN sample horizons.

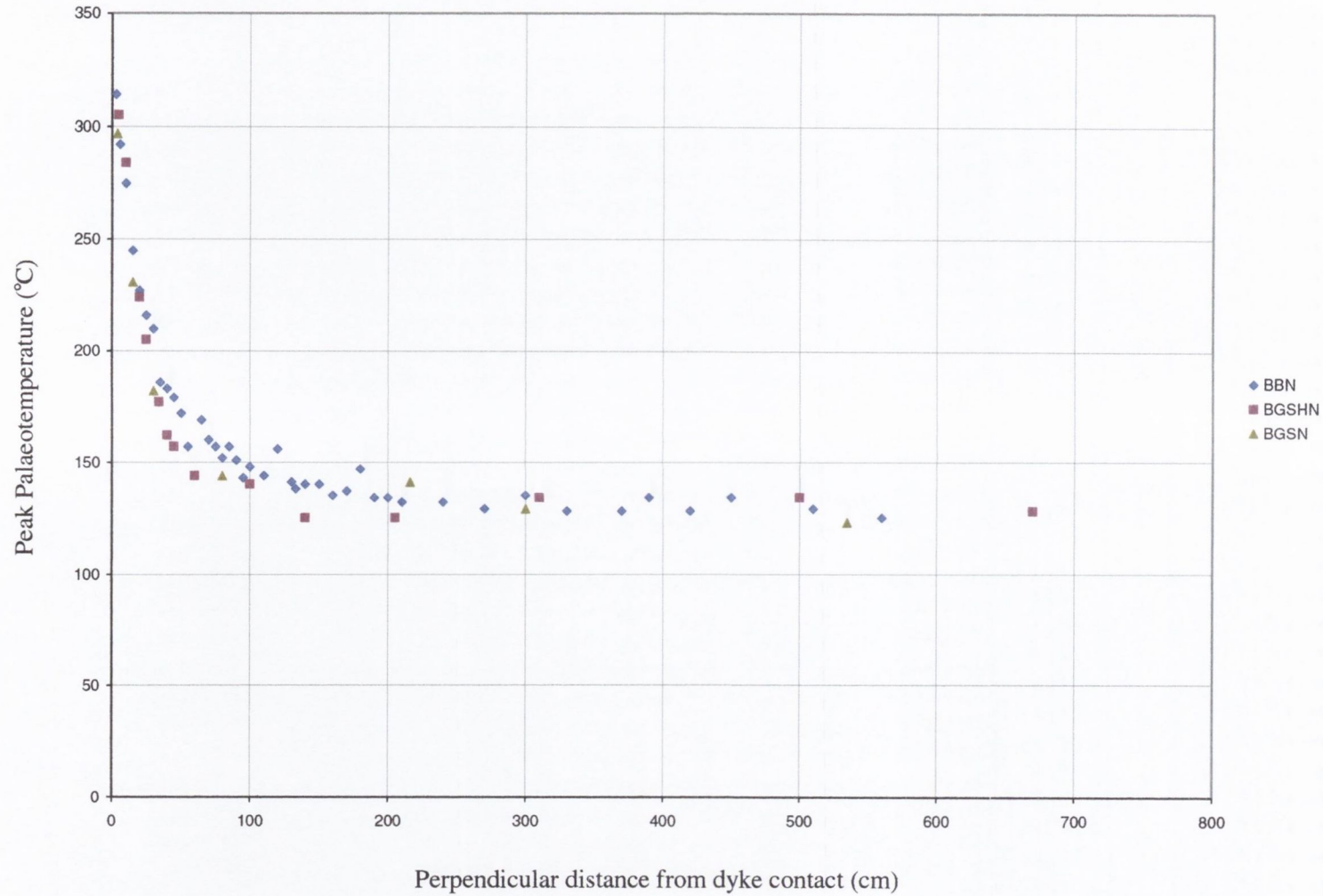


Figure 4.12. Plot of peak palaeotemperatures computed using Barker and Goldstein's (1990) algorithm against perpendicular distance from the dyke contact for the BBN, BGSHN and BGSN sample horizons.

Plots of maximum palaeotemperatures computed using the models of Barker (1988) and Barker and Goldstein (1990), and the geothermal model of Barker and Pawlewicz (1994), against perpendicular distance from the dyke are presented in Figures 4.10, 4.11 and 4.12.

The computed temperature profiles illustrate that a dramatic temperature increase occurs approaching the intrusion (Figures 4.10, 4.11 and 4.12). Elevated temperatures are restricted to a narrow zone approximately equal to the thickness of the dyke. Temperatures computed via the Barker and Pawlewicz (1994) model show the greatest range, from unaltered background temperatures of 112 - 113°C to temperatures of 298 - 316°C adjacent to the dyke (Table 4.1). The most conservative temperature increase is predicted by Barker's (1988) scheme. Temperatures computed via this method range from 114 - 115°C at background levels to 266 - 281°C adjacent to the dyke contact. Below ~ 1.2% R_r , Barker and Goldstein's (1990) scheme overestimates temperatures, relative to the Barker and Pawlewicz (1994) and Barker (1988) methods. However, in the vicinity of the dyke, temperatures predicted by this model are similar to those computed via the Barker and Pawlewicz (1994) scheme.

VR-Temperature Model		BBN	BGSHN	BGSN
Barker & Pawlewicz (1994)	Maximum T_{peak} (°C)	316	306	298
	Minimum T_{peak} (°C)	112	112	112
Barker (1988)	Maximum T_{peak} (°C)	281	273	266
	Minimum T_{peak} (°C)	115	115	114
Barker & Goldstein (1990)	Maximum T_{peak} (°C)	314	305	297
	Minimum T_{peak} (°C)	125	125	123

Table 4.1 Maximum and minimum values of T_{peak} for the three sample horizons, computed via the VR-temperature models of Barker and Pawlewicz (1994), Barker (1988) and Barker and Goldstein (1990).

Carslaw and Jaeger (1959) suggested that the maximum temperature reached in the host rock at the dyke contact ($T_{contact}$) at the instant of intrusion and the initial stage of cooling by conductive heat flow is given by:

$$T_{contact} = (T_{magma} + T_{host}) / 2$$

where T_{magma} and T_{host} are the initial temperature of the magma and host rock respectively. Assuming that the intrusion temperature of the basaltic magma was at least 1000°C (see Chapter 6), T_{contact} calculated by the above equation is considerably greater than that predicted by the VR-temperature models. This suggests that, although the vitrinite has reacted rapidly to the high temperatures associated with the dyke intrusion, the event was too short-lived for vitrinite reflectance to equilibrate to maximum temperatures attained at the contact. Modelling of the temperatures outside the cooling dyke is discussed in detail in Chapter 6.

Local background temperatures of 112-115°C are predicted by the VR-temperature models of Barker and Pawlewicz (1994) and Barker (1988) for these sediments. Given that maximum burial depths of these sediments are unlikely to have exceeded *ca.* 900m prior to Latest Jurassic / Early Cretaceous inversion (Morton 1987), a significantly elevated palaeogeothermal gradient (*ca.* 110°C/km) would be required to explain these temperatures.

The two most common sources of geothermal anomalies are: (1) intrusion of molten rock from great depth to high levels in the earth's crust; and (2) ascent of groundwater that has circulated to depths of 1 to 5km and has been heated via the normal or enhanced geothermal gradient without occurrence of a nearby intrusion. There is no evidence to suggest the presence of elevated heat flow in the Hebrides Basin, prior to exhumation in Latest Jurassic to Early Cretaceous times. However, during Early Tertiary rifting stages, this area was the site of intense igneous activity. The associated crustal tension allowed magma to inject along NW-SE oriented zones defined by the dyke swarms (Emeleus 1983). On Skye, igneous activity lasted about 6 My, beginning around 59 Ma with the development of thick basalt lava fields over much of central and northern Skye (Mussett *et al.* 1988). Most of these flows probably originated via fissure eruptions over a considerable period of time (Bell and Harris 1986). Anderson and Dunham (1966) estimate that, prior to Late Tertiary and Pleistocene erosion, the total thickness of lavas in parts of central and north Skye may have been as much as 1200m. However, it is believed that the original extent of the lava fields did not extend any great distance further than that preserved at present, and Emeleus (1983) estimates that the thickness of the lava pile in north Skye was more like 600m. Although erosion of the lava pile occurred soon after the cessation of igneous activity, the Jurassic sediments of northern Skye would have experienced significant reburial during this

time. Beneath 1200m of pre-Tertiary sediments and Palaeocene lavas (see Section 6.5.3), an average geothermal gradient of only *ca.* 80°C/km would be required to heat these sediments above 110°C. A figure such as this would not in any way be at odds with the thermal regime present in the Hebridean area at that time.

The development of the central intrusive complexes in central Skye followed shortly after the cessation of lava extrusion. These central complexes are clearly deep-rooted features in the crust of northwest Scotland (Emeleus 1983). Based on gravity evidence, Bott and Tuson (1973) suggested that about 3500km³ of probable gabbroic material underlies the plutonic centres of Skye to a depth of approximately 14km. When very large quantities of heat are brought close to the surface by the intrusion of large volumes of molten lava originally at great depth, the geothermal gradient is much higher, resulting in high rock temperatures close to the surface. Such vast deep-rooted magmatic structures must have had a significant effect on the geothermal gradient in this region at the time the Berreraig Bay sediments were reburied under the Tertiary basalt lava pile.

Stable isotope evidence suggests that extensive hydrothermal systems developed in association with these intrusive centres (Taylor and Forester 1977). Large convection systems have the ability to transfer geo-heated water laterally over distances of several kilometres. However, based on biomarker evidence, Thrasher (1992) suggested that the lateral extent of these systems was limited to within 15km of the complex margin. The sediments in Berreraig Bay, some 20km to the North, would therefore fall outside this zone of alteration.

Some time after the extrusion of the plateau lavas, the Jurassic sedimentary rocks of northern Skye were intruded by sills from a large basic sill complex, which is believed to have a focal point locally, at depth (Anderson and Dunham 1966). Aside from the Cuillin and Red Hills centres, this represents the most voluminous group of the Tertiary igneous intrusions on Skye. These sills form a prominent feature of the eastern and northern coastal areas of the Trotternish Peninsula, but they are even more extensive on the seabed of the Southern Minch and Little Minch. The total thickness of the complex is a near-constant 250m, with individual sills achieving thicknesses in excess of 90m (Bell and Harris 1986). The thick sill complex has locally altered the Jurassic sediments below.

4.6 SUMMARY

The results of the vitrinite reflectance analysis indicate a 'reflectance aureole', in which the vitrinite shows a marked reaction to the high temperatures close to the dyke. Within this 'reflectance aureole', rank changes from the high-volatile bituminous (0.72-0.79% R_r) through medium volatile bituminous, low volatile bituminous, semi-anthracite to anthracite (3.1-3.6% R_r) are observed. A reflectance reversal, sometimes reported next to igneous intrusions, was not observed in any of the sample horizons. For each sample horizon, the *sharpest* increase in R_r values occurs within *ca.* 0.5 - 0.6m of the dyke contact. Beyond this distance, R_r values fall gradually to background levels. The full extent of the reflectance aureole, defined by the R_r profiles, differs slightly between each of the three sample suites. This may be a consequence of differing sampling resolution between the sample horizons, or may reflect differences in the thermal properties of the host lithologies, and/or differing mechanisms of heat transfer.

Peak palaeotemperatures were computed from the measured R_r data for each sample horizon, using several temperature dependent models (Barker and Pawlewicz 1986; Barker 1988; Barker and Goldstein 1990; Barker and Pawlewicz 1994). The computed temperature profiles show dramatic increase in response to the high temperatures associated with the intrusion. Elevated temperatures are restricted to a narrow zone approximately equal to the thickness of the dyke. Temperatures in excess of 300°C are indicated in the host rocks adjacent to the dyke contact, however computed temperatures differ somewhat between the various VRGs. The geothermal geothermometer of Barker and Pawlewicz (1994) shows the greatest range of predicted temperatures, while the most conservative temperature range is predicted by their (1994) burial geothermometer. The results indicate that VRGs are sensitive to differing thermal regimes, and selection of VRGs should involve consideration of thermal history.

VRG predicted local 'background' temperatures of 112-115°C appear rather high, assuming that they represent maximum burial temperatures for these sediments. Reburial of the Jurassic sedimentary rocks of northern Skye occurred during the Early Tertiary under the extensive plateau lavas. The thickness of the overburden cover is estimated to have been in excess of 1200m in north Skye, before Late Tertiary and Pleistocene erosion.

During the Early Tertiary, there is a considerable body of evidence to indicate the presence of vast volumes of magma at high levels in the continental crust of Skye. These magmas invaded a continental crust that was stretched and thinned during the early rifting stages of the North Atlantic. During this time, three major deep-rooted central intrusive complexes were emplaced in central Skye, causing extensive hydrothermal alteration in the host rocks over a distance several kilometres. At this time also, the Jurassic sediments of northern Skye were intruded by a major basic sill complex, which caused local metamorphism of the sediments below. Throughout this period, mafic dyke injection occurred as part of the regional NW-SE trending swarm, until igneous activity finally waned in the Hebrides area between 55 and 52 Ma. It is not difficult to envisage the high heat flow in the Early Tertiary crust of north Skye, necessary for the Jurassic sediments of Berreraig Bay to attain the background temperatures indicated by the R_r data. However, it is also possible that this 'background' maturity level is only very local and has been partly achieved by heat associated with the dyke.

CHAPTER 5

AOM COLOUR AND FLUORESCENCE RESULTS

5.1 INTRODUCTION

The results of the AOM colour investigation of sediments through the aureole of the Berreraig Bay dyke are presented in this chapter. The results of the organic matter fluorescence investigation are also presented here, in Section 5.3. Using Colour Image Analysis (CIA), colour (RGB) determinations of AOM were completed on all three sample horizons (BBN, BGSHN, BGSN). Mean RGB values were calculated from cumulative RGB measurements taken from 25 AOM particles per sample. Visual TAI estimates of AOM colour from the same samples are also presented here for comparison. However, it is the opinion of this author that the Spore Colour Standard of Pearson (1984) does not adequately represent the observed colours in AOM, which are more complex due to the heterogeneity and variable thickness of AOM particles. TAI estimates presented here should therefore only be considered rough approximations. The results of both the quantitative RGB colour and visual colour investigations are presented in Appendix IV. The results of the RGB colour investigation are also presented in Appendix III in the form of Red, Green and Blue frequency histograms. For all samples, the mean Red, Green and Blue values, standard deviation and number of measurements used to calculate the mean is stated beside the histogram.

5.2 DESCRIPTION OF AOM USED IN COLOUR INVESTIGATIONS

The ultimate composition and source potential of amorphous kerogen is determined by its botanical precursor, the duration of exposure to aerobic and anaerobic breakdown, and the amount of thermal alteration subsequent to burial. In an oxygenated depositional environment, sedimentary organic matter is ultimately converted to carbon dioxide and water, leaving no remains. In the absence of adequate oxygen the degradation is arrested

before complete destruction is effected. The appearance of AOM is strongly controlled by its preservation state. This allows generalised qualitative conclusions to be made on the redox state of the depositional environment. During degradation, AOM fluorescence becomes increasingly more dull and heterogeneous. In transmitted light, it often becomes more greyish in colour, matte rather than lustrous, of lower relief, and less cohesive and less resistant to palynological oxidation treatment (Tyson 1989). The morphology of AOM is also controlled somewhat by the nature of the mineral matrix from which it is extracted (Tyson 1995).

5.2.1 DESCRIPTION OF AOM FROM THE BBN SAMPLE HORIZON

Under transmitted light, the AOM in unaltered samples varies in colour from green-yellow to brown, depending on particle thickness. In general, particles are high relief, rather lustrous and have a granular texture. Particle shapes are irregular, ranging from sub-circular to elongate. The particle boundaries also vary: some are distinct and pronounced, while others are difficult to discern, diffusing gradually into the background. The sharp boundaries usually represent some indeterminate precursor algal material that has been only partly sapropelized. This AOM is also characterised by inclusions of bacterially-produced iron sulphide. Inclusions of bitumen and small phytoclasts in the amorphous matrix are also common. Under the fluorescent microscope, the heterogeneous nature of the AOM is evident. The AOM consists of numerous small unidentifiable moderately to strongly fluorescent fragments (equivalent to the maceral liptodetrinite) within a weaker fluorescent amorphous matrix. In unaltered samples, the overall appearance is of moderate fluorescence intensity, golden-yellow in colour.

With increasing maturation, the AOM particles become smaller, and their boundaries become more distinct. In higher rank samples ($\geq 1.55\% R_r$), AOM particles appear brittle and often show fracturing.

5.2.2 DESCRIPTION OF AOM FROM THE BGSBN SAMPLE HORIZON

This AOM is strikingly similar in morphology to that which is found in the BBN samples. In unaltered samples, its colour ranges from dull green-yellow to brown depending on the thickness/density of the particle. It is generally more dull or greyish in appearance than the type found in the BBN samples. Particles generally have a granular texture and show high relief. Particle boundaries are often diffuse, but like the BBN type, partly-sapropelized indeterminate relict precursor material commonly forms distinct edges. Small phytoclasts and bitumen particles are frequently incorporated into the amorphous matrix. Inclusions of bacterially-produced iron sulphide are also common. Under the fluorescence microscope, the heterogeneity of the AOM is again apparent with numerous tiny indeterminate fluorescent liptodetrinitic fragments within a weaker fluorescent matrix. Overall, the AOM shows moderate golden-yellow to dark-yellow fluorescence.

5.2.3 DESCRIPTION OF AOM FROM THE BGSN SAMPLE HORIZON

The type of amorphous kerogen found in this horizon is markedly different in its appearance from the types found in both the BBN and BGSBN samples. In unaltered samples, its transmitted light appearance is generally a 'cleaner', more lustrous, bright yellow colour rather than the green-yellow of the other sample horizons. Thicker particles are more amber in colour. Under fluorescent light, the AOM exhibits golden-yellow moderate fluorescence colours. Particles form larger surface areas, but generally tend not to be as thick. They are less granular than the other types, having a more membranous and sometimes fibrous texture. Consequently, the particle boundaries are usually distinct and easier to discern. This amorphous kerogen type is ubiquitous with unusual near-translucent membranous sheath-like structures. These 'sheaths' or membranes are commonly found in various stages of sapropelization. Under the fluorescence microscope, their colour and intensity is identical to that of the amorphous kerogen. They are usually crinkled or folded giving these structures a pseudocellular appearance. They may be a likely precursor of this amorphous kerogen type. However, it is possible that this is pelicular AOM *sensu* Combaz (1980) (Tyson⁴, personal communication), i.e., AOM which has become deformed and imprinted by the growth of diagenetic carbonate crystals; when the rock is

dissolved these imprints are left as craters in the kerogen, sometimes imparting a pseudocellular appearance. As well as these membrane structures, the amorphous kerogen occurs in association with rare tasmanitids and a number of thin-walled palynomorphs. These include acritarchs, but mostly comprise near-translucent indeterminate sac-like palynomorphs of probable marine origin. Filamentous algal remains are also found in association with the AOM, in various stages of advanced biodegradation, and these are perhaps another principal source. Inclusions of iron sulphide are also present, however there are less phytoclasts incorporated into the amorphous matrix of this AOM type. This may be a result of the thinner, more membranous nature of the AOM, or may simply be due to the fact that there are less small phytoclasts present in the kerogen to become incorporated into the AOM.

All three sample horizons have kerogen assemblages that are dominated by well preserved fluorescent AOM, with lesser amounts of terrestrial macerals. This is indicative of a Type II kerogen composition, with good petroleum source potential.

5.3 ORGANIC MATTER FLUORESCENCE RESULTS

The results of the organic matter fluorescence investigation are presented in this section and in Appendix IV. In this section, the results are presented graphically in Figures 5.1 and 5.2. Figure 5.1 depicts the observed changes in AOM fluorescence in each of the three sample horizons, with increasing proximity to the dyke contact. The error bars delimit the sample intervals. Figure 5.2 illustrates the observed changes in AOM fluorescence in each of the three sample horizons, with increasing vitrinite reflectance. The fluorescence colours depicted in Figures 5.1 and 5.2 are a rather crude attempt to visually match the observed fluorescence colours, and are purely subjective. Nevertheless, they adequately illustrate the interval of marked change in fluorescence intensity and the positions of fluorescence extinction in all three sample horizons.

⁴ R.V. Tyson, Newcastle Research Group in Fossil Fuels and Environmental Geochemistry, Drummond Building, University of Newcastle upon Tyne, NE1 7RU United Kingdom. <http://nrg.ncl.ac.uk/people/staff/tyson.html>

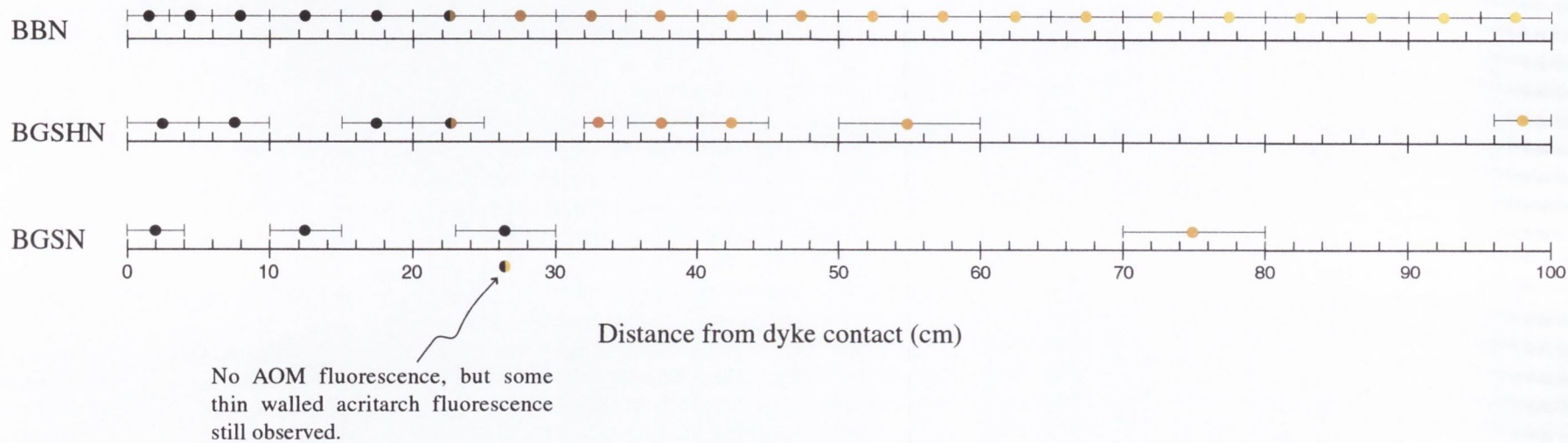


Figure 5.1. Comparison of AOM fluorescence colour against distance from the dyke contact for the BBN, BGSHN, and BGSN sample horizons.

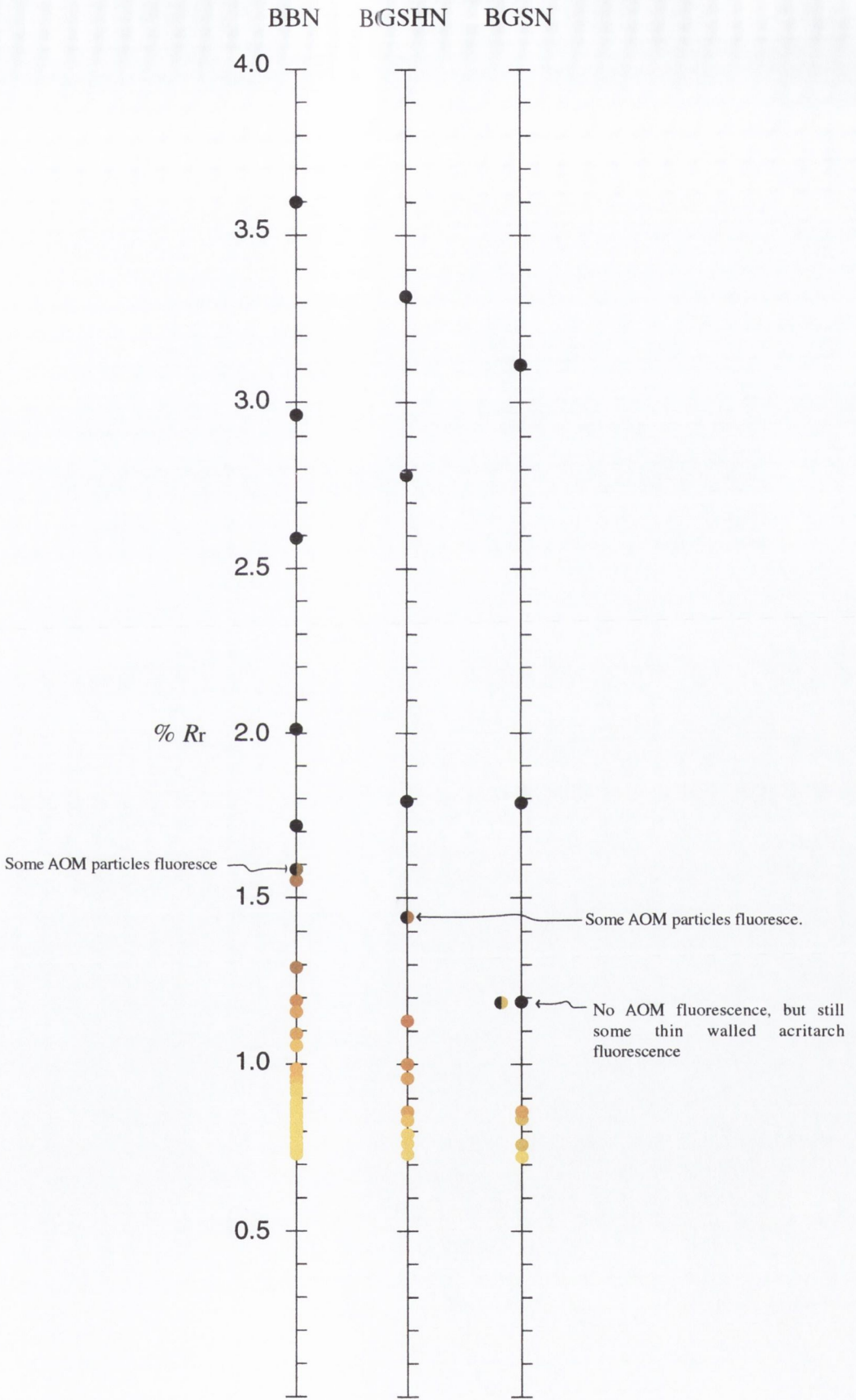


Figure 5.2. Comparison of AOM fluorescence colours against vitrinite reflectance (R_r) in the BBN, BGSHN and BGSN sample horizons.

5.3.1 AOM FLUORESCENCE IN BBN SAMPLES

AOM in the unaltered zone showed moderate fluorescence intensities, shifting gradually from golden- to dark-yellow colours in the direction of the dyke. Between 0.7 and 0.8m from the contact, fluorescence colours shifted from dark-yellow to yellow-orange. In BB12N (0.5 - 0.55m from contact) a marked drop in fluorescence intensity was observed coupled with a shift to orange colours. At 0.25 to 0.3m only faint orange-brown fluorescence was observed, with only a few particles still fluorescing between 0.2 - 0.25m. No further fluorescence was observed within 0.2m of the contact (15% d.t.). In terms of vitrinite reflectance, the extinction point of fluorescence occurs between 1.58 and 1.72% R_r .

Some tasmanitid fluorescence was observed in a number of samples, more distal from the dyke. These showed intense fluorescence with bright- and golden-yellow colours. No tasmanitids were found within 1.6m of the dyke contact. A small number of samples contained acritarchs. These showed strong fluorescence, shifting from bright- to golden-yellow colours in the direction of the dyke. No acritarchs were observed in samples within 0.75m from the dyke.

5.3.2 AOM FLUORESCENCE IN BGS HN SAMPLES

AOM in the unaltered zone (0.95 to 6.7m) displayed moderate fluorescence intensities, golden-yellow to dark-yellow in colour. Yellow-orange fluorescence colours were observed 0.5 - 0.6m from the contact (BGS H06N), followed by marked drop in fluorescence intensity and a shift to orange in BGS H07N (0.4 - 0.45m from contact). Between 0.3 and 0.4m from the contact, the AOM showed only faint orange-brown fluorescence. In BGS H04N (0.2 - 0.25m), only some AOM particles exhibited a faint brown fluorescence, with no fluorescence observed within 0.2m of the contact (15% d.t.). This places the ceiling for fluorescence between 1.44 and 1.69% R_r .

A number of samples contained rare tasmanitids. Distal samples showed strong bright-yellow fluorescence to a distance of 0.96 - 1.0m from the intrusion. Fluorescence colours shifted gradually from golden-yellow to yellow-orange between BGS H08N and BGS H07N

(0.6 to 0.35m from contact). No tasmanitids were observed in samples closer to the intrusion. No acritarchs were observed through BGS04N sample horizon.

5.3.3 AOM FLUORESCENCE IN BGSN SAMPLES

In the most distal sample (BGS07N, 5.25 - 5.35m from the dyke), AOM showed moderate fluorescence of golden-yellow colour. Between 2.06 and 3.0m, AOM fluorescence colours shifted to dark-yellow. In BGS04N (0.7 - 0.8m), a marked drop in fluorescence intensity was observed with a shift to orange. The sample next nearest the dyke, BGS03N (0.23 - 0.3m from the contact), showed no visible AOM fluorescence. However, some thin walled acritarch fluorescence was still observed. Complete extinction of all observed fluorescence was effected by BGS02N (0.1 - 0.15m from contact).

Some rare tasmanitids were observed in samples to a distance of 0.23m from the dyke contact. These showed strong bright-yellow fluorescence, with no obvious reduction in intensity with increasing proximity to the dyke. Extinction of tasmanitid fluorescence occurred abruptly in BGS03N (0.23 - 0.3m from the dyke). Tasmanitid occurrence disappears completely in the remaining more dyke-proximal samples. According to Taylor *et al.* (1998), *Tasmanales* alginites leave no residue, or only fine shreds of inertinite above 1.3% R_r . Acritarchs from background samples exhibited strong bright-yellow fluorescence. With increasing proximity to the dyke contact, acritarch fluorescence colours shifted towards golden-yellow, coupled with a slight decrease in intensity. Acritarchs and some indeterminate thin walled palynomorphs remained fluorescing 0.23 - 0.3m from the dyke contact, after extinction of AOM fluorescence had occurred.

The ceiling for AOM fluorescence in this case must therefore occur below 1.18% R_r . While some thin-walled acritarch fluorescence was still observed at this maturity level, complete extinction of all fluorescence was effected by < 1.79% R_r .

5.3.4 DISCUSSION

Under normal maturation conditions, sporinities generally fluoresce up to the medium-volatile bituminous coal stage, which corresponds to approximately 1.2 - 1.35% R_r (Teichmüller 1974). This marks the rank at which the potential for generation of liquid hydrocarbons has ceased. Although well documented, the normal extinction range for sporinite fluorescence varies slightly in the literature: $\leq 1.2\%$ R_r (Teichmüller and Wolf 1977); 1.2 - 1.3% R_r (Robert 1980); $\leq 1.3\%$ R_r (Tissot and Welte 1978); 1.2 - 1.5% R_r (Robert 1988); $\sim 1.3\%$ R_r (Traverse 1988); 1.1 - 1.3% R_r (Schwab 1990); $\leq 1.1\%$ R_r (Gregory *et al.* 1991). The fluorescence threshold may vary depending on bulk organic matter type (Tissot and Welte 1978; Taylor *et al.* 1998) and natural inter-laboratory variation. Teichmüller (1982) has suggested liptinite fluorescence up to a reflectance level of 1.5% R_r . While the ceiling for fluorescence in sporinities is well documented, the disappearance of fluorescence in amorphous kerogen is less well defined. This is partly due to a lack of widely accepted maceral terminology to describe amorphous kerogen, and partly because amorphous kerogen is a heterogeneous composite of decomposition products of several biological entities. Its fluorescence may be derived from one maceral only, or from a mixture of several liptinites (Smith 1984). As such, its fluorescence behavior will depend on the type and relative proportions of these sub-components that constitute the amorphous product. As fluorescence properties are also affected by preservation state (Tyson 1984, 1990), the extent and nature of diagenetic degradation will also control the fluorescence behaviour of the amorphous kerogen. Collins (1990) indicated that spore fluorescence ceases at reflectance levels of 0.9 - 1.0% R_r , while AOM fluorescence ceases somewhat earlier at 0.7 - 0.8% R_r . Taylor *et al.* (1998) state that the liptinite maceral bituminite, the main component of Type II amorphous kerogen, loses its fluorescence at a stage corresponding to 0.8 - 0.9% R_r , while loss of fluorescence of *Tasmanites* alginites is reached slightly later at 0.9 - 1.0% R_r . Oil generation from bituminite in source rocks begins at lower maturity levels than from telalgintes (Masran and Pocock 1981; Gutjahr 1983). After the generation and expulsion of oil, no residues or only very fine micrinitic residues are left by bituminite (Teichmüller and Wolf 1977).

There is a clear anomaly between the documented ceiling for AOM fluorescence and the observed fluorescence cut-off in the BBN and BGSHN samples. Goodhue (1996) observed a similar retardation of fluorescence extinction, in *Lycospora* sp. from Carboniferous

siltstones adjacent to the 4m thick, North Star Dyke at Ballycastle, Co. Antrim. Some mild *Lycospora* sp. fluorescence was still observed up to 1.64% R_r , with extinction of all fluorescence effected within 2.1m of the dyke contact (50% d.t.). Experimental heating of a low rank coal at a rate of 3°/min has shown that the reflectance changes of vitrinite occur at lower temperatures than the fluorescence of liptinites (Teichmüller 1980). Goodhue (1996) suggested that the intense heating caused by dyke intrusion may be too short-lived to alter the liptinitic fraction in accordance with peak temperatures. This indeed may be the case in sediments in the aureole of the Berreraig Bay dyke.

The cessation of kerogen fluorescence occurs with (fluid or volatile) hydrocarbon release, when the residual, heavier part of the kerogen 'gelifies' or 'condenses' on release from the mobile phase (Robert 1980). The formerly fluorescent tissue loses its structure and the p-electrons, responsible for fluorescence, become delocalised. Retardation of fluorescence extinction may indicate prolonged release or cracking of the liquid hydrocarbons, relative to vitrinite reflectance. If this is the case, the BBN and BGSN samples may still have been generating significant liquid hydrocarbons from AOM up to vitrinite reflectance levels of 1.58% R_r and 1.44% R_r respectively.

There is good agreement between the observed extinction positions of AOM fluorescence from the BBN and BGSN sample horizons (Figure 5.1). In both cases, fluorescence persists to a distance of 0.2m from the dyke contact. There is a clear disparity between the observed extinction position of AOM fluorescence in the BGSN samples and that, which is observed in the shales (BBN, BGSN). In the BGSN horizon, all AOM fluorescence is arrested at some point between 0.3m and 0.7m from the dyke. The precise position at which AOM fluorescence is quenched is impossible to resolve due to the wide spacing between samples in this horizon.

The possibility of increased heating in the BGSN horizon must be addressed. As the BGSN sample horizon is only *ca.* 0.2m above the BBN horizon, any variation in heat input due to variable dyke thickness may be ruled out. Published figures of thermal conductivity (k) averages in sedimentary rocks, indicate that carbonates generally have higher conductivity values (2.8 - 3.5 $\text{W}\cdot\text{m}^{-1}\cdot\text{°C}^{-1}$) than shales (1.5 - 2.9 $\text{W}\cdot\text{m}^{-1}\cdot\text{°C}^{-1}$) (Evans 1977; Oxburgh and Andrews-Speed 1981). Assuming that maturation of these sediments

above the local background level was due to intrusion of the dyke, and that conduction was the principal mechanism for heat transfer, the dissipation of heat may have been greater through the BGSN horizon. This could increase the extent of the igneous aureole in this horizon beyond that in the adjacent shale horizons, pushing back the position of fluorescence extinction further from the dyke. However, thermal conductivity experiments conducted as part of this study (Section 6.5.1.1), indicate slightly below average k values ($2.57 \text{ W.m}^{-1}.\text{°C}^{-1}$ and $2.46 \text{ W.m}^{-1}.\text{°C}^{-1}$) for the BGSN samples. This would put the k value of the BGSN samples within the published range of shale averages. Unfortunately, the fragile nature of the Berreraig Bay shales precluded conductivity estimation of all but the most thermally altered samples. The BGSN02N shale sample (0.05 - 0.1m from dyke) yielded k values of $2.86 \text{ W.m}^{-1}.\text{°C}^{-1}$ and $2.94 \text{ W.m}^{-1}.\text{°C}^{-1}$. This would fall within the upper end of the published range of shale averages, but it is not known how this value would compare to one from an unaltered sample. Comparison of the BGSN vitrinite reflectance profile with those of the BBN and BGSN samples (Figure 4.4) does not indicate any evidence of increased heat flow in the BGSN sample horizon. It is very similar to the reflectance profile of the BGSN shales. In any case, extinction of AOM fluorescence was observed at a lower level of reflectance in the BGSN horizon ($1.18\% R_T$) than in the BBN and BGSN samples ($1.72\% R_T$ and $1.69\% R_T$ respectively) (Figure 5.2).

Fluorescence colour and intensity are strongly dependent on organic matter type, species and preservation state (Collins 1990; Tyson 1990, 1995; Taylor *et al.* 1998). It is possible that the observed discrepancy in the fluorescence properties of the BGSN AOM may simply reflect compositional or derivational differences in this AOM type. The BGSN AOM is markedly different in its appearance from the type found in both the BBN and BGSN samples. Not only does it differ in terms of its fluorescence properties, but it is different in colour and texture from that found in the BBN and BGSN samples. A compositional explanation is supported by the fact that fluorescence persists in acritarchs from this horizon, after the observed quenching of AOM fluorescence. Diagenetic degradation can produce changes that are similar to those due to maturation (Tyson 1995). It is also possible that diagenetic modification of the amorphous kerogen in the BGSN horizon was more severe than the AOM from the shale horizons.

5.4 AOM COLOUR RESULTS

The BBN sample suite, being the most comprehensively sampled of the three horizons, afforded the most detailed analysis. RGB colour determinations were conducted on 34 out of the 43 BBN samples. Samples were chosen for measurement so as to provide an even distribution of RGB values with distance from dyke contact. Some samples were deemed of limited importance, due to their position outside the aureole and/or their proximity to adjacent samples, and were not included in the study. In the case of the BGSHN and BGSN sample suites, all samples were used.

The entire datasets of measured RGB intensities of AOM against distance from the dyke contact for each of the three sample suites are shown in Figures 5.3(a), 5.4(a) and 5.5(a). RGB histograms for all samples give an indication of the spread of colour within a single sample (Appendix III). A number of initial observations are possible (Figures 5.3(a), 5.4(a) and 5.5(a)). Firstly, although quite scattered, the ranges of R, G and B values are consistent between datasets. In all three cases, the R and G parameters have higher intensities than B. This disparity between R/G and B is most pronounced in AOM from unaltered background samples, where the intensities of R and G show an overlap. In the vicinity of the dyke, all three parameters show a progressive decrease in intensity with increasing proximity to the dyke contact. This drop in intensity is greater for the R and G parameters than for B, resulting in a converging trend of R and G with B at the contact. Initial observations suggest that AOM colour, defined by measured RGB pixel intensities, is therefore sensitive to thermal changes associated with the dyke intrusion.

To better assess the variation between samples, the mean RGB intensities were plotted against distance from the dyke (Figures 5.3(b), 5.4(b) and 5.5(b)). Despite the wide range of RGB values within each sample, a clear progression of colour averages is observed, with increasing proximity to the dyke contact. Vitrinite reflectance data was available for all of the measured samples and an inverted R_r against distance profile for each sample horizon is included on a secondary axis for comparison.

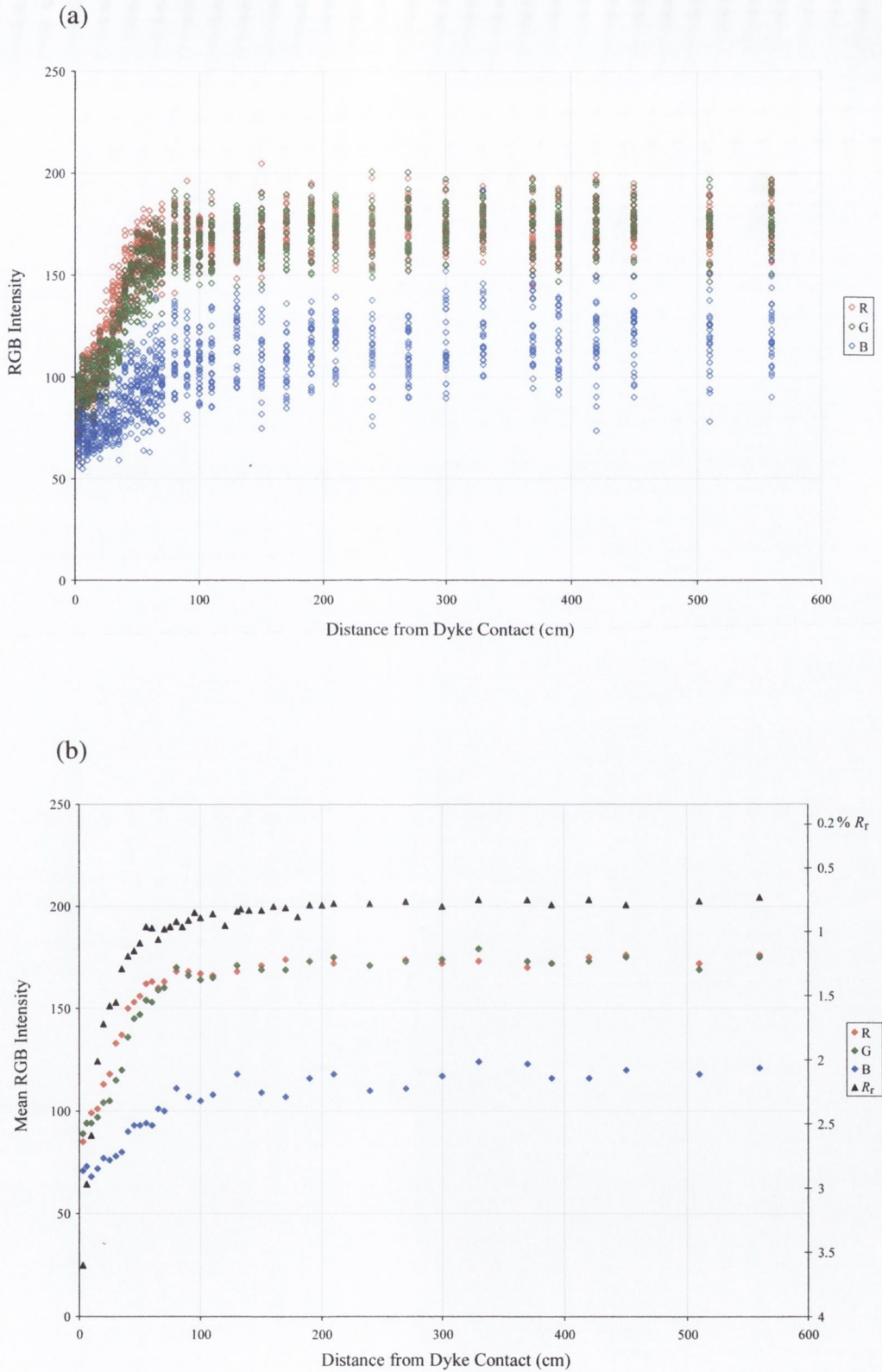


Figure 5.3. (a) Plot of all RGB intensity data against distance from dyke contact for the BBN sample horizon. (b) Plot of mean RGB intensities against distance from dyke contact for the BBN sample horizon. An inverted vitrinite reflectance profile is included on the secondary axis for comparison.

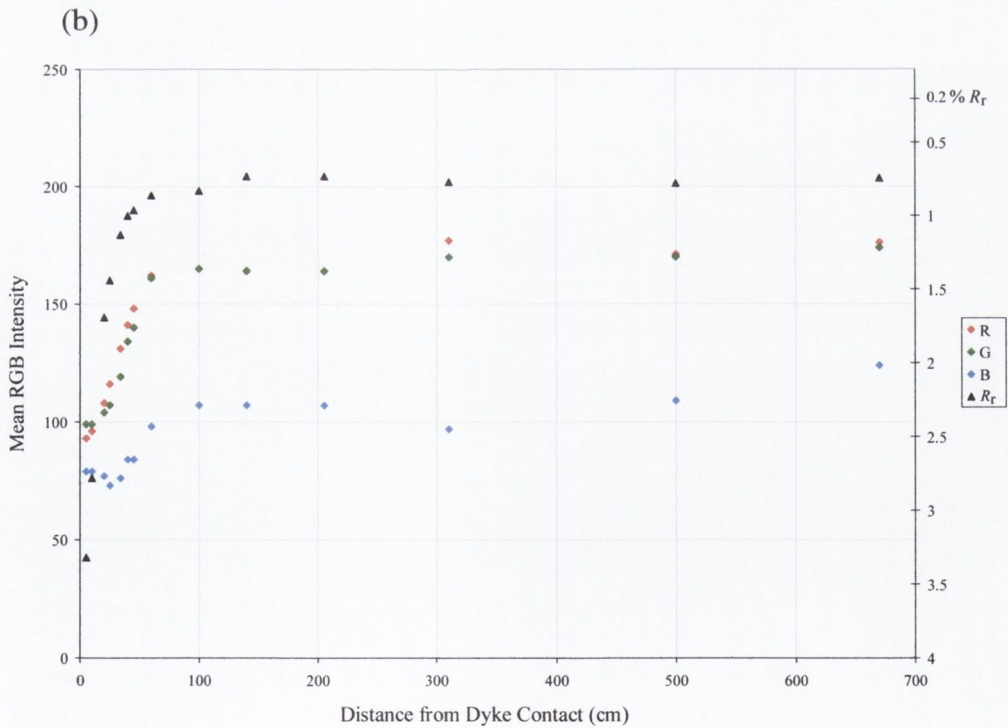
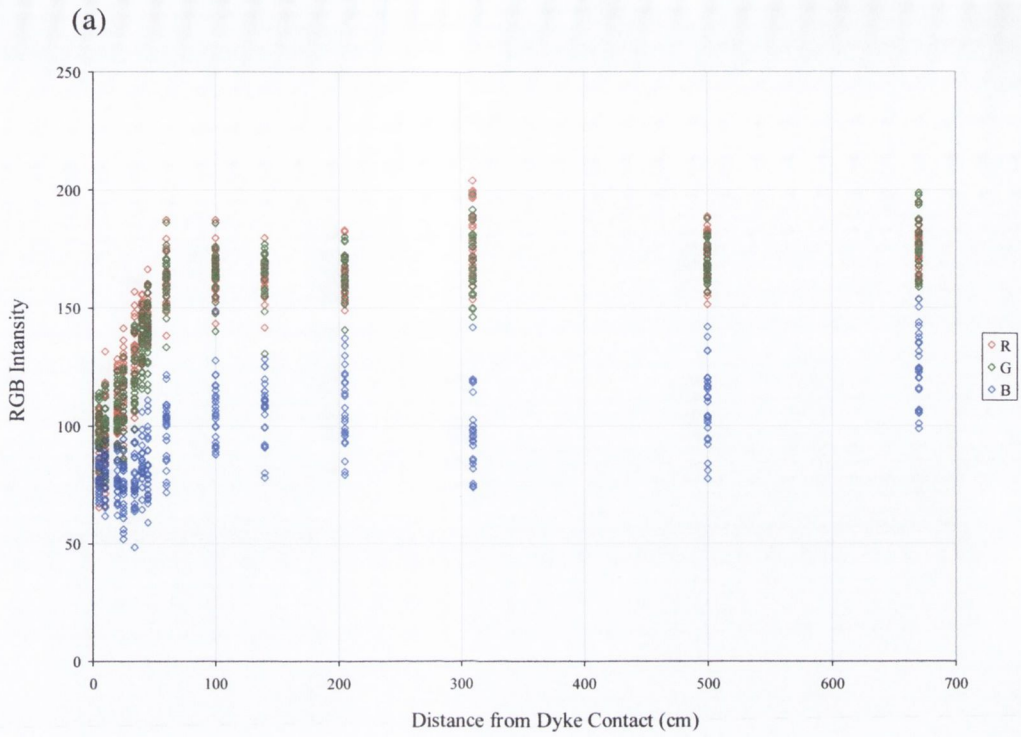


Figure 5.4. (a) Plot of all RGB intensity data against distance from dyke contact for the BGSHN sample horizon. (b) Plot of mean RGB intensities against distance from dyke contact for the BGSHN sample horizon. An inverted vitrinite reflectance profile is included on the secondary axis for comparison.

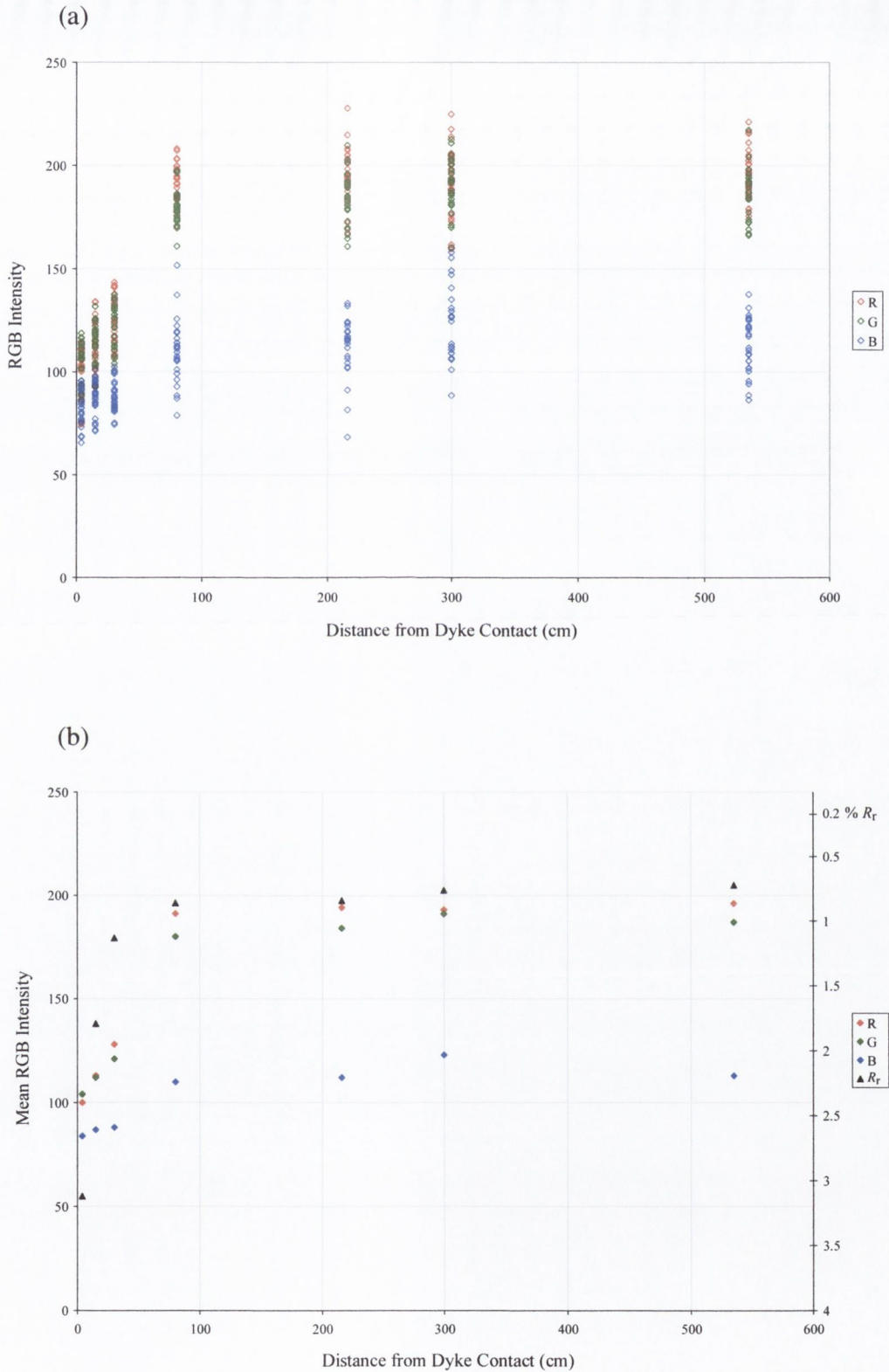


Figure 5.5. (a) Plot of all RGB intensity data against distance from dyke contact for the BGSN sample horizon. (b) Plot of mean RGB intensities against distance from dyke contact for the BGSN sample horizon. An inverted vitrinite reflectance profile is included on the secondary axis for comparison.

5.4.1 BBN SAMPLE HORIZON

The mean RGB intensities of the BBN samples are plotted against distance from the dyke contact in Figure 5.3(b). Mean R and G values follow a tightly constrained path with distance from the dyke contact, whereas the mean B path is more scattered. Mean RGB values range from R176 G175 B121 in unaltered 'background' samples (BB44N, 5.6m from dyke contact) to R85 G89 B71 at the dyke contact. The mean RGB values remain at background levels at distances greater than 1.7m from the dyke contact. In this zone TAI values of 2/2- were recorded for the AOM. At distances between 1.7m and 0.65m from the dyke contact, samples show a very gradual decrease in RGB intensities. TAI values increase from 2 to 3-. Within 0.65m of the dyke contact mean RGB values show a marked and progressive decrease towards the contact. TAI values for the AOM change rapidly from 3- through to 4-/4. This is approximately the point at which mean random vitrinite reflectance values begin to increase markedly.

5.4.2 BGSHPN SAMPLE HORIZON

Mean RGB values for the BGSHPN samples are plotted against distance from the dyke contact in Figure 5.4(b). A similar progression of sample means is observed towards the dyke. Mean RGB intensities range from background levels of R176 G174 B124 at 6.7m from the dyke, to R93 G99 B79 at the dyke contact. The most marked change in RGB levels occurs within 0.6m of the dyke contact, where mean RGB values decrease sharply and progressively to basal values. In this zone, TAI values recorded from the AOM, change rapidly from 3- through to 4-/4. As in the case of the BBN samples, the break in slope of the BGSHPN RGB profile correlates well with that of the R_r profile.

5.4.3 BGSN SAMPLE HORIZON

Mean RGB values for the BGSN samples are plotted against distance from the dyke contact in Figure 5.5(b). In general, mean RGB intensities for the BGSN samples are slightly elevated relative to the BBN and BGSHPN datasets. Mean RGB intensities range from background levels of R196 G187 B113 at *ca.* 5.3m from the dyke, to R100 G104 B84

at the dyke contact. The zone of marked colour change is poorly constrained due to a lack of sample material. However mean RGB values drop sharply between samples BGS04N (70 - 80cm from contact) and BGS03N (23 - 30cm from contact), from R191 G180 B110 to R128 G121 B88. Once again, this zone corresponds to the zone of elevated R_r values. Slightly lower TAI estimates (2-) were recorded from background samples than from the BBN or BGSHN sample horizons. Where the RGB values fall markedly, between BGS04N and BGS03N, TAI values shift from 2/2+ to 3+. TAI estimates of 4-/4 were recorded from the two most proximal samples to the dyke.

Preliminary observations indicate that AOM colour can be quantified in terms of a combination of red, green and blue parameters, and that the colour changes that occur with progressive maturation associated with dyke intrusion can be mapped by the RGB intensity pathways. A narrow zone within 0.65m of the dyke contact, in which RGB intensities show a progressive and rapid decrease, corresponds to the zone of increased maturity indicated by elevated R_r values. The data suggests that, as an indicator of thermal maturation, the sensitivity of vitrinite reflectance is similar to AOM colour, defined by mean RGB intensities.

The calculated mean RGB intensities for the BGSN samples are slightly elevated relative to the BBN and BGSHN datasets. This suggests that the AOM in the BGSN samples (carbonate) is different in colour to the variety found in the BBN and BGSHN (shale) samples. This colour discrepancy reflects differences between the type of amorphous kerogen found in the shales and that found in the limestones.

Although a disparity is observed between the calculated RGB intensities in the shales and the carbonates, the RGB intensity profiles against distance from the dyke are essentially of the same form. This suggests that the observed colour changes that occur with increased maturity are the same in all three cases, with proportionate reductions in the amounts of red, green and blue with increasing thermal alteration.

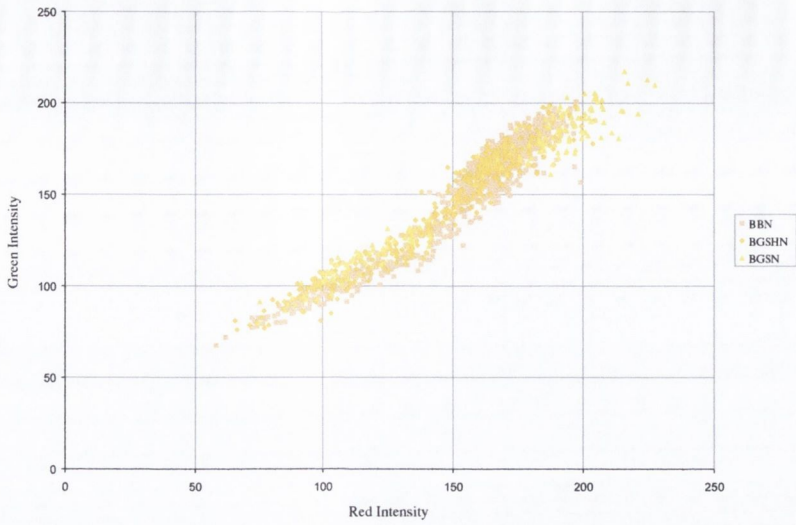


Figure 5.6 (a) Plot of red intensity against green intensity for BBN, BGSHN and BGSN sample sets.

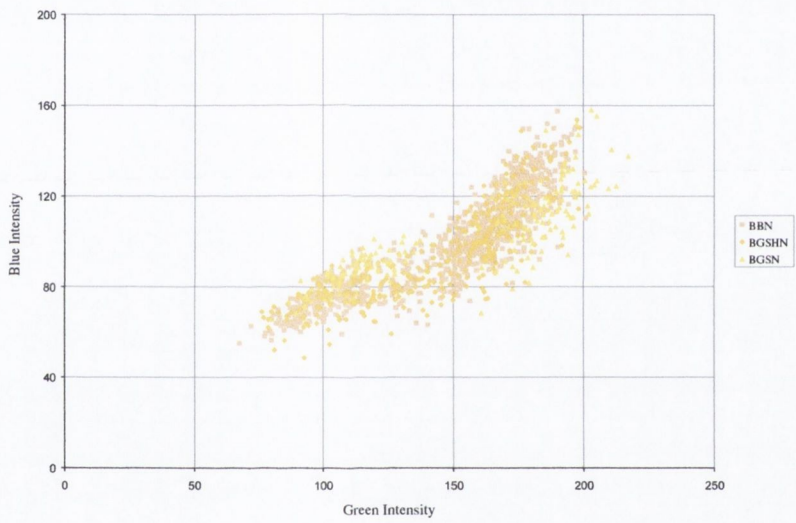


Figure 5.6 (b) Plot of green intensity against blue intensity for BBN, BGSHN and BGSN sample sets.

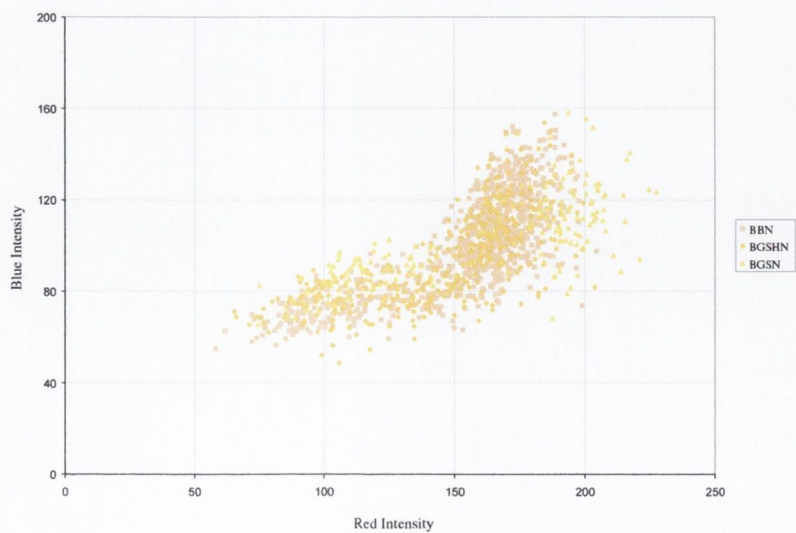


Figure 5.6 (c) Plot of red intensity against blue intensity for BBN, BGSHN and BGSN sample sets.

5.5 ANALYSIS OF RGB RESULTS

5.5.1 ANALYSIS OF RAW RGB DATA

In an attempt to characterise the relationship between each parameter with increasing maturation, plots of R versus G, G versus B, and R versus B were constructed for all datasets. Crossplots of R and G show a fairly well constrained linear relationship between the two parameters (Figure 5.6(a)). The data points progress steadily along a maturation pathway in the direction of decreased R and G intensities. The BBN and BGSHN data plot neatly together, reflecting the similarities in the colour and their associated thermally-induced colour changes observed in the AOM in the shales. Accordingly, the BGSN data plot at slightly higher values of R and G, reflecting differences in the colour range displayed by the AOM from this horizon. When G is plotted against B for all datasets, the data are considerably more scattered (Figure 5.6(b)). A maturity pathway can again be seen, but the relationship between the two parameters is less clear, the data profile having a stepped or curved morphology. Crossplots of R and B show the most scatter, but a similar data profile to that observed in G and B crossplots is seen (Figure 5.6(c)).

5.5.2 STATISTICAL ANALYSIS OF RGB PARAMETERS

In order to assess the degree to which each parameter (R, G or B) responds to increased maturation a *single factor analysis of variance* (ANOVA) was used. The method and terminology followed is detailed in Swan and Sandilands (1995, p128-135). Here, the factor of interest is red, green or blue intensity. Each *treatment* or *level* of that factor is a different % R_r value. Twenty five independent observations (RGB measurements) were made on each level of the factor and a test was carried out of:

$H_o: \mu_1 = \mu_2 = \dots = \mu_i$ (the means of each level are equal, i.e., no maturity effects, on average)
against

H_A : at least one level produces a different mean from the rest,

where H_0 is the *null hypothesis* to be tested, H_A is the *alternative hypothesis* and μ is the mean R, G or B for the level.

Sample	% R_r	TAI (Staplin)	Mean Red	Mean Green	Mean Blue
BB01N	3.60	4-/4	84.54	88.75	70.71
BB02N	2.97	4-/4	94.30	94.23	73.05
BB03N	2.59	4-	98.54	93.89	68.37
BB04N	2.01	4-	100.57	97.13	72.02
BB05N	1.72	3+	113.15	104.28	76.63
BB06N	1.58	3+	117.93	104.75	75.76
BB07N	1.55	3/3+	132.59	114.80	77.96
BB08N	1.29	3/3+	137.20	120.44	79.56
BB09N	1.19	3/3+	149.74	135.93	89.53
BB10N	1.15	3	152.89	144.58	92.87
BB11N	1.09	3	156.30	147.00	93.26
BB12N	0.96	3-	162.45	153.52	94.13
BB19N	0.91	3-	168.32	165.57	106.65
BB24N	0.84	2+	167.58	171.14	117.80
BB40N	0.79	2-	171.60	171.87	116.39

Table 5.1. % R_r , TAI and mean RGB intensity levels of samples used in single factor ANOVA.

This may appear to be a pointless exercise, as the intensities of red, green and blue are all obviously decreasing with increasing maturity. However, the purpose of the test is not only to establish that the average RGB intensities are decreasing with increasing maturity, but to establish the extent to which each parameter is affected by maturation.¹

From the BBN suite, fifteen samples were selected that follow a maturity progression from 0.79% R_r to 3.6% R_r (Table 5.1). Formal statistical tests require that the data are independent observations from *normal* distributions, but departures from this condition are not very serious provided that the distribution is reasonably symmetric. From the RGB histograms (Appendix III) it can be seen that, in general, individual data sets are reasonably symmetrical. The means and variances were calculated for each sample. Denoting the number of observations on each treatment by n_1, n_2, \dots, n_{15} and the various sample variances by $s_1^2, s_2^2, \dots, s_{15}^2$, the *corrected sum of squares* (CSS) are $(n_1-1)s_1^2 + (n_2-1)s_2^2 + \dots + (n_{15}-1)s_{15}^2$. The best estimate of the variance σ^2 can be shown to be the total value of these CSS divided by the total of the *degrees of freedom* (df).

Degrees of freedom are expressed as:

$$\sum_{i=1}^{15} (n_i - 1)$$

The total CSS is expressed as the sum of two parts: the treatment SS, associated with differences between the levels of the factor (SS between groups), and the residual SS, which is associated with random variation (SS within groups).

i.e. Total CSS = Treatment SS + Residual SS

Mean Squares (MS) are obtained by dividing the treatment and residual SS by their respective df. The residual MS provides an unbiased estimate of the variance, σ^2 . The treatment MS provides an estimate of the quantity:

σ^2 + a positive term, related to systematic differences between the means for each level.

If there are no differences between the means (H_0), the treatment MS (between groups) will have a value close to the residual MS (within groups). The greater the difference, the more reason there is to suppose that there are some differences between the levels of the factor (H_A). This difference can be quantified by the *MS ratio*, F , which is the treatment MS divided by the residual MS. The greater this quantity is, the more reason there is to believe that there is a difference between the means, i.e., there are maturity effects (H_A). Details of the ANOVA are presented in Appendix IX and the results are summarised in Table 5.2.

Table 5.2. ANOVA table, demonstrating the sources of variances for Red Green and Blue parameters.

Colour	Source of Variance	SS	df	MS	F	P-value
Red	Between Groups	318334.4791	14	22738.1771	210.1617	1.49×10^{-163}
	Within Groups	38949.7356	360	108.1937		
	Total	357284.2148	374			
Green	Between Groups	316725.9977	14	22623.2856	233.2133	8.18×10^{-171}
	Within Groups	34922.4598	360	97.0068		
	Total	351648.4575	374			
Blue	Between Groups	93304.0645	14	6664.5760	58.4114	1.72×10^{-83}
	Within Groups	41074.9816	360	114.0972		
	Total	134379.0462	374			

From the Table 5.2, red, green and blue all have high F values, proving that, on average, all three colour components are sensitive to thermal maturation (H_A). The F values for red and green are considerably higher than for blue, suggesting that maturity effects are greater for these parameters. The variation within individual samples, characterised by the residual MS, on average is greatest for the blue component. While the variation between groups is highest for red, its residual MS is higher than that of green, implying greater variation within individual samples. The green parameter consequently has a higher F value, suggesting that, on average, it is most sensitive to thermal maturation, closely followed by red, with blue being the least sensitive for the measured samples. Each F value has a probability value (P-value) associated with it. The P-value is a measure of the risk one would have to take, in order to say that the means of the various levels were equal. Once again, whilst all the P-values are extremely low proving that the various levels of intensity are different, the risk is greatest for the blue component. The P-values of both red and green are much smaller, indicating greater differences between the levels for these factors, with green having the smallest risk. Thus green is considered to be the most useful single component of colour change in maturation studies, however AOM colour is dependent on all three (RGB) components.

5.5.3 COMPARISON WITH VITRINITE REFLECTANCE

Vitrinite reflectance data were available for all of the samples studied (Chapter 4). Plots of R_r against mean RGB intensity are presented for the three datasets (Figure 5.7). Once again, the BBN dataset being the most comprehensively sampled, shows the greatest resolution over the maturity range observed in the vicinity of the dyke. An excellent linear correlation between mean RGB intensity and mean random vitrinite reflectance (R_r) is observed, from the lowest rank sample at *ca.* 0.75% R_r up to *ca.* 1.3% R_r . Above this level of vitrinite reflectance, B intensities level off, showing little or no change with increasing maturity. Considering the R and G parameters alone, this correlation can be extended as far as 1.5 - 1.6% R_r . Above this level of vitrinite reflectance, although they continue to decrease, there is relatively little change in RGB intensities with increasing maturation. No organic matter fluorescence occurs above this level of vitrinite reflectance.

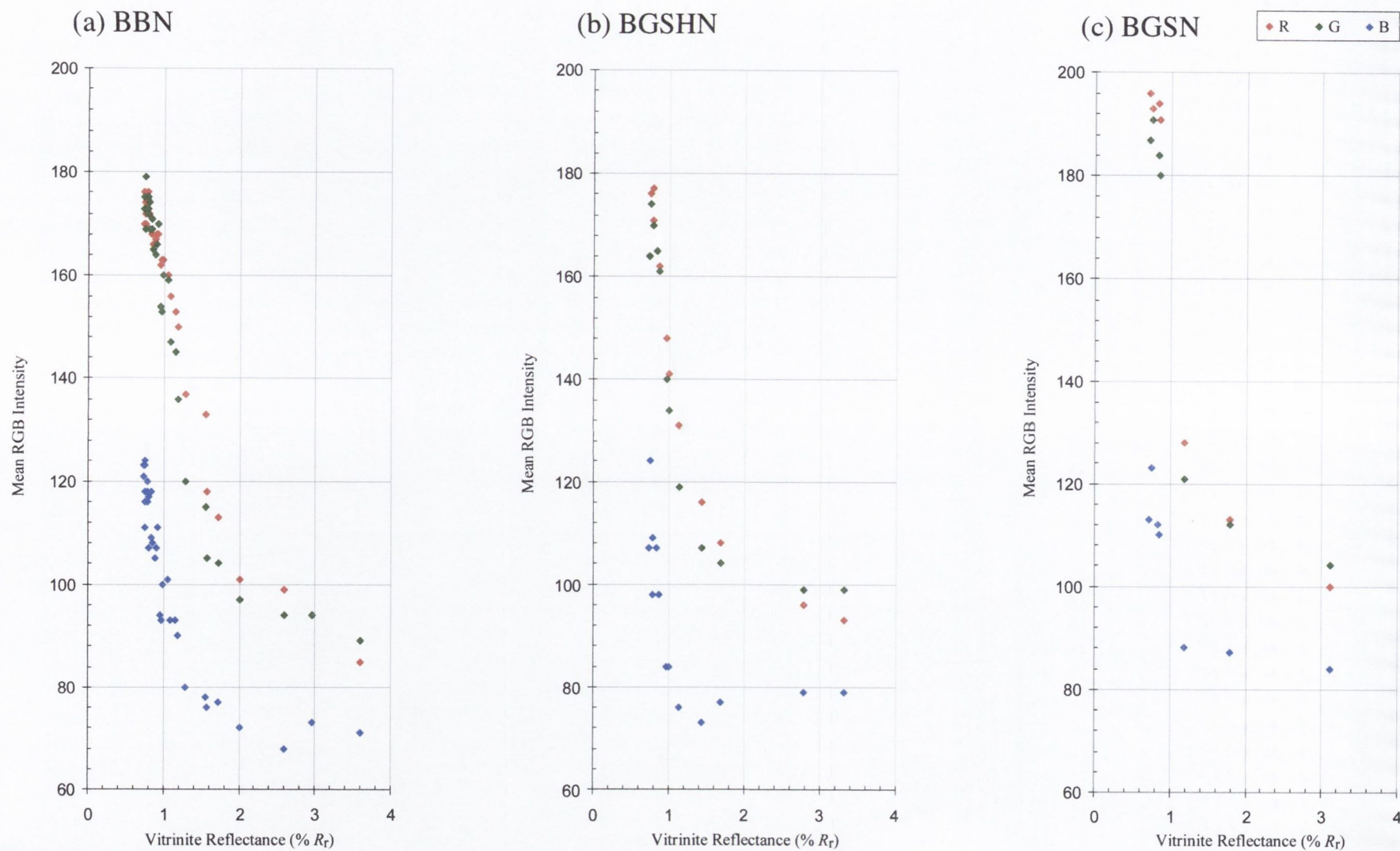


Figure 5.7. Plots of mean RGB intensity versus mean random vitritine reflectance (% R_r) for the Bearreraig Bay samples: (a) BBN samples, (b) BGSHN samples, (c) BGSN samples.

The data suggests that, as a maturity parameter, RGB colour determination of AOM by CIA is sensitive up to *ca.* 1.6% R_r . The lower limiting R_r value of this sensitivity range with AOM (RGB) colour is unknown, as samples of lower maturity than 0.7% R_r were not investigated.

Any direct correlation of AOM RGB intensity with vitrinite reflectance must only be considered tentative for a number of reasons. The chemical structure of vitrinite is different from that of AOM, and the kinetics controlling changes in the properties of both are considerably different (Barnard *et al.* 1981). Different geological histories result in different durations of thermal input. Depending on its thermal/geological history, each basin will have a somewhat different correlation. This will be especially true for sediments whose maturation has been enhanced by 'flash' heating resulting from the intrusion of igneous bodies. Also, there may be other factors affecting the colour or chemistry of the organic matter, causing subsequent differences between and within samples of the same rank e.g., diagenetic environment, lithology, oxidation, weathering, etc. (Yule *et al.* 1998). Correlation with vitrinite reflectance is complicated further by the fact that RGB colours are quantified in terms of three independent variables (R/G/B). An exact match of all three parameters with R_r is unlikely, even within the same basin. Marshall and Yule (1999) attempted a general correlation of spore colour with R_r by comparison of the G parameter alone, however no details are provided of the system calibration/illumination with which the data were obtained. Values ranging from G175 to G10, corresponding to R_r values between *ca.* 0.2% and < 2.0%, appear to match the range presented in Yule *et al.* (1998).

Yule, *et al.* (1998) cited crossplots of R and G as a means to quantify spore colour and compared mean G intensity to R_r and Rock-Eval pyrolysis T_{max} data. A good linearity was observed between mean G intensity and R_r for $G > 40$ (approximately $\leq 1.0\%$ R_r). Above this level of vitrinite reflectance, no further apparent change in mean G intensity is observed (Yule *et al.* 1998, Fig. 5a). The RGB range of spore colour presented in Yule *et al.* (1998) is clearly different to the measured RGB range of AOM colour presented in this study. Whilst it is recognised that the RGB colours of spores and AOM from the same sample are different, the observed disparity between the RGB ranges is primarily due to differing calibration conditions between the colour measurement systems. In order that their RG scale detail the colour changes over the lower maturity range, Yule *et al.* (1998)

used a rather dim microscope illumination (R137 G170 B147) (Figure 3.6(d)). Consequently, the RG scale of Yule *et al.* (1998) terminates at the dark brown stage, at samples of maturity $R_r > 1.5\%$. At this illumination, the B component is reduced to zero by the point at which the spores are mid/dark yellow in colour ($G < 120$). Furthermore, it is clear from the RG crossplots presented in Yule *et al.* (1998) that in some cases, the measured (RG) intensities of spores are higher than the quoted background illumination value. Clearly this is unrealistic and a higher background intensity would appear to be more appropriate.

5.5.4 RELATIVE RGB INTENSITY OF SAMPLES

In recognition of the difficulties in calibrating three independent variables (R/G/B) to an established maturity scale (e.g., % R_r), previous attempts at producing a quantitative colour scale Yule *et al.* (1998) and Marshall and Yule (1999) have attempted to reduce the tripartite RGB colour space to one or two variables (G, RG). However RGB colour cannot be defined correctly without consideration of all three variables. Although red, green and blue intensity are measured on three independent 0-255 scales, it is the combination of all three parameters that produces the end colour. From Figure 5.6, it can be seen that the pathways followed by each colour parameter with increasing maturation are different. Each parameter responds somewhat differently over the range of maturation (Table 5.2). The observed colour changes of organic matter in response to increased maturation cannot therefore be described simply as a reduction in the intensity of one, or all three RGB parameters.

By expressing each colour parameter as a percentage of the sum of the total RGB that define that colour, it is possible to relate each parameter to the others, e.g.:

$$\%G = \frac{G \times 100}{(R + G + B)}$$

When % R, % G and % B are plotted against vitrinite reflectance, it is possible to observe the manner in which each colour parameter behaves in relation to the others, with increased

maturation. Plots of the relative RGB means (%) for the BBN, BGSHN and BGSN samples against R_r in are presented in Figure 5.8.

Figure 5.8 reveals a series of distinctive and recurring relationships between the three colour parameters with maturity. Most striking is the zone between *ca.* 1.0% and *ca.* 1.7% R_r , in which a marked perturbation in the proportions of the RGB percentages occurs. Within this zone, a deviation is observed from the otherwise rather linear relationship between % R and % G. At *ca.* 1.0% R_r the paths of % R and % G are seen to diverge, before converging again at *ca.* 1.7% R_r . Maximum deviation between % R and % G occurs between approximately 1.15% and 1.55% R_r . After an initial decrease between *ca.* 0.7% and *ca.* 1.0% R_r , a steady increase is observed in % B within the 1.0% to 1.7% R_r zone. Above 1.7% R_r there is comparatively little change in the mean RGB percentages. However, % B continues to increase gradually relative to % R, while % G shows no apparent change with increasing maturity. Importantly, these relationships between the relative percentages of red, green and blue with maturation are consistent for all three datasets. Only the BGS03N data point (1.18% R_r , 38%R 36%B 26%B) appears anomalous. A higher % R_r value for this data point would appear to produce a better fit on the graph.

This zone of divergence of the relative red, green and blue percentages corresponds to the dull orange and brown colours (TAI 3- to 3/3+), which commonly mark the mature main phase of potential oil generation. The subsequent convergence and steady flattening out of the relative RGB percentages characterises the dark brown and black colours (TAI 3+ to 4-/4), usually associated with the post-mature phase for liquid hydrocarbons. Furthermore, the re-convergence of the relative RGB percentages coincides well with the observed quenching of fluorescence in the AOM. Interestingly, the premature extinction of AOM fluorescence observed in the BGSN horizon, compared with the BBN and BGSHN horizons, is picked out well by the 'anomalous' BGS03N data point on the relative % RGB against % R_r plot.

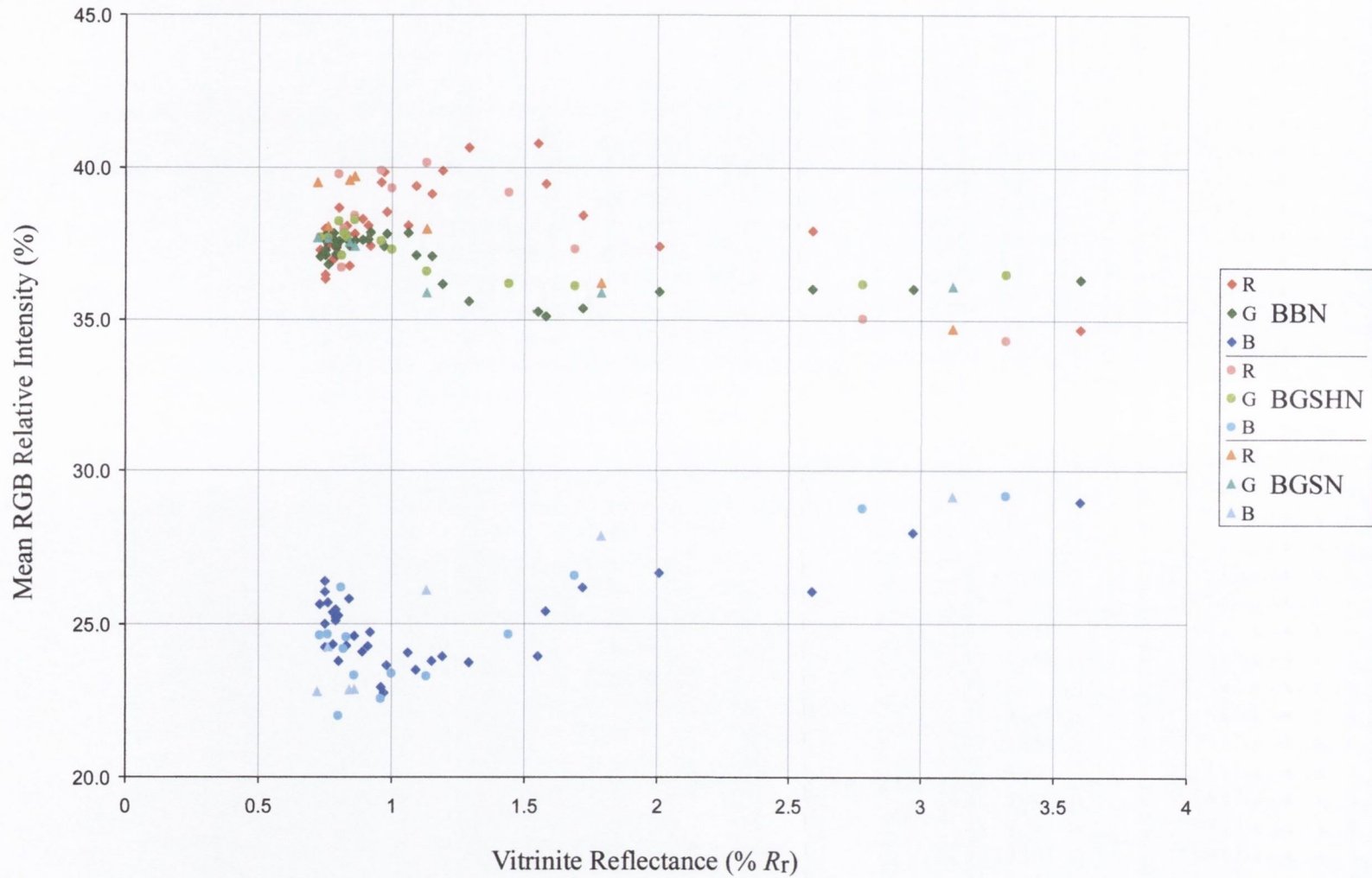


Figure 5.8. Plot showing relative mean RGB intensities of AOM against vitrinite reflectance for the BBN, BGSHN and BGSN sample horizons.

5.5.5 CONVERSION OF RGB TO HSB

The RGB values can be mathematically converted to hue, saturation and brightness (intensity) values (HSB). Based on the human perception of colour, the HSB colour system describes three fundamental characteristics of colour: Hue, measured as a location between 0 and 360° on the standard colour wheel, is the colour reflected from, or transmitted through an object. In common use, hue is identified by the name of the colour such as red, orange or green. Saturation, or chroma, is the strength or purity of the colour, representing the amount of grey in proportion to the hue, measured as a percentage from 0% (grey) to 100% (fully saturated). On the standard colour wheel, saturation increases from the centre to the periphery. Brightness (or intensity) is the relative lightness or darkness of a colour, usually measured as a percentage from 0% (black) to 100% (white). Of the HSB colour parameters, Schwab *et al.* (1995a) determined that hue and brightness are the only components required to define the level of thermal maturity of a palynomorph. Using microspectrophotometry (ICA/SPD), Schwab *et al.* (1995b) measured the percentages of red, green and blue light transmitted through Staplin's (1969) set of TAI standards. The RGB values were converted to HSB values, and H/I plots were constructed that mapped out a 'cusp-shaped' maturation pathway (Jansonius and Schwab 1996).

Conversion of the Bearreraig Bay RGB mean values to HSB was carried out using the Adobe® Photoshop® colour palette. When the data is plotted on a hue/brightness chart, a similar thermal maturity pathway is evident (Figure 5.9). Whilst the Bearreraig Bay intensity data are expressed as percentages (conventionally used to express intensity or brightness values), Schwab's intensity data are scaled differently. The magnitude of I scale, presented in Jansonius and Schwab (1996) is unknown, and it is therefore difficult to compare the two plots directly. However, the hue values in Figure 5.9 compare well with values obtained by Schwab from Staplin's TAI standards. TAI data from the BBN dataset are included in Figure 5.9 for comparison. Once again, it is possible to divide the data into mature and post-mature trends, mapped respectively by decreasing and subsequent increasing hue. The hinge area roughly coincides with extinction of AOM fluorescence.

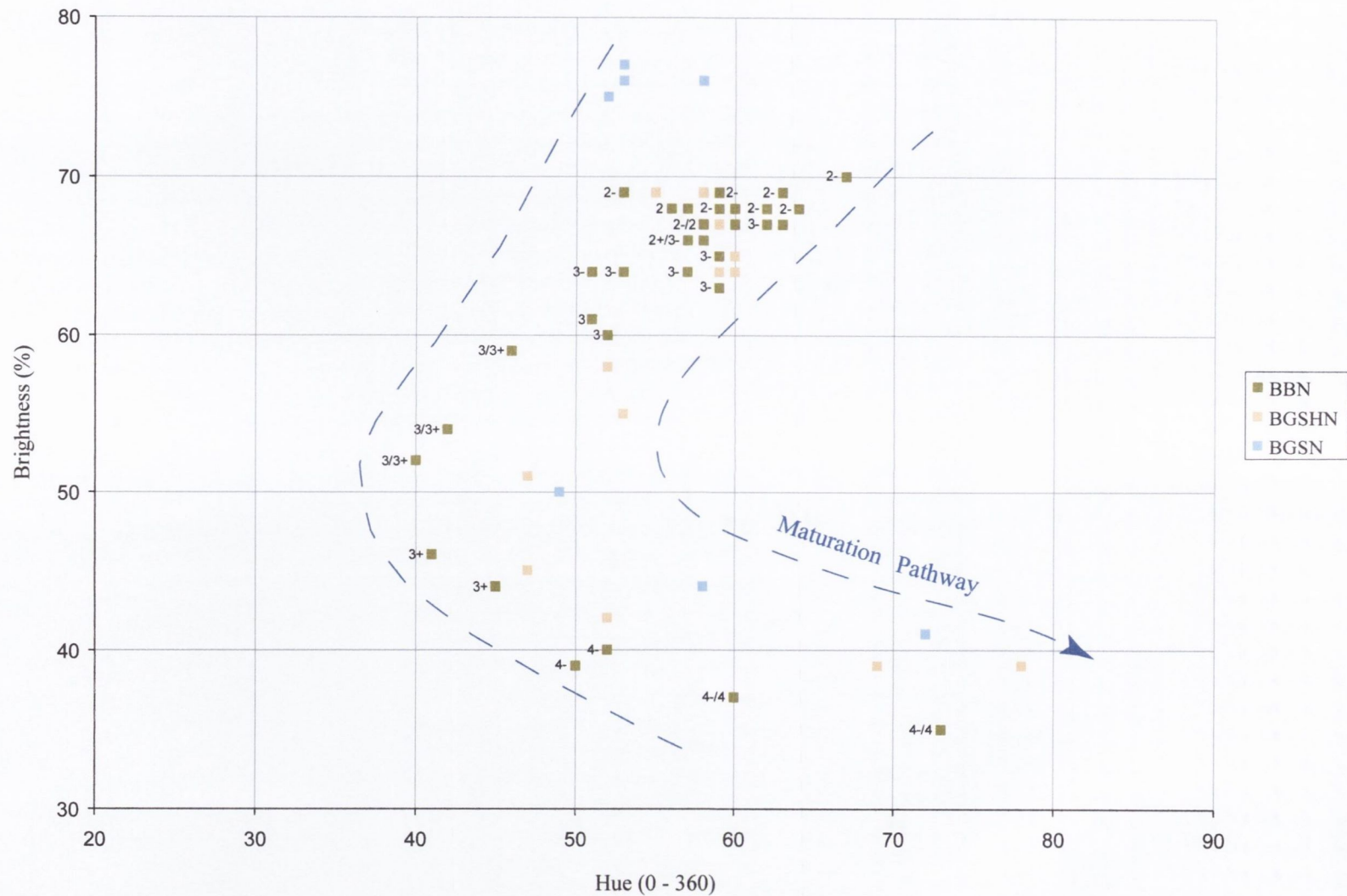


Figure 5.9. Plot showing Hue (H) against Brightness (B) colour components of AOM from the BBN, BGSHN and BGSN sample horizons. TAI values for the BBN samples are included adjacent to the BBN H/B data points. The dashed lines represent the H/B maturation pathway followed by the AOM. The HSB values are derived from measured RGB intensities.

The AOM colour changes observed in the aureole of the dyke follow a maturation pathway that can be mapped by the hue/brightness plot. The similarity between the hue values of the AOM and the spectrally derived values of Staplin's TAI standards (Jansonius and Schwab 1996) add confidence to the use of AOM in kerogen colour studies.

5.6 DISCUSSION

The main objective of this part of the project was to investigate the thermally induced kerogen colour changes associated with the dyke intrusion and subsequent cooling. In the absence of significant numbers of palynomorphs, normally used for kerogen colour designations, a colour investigation of the abundant amorphous kerogen was attempted. It was decided to explore a relatively new approach for the quantification of kerogen colour, through the use of colour image analysis software. The quantification of kerogen colour through image analysis has thus far been relatively little explored, and previous studies have mainly concentrated on spores (van de Laar and David 1998; Yule *et al.* 1998), which facilitate more consistent colour estimation. The variable thickness and heterogeneous nature of amorphous kerogen presented additional difficulties. Within a population of 25 AOM particles from a single sample, a wide range of RGB values is observed (RGB Histograms, Appendix III). Nevertheless, despite the wide range of RGB values within each sample, a clear progression of RGB means can be observed in all three sample horizons, with increasing proximity to the dyke. Plots of mean RGB intensity versus distance from the dyke identify a narrow zone within 0.6 - 0.65m (*ca.* 50% d.t.) of the contact, in which RGB intensities decrease sharply in the direction of the dyke (Figures 5.3(b), 5.4(b) and 5.5(b)). Although the resolution is greatest through the BBN sample horizon, this appears to be consistent for all three horizons. The break in slope of the RGB intensities compares well with that of the R_r profiles for the same samples. This suggests that the reaction time of AOM colour to thermal alteration due to dyke intrusion is similar to that of vitrinite reflectance (see Chapter 7). Average background (> 3m from contact) RGB intensities of R173 G173 B120 and R174 G171 110B, for the BBN and BGSHN sample horizons respectively, correspond to visual TAI estimates of 2-/2. Slightly higher average background RG intensities of R195 G189 B118 from the BGSN horizon are

consistent with slightly lower TAI estimates of 2-. Assuming that these sediments experienced the same thermal history prior to intrusion of the dyke, this must reflect differences in the type or preservation state of the AOM rather than differing degrees of thermal alteration.

Analysis of variance (ANOVA) of RGB means from selected samples from the BBN suite indicates that the colour alteration of AOM in response to thermal maturation is considerably more sensitive in the red and green regions of the visible spectrum than in the blue. The G parameter has a slightly higher F value than the R, and is therefore the most sensitive colour component to thermal stress. This is mainly attributed to the fact that it shows the least within-sample variation. No account was taken of the variance due to variation within a single AOM particle. Crossplots of R and G produce a fairly linear profile, with little scatter of data, reflecting the regular behaviour of organic material within these parts of the visible spectrum in response to thermal maturation. The data are considerably more scattered when R and G are plotted against B, reflecting the irregular behaviour and comparatively poor sensitivity of the blue colour component to thermal maturation. Furthermore, these profiles have a more stepped appearance, suggesting that the B parameter behaves somewhat differently to R and G over the range of maturation investigated. Closer inspection of the RGB parameters, through plots of the relative percentages of red, green and blue against % R_r reveal a distinct maturation pathway for each of the three colour parameters. The data show that, proportionately speaking, the changes that occur in the red and blue components in response to increased maturation are almost equal and opposite. However, these changes are not quite equal, as the proportion of green also varies with rank, but to a lesser degree. This would seem to support the evidence that green parameter behaves most regularly in response to thermal maturation.

Marshall and Yule (1999) cite G as a good, relatively linear colour parameter. The results from this study would seem to support that contention. The G parameter was found here to be the most sensitive colour component to thermal stress. Furthermore, the intensity changes associated with thermal maturation are most regular for the green parameter. A good linear correlation was observed between mean G intensity and R_r up to *ca.* 1.6% R_r . However, any direct correlation of kerogen colour with vitrinite reflectance must only be considered tentative. The chemical structure of vitrinite is different from that of AOM, and

the kinetics controlling changes in the properties of both are considerably different (Barnard *et al.* 1981). Different geological histories result in different durations of thermal input. Depending on its thermal/geological history, each basin will have a somewhat different correlation. This will be especially true for sediments whose maturation has been enhanced by rapid heating events such as the intrusion of igneous bodies.

The relationships between relative proportions of each colour component and rank are complex, and are consistent for each sample horizon. Two main trends are evident from Figure 5.8: a zone of marked change between relative proportions of the three colour components, followed by a stable zone, with little change in the relative RGB proportions. By comparison with R_r , visual TAI and fluorescence data, it is possible to draw tentative correlations between the relative proportions of red, green and blue, and stages of maturity. A zone of divergence of the relative percentages of Red, Green and Blue appears to characterise the mature main phase of potential oil generation in AOM. The subsequent convergence of the relative RGB parameters to a more stable, flatter profile correlates well with extinction of AOM fluorescence, and appears to mark the onset of the post-mature phase for oil. This suggests that an intrinsic relationship exists between the colour of the AOM and its fluorescence characteristics. Conversion of the RGB data to HSB values identifies yet another maturation pathway that can be mapped by plotting H/B. This further suggests that the colour changes of AOM in response to thermal maturation are regular and consistent. Again, it is possible to divide the data into mature and post-mature trends, mapped respectively by decreasing and subsequent increasing hue. The similarity between the hue values of the AOM and the spectrally derived values of Staplin's TAI standards (Jansonius and Schwab 1996) add confidence to the use of AOM in kerogen colour studies.

Colour image analysis provides a quantitative scheme, which allows kerogen (including AOM) colour to be plotted on a progressive maturation trend (either as simple RGB means, relative RGB percentages, or as H/B data). If colour determination of kerogen through CIA is to have wider application and implication, standardised conditions (software, camera shutter speed, white balance, light source, voltage, diaphragm settings, filters, lenses, etc.) need to be established. As previously discussed in Sections 3.3.2 and 5.5.3, the calibration settings of Yule, *et al.* (1998) appear to be seriously flawed. Van de

Laar and David (1998) offer no details whatsoever on the system calibration settings used in their determination of spore colour. The camera/microscope setup used in this study is detailed in Sections 3.3.1 and 3.3.2, and in Figure 3.5. During the course of this study it was necessary to replicate this setup several times. By taking care during the setup stage, it was possible to replicate measurements from a previous sitting. However, the reproducibility of results has not been tested from other imaging/camera/microscope outfits. It was deemed to be beyond the scope of this work to attempt any external calibration with other such systems, but future work in this area would help to better contextualize the results from this study. This could perhaps be approached by using standards of uniform colour, that are readily available and easily accessible, such as standard colour lens filters used in photography.

5.7 SUMMARY

Amorphous organic matter (AOM) is valuable for kerogen colour studies of sequences barren of palynomorphs. The colour investigation of the AOM in three sedimentary horizons adjacent to the dyke identified a narrow zone within 0.6 - 0.65m of the contact, within which AOM colour averages decrease sharply in the direction of the dyke. The thickness of this zone is equivalent to 50% of the dyke thickness (d.t.). The break in slope of the mean RGB intensities correlates well with that of the R_r data. Analysis of variance (ANOVA) of the RGB intensity means identified G as the most sensitive parameter in relation to thermal maturation. Plots of the relative percentages of red, green and blue against % R_r reveal a unique maturation pathway for each of the three colour parameters, and suggest a close relationship with fluorescence intensity. The G maturation pathway is the most linear. A good correlation of mean RG intensities with vitrinite reflectance exists up to *ca.* 1.6% R_r . Conversion of the RGB data to HSB values identifies a maturation pathway that can be mapped by plotting H/B. The good agreement between RGB derived hue values of the AOM and the spectrally derived values of Staplin's TAI standards (Jansonius and Schwab 1996) add confidence to the use of AOM in kerogen colour studies. Further work is needed to extend the calibration to other such measurement systems in order to standardise this technique.

CHAPTER 6

NUMERICAL MODELLING OF HEAT FLOW

6.1 INTRODUCTION

This chapter is concerned with the mathematical modelling of the thermal history of the cooling intrusion and adjacent country rocks. A standard numerical model of one-dimensional transient conductive heat flow, the *Schmidt Plot* (Schmidt 1924; Nussbaum 1928), is used to estimate the temperature change produced in the host rocks at an initial temperature T_{host} , by heat transfer from the dyke as an infinite sheet that is emplaced at an initial temperature T_{magma} . The resulting maximum temperature distribution computed via the numerical model is then compared to that predicted by the VR-temperature models (Section 4.5) in Chapter 7. This is intended to provide an estimate of the reaction time of vitrinite reflectance to the elevated temperatures caused by the intrusion.

6.2 BASIS FOR THE SCHMIDT METHOD: HEAT FLOW THEORY

Heat is a form of energy and it is conserved. Bodies have an internal energy due to their heat, and heat cannot flow from a cold body to a hot body without the input of energy. In the lithosphere, heat is transferred primarily through conduction. Conduction is a diffusive process, whereby kinetic energy is transferred by intermolecular collisions. The rate at which heat is transferred by conduction depends on the thermal conductivity of the material conducting the heat, and its specific heat capacity. The fundamental relation for conductive heat transport is given by *Fourier's Law*. It states that the heat flux Q is directly proportional to the temperature gradient:

$$Q = -k \frac{\partial T}{\partial x} \quad (6.1)$$

where k is the coefficient of thermal conductivity, T is the temperature at a given point in the medium, and x is the coordinate in the direction of the temperature variation. Conservation of energy for a motionless material undergoing one-dimensional conductive heat transfer is given by (Carslaw and Jaeger 1959):

$$\rho C \frac{\partial T}{\partial \tau} = \frac{\partial}{\partial x} k \frac{\partial T}{\partial x} \tag{6.2}$$

This equation states that the heat conducted into a body minus the heat conducted out is equal to the accumulation of heat within the body. The right-hand side of Eq. (6.2) is the gradient in heat flux given by Fourier's Law, and the left-hand side of the equation is the rate of accumulation of heat, where ρC is the heat capacity per unit volume. If k is constant, then

$$\frac{\partial T}{\partial \tau} = \kappa \frac{\partial^2 T}{\partial x^2} \tag{6.3}$$

Thermal diffusivity, $\kappa = k/\rho C$, measures the ability of a body to conduct heat relative to its ability to accumulate heat. It is a physical property that controls the rate at which heat is dissipated through a material. The second spatial derivative of temperature may be approximated by (Holman 1990):

$$\frac{\partial^2 T}{\partial x^2} \approx \frac{1}{(\Delta x)^2} (T_{i-1} + T_{i+1} - 2T_i) \tag{6.4}$$

The time derivative is approximated by (Holman 1990):

$$\frac{\partial T}{\partial \tau} \approx \frac{T_i^{p+1} - T_i^p}{\Delta \tau} \tag{6.5}$$

In this relation the superscripts designate the time increment. Combining the relations above gives the difference equation equivalent to Eq. (6.3):

$$\frac{T_{i-1}^p + T_{i+1}^p - 2T_i^p}{(\Delta x)^2} = \frac{1}{\kappa} \frac{T_i^{p+1} - T_i^p}{\Delta \tau} \tag{6.6}$$

Thus, if the temperatures of the various nodes are known at any particular time, the temperatures after a time increment $\Delta\tau$ may be calculated by rewriting Eq. (6.6) for each node and obtaining the values of T_i^{p+1} :

$$T_i^{p+1} = \frac{\kappa\Delta\tau}{(\Delta x)^2}(T_{i-1}^p + T_{i+1}^p) + \left[1 - \frac{2\kappa\Delta\tau}{(\Delta x)^2}\right]T_i^p \quad (6.7)$$

The *Schmidt method* for transient heat transfer in a one dimensional system, is based on the choice of the parameter:

$$\frac{(\Delta x)^2}{\kappa\Delta\tau} = 2 \quad (6.8)$$

This grouping relates the time step, $\Delta\tau$, to the distance increment, Δx . In this way, the time and distance increments are controlled, so that the temperature of a node i after the time increment $\Delta\tau$ is given as the arithmetic mean of the two adjacent nodal temperatures, Δx units away, at the beginning of the time increment (Figure 6.2):

$$T_i^{p+1} = \frac{T_{i-1}^p + T_{i+1}^p}{2} \quad (6.9)$$

Thus, to find the temperature distribution in a solid after some specified time, the solid is divided into increments of Δx . Then, by using Eq. (6.8), the value of $\Delta\tau$ is obtained. This value of $\Delta\tau$, when divided into the total time, gives the number of time steps necessary to establish the desired temperature distribution. The choice of time step involves a trade-off between solution accuracy and computation time. A smaller time step will produce greater accuracy, whereas a solution will be achieved more rapidly for larger values of $\Delta\tau$. The accuracy of the method is therefore improved when smaller Δx increments are taken, but this requires a larger number of time steps (smaller $\Delta\tau$ value) to obtain a temperature distribution after a given time. When computing is done numerically by machine, a small time step can be used without much difficulty.

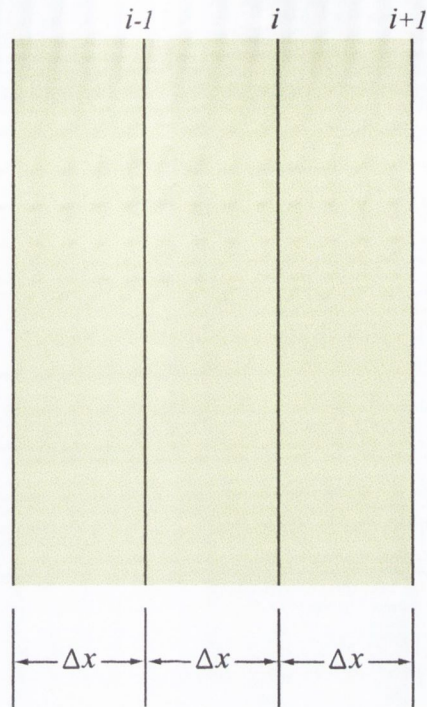


Figure 6.1. Nomenclature for numerical solution of one-dimensional unsteady-state conduction.

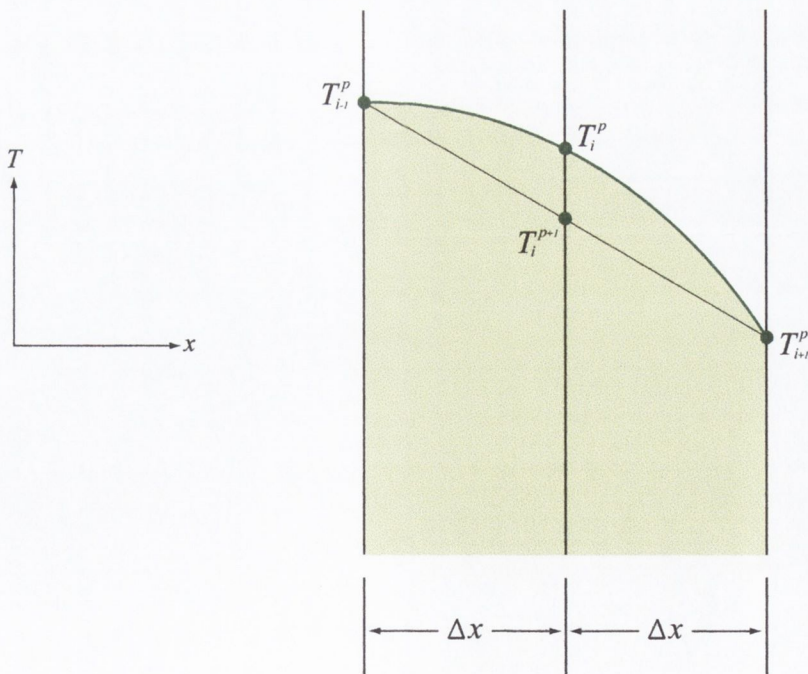


Figure 6.2. The Schmidt Plot: graphical construction for one-dimensional unsteady-state conduction.

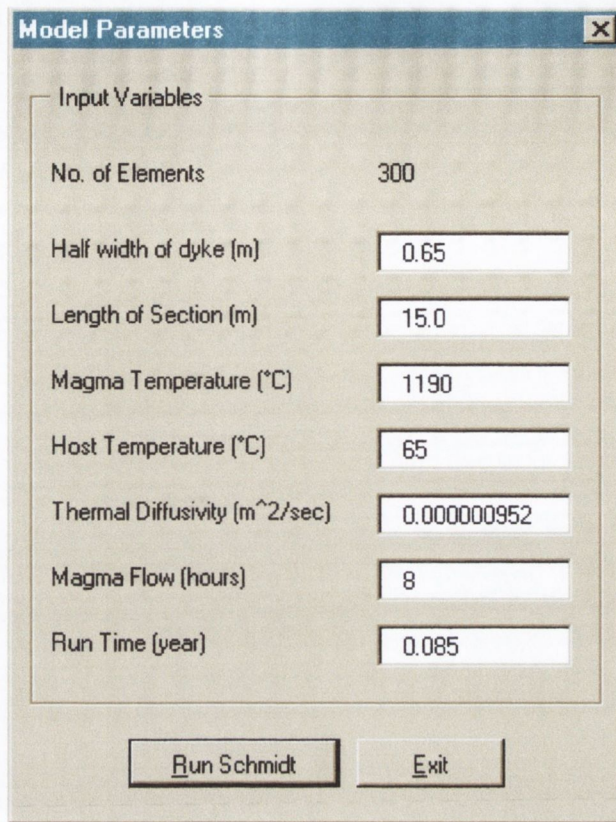
A computer simulation of the Schmidt Plot was developed to model the transient temperature distributions in the country rocks adjacent to the cooling dyke. An early simulation of the Schmidt Plot was created in TCD by D. Doff and others (Goodhue 1996; McCormack *et al.* 1997; McCormack 1998). This simulation was created using Microsoft QuickBasic (QBasic) under the DOS operating system. A major disadvantage of the QBasic program is that the user lacks the ability to access the results data associated with the plot.

The QBasic simulation of the Schmidt Plot was modified and recreated in Microsoft Excel by the author, in conjunction with M. Cunningham, using Excel's Visual Basic for Applications facility (VBA). This allows the program to run under the Windows operating system, a more user-friendly environment (Figure 6.3). The main improvement of the program however, is the facility of accessing the results data in spreadsheet form for further analysis. The complete source code for the Visual Basic simulation of the Schmidt Plot is provided in Appendix VIII.

6.3 VALIDITY OF THE SCHMIDT PLOT

The Schmidt method is only valid if the following assumptions are true:

1. Heat transfer is one-dimensional. That is to say, that heat transfer occurs in one direction only and no heat is lost along the length of the intrusion.
2. The rock mass is assumed to be homogenous. That is to say, that there are no boundary effects between dyke and host rocks and the thermal properties of both magma and host rocks are considered to be the same.
3. The thermal properties of the rock mass are assumed to be independent of temperature. The model requires that a fixed thermal diffusivity (κ) be used.
4. Heat is transferred by conduction only.



Microsoft Excel - Averaged Schmidt300

File Edit View Insert Format Tools Data Window Help Schmidt Plot

Geneva 9 B I U

A1 = Distance from Dyke Centre

	A	B	C	D	E	F	G	H	I	J
	Distance from Dyke Centre	T(0Yr)	Tmax	T(0.0004Yr)	T(0.0008Yr)	T(0.0012Yr)	T(0.0017Yr)	T(0.0021Yr)	T(0.0025Yr)	T(0.0030Yr)
1	0.0000	1190	1190	1190	1190	1190	1190	1190	1190	1190
2	0.0500	1190	1190	1190	1190	1190	1190	1190	1190	1190
3	0.1000	1190	1190	1190	1190	1190	1190	1190	1190	1190
4	0.1500	1190	1190	1190	1190	1190	1190	1190	1190	1190
5	0.2000	1190	1190	1190	1190	1190	1190	1190	1190	1190
6	0.2500	1190	1190	1190	1190	1190	1190	1190	1190	1190
7	0.3000	1190	1190	1190	1190	1190	1190	1190	1190	1190
8	0.3500	1190	1190	1190	1190	1190	1190	1190	1190	1190
9	0.4000	1190	1190	1190	1190	1190	1190	1190	1190	1190
10	0.4500	1190	1190	1190	1190	1190	1190	1190	1190	1190
11	0.5000	1190	1190	1190	1190	1190	1190	1190	1190	1190
12	0.5500	1190	1190	1190	1190	1190	1190	1190	1190	1190
13	0.6000	1190	1190	1190	1190	1190	1190	1190	1190	1190
14	0.6500	1190	1095.39417	1051.57227	1090.88916	948.669067	887.046265	852.093384	828.515442	811.111111
15	0.7000	65	914.066406	774.718797	892.66748	848.437378	806.874634	782.717651	766.355164	754.111111
16	0.7500	65	750.628784	544.003906	712.465942	740.24231	722.248718	710.427368	702.099121	696.111111
17	0.8000	65	636.12146	359.433594	550.284546	624.083984	633.168579	635.222534	635.747314	634.111111
18	0.8500	65	594.801147	227.597656	415.133392	514.895813	546.444092	561.220337	570.13739	574.111111
19	0.9000	65	563.170654	148.496094	307.012482	412.677979	462.075256	488.420746	505.269379	514.111111
20	0.9500	65	535.952209	99.0576172	223.84256	325.689697	385.506927	420.447876	443.747009	461.111111
21	1.0000	65	511.934509	79.2822266	165.623596	253.93103	316.739044	357.301758	385.57019	404.111111
22	1.0500	65	490.451813	68.2958984	124.038635	197.065491	258.015259	301.111084	332.515015	354.111111
23	1.1000	65	471.060608	66.0986328	99.0876617	155.093079	209.335541	251.875946	284.581421	304.111111
24	1.1500	65	453.435701	65	82.4536743	123.613785	169.005853	209.054102	247.440500	264.111111

Ready NUM

Figure 6.3. Input and output display examples of the Excel Visual Basic for Applications (VBA) simulation of the Schmidt Plot.

Thermal property contrasts between dyke and host rocks affect the maximum temperature achieved in the host rocks, but their influence is not very great (Delaney 1987). Thermal penetration to the dyke centre will be slower, and the time that the dyke contact remains at its initial temperature will be longer, if $k_{\text{magma}} < k_{\text{host}}$ and $\kappa_{\text{magma}} < \kappa_{\text{host}}$. However, thermal conductivity (k) measurements made as part of this study, on a BGSN shale sample, a BGSN limestone sample and a sample of the dyke produced values of a similar order of magnitude for these three lithologies (Section 6.4.1). This similarity justifies the use in the model of a single κ value for both magma and host rock.

The effect of temperature on thermal conductivity and diffusivity is ambiguous (Midttomme and Roaldset 1999). Temperature is known to affect thermal conductivity, but how and to what degree is still uncertain, as both increases (Morin and Silva 1984; Gilliam and Morgan 1987; Barker *et al.* 1998; Fenster *et al.* 1999) and decreases (Delaney 1987; Brigaud *et al.* 1990; Demongodin *et al.* 1991) have been reported. The thermal conductivity of water increases with increasing temperature, whereas the thermal conductivities of most minerals decrease with increasing temperature. The thermal conductivity of water-saturated rocks can therefore vary widely, depending on the proportion of water to mineral matrix (Midttomme and Roaldset 1999). Within the temperature interval of 300° to 700°C, thermal conductivity varies little with temperature or composition (Furlong *et al.* 1991). Therefore, although thermal property contrasts affect cooling rates early in the cooling history, they subsequently have less influence upon cooling rate (Delaney 1987). Barker *et al.* (1998) conducted thermal conductivity measurements on a gabbro dyke and adjacent host sandstone, at sample temperatures of 20° to 150°C, and constant pressure conditions. They found good agreement of thermal conductivity in both dyke and host rock, and observed a convergence to a similar value with increasing temperature. Given the uncertainties in the behaviour of thermal conductivity (and diffusivity) of rocks with varying temperature, a single fixed value for the model is justified.

The Schmidt model does not consider heat transfer by convection. Early in the cooling history of dykes, thermal expansion of groundwater in the host sediments can generate substantial increases in pore pressure. However, groundwater flow arising from pore-

pressure gradients does not carry an appreciable quantity of heat, and therefore has a minor influence on temperatures (Delaney 1982; Delaney 1987). Hydrothermal circulation of groundwater may be an important process during the cooling of large igneous bodies intruded into permeable host rocks, although results indicate that most dykes cool too quickly for circulation to become established (Delaney 1982; Delaney 1987). The 1.3m thick dyke in this study is unlikely to have remained sufficiently hot to establish a convection cell. The host sediments in Berreraig Bay are fine-grained and were fully lithified at the time of dyke intrusion. There is no obvious vein development adjacent to the intrusion, which suggests that fluid flow in this area during cooling was minimal.

A potentially important secondary heat source that must be addressed is the latent heat of crystallization, released from the solidified magma (Jaeger 1959; Delaney and Pollard 1982; Delaney 1987). When heat of crystallization is released, cooling rates can be three times slower than when this heat is not released (Delaney 1987). Dykes with thickness in excess of 10m often display crystalline textures, and the influence of latent heat is important, greatly increasing the time required for cooling to begin at the dyke centre. In contrast, most dykes with 1 to 2m thicknesses have dominantly glassy textures, and so thermal energy derived from crystallization is minor (Delaney 1987). The Schmidt model does not account for latent heat of crystallization, however as the Berreraig Bay dyke is only 1.3m thick, with a glassy texture, this is not considered to have been an important factor during its cooling history.

6.4 BOUNDARY CONDITIONS

The Schmidt temperature calculation is performed for each node in a finite array representing the distance elements in the direction of heat transfer (in this case the north side of the dyke centre). In order that the Schmidt method function correctly, it is necessary to impose certain boundary conditions at the first and last nodes in the array. The first node $i = 0$, represents the centre of the dyke. In order to maintain symmetry on either side of the dyke centre, the following condition is imposed at this node:

$$T_{i-1} = T_{i+1}$$

so that the temperature of the node immediately left of the dyke centre will be equal to the temperature immediately right of the dyke centre.

In real geological situations, the heat from the intrusion would be infinitely dissipated away into the country rocks. To simulate this infinite heat sink, the following condition is imposed at the last node in the array, n :

$$T_{n+1} = T_{\text{host}}$$

so that the node beyond the final node in the array is held at the initial host rock temperature. Greater accuracy can be achieved by using the maximum number distance steps, $\Delta x = x/n$, over which to apply the Schmidt calculation, whilst still maintaining a time step $\Delta \tau$ that permits the calculations to proceed over a realistic computation time.

6.5 ASSESSMENT OF THERMAL PARAMETERS

6.5.1 THERMAL DIFFUSIVITY

The Schmidt model employs *thermal diffusivity*, κ ($\text{m}\cdot\text{s}^{-1}$), as the thermal property controlling the rate of heat dissipation through the rock mass. It is a function of the *thermal conductivity*, k , and the *volumetric heat capacity*, ρC , of the material ($\kappa = k/\rho C$). A single averaged thermal diffusivity of $9.52 \times 10^{-7} \text{ m}\cdot\text{s}^{-1}$ was used in the model for both dyke and host rocks, based on both experimental data and published values.

6.5.1.1 THERMAL CONDUCTIVITY

Thermal conductivity measurement of each of the sampled lithologies from the Berreraig locality was attempted as part of this study. There is no standard method for measuring the thermal conductivity of sedimentary rocks, and several steady-state and transient

techniques have been developed. A steady-state technique, known as the *divided-bar method*, was employed in this study for thermal conductivity measurement. By this method, the thermal conductivity of discs or cylindrical plugs of material is determined by Fourier's Law (Eq. 6.1), where there is a constant temperature gradient across the samples and the heat flow is stable. The apparatus and procedure followed are based on a method described by M. Kostic⁵ at <http://www.kostic.niu.edu/th-cond-lab.html>.

Apparatus

The divided-bar apparatus was created and assembled in conjunction with G. Clayton. A pair of brass cylinders was constructed according to the specifications shown in Figure 6.4. The 'collar' on 'cylinder 2' was fitted to a piece of copper piping, which in turn was attached to a cold water supply. 'Cylinder 1' was arranged with a flat, copper wire electrical heat source at one end. The entire apparatus was arranged vertically, with the sample placed across the temperature gradient between the 'hot' and 'cold' brass cylinders (Figure 6.4).

Procedure

1. The apparatus was set up as shown in Figure 6.4.
2. Cylindrical cores of rock sample, *ca.* 23mm in diameter, were cut using a water-cooled, diamond-coated core drill. The thickness and diameter of the sample cores was carefully measured using a micrometer.
3. The sample core was carefully placed between the 'hot' and 'cold' brass cylinders, ensuring a good contact between sample and the brass. This was achieved by grinding the sample to ensure a smooth and well-prepared surface that fitted evenly against the brass. A small retaining pressure was exerted by a spring above the 'cold' brass cylinder.
4. Before conducting each experiment, all temperature points were checked to ensure that the apparatus was in thermal equilibrium.
5. The cold water supply was opened to the 'cold' cylinder.
6. The heater to the 'hot' cylinder was switched on, so that the power supplied was about 15 W. An optimum heating power is required, so that the heat lost to the surroundings by radiation and convection is minimal.

⁵ Professor Milivoje M. Kostic, Department of Mechanical Engineering, Northern Illinois University.

7. A thermocouple junction was inserted into one of the narrow holes in the 'hot' cylinder, and monitored until a steady state was achieved, i.e., no further temperature change with time. This often took several hours to achieve.
8. Temperature readings were recorded from each of the six measurement points (1, 2, and 3 on the hot side, and 6, 7, and 8 on the cold side, see Figure 6.4). The temperatures at points 4 and 5 are calculated by curve fitting, and extrapolation of the temperature profiles of the 'hot' and 'cold' sections (Figures 6.5, 6.6 and 6.7).

For each sample, the sample disc was overturned and experiment was repeated to check for consistency. Thermal conductivity, k , was calculated using the equation:

$$A = D^2 \frac{\pi}{4} \quad (6.10)$$

where Q is the heat flux in W and T is temperature in °C. Δx (m), D (m) and A (m²) are the thickness, diameter and cross-sectional area of the sample disc respectively.

Sources of error

There are a number of possible sources of error involved in the experiment. These are difficult to quantify, however they are addressed here.

The most important source of error, which is always present and cannot be removed, is the contact resistance at the sample-equipment interfaces (Roy *et al.* 1981). This error can be substantial if the rocks are coarse grained and porous. The measured rock samples in this study are all fine grained with low porosities. In order to minimise this error, the rock sample discs were ground down to a flat surface using water-wet silicon carbide paper of 320 and 1200 grade respectively. The contact ends of the brass cylinders were also smoothed and polished.

By calculating the thermal conductivity in this way, it is assumed that heat conduction along the apparatus is 100% efficient, with no loss of heat through the sides of the brass cylinders or sample. It is thermodynamically impossible to achieve zero side loss, but loss can be minimised with insulation (Beardsmore and Cull 2001). In this study, a commercial foam insulating material for water pipes was used to insulate the apparatus.

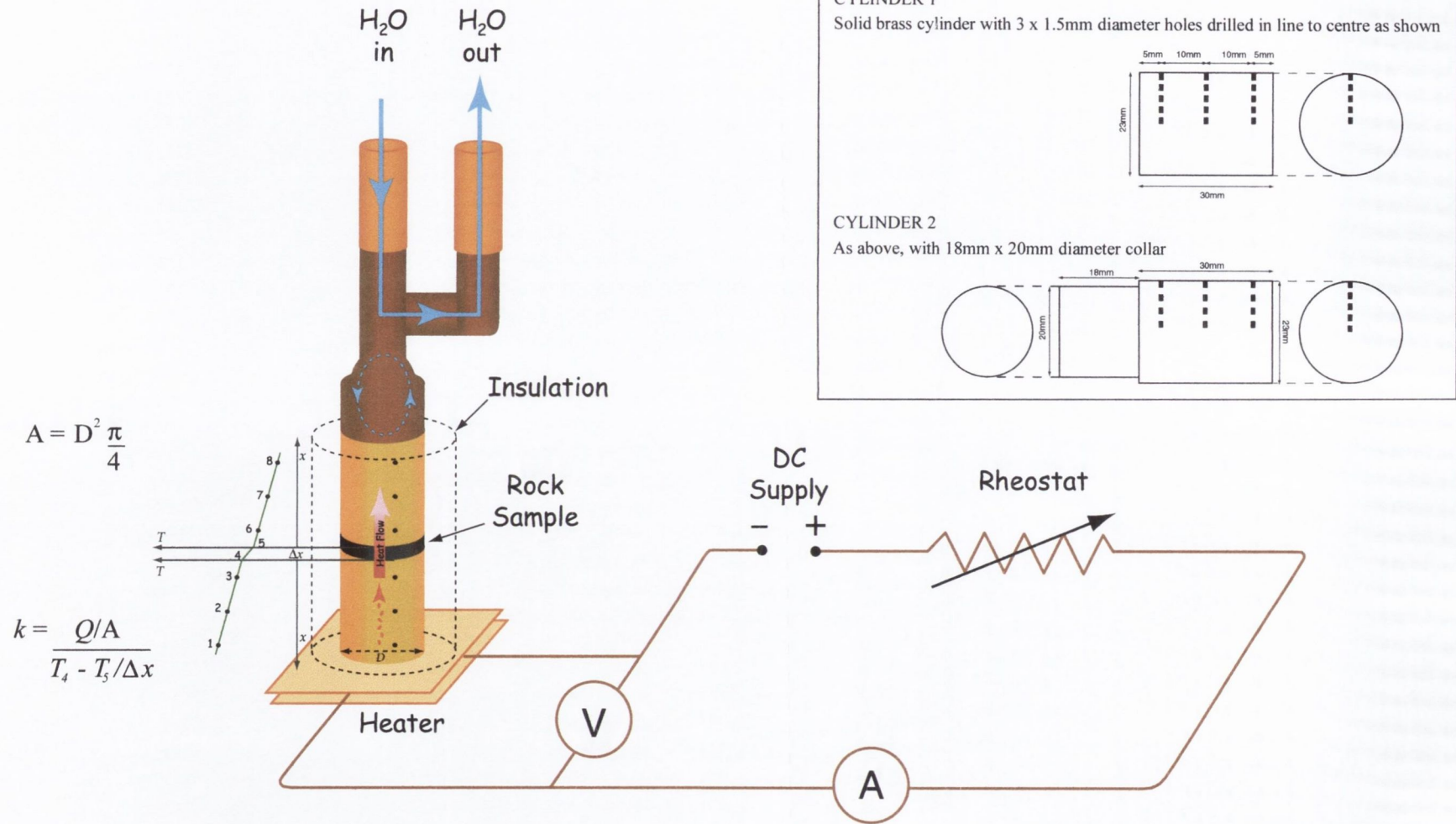
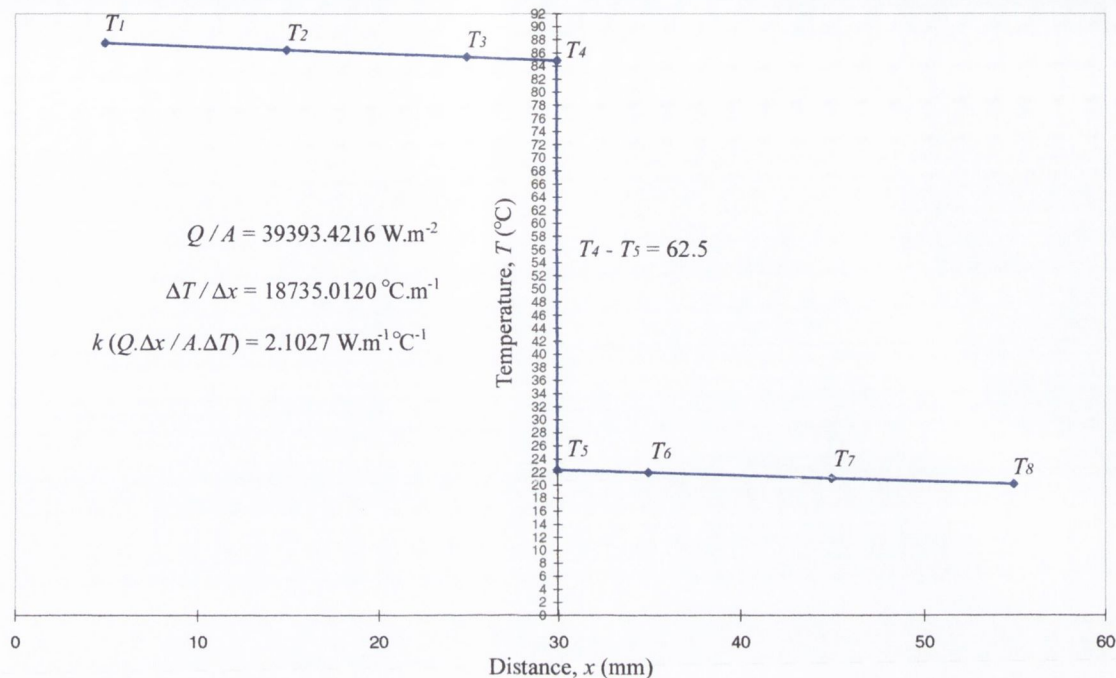


Figure 6.4. Apparatus used in this study for determination of thermal conductivity of rock. Inset: dimensions of solid brass cylinders used as part of the apparatus for the thermal conductivity experiments.

BBD01^a



BBD01^b

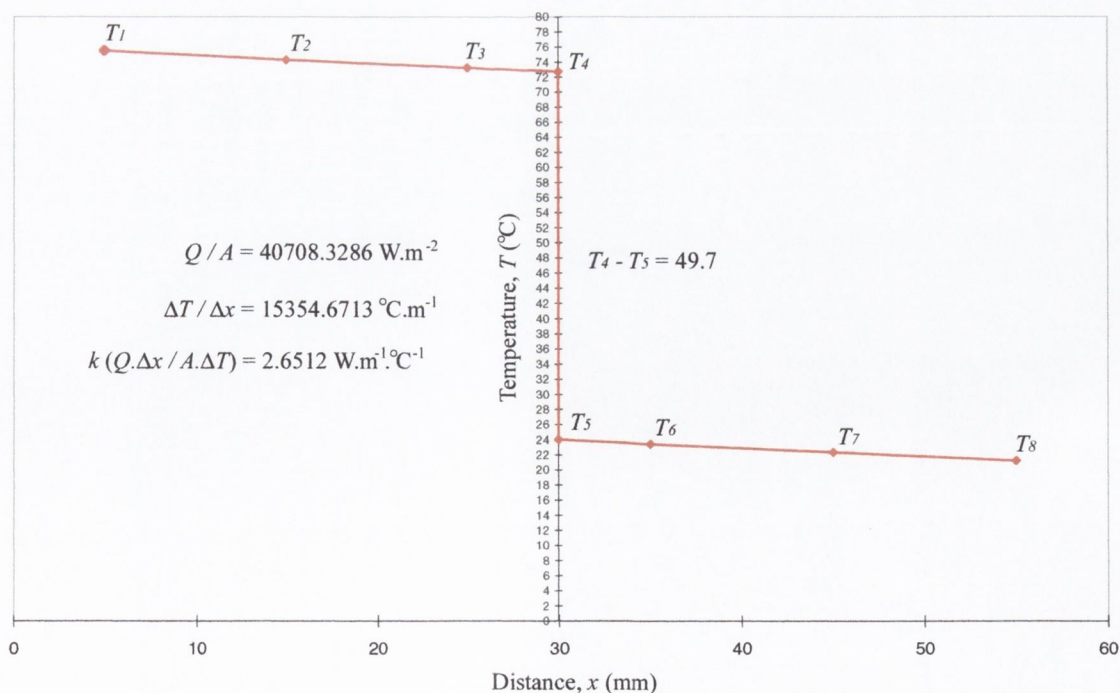


Figure 6.5(a) Thermal conductivity measurement: plots showing temperature gradients across the dyke lithology sample (BBD01).

BBD01^c

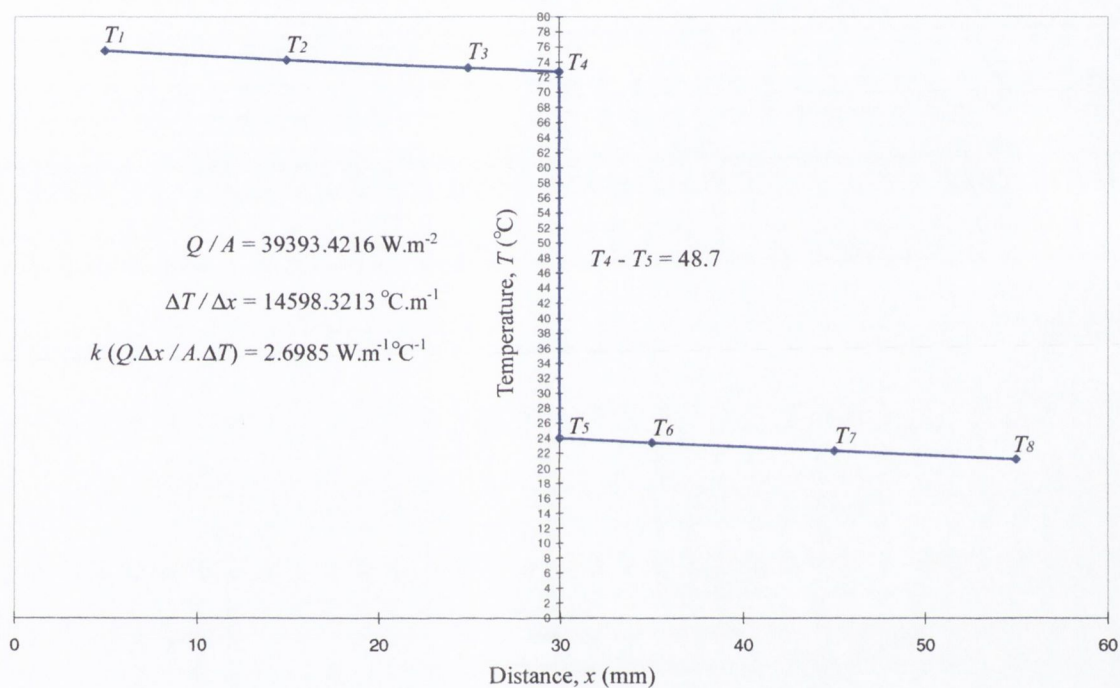
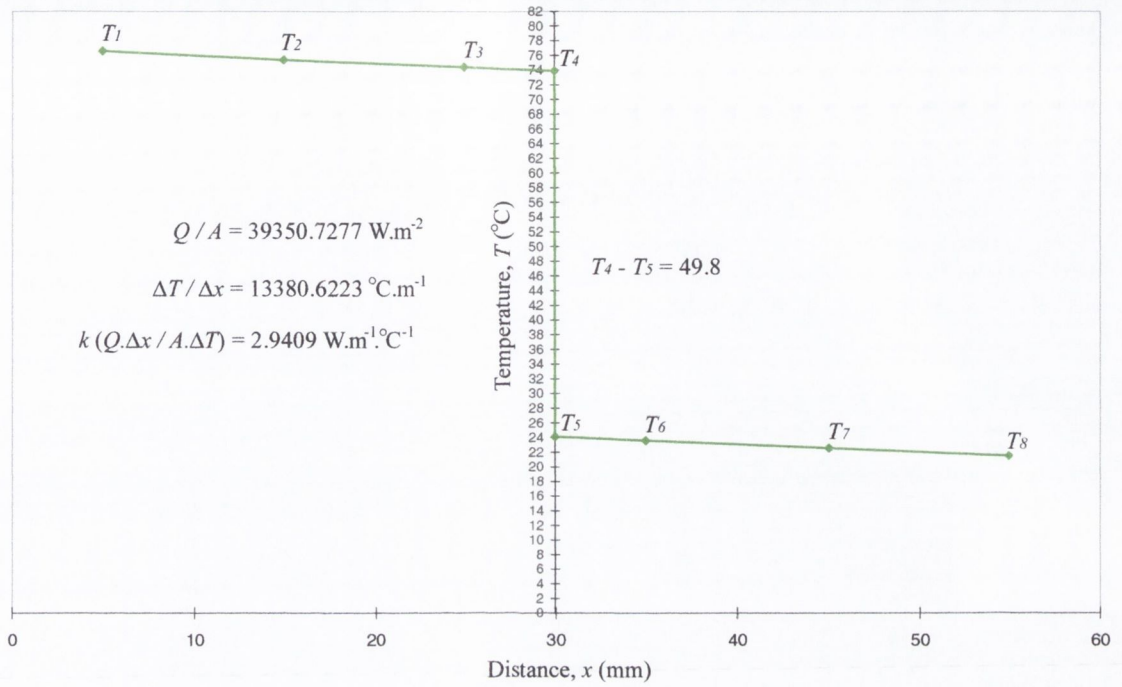


Figure 6.5(b) Thermal conductivity measurement: plot showing temperature gradient across the dyke lithology sample (BBD01).

BGSH02N^a



BGSH02N^b

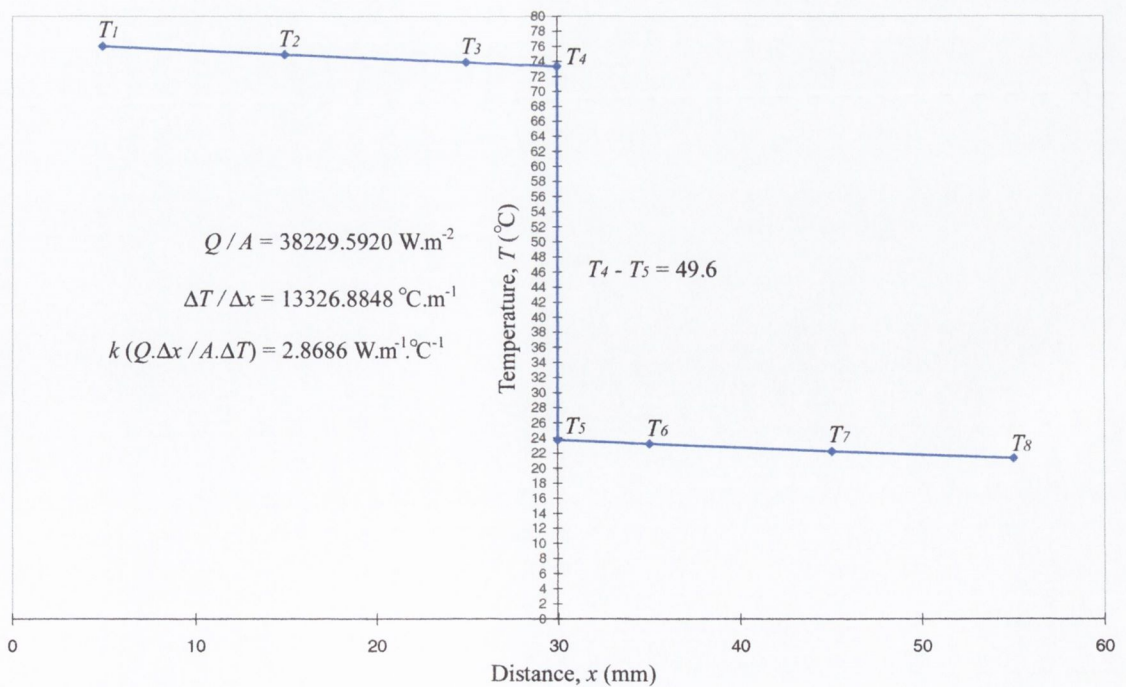
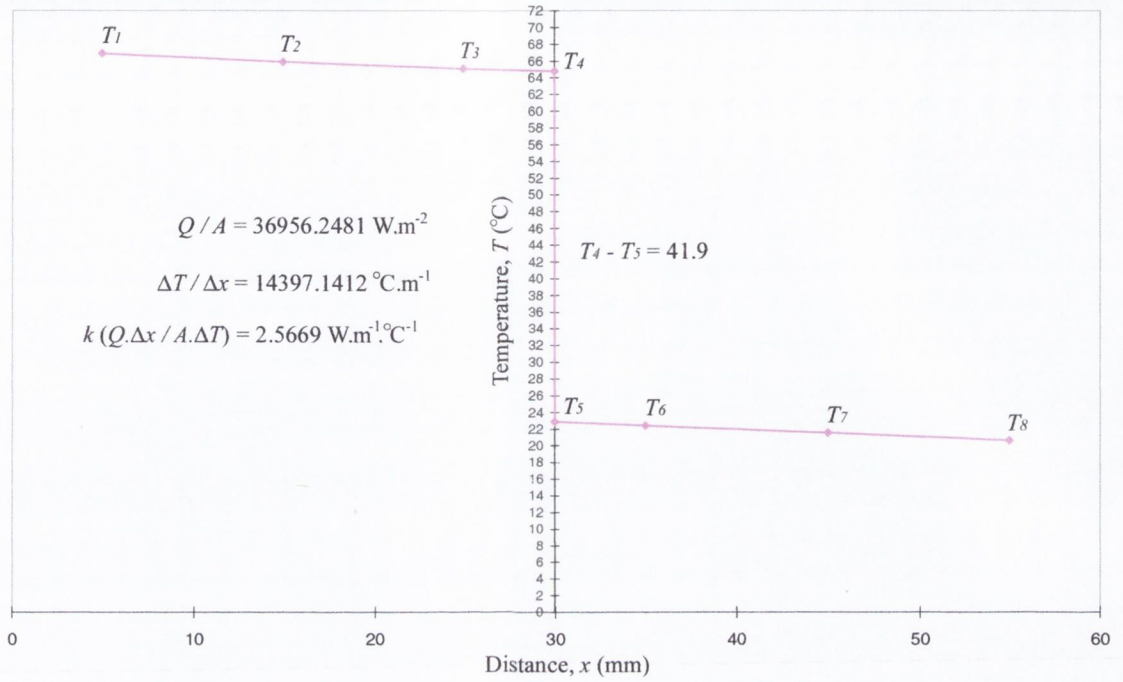


Figure 6.6. Thermal conductivity measurement: plots showing temperature gradients across a sample of the BGSHN shale lithology (BGSH02N).

BGS04N^a



BGS04N^b

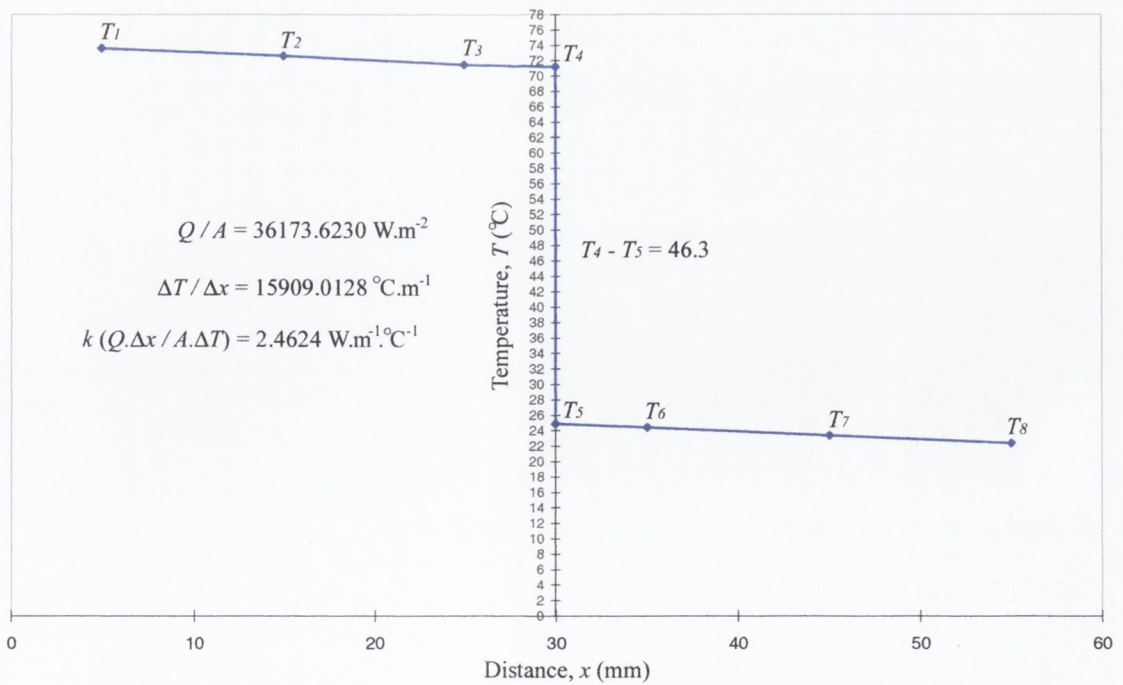


Figure 6.7. Thermal conductivity measurement: plots showing temperature gradients across a sample of the BGSN sandy limestone lithology (BGS04N).

A further potential error source involves the selection a representative sample for measurement. Due to the fragile nature of the shale samples, it was necessary on one occasion, to select a more competent sample close to the intrusion. It is not known how the measured k value for this sample would differ from one for a more distal sample. Finally, the accuracy of any apparatus largely depends on that of its various component parts. Potential error sources exist in the readings given by the ammeter and voltmeter (approximately $I \pm 0.1A$ and $V \pm 0.1V$).

Results

Problems were encountered during the coring of the shale samples, as these had a tendency to break up with the vibrations caused by the drill. For this reason, coupled with a paucity of suitably sized sample material for further coring attempts, no k values were obtained for the BBN lithology. However, results were successfully measured for both of the remaining host lithologies, and a sample of the dyke. The results are summarised in Table 6.1, and detailed in Appendix VII.

Sample	Lithology	k ($W.m^{-1}.^{\circ}C^{-1}$)
BBD01 ^a	Basalt	2.1027
BBD01 ^b	Basalt	2.6985
BBD01 ^c	Basalt	2.6515
BGSH02N ^a	Shale	2.9409
BGSH02N ^b	Shale	2.8686
BGS04N ^a	Sandy limestone	2.5669
BGS04N ^b	Sandy limestone	2.4624

Table 6.1 Measured thermal conductivity values of rocks from Bearreraig Bay.

The measured k values from this study fall within the range of published k values for these lithologies (Figure 6.8). The measured k values for the BGSHN shale lithology fall towards the upper end of the published range of k values for shale. Furthermore, the shale sample yielded the highest k value of the lithologies measured. This may be a consequence of the proximal position of the measured sample relative to the intrusion. After a number of failed attempts at coring the more fragile distal samples, the measured sample was chosen on the basis of its greater competency resulting from its close proximity to the dyke.

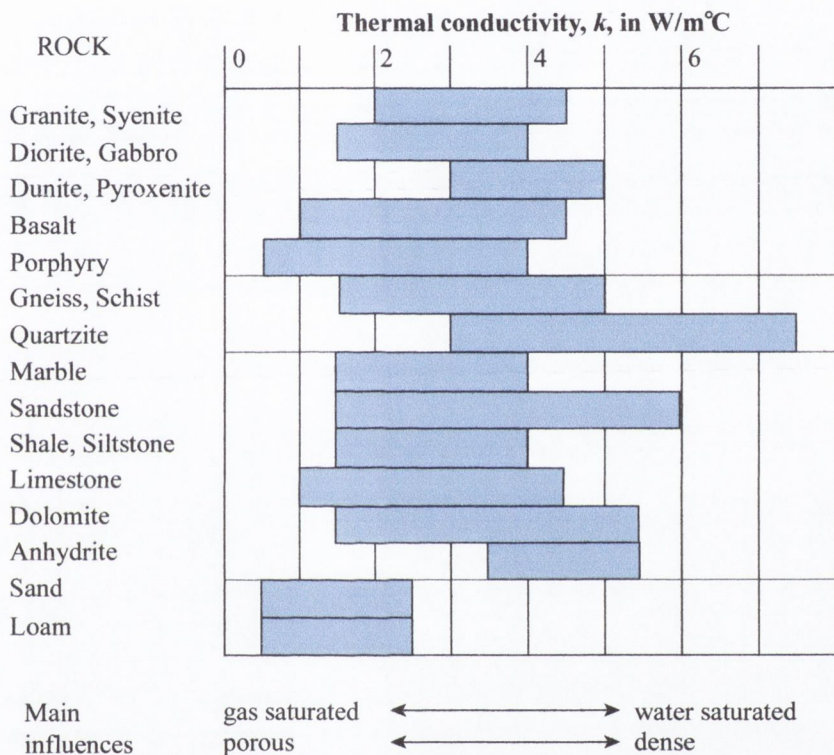


Figure 6.8. Mean range of thermal conductivity for abundant rock types (after Schön 1996).

It is not known how the measured value would compare with one obtained from a 'background' shale sample.

An average bulk thermal conductivity of $2.6 \text{ W.m}^{-1}.\text{°C}^{-1}$ was used to calculate the bulk thermal diffusivity of the dyke and host rocks. As the thermal diffusivity of a material is directly proportional to its thermal conductivity, the good agreement of measured k values for dyke and host lithologies (Table 6.1) validates a major simplifying assumption of a single κ value in the model.

6.5.1.2 VOLUMETRIC HEAT CAPACITY

Thermal diffusivity, κ , is related to thermal conductivity, k , by the volumetric heat capacity. The volumetric heat capacity of a material is the product of its heat capacity C and its bulk density ρ . Volumetric heat capacity values for both dyke and host rocks were obtained from published data.

Typical basalt has a density between 2950 and 3000 kg.m^{-3} (Hanley *et al.* 1978; Barker *et al.* 1998; Turcotte and Schubert 2002). Measured values for shales range between 2100 – 2700 kg.m^{-3} (Turcotte and Schubert 2002). Published densities for limestone are similar: 2320 kg.m^{-3} (Hanley *et al.* 1978) and 1600 – 2700 kg.m^{-3} (Turcotte and Schubert 2002). Based on these data, a single averaged bulk density of 2675 kg.m^{-3} was used in the model for the both dyke and host rocks. Published heat capacity values for rocks are more variable. Based on published experimentally determined averages for shale ($1180 \text{ J.kg}^{-1}\text{°C}^{-1}$ (Cermak and Rybach 1982), limestone ($933 \text{ J.kg}^{-1}\text{°C}^{-1}$ (Cermak and Rybach 1982)) and basalt (880 - $890 \text{ J.kg}^{-1}\text{°C}^{-1}$ (Cermak and Rybach 1982); $840 \text{ J.kg}^{-1}\text{°C}^{-1}$ (Connor *et al.* 1997)), a single averaged heat capacity of $1020 \text{ J.kg}^{-1}\text{°C}^{-1}$ was used in the model for the both dyke and host rocks.

From the averaged values of ρ and C , a single bulk volumetric heat capacity of $2.73 \times 10^6 \text{ J.m}^{-3}\text{°C}^{-1}$ was calculated and used, in conjunction with the thermal conductivity k to estimate a bulk thermal diffusivity for both dyke and host rocks.

6.5.2 MAGMA TEMPERATURE

Basalt is found to erupt at temperatures in the neighbourhood of 1100°C, although values as much as 100°C higher or lower have been reported (Hughes 1982). Delaney and Pollard (1982) suggest a magma temperature of 1200°C for basalts intruded into high crustal levels. Solidification of basalt takes place over a range of temperature, represented by the liquidus-solidus interval.

Petrological and geochemical analysis indicates that the studied dyke in Berreraig Bay is of the alkali basalt type common in the Skye Main Lava Series (SMLS) (Figures 1.13, 1.14 and 1.15). Estimates of magma temperature can be made based on the liquidus temperatures of model basalts. Thompson *et al.* (1972) conducted one-atmosphere experimental melting experiments on 21 basalt samples from Skye. The calculated silicate liquidus temperatures of these rocks were plotted against their iron/magnesium ratios (Figure 6.9) to reveal separate liquidus-iron enrichment trends reflecting two main differentiation trends in the Skye basalt lavas (to benmoreite and trachyte). Iron magnesium ratios of 0.71 and 0.74 (Table 6.2), calculated from two dyke samples from this study, indicate liquidus temperatures of between 1145° and 1190°C on the diagram of Thompson *et al.* (1972) (Figure 6.9).

6.5.3 HOST ROCK TEMPERATURE

The ambient temperature of the host rocks, T_{host} , at the time of dyke intrusion is estimated from thermal history reconstruction. Given the uncertainties of maximum burial depth estimates for these sediments and the complicated Early Tertiary thermal regime in the Skye area, T_{host} is difficult to assess accurately. In relation to hydrocarbon generation from Jurassic source rocks on the UK North Atlantic margin, the most important palaeothermal episodes occurred in the Early Cretaceous, Early Tertiary and mid to Late Tertiary (Green *et al.* 1999). Given that maximum burial depths of these sediments are unlikely to have exceeded 900m prior to Early Cretaceous exhumation (Morton 1987), those episodes that occurred during reburial beneath the extensive Palaeocene lava pile are likely to be of greater significance. Anderson and Dunham (1966) estimate that, prior to Late Tertiary and Pleistocene erosion, the total thickness of lavas in north Skye exceeded 1200m.

Wt. %	BBD01	BBD02
SiO ₂	45.91	44.86
Al ₂ O ₃	16.10	17.39
Fe ₂ O ₃	0.00	0.00
FeO	0.00	0.00
MgO	4.66	4.09
CaO	5.15	6.64
Na ₂ O	4.59	4.23
K ₂ O	0.64	0.65
TiO ₂	3.45	3.43
P ₂ O ₅	0.39	0.44
MnO	0.10	0.13
LOI	6.40	4.94
Total iron as Fe ₂ O ₃	12.39	12.95
Fe ₂ O ₃ /FeO ratio	0.20	0.20
TOTAL (with Fe ₂ O ₃ & FeO)	98.73	98.65
TOTAL (with total iron as Fe ₂ O ₃ (or FeO))	99.78	99.78

Normalised %	BBD01	BBD02
SiO ₂	49.72	47.87
Al ₂ O ₃	17.44	18.56
Fe ₂ O ₃	2.05	2.11
FeO	10.23	10.54
MgO	5.05	4.36
CaO	5.58	7.09
Na ₂ O	4.97	4.51
K ₂ O	0.69	0.69
TiO ₂	3.74	3.66
P ₂ O ₅	0.42	0.47
MnO	0.11	0.14
TOTAL	100.00	100.00
<u>FeO + Fe₂O₃</u>	0.71	0.74
FeO + Fe ₂ O ₃ + MgO		

Table 6.2. Geochemical analyses data for Bearreraig dyke samples. Normalised data calculated using PETRO.CALC.PLOT (Sidder 1994).

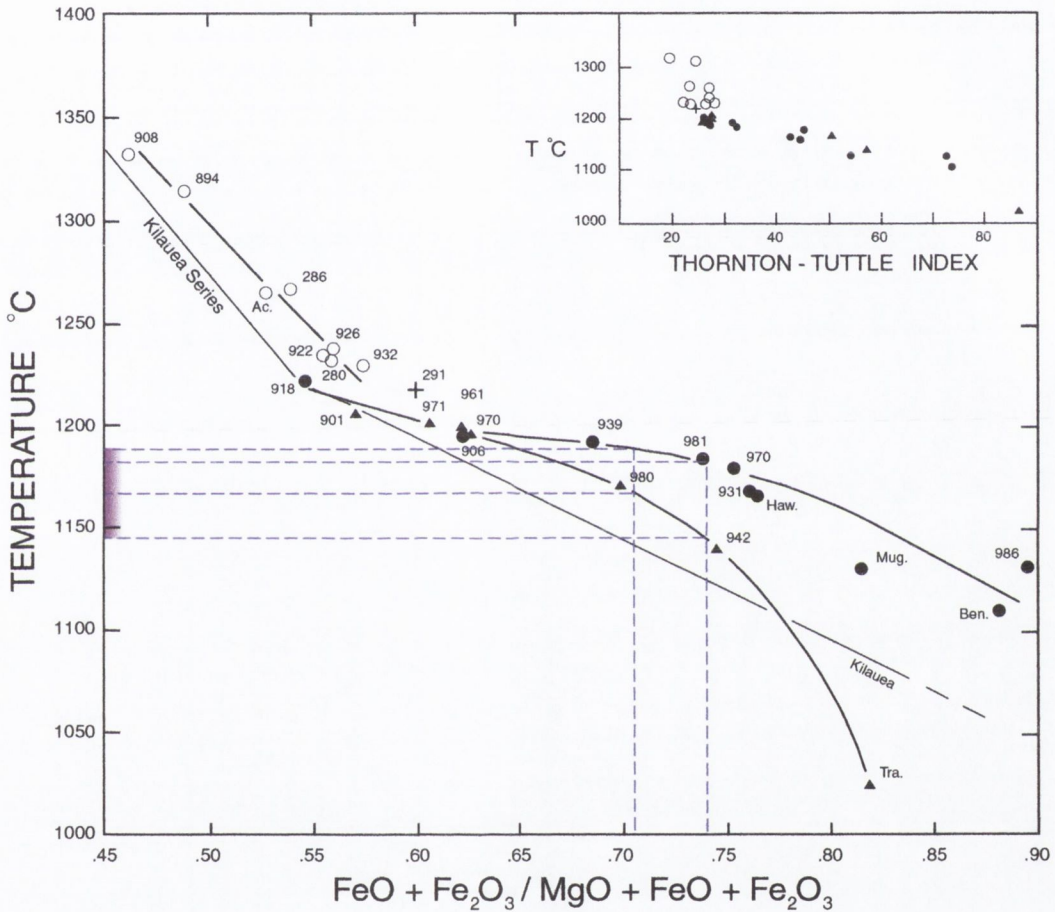


Figure 6.9. Silicate liquidus temperatures at 1 atm versus iron/magnesium ratios for selected Skye lavas. The dashed lines indicate the iron/magnesium ratios of two dyke samples from this study and their corresponding silicate liquidus temperature correlation on this diagram. Modified from Thompson *et al.* (1972).

In the Trotternish area, this cover consisted of the Beinn Totaig and Beinn Edra lava groups, forming a cumulative thickness of approximately 600m (Anderson and Dunham 1966; Morton 1987). Based on apatite fission track analysis (AFTA) and vitrinite reflectance data from an offshore well L134/5-1, in the Sea of the Hebrides Trough southwest of Skye, Green *et al.* (1999) estimate an upper limit of *ca.* 55°C.km⁻¹ for the Early Tertiary palaeogeothermal gradient at this site. Bearing in mind that dyke intrusion could have occurred at any stage during extrusion of the lava pile, a range of maximum burial temperatures are possible for these sediments at the instant of intrusion. Given that maximum burial depths for these sediments immediately prior to the onset of Palaeocene volcanism was approximately 620m (Morton 1987), and assuming an Early Tertiary palaeogeothermal gradient of 55°C.km⁻¹, minimum and maximum burial temperatures of 50° and 80°C respectively, are predicted for these sediments at the instant of dyke intrusion. Based on these figures, an averaged T_{host} of 65°C was used in the model for the host sediments at Bearreraig during the Early Tertiary.

6.5.4 MAGMA FLOW

Three stages of typical basaltic eruptions have been identified (Delaney and Pollard 1982). Eruptions commonly commence with the effusion of lava along the entire length of the eruptive fissure, forming a “curtain of fire”. After a period of what is usually measured in hours, the effusion begins to localise to a few vent areas. With continued activity at one or a few vent sites, a third phase of eruption is marked by the growth of cones or a parasitic shield. Using measured lava effusion rates and dyke thicknesses observed in exhumed volcanic rift zones, Delaney and Pollard (1982) showed that the decay of the curtain of fire is best explained by the inward growth of a solidified layer of magma. Even where latent heat effects are included, the temperature at the intrusive contact can be approximated by (Carslaw and Jaeger 1959):

$$T_{\text{contact}} = \frac{T_{\text{magma}} + T_{\text{host}}}{2} \tag{6.11}$$

For representative conditions of intrusion into high levels in the crust, $T_{\text{magma}} = 1200^{\circ}\text{C}$ and $T_{\text{host}} = 100^{\circ}\text{C}$, the contact temperature is about 500° to 600°C, well below the solidus

temperatures of basaltic magmas (Delaney and Pollard 1982). Inward growth of a 'solidification surface' of stagnant magma occurs rapidly, inhibiting the flow of less viscous magma towards the centre of the conduit (Delaney and Pollard 1982). The rate of growth of this layer is mainly controlled by dyke thickness, magma flow rate, distance from the source region, and temperature difference between magma and host rocks. Delaney and Pollard (1982) calculate that magmas flowing distances more than a few kilometers from an upper crustal source region, at typical initial velocities of $1\text{m}\cdot\text{s}^{-1}$ in dykes that are 2m thick solidify within a matter of hours.

The thickness of the studied dyke in Bearreraig Bay is only 1.3m. A narrow baked zone is evident in the mudrocks within *ca.* 18cm of the dyke. There is no evidence of internal chilled margins to suggest that multiple intrusions occurred within this conduit. It is therefore reasonable to assume that the magma solidified shortly after emplacement, probably within a matter of hours. In the model, a magma flow duration of 8 hours was used. During this period of time, the dyke is maintained at its initial intrusion temperature.

6.6 RESULTS OF HEAT FLOW MODELLING

6.6.1 TEMPERATURE DISTRIBUTION OVER TIME

Based on the thermal parameters listed in Table 6.3, the Schmidt Plot was used to model the temperature distribution in the rocks in the vicinity of the dyke over time (Figures 6.10 and 6.11). The model indicates that significant cooling of the dyke occurs within days and weeks of its emplacement. During the first 8 hours before emplacement/flow is complete, the temperature at the dyke-host rock contact rises from 628° to 1095°C . During this initial period, significant and rapid heat exchange occurs from the dyke to the host rocks immediately adjacent to it (cms). Temperatures immediately adjacent to the dyke margin achieve a maximum within hours of intrusion and fall rapidly thereafter. After 2 weeks the temperature at the centre of the dyke (529°C) has fallen below half of its initial intrusion temperature of 1190°C . At this stage, temperatures at the dyke margin are in the vicinity of *ca.* 500°C and the host rocks *ca.* 4m away are just beginning to experience a temperature increase above T_{host} .

Parameter	Method used to estimate value
Dyke width: 1.3m	Fixed by field measurement.
Magma flow duration: 8 hours	Mainly controlled by dyke thickness, magma flow rate, distance from the source region, and temperature difference between magma and host rocks. Delaney and Pollard (1982) estimate that, under standard upper crustal conditions, most dykes that are 2m thick solidify within a matter of hours.
Host rock temperature: 65°C	Averaged from geological and thermal history reconstruction: Under between 620 and 1200m of cover during the Early Tertiary, with an estimated maximum palaeogeothermal gradient of 55°C/km for this time (Green <i>et al.</i> 1999).
Magma temperature: 1190°C	1100±100°C for basaltic intrusions (Hughes 1982); 1200°C (Delaney and Pollard 1982). Iron magnesium ratios of 0.71 and 0.74, calculated from two dyke samples from this study, indicate liquidus temperatures of between 1145° and 1190°C on the diagram of Thompson <i>et al.</i> (1972).
Thermal conductivity: 2.6 W/m.°C	Assumed in the model to be equal in dyke and host rock. Averaged from measured values from the BGSN shale, BGSN sandy limestone and a dyke sample.
Heat capacity: 1020 J/kg.°C	Assumed in the model to be equal in dyke and host rock. Averaged from published experimentally determined averages: for shale (1180 J/kg.°C) and limestone (933 J/kg.°C) (Cermak and Rybach 1982), basalt 880 - 890 J/kg.°C (Cermak and Rybach 1982); 840 J/kg.°C (Connor <i>et al.</i> 1997).
Density: 2675 kg/m ³	Assumed in the model to be equal in dyke and host rock. Averaged from published values: typical basalt has a density between 2950 and 3000 kg/m ³ (Barker <i>et al.</i> 1998; Hanley <i>et al.</i> 1978; Turcotte and Schubert 2002). Measured values for shales range between 2100 - 2700 kg/m ³ (Turcotte and Schubert 2002). Published densities for limestone: 2320 kg/m ³ (Hanley <i>et al.</i> 1978) and 1600 - 2700 kg/m ³ (Turcotte and Schubert 2002).

Table 6.3. Thermal parameters used to model temperature distribution in the studied dyke and host rocks at Bearreraig, and methods used to estimate same.

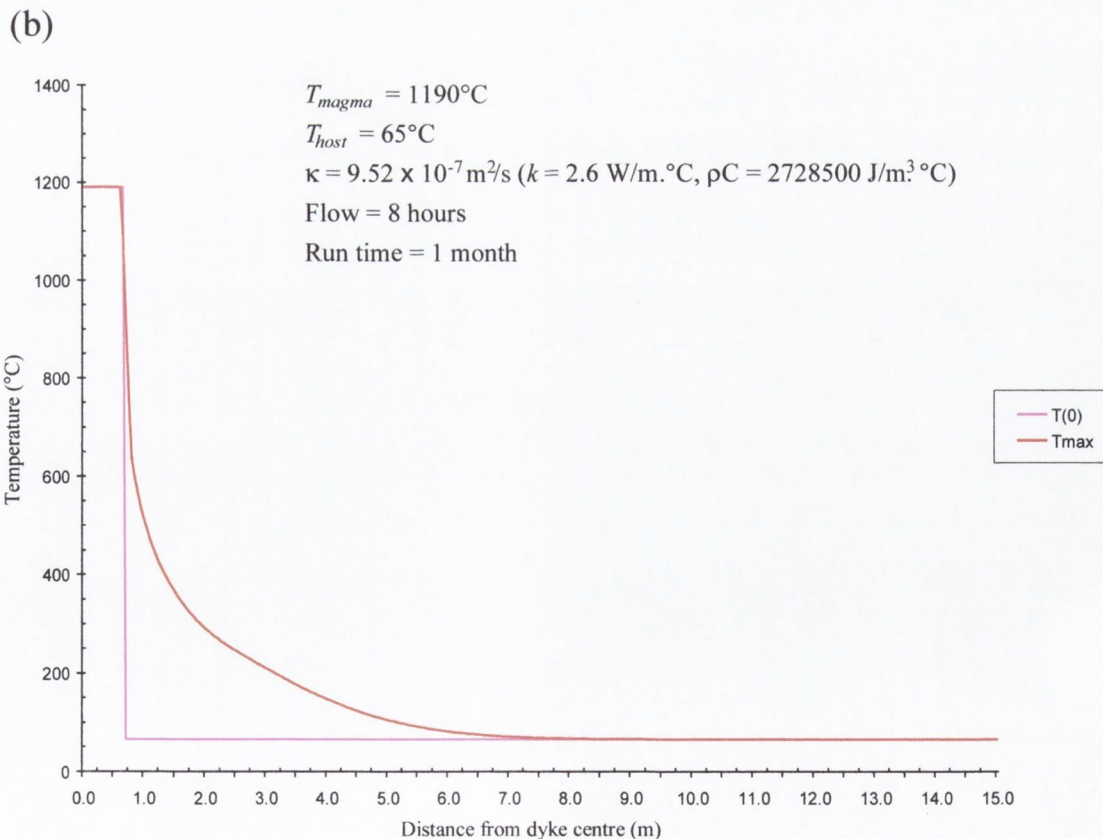
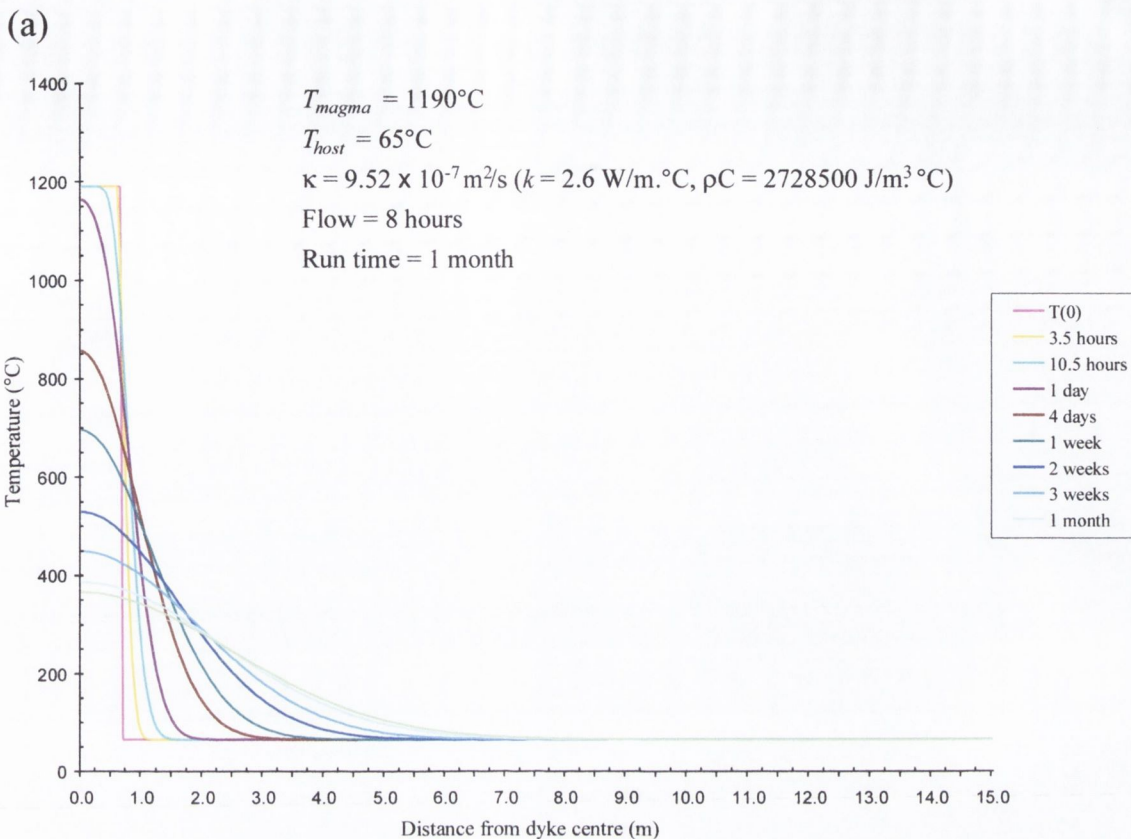


Figure 6.10 (a) Modelled temperature as a function of distance from the dyke centre and time for 1 month after emplacement of the 1.3m thick dyke at Bearreraig. (b) Modelled maximum temperature after 1 month as a function of distance from the dyke centre

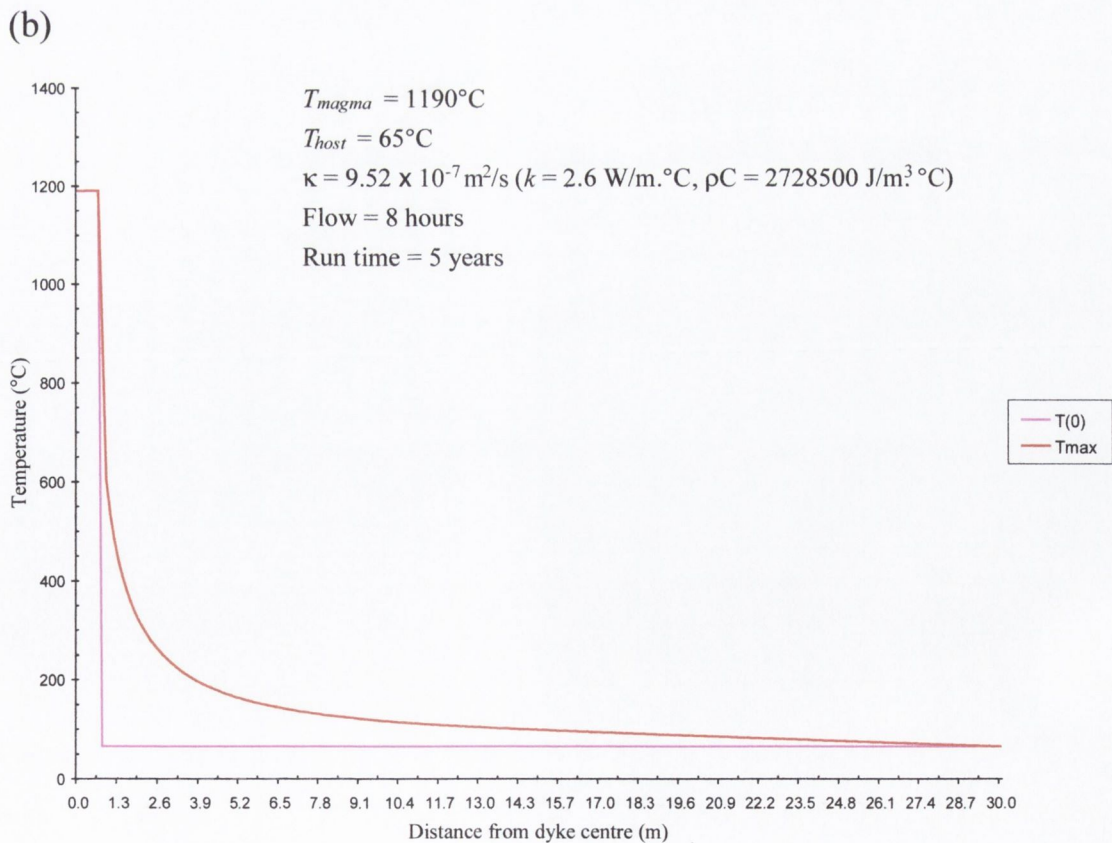
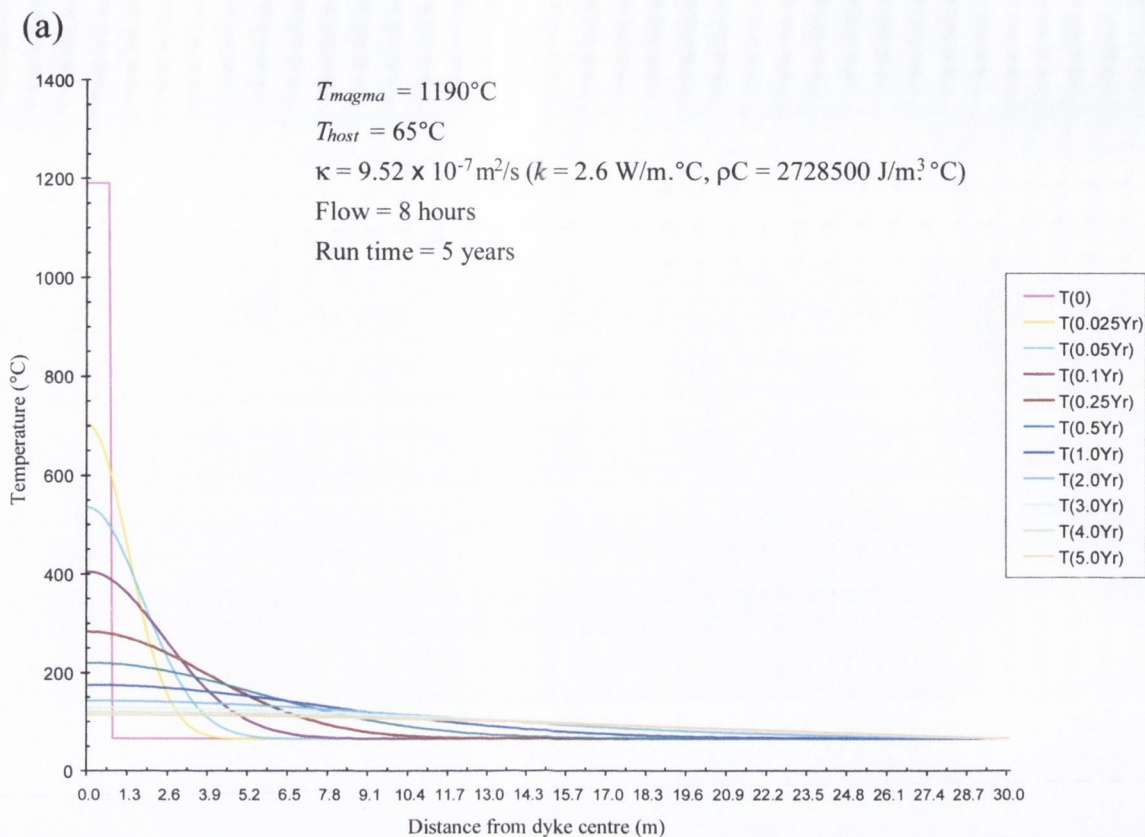


Figure 6.11 (a) Modelled temperature as a function of distance from the dyke centre and time for 5 years after emplacement of the 1.3m thick dyke at Berreraig. (b) Modelled maximum temperature after 5 years as a function of distance from the dyke centre.

After 1 month, temperatures at the dyke margin have fallen to *ca.* 400°C. At this time, temperatures *ca.* 6.5m from the dyke margin, the limit of the sample range, are only just beginning to rise above T_{host} (Figure 6.10b).

The rate of dyke cooling indicated by the model decreases markedly after 1 year, as the heat from the intrusion is dissipated further away into the host rocks. The temperature at the dyke contact decreases progressively from 174° through 142°, 128°, and 120° to 114°C, at times of 1 through to 5 years after intrusion respectively. The model predicts that a T_{max} of 135°C is achieved 6.7m from the dyke margin - the limit of the sample range - after just under 1 year and thereafter begins to cool slowly (Figure 6.11a).

6.6.2 SENSITIVITY OF SCHMIDT MODEL TO THERMAL PARAMETERS

In order to examine the effect of the various thermal input parameters on the maximum temperatures (T_{max}) reached in the host rocks, the model was run for various values of dyke thickness, magma flow duration, thermal conductivity, T_{magma} and T_{host} (Figures 6.12 to 6.16).

Although the thickness of the Berreraig Bay dyke is fixed by field measurement, the model was run for dykes of thickness 1, 2 and 3m to investigate the effect of this variable on the resultant maximum temperature profile. The results show that dyke thickness has a significant effect on the width of the contact aureole indicated by the model (Figure 6.12). The thickness of the dyke determines the amount of heat initially input into the system. The greater this body of heat, the longer the cooling time will be. Before heat flow modelling, accurate measurement of dyke thickness must be conducted in the field, and any variations in thickness along the length of the dyke should be accounted for.

With all other parameters fixed, the model was run for magma flow durations of 0, 6 and 36 hours. The results show that the duration of magma flow in the dyke can significantly affect the width of the aureole indicated by the model, increasing the maximum temperatures reached by the adjacent host rocks during the early stages of cooling (Figure 6.13).

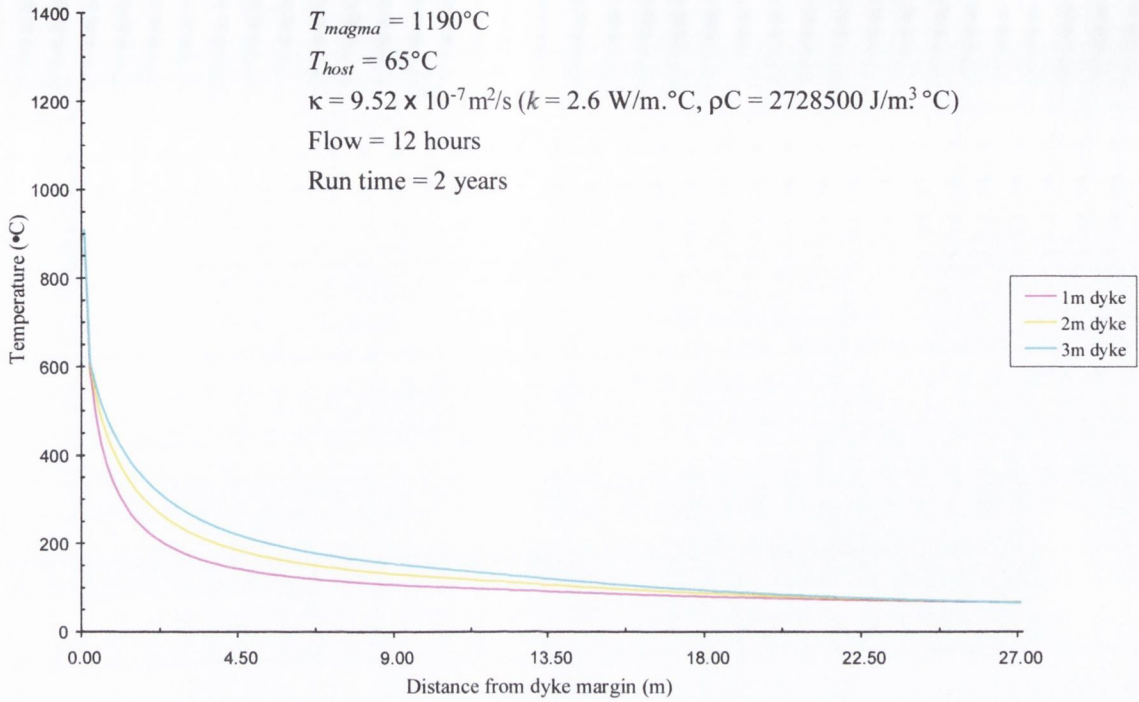


Figure 6.12. Variation of T_{max} with dyke thickness: maximum temperature (T_{max}) after 2 years as a function of distance from the dyke margin for different thickness of dyke.

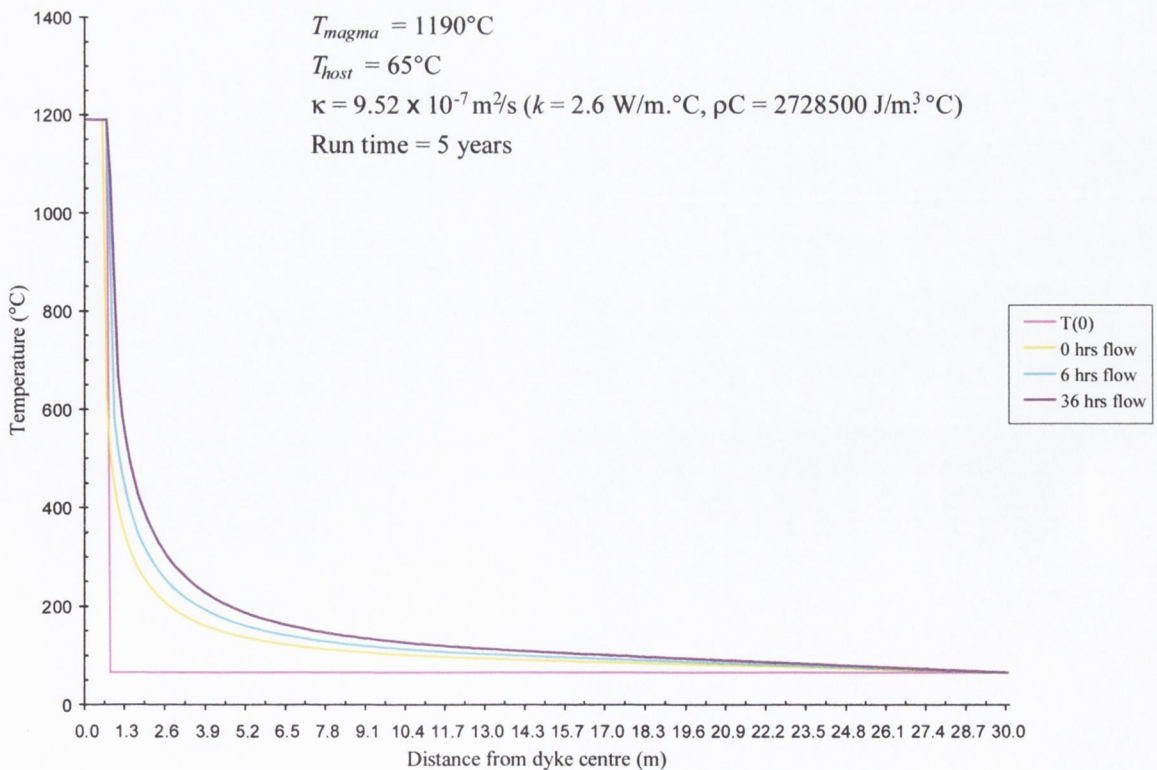


Figure 6.13. Variation of T_{max} with magma flow time: Maximum temperature (T_{max}) after 5 years as a function of distance from the centre of a 1.3m thick dyke for different durations of magma flow.

Like dyke thickness, magma flow duration controls the amount of heat input into the system, and together with dyke thickness, is one of the most important variables in the model. Several published mathematical cooling models exclude this variable and assume immediate arrest of magma flow upon emplacement (Delaney 1987; Delaney 1988; Peacock 1989, 1990). The results here show that this assumption may be a serious oversimplification, particularly for thicker dykes, where the duration of magma flow can be substantial. Unlike dyke thickness however, the duration of magma flow is a difficult parameter to quantify with much certainty. The factors controlling the duration of magma flow are discussed in Section 6.5.4. A flow duration of 8 hours was used in the model for the 1.3m thick dyke at Berreraig. However, due to the large uncertainty regarding this parameter, and the magnitude of its influence on the width of the aureole indicated by the model, it is perhaps wiser to run the model over a range of flow duration.

With all other parameters fixed, the model was run for different values of thermal conductivity, k (Figure 6.14). As a single averaged bulk thermal conductivity was used in the model for both dyke and host rocks, it is important to assess the influence of this variable on the resultant T_{max} output. Thermal conductivity, in conjunction with volumetric heat capacity, is used to calculate the thermal diffusivity ($\kappa = k/\rho C$), which in turn controls the magnitude of the time step, $\Delta\tau$ (Eq. 6.8). The greater the thermal conductivity/diffusivity, the smaller the time step, and the quicker the dyke cools. The effect of doubling the thermal conductivity is to halve the time step (and therefore the cooling time). The results indicate that the influence of thermal conductivity on T_{max} is greatest during the early stages of cooling, but it subsequently has less influence (Figure 6.14). The effect of increasing the value of k is to increase T_{max} , however compared to the effect of magma flow duration, its influence is relatively minor.

k (W/m.°C)	ρC (J/m ³ .°C)	κ (m ² /s)	Δx (m) [n = 300]	$\Delta\tau$ (s)
1.2	2728500	4.39×10^{-7}	0.05	2847.38041
3.0	2728500	1.10×10^{-6}	0.05	1137.39763
5.0	2728500	1.83×10^{-6}	0.05	682.314412

Table 6.4 Effect of thermal conductivity on cooling rate.

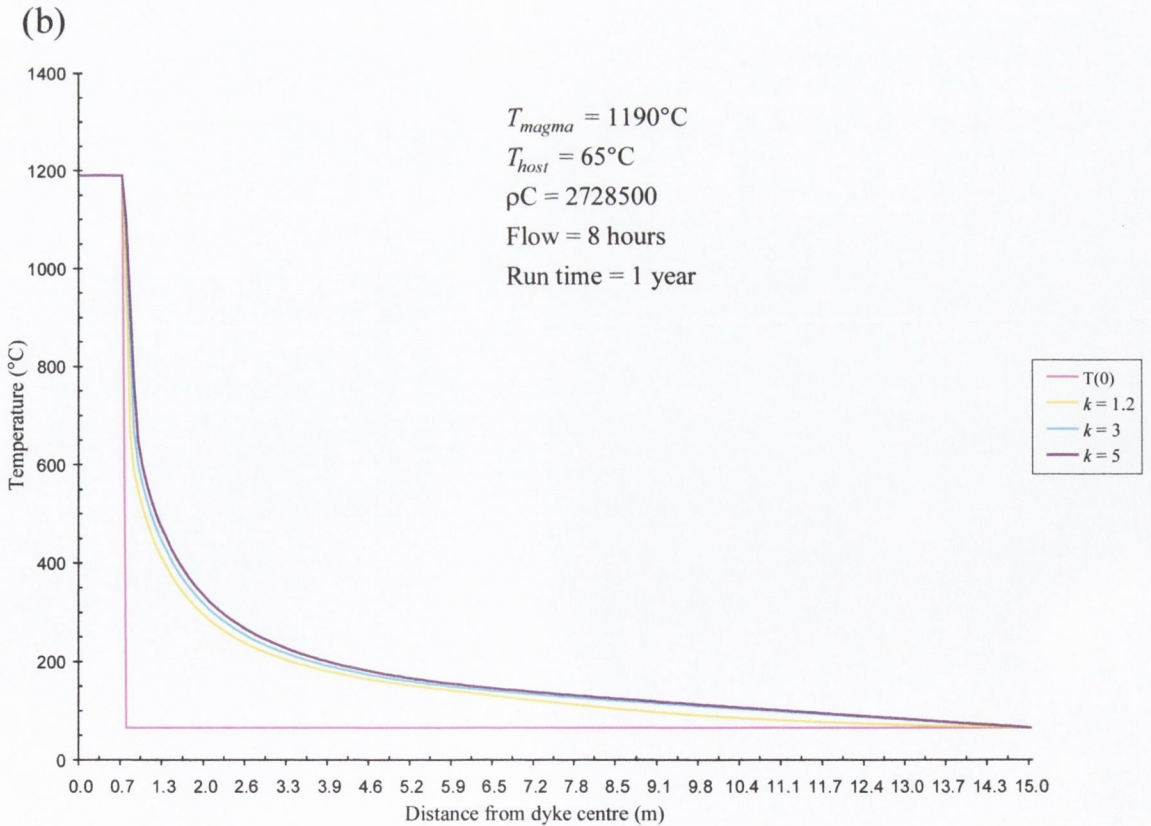
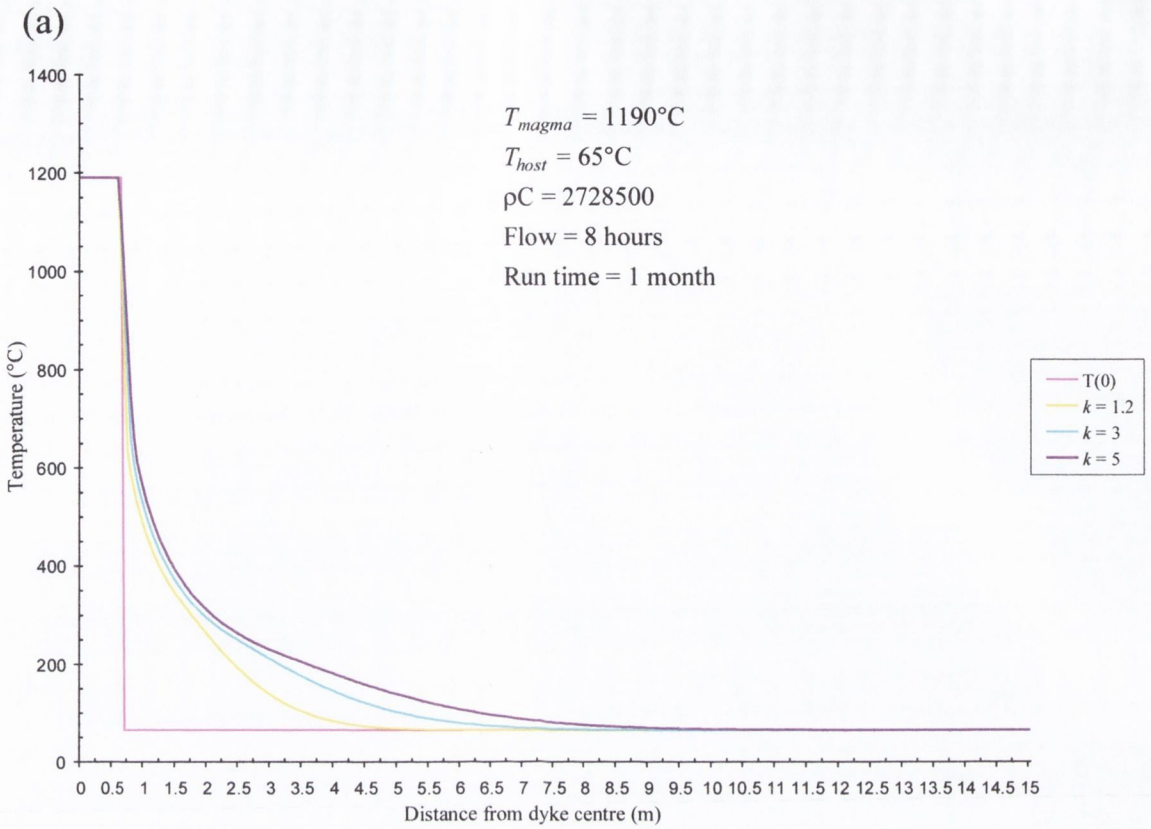


Figure 6.14. Variation of T_{max} with thermal conductivity, k . (a) Maximum temperature (T_{max}) after 1 month as a function of distance from the centre of a 1.3m thick dyke for 3 different k values. (b) Maximum temperature after 1 year as a function of distance from the centre of a 1.3m thick dyke for the same k values.

With all of the other parameters fixed, the model was run for different values of T_{host} and T_{magma} (Figures 6.15 and 6.16). T_{magma} sets the maximum temperature value for those nodes representing the dyke. Increasing T_{magma} has the effect of increasing the initial T_{contact} , and therefore T_{max} in the host rocks (Figure 6.16). T_{contact} will increase for the duration of magma flow, increasing the width of the T_{max} profile indicated by the model (Figure 6.16, Table 6.5).

T_{magma} (°C)	Initial T_{contact} (°C)	T_{contact} - 8 hrs flow (°C)
1000	532.5	921.4
1250	657.5	1150.4

Table 6.5 Variation of T_{contact} with T_{magma} and duration of magma flow.

The initial temperature of those nodes representing the host rocks over the length of section, X, are set by T_{host} . The lower the value of T_{host} , the less time the dyke will take to cool. Like T_{magma} , T_{host} controls the initial T_{contact} in the model, and affects the width of the resultant T_{max} profile (Figure 6.15). However, as the duration of magma flow only controls T_{magma} and is independent of T_{host} , the effect of T_{host} on T_{max} values in the host rocks close to the dyke is comparatively minor. Its effect is more significant on T_{max} values at more distal positions from the dyke.

6.6.3 RANGE OF T_{max} IN HOST ROCKS

In light of the significant effects of small variations in some of the model parameters (particularly the duration of magma flow) on T_{max} of the host rocks, the model was run using a realistic *range* of values for each parameter. The objective of this approach was to find a range of T_{max} , delimited by an ‘upper’ and ‘lower’ T_{max} profile. The range of thermal parameters used for this approach is detailed in Table 6.6. The model results define an appreciable band representing the possible range of T_{max} in the host sediments adjacent to the 1.3m dyke at Berreraig (Figure 6.17). This numerically modelled band of T_{max} is compared to the T_{max} profile derived from measured vitrinite reflectance values in Chapter 7.

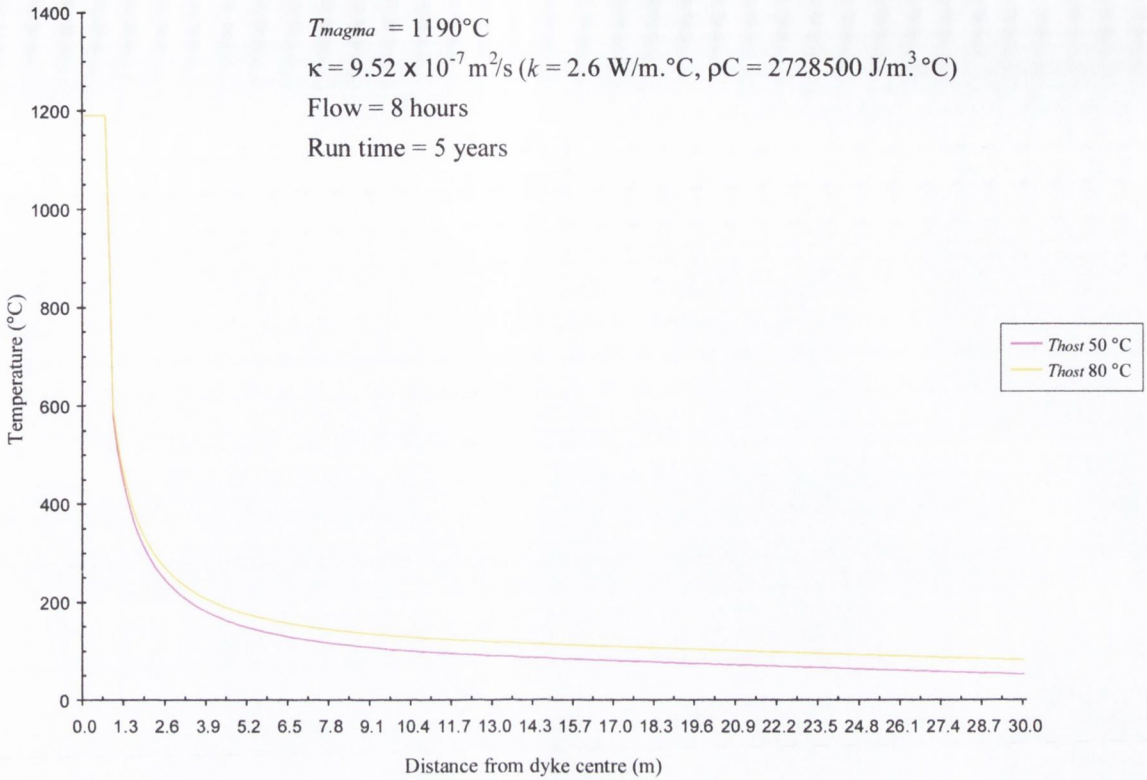


Figure 6.15 Variation of T_{max} with T_{host} . Maximum temperature (T_{max}) after 5 years as a function of distance from the centre of a 1.3m thick dyke for different initial host rock temperatures (T_{host}).

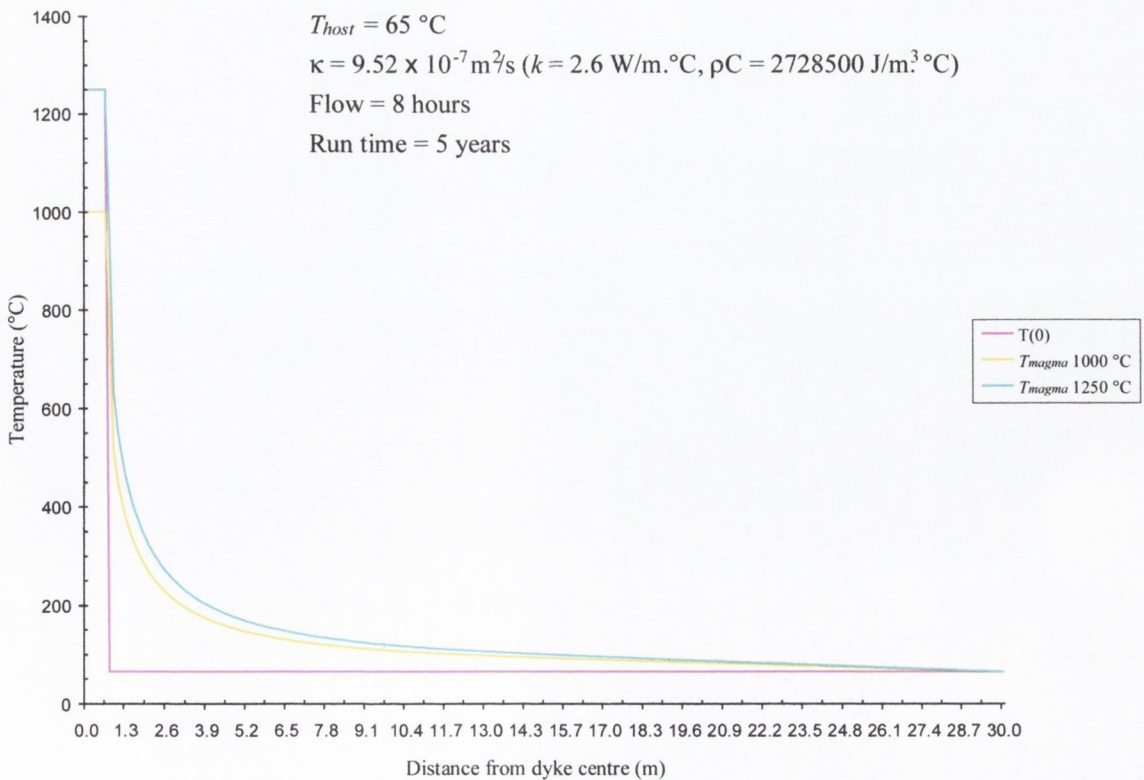


Figure 6.16. Variation of T_{max} with T_{magma} . Maximum temperature (T_{max}) after 5 years as a function of distance from the centre of a 1.3m thick dyke for different initial magma temperatures (T_{magma}).

Parameter	Model sensitivity to value	Comments
Dyke width: 1.3m	Determines the amount of heat initially input into the system. A key factor in determining the width of the contact aureole indicated by the model.	Fixed by field measurement.
Magma flow duration: 6 - 36 hours	Holds the dyke at its initial intrusion temperature for the specified period, increasing T_{max} reached by the host rocks during the early stages of cooling. A major factor in determining the width of the contact aureole indicated by the model.	Under standard upper crustal conditions, most dykes that are 2m thick solidify within a matter of hours. The 1.3m dyke at Berreraig is unlikely to have flowed for longer than a day and a half.
Host rock temperature: 50 - 80°C	T_{host} controls the initial $T_{contact}$ in the model, and affects the width of the resultant T_{max} profile. Its effect is more significant on T_{max} values at more distal positions outside the dyke.	Estimated from thermal and geological history reconstruction: 620 to 1200m of Early Tertiary cover with a palaeogeothermal gradient of 55°C/km.
Magma temperature: 1000 - 1250°C	Increasing T_{magma} has the effect of increasing the initial $T_{contact}$, and therefore T_{max} in the host rocks. $T_{contact}$ will increase for the duration of magma flow, increasing the width of the T_{max} profile indicated by the model	Typical range of basaltic magma temperature intruded into upper crustal levels.
Thermal diffusivity: 4.39×10^{-7} to 1.47×10^{-6} (m^2/s)	The greater the thermal conductivity/diffusivity, the smaller the time step, and the quicker the dyke takes to cool. Influence on T_{max} is greatest during the early stages of cooling, but subsequently has less influence	Calculated using a range of k from 1.2 to 4.0 W/m.°C, with a volumetric heat capacity of 2728500 J/m ³ .°C.

Table 6.6. Thermal parameters used to model the range of T_{max} for the Berreraig Bay dyke and host

Low temperature scenario

$T_{magma} = 1000^{\circ}\text{C}$
 $T_{host} = 50^{\circ}\text{C}$
 $\kappa = 4.39 \times 10^{-7} \text{ m}^2/\text{s}$ ($k = 1.2 \text{ W/m}\cdot^{\circ}\text{C}$, $\rho C = 2728500 \text{ J/m}^3 \cdot^{\circ}\text{C}$)
 Flow = 6 hours
 Run time = 5 years

High temperature scenario

$T_{magma} = 1250^{\circ}\text{C}$
 $T_{host} = 80^{\circ}\text{C}$
 $\kappa = 1.47 \times 10^{-6} \text{ m}^2/\text{s}$ ($k = 4.0 \text{ W/m}\cdot^{\circ}\text{C}$, $\rho C = 2728500 \text{ J/m}^3 \cdot^{\circ}\text{C}$)
 Flow = 36 hours
 Run time = 5 years

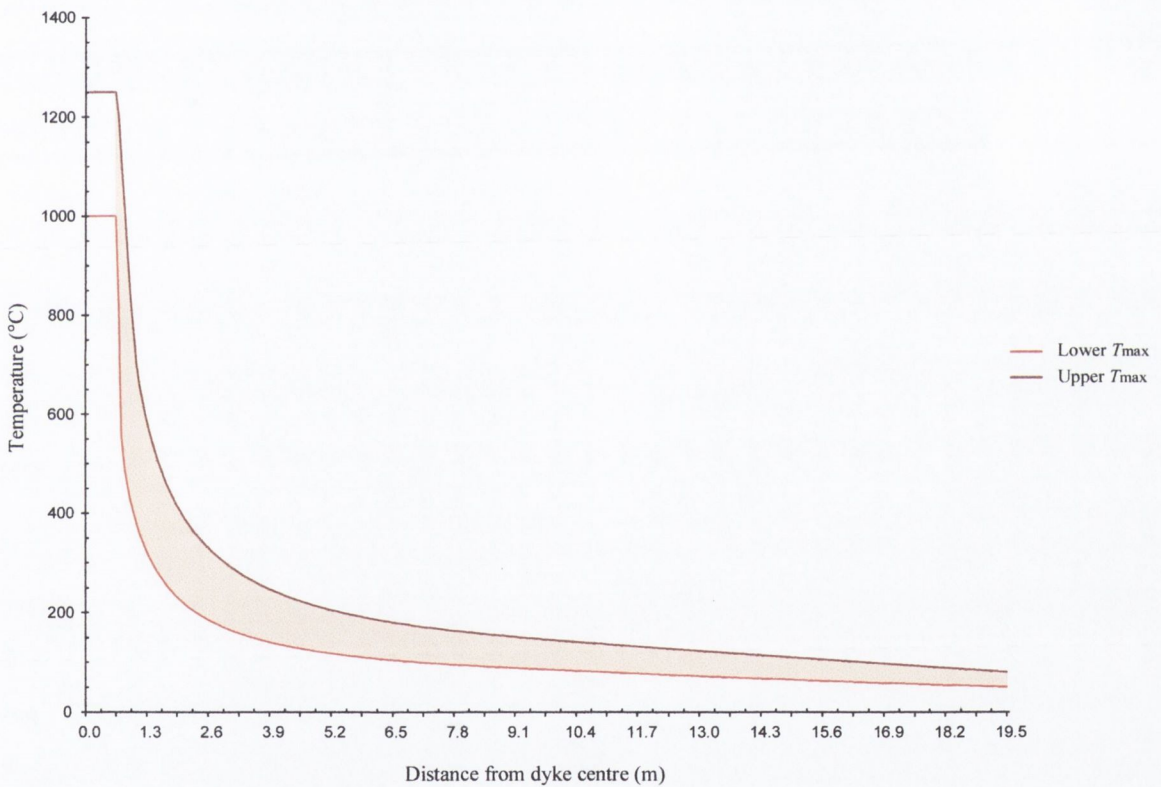


Figure 6.17. Modelled range of T_{max} after 5 years as a function of distance from the centre of the 1.3m thick dyke at Berreraig. The lines on the plot represent the modelled maximum temperature (T_{max}) for the upper and lower temperature scenarios described above.

6.7 SUMMARY

A simple one-dimensional model of transient conductive heat flow, the *Schmidt Plot*, was used to model the temperature change produced in the host rocks by heat transfer from the dyke. A computer simulation of the Schmidt Plot was developed using Microsoft Excel's VBA macro-programming facility. Thermal model input parameters were derived from both published data and experimental data from this study. A simple 'divided-bar' apparatus was constructed and used to measure the thermal conductivity (k) of selected rock samples. Experimentally determined k values from this study fall within the range of published k values for the measured lithologies. Good agreement was observed of measured k values for the dyke and host lithologies. As the thermal diffusivity (κ) of a material is directly proportional to its thermal conductivity, this justified the use of a single κ value in the model for both dyke and host rocks.

The model sensitivity to the various thermal input parameters was tested, in order to critically assess the relative contribution of each parameter to the resulting maximum temperature (T_{\max}) distribution in the host rocks. The thickness of the dyke and the duration of magma flow were found to have the most significant effect on the width of the contact aureole indicated by the model, as they have the greatest control on the amount of heat input into the system. The effect of thermal conductivity on T_{\max} was found to be greatest during the early stages of cooling, but it subsequently has less effect. The effect of increasing the value of k was to increase T_{\max} , but compared to some of the other variables, its overall influence is relatively minor. T_{magma} and T_{host} control the initial temperature at the contact between dyke and host rocks (T_{contact}). Increasing the value of either of these parameters will increase T_{contact} , and the width of the contact aureole indicated by the model. However, as magma flow duration only maintains T_{magma} , and is independent of T_{host} , the effect of T_{host} on T_{\max} values close to the dyke is considered relatively minor. The results suggest that heat flow models which assume immediate arrest of magma flow upon emplacement may be oversimplified, particularly for thicker dykes, where the duration of magma flow can be substantial.

The model indicates that significant cooling of the dyke occurs within days and weeks of its emplacement. During the initial period before emplacement/flow is complete, T_{contact} rises markedly, as significant and rapid heat exchange occurs from the dyke to the host rocks immediately adjacent to it (cms). Temperatures immediately adjacent to the dyke margin achieve a maximum within hours of intrusion and fall rapidly thereafter. After 2 weeks the temperature at the centre of the dyke falls below half of its initial intrusion temperature. The rate of dyke cooling indicated by the model has decreased markedly after 1 year, as the heat from the intrusion is dissipated further away into the host rocks. The model predicts that a T_{max} of 135°C is achieved 6.7m from the dyke margin - the limit of the sample range - after just under 1 year and thereafter begins to cool slowly

CHAPTER 7

COMPARISON OF MODELLED T_{\max} WITH MATURITY DATA

Peak palaeotemperatures reached in the host rocks in the neighbourhood of the cooling dyke at Berreraig, computed using Schmidt's conductive cooling model (Chapter 6), are here compared with measured maturity data.

7.1 COMPARISON OF MODELLED T_{\max} WITH VR-DERIVED PALAEO-TEMPERATURES

The numerically modelled range of T_{\max} adjacent to the Berreraig dyke (Section 6.6.3) is here compared with temperatures derived from measured vitrinite reflectance data (Figure 7.1). The VR-derived peak temperatures close to the dyke fall outside the T_{\max} range computed using the conductive cooling model. At distances $\geq 3\text{m}$ from the contact, the VR-derived peak temperatures correspond well with the lower T_{\max} estimate of the Schmidt model. At distances less than 3m from the dyke margin, peak temperatures calculated from measured VR data underestimate those predicted by the model. Accordingly, the width of the contact aureole indicated by the model is greater than that calculated from the vitrinite reflectance data (Figure 7.1).

In order that the model T_{\max} profile approach the observed VR-derived peak temperature data, unrealistic thermal input parameters are required. Using a T_{magma} of 700°C , T_{host} of 70°C , a magma flow duration of 0 hours, and a thermal diffusivity of $4.39 \times 10^{-7} \text{ m}\cdot\text{s}^{-1}$, peak temperatures predicted by the model are of similar magnitude to the VR-derived peak temperature data. Although good agreement of peak temperature data is observed immediately adjacent to the dyke contact, and at distances greater than *ca.* 2m, a flatter T_{\max} profile is predicted by the model, indicating a wider contact aureole (Figure 7.2).

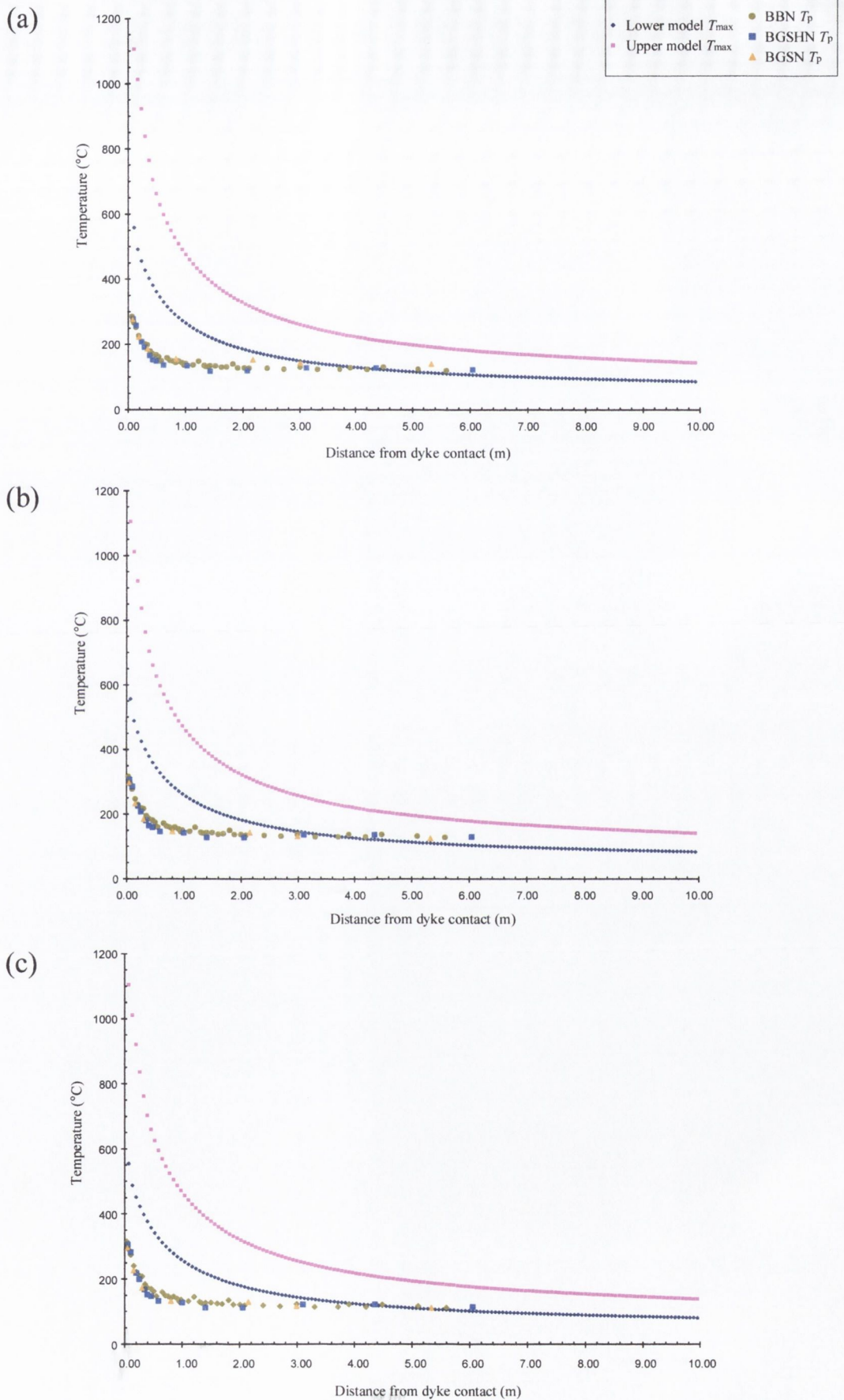


Figure 7.1 Comparison of T_{max} range predicted by the Schmidt conductive cooling model and measured VR-derived peak temperature (T_p) data, computed using the algorithms of (a) Barker (1988), (b) Barker and Goldstein (1990), and (c) Barker and Pawlewicz (1994) geothermal, versus distance from the dyke

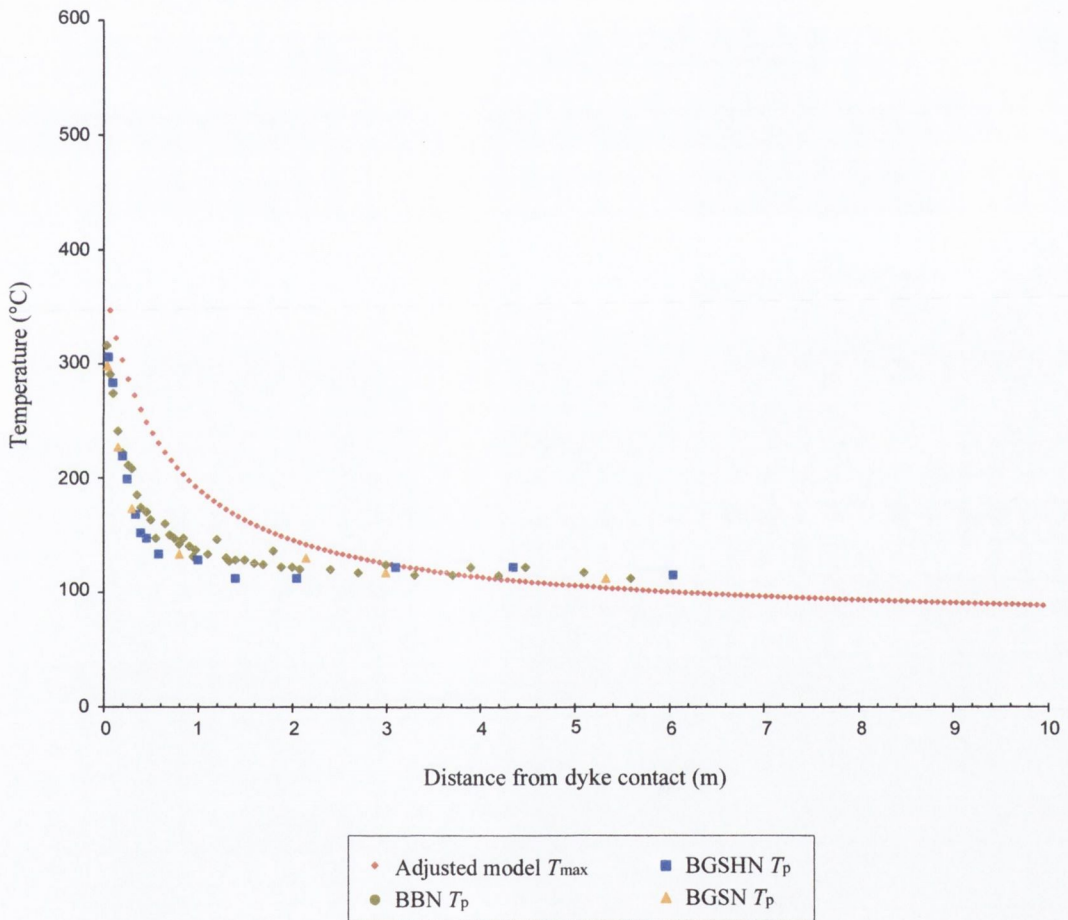


Figure 7.2 Comparison of model T_{max} and VR-derived peak temperatures (T_p) versus distance from the dyke contact. The model-derived maximum temperature profile is computed based on the adjusted thermal parameters described in the text. VR-derived peak temperatures (T_p) are computed using the geothermal VRG of Barker and Pawlewicz (1994).

While the values for T_{host} and κ in this low temperature case fall within the realistic range for these rocks, the value for T_{magma} is too low for a basaltic magma. Furthermore, an instantaneous cessation of magma flow upon dyke emplacement is unrealistic, even for a thin dyke, such as the 1.3m thick example in this study.

7.2 DISCUSSION

Differences between the observed extent of contact aureoles approximated by the form of vitrinite reflectance profiles and that, which is predicted by conductive cooling models have been reported by a number of workers (Raymond and Murchison 1988; Bishop and Abbott 1995; Goodhue 1996; McCormack *et al.* 1997; Barker *et al.* 1998; McCormack 1998). A number of factors are considered likely to be responsible for this disparity of predicted palaeotemperatures:

1. The heating episode at peak temperature may have been too brief for vitrinite in the host rocks adjacent to the dyke to stabilise and record the maximum palaeotemperatures achieved
2. The rate of heating in the host rocks adjacent to the dyke may have been too rapid to facilitate equilibration of complex vitrinite maturation reactions.
3. Standard empirical calibrations used to translate % R_r data to peak palaeotemperatures (Barker and Pawlewicz 1986; Barker 1988; Barker and Goldstein 1990; Barker and Pawlewicz 1994) may be inappropriate for contact metamorphic systems.
4. Alternative mechanisms of heat transfer may be influential in the cooling of the dyke.

These considerations are addressed below.

The underlying basis for vitrinite reflectance geothermometers (VRG), is that maximum temperature (T_{max}) largely determines the reflectance of vitrinite (Suggate 1982; Barker 1983; Price 1983; Barker and Pawlewicz 1986; Barker 1988; Barker and Goldstein 1990; Barker 1991; Barker *et al.* 1998; Tobin and Claxton 2000). However, it is generally accepted that the time at peak temperature necessary for organic matter to attain stability is important (Suggate 1982; Barker 1983; Price 1983; Barker and Pawlewicz 1986; Barker 1991; Tobin and Claxton 2000). That is to say, organic matter in subsiding parts of the

crust must constantly readjust to increasing temperature, and that this reaction is time-dependent until it once again establishes stability (Barker 1983). It is likely that the heating episode caused by intrusion of the dyke was too brief for vitrinite in the host sediments close to the contact to fully equilibrate to the peak temperatures attained.

Using the Schmidt computer model, the temperatures at a various distances from the intrusion were modelled as a function of time (Figure 7.3). The model shows that samples closest to the dyke were virtually instantaneously heated to maximum temperatures. As the distance from the dyke increases, the time to reach maximum temperature increases, whilst the maximum temperature attained is reduced. Apparently, maximum temperatures reached in the host rocks close to the dyke were not maintained long enough to enable the reactions controlling vitrinite reflectance to re-equilibrate and record the peak temperature achieved. Raymond and Murchison (1992) illustrate that the heating that accompanied intrusion of magma into Scottish Carboniferous coals was evidently so rapid that the expected full thermal maturation of heat-sensitive biomarker molecules closest to the intrusion was not achieved. How much heating time at peak temperature is required in order for vitrinite reflectance to stabilise is still uncertain (Section 4.4.2). Barker (1991) suggested that it may be as little as 10^1 yr. Heating durations at peak temperatures close to dyke contacts, a matter of hours, days and weeks (Section 6.6.1), are apparently insufficient to afford complete stabilisation of vitrinite reflectance. As distance from the contact increases, heating times at (or near) peak temperatures increase, and the disparity between modelled and VR-derived temperatures decreases. The modelled heating time (based on the parameters listed in Table 6.3) above the measured VR-derived temperatures (T_p), calculated using the geothermal VRG of Barker and Pawlewicz (1994), is plotted against the observed disparity between modelled and VR-derived temperatures in Figure 7.4. The results show that, in general, as heating time above measured vitrinite T_p increases, the observed temperature disparity decreases. Further from the dyke, although the total heating time above T_p decreases slightly, the heating time within 15°C above the T_p continues to increase as VR-derived temperatures approach modelled peak temperatures (Figure 7.5). The results would appear to indicate that stabilisation time of vitrinite reflectance near peak temperatures may be even less than 10^1 yr.

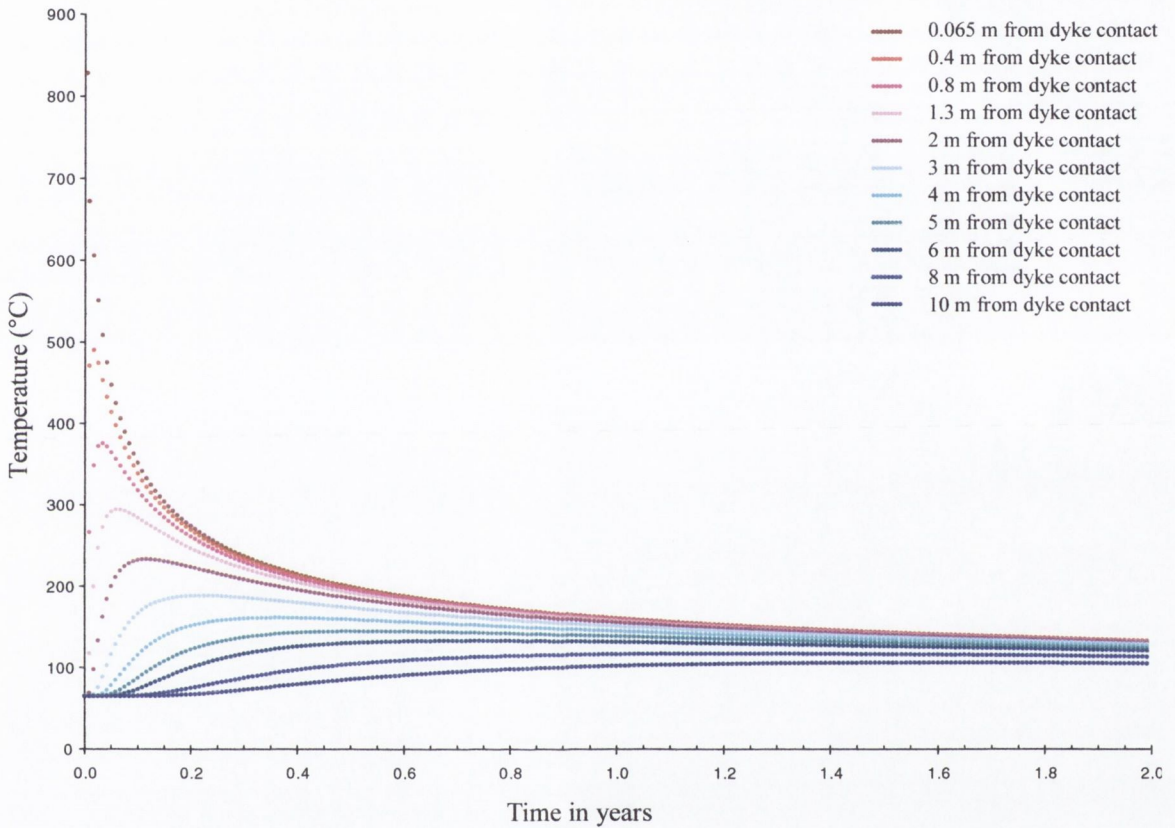


Figure 7.3. Modelled temperatures at various distances from the dyke contact as a function of time, based on the thermal parameters listed in Table 6.3. The model shows that samples closest to the dyke are virtually instantaneously heated to peak temperatures, and cool rapidly. As the distance from the dyke increases, the time to reach peak temperature increases, and the period of time at peak temperature increases.

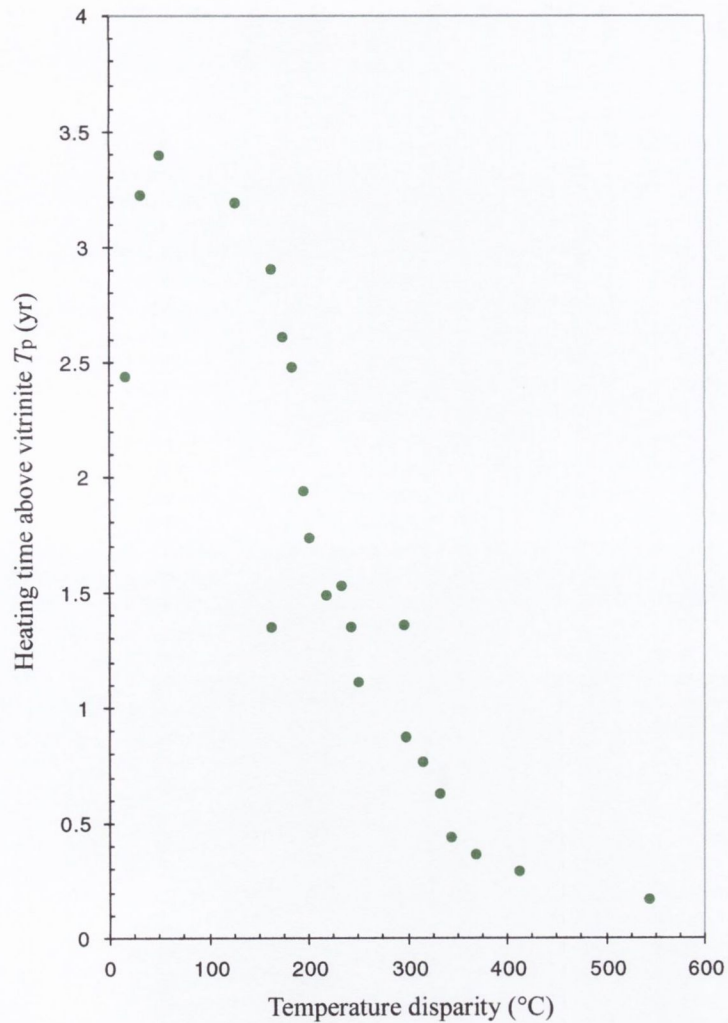


Figure 7.4. Modelled heating time above vitrinite T_p (from Barker and Pawlewicz's (1994) geothermal VRG) versus observed disparity between modelled and VR-derived temperatures.

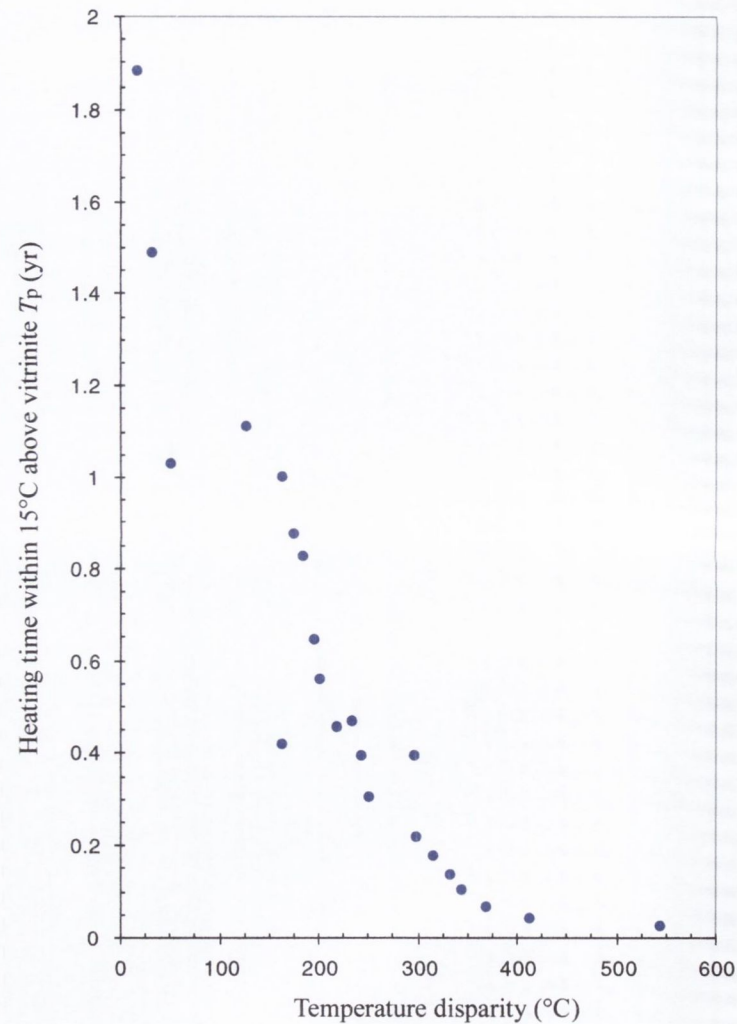


Figure 7.5. Modelled heating time within 15°C above vitrinite T_p (from Barker and Pawlewicz's (1994) geothermal VRG) versus observed disparity between modelled and VR-derived temperatures.

Other factors may, however, be influential towards the disparity between observed and modelled temperatures. Organic maturation experiments carried out in pressurised, water-wet closed systems show that the major extent of the reaction occurs during the first part of the reaction, with little, or no reaction products occurring over much longer time periods (Ishiwatari *et al.* 1977; Price 1983) (Figure 7.6). This being the case, under rapid heating rates, significant amounts of the volatile reaction products of organic maturation will be generated during the early reaction stages. It is possible that overpressure retardation of vitrinite maturation may have occurred as a result of a pressure wave of entrapped reaction gases from these dehydration and decarbonation reactions. The retardation effect of pressure on vitrinite reflectance has been recognised by a number of workers (Cecil *et al.* 1977; McTavish 1978; Law *et al.* 1989; Khorasani and Murchison 1990; Dalla Torre *et al.* 1997; McTavish 1998; Taylor *et al.* 1998; Carr 2000). Volatiles generated by the thermal cracking of vitrinite pass into the vitrinite microporous network before being expelled into the rock porosity (Carr 2000). Only after these volatiles have been expelled does the reflectance begin to increase, due to aromatisation and condensation of the residual solid structure. For unsuppressed vitrinite at heating rates prevalent in sedimentary basins, the rate of volatile generation is not limited by the rate at which the liquid and gaseous volatiles can be expelled, via the micro-porous network (Carr 2000). Under the rapidly induced high temperature conditions associated with dyke intrusion, the rate of volatile generation may exceed the capacity of the vitrinite microporous network to transport and expel the generated gases and liquids. The entrapment and immobilisation of the volatile products of maturation reactions within the vitrinite structure would suppress further volatile generation and aromatisation of vitrinite (Carr 2000) (Figure 7.7). Retention of volatiles in coals near the margins of igneous intrusions has been invoked by a number of workers to explain observed increases in volatile matter content in the direction of intrusions (Crelling and Dutcher 1968; Gurba and Weber 2001). Meyers and Simoneit (1999) observed increases in TOC concentration, elevated C/N ratios and anomalously negative $\delta^{13}\text{C}$ ratios from an Upper Cretaceous coal close to a sill contact in Colorado. They suggested that thermal alteration of the coal closest to the sill may have occurred too rapidly for all of the degradation products to have migrated away (Meyers and Simoneit 1999). In extreme cases, this may partly account for the dip in vitrinite reflectance frequently reported in host rocks adjacent to the margins of igneous intrusions.

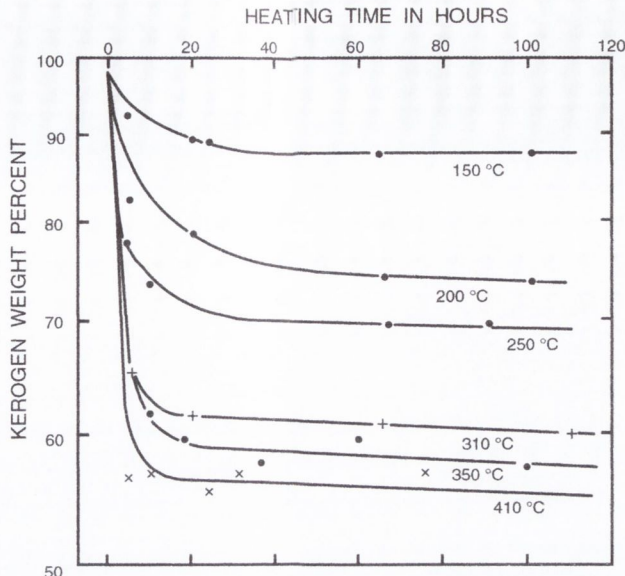


Figure 7.6. Plot of reaction extent (kerogen weight %) versus heating time for kerogen at various temperatures. Modified from Ishiwatari *et al.* (1977).

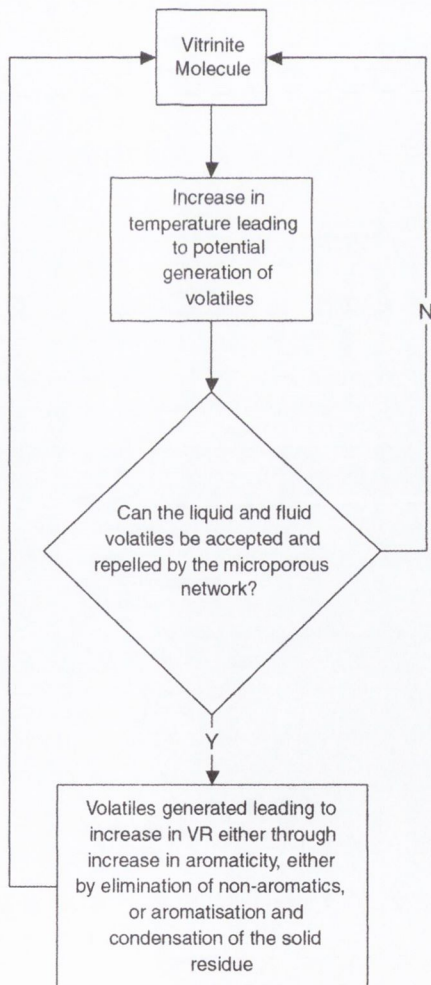


Figure 7.7. Schematic flow diagram to illustrate the control exerted by the capacity of the microporous network. In unsuppressed vitrinite, the volatiles generated during maturation are expelled via the microporous network, enabling the aromaticity to increase, thereby producing an increase in VR. In suppressed vitrinite, the additional volatiles rapidly saturate the microporous network, and further generation and expulsion of these volatiles is restricted, and the VR is suppressed. After Carr (2000).

The influence of pressure on suppressing vitrinite reflectance is greater under wet than under dry conditions (Dalla Torre *et al.* 1997). Low hydrostatic pressure during diagenesis (an open thermodynamic system) allows volatile matter to escape; this enhances the probability of continued maturation of organic macromolecules (Cecil *et al.* 1977). Water trapped in the pores of the host rocks can undergo enormous pressure increases during heating from an intrusion (Delaney 1982; Delaney 1987). In addition, water undergoes a tremendous volume increase when it flashes to steam (Delaney 1982). When hydrostatic pressure approaches or is equal to lithostatic pressure (a closed thermodynamic system), the escape of volatiles is retarded, thus inhibiting organic maturation (Cecil *et al.* 1977). If a closed system existed at peak temperature, pressure retardation of vitrinite reflectance would be enhanced. However, it is possible that the system might open rapidly due to shear and compressional stresses, associated with dyke emplacement.

The disparity from temperatures computed using the conductive model might also reflect errors in the temperatures inferred from vitrinite reflectance data. Converting the standard deviation (S.D.) 'error bars' on the R_r plots to temperatures, using a particular VR-geothermometer (e.g., Barker and Goldstein 1990), gives an estimate of the errors involved in VR-temperature translations (i.e., % $R_r \pm$ S.D. \rightarrow 'upper', 'lower' and 'mean' temperature estimates). The geothermometers show greater sensitivity at lower levels of vitrinite reflectance, indicated by a greater temperature spread around the translated mean R_r value (Figure 7.8). As the level of vitrinite reflectance increases, the spread about the mean R_r -translated temperature is reduced. This is essentially a consequence of the logarithmic function present in the conversion equations. The decreased spread about translated temperatures with increased R_r effectively counterbalances the anisotropic effect of vitrinite at higher ranks. To this end, the application of R_r as a geothermometer is limited, due to the behaviour of R_{\min} above the ~ meta-anthracite stage of coal rank (Figure 7.10). Consequently, measurement of R_{\max} is considered better practice at higher ranks (Taylor *et al.* 1998). Since VR-geothermometers are calibrated only to R_r , their usefulness is therefore limited at higher ranks.

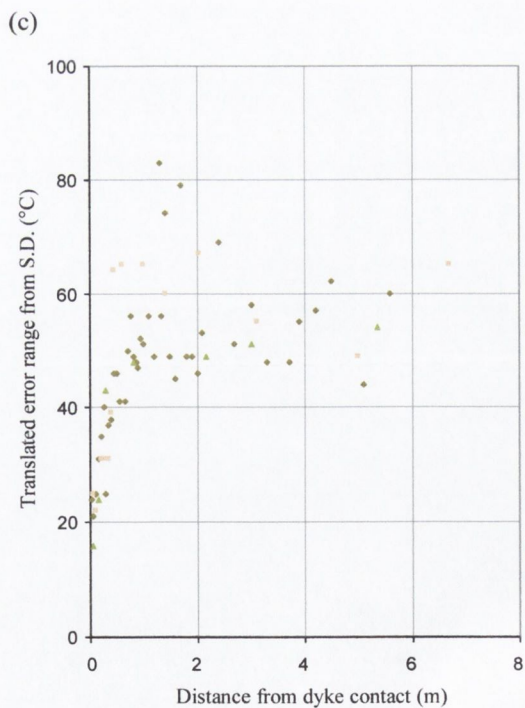
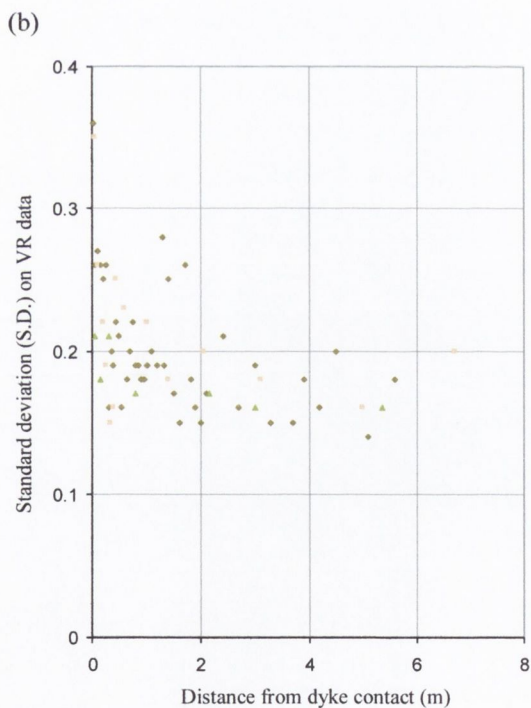
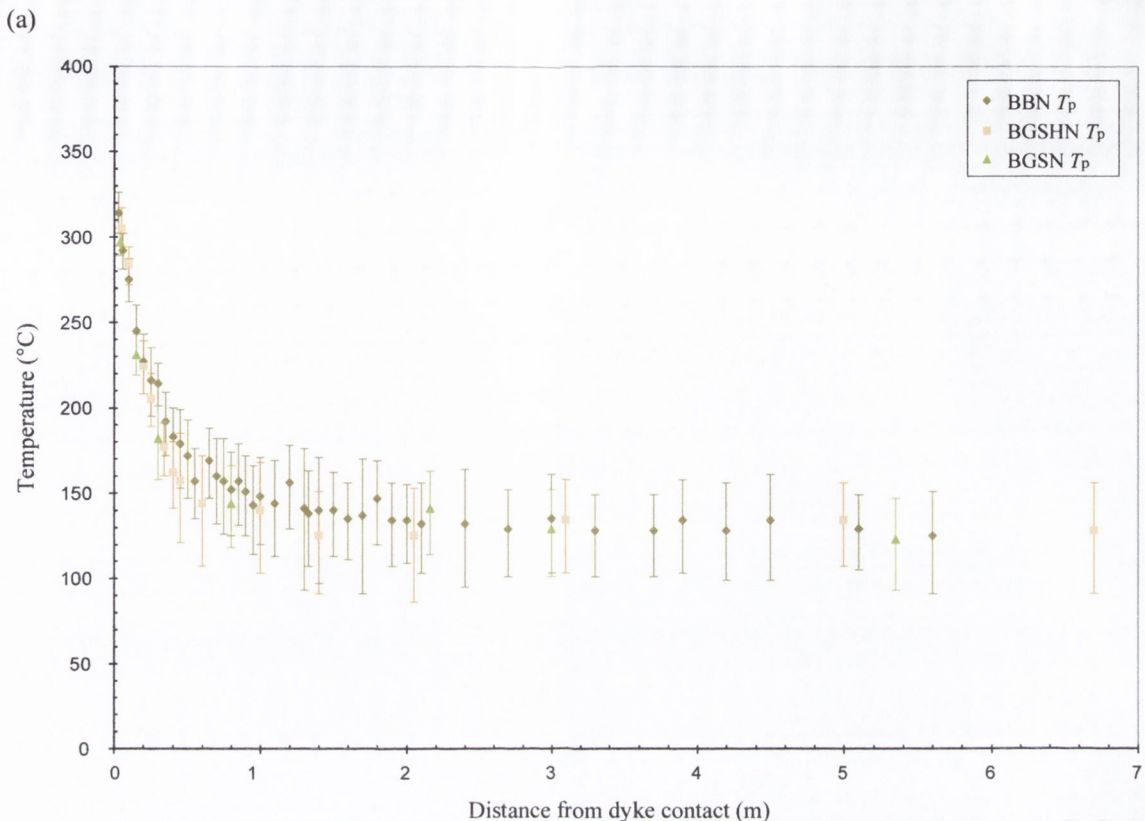


Figure 7.8. (a) Translated peak temperatures and associated error range, based on standard deviations of measured VR data, as a function of distance from the dyke contact. (b) Variation of standard deviation on measured VR data with distance from the dyke contact. (c) Error range of translated temperatures, based on standard deviations on measured VR data, versus distance from the dyke contact. Translated temperatures after Barker and Goldstein (1990).

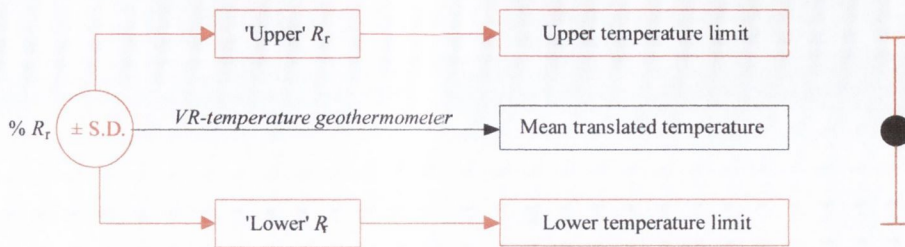


Figure 7.9. Construction of error bars on VR-translated temperatures. The standard deviation about the mean R_r is added to, and subtracted from the mean, then translated to upper and lower temperature limits using the VR-temperature algorithm.

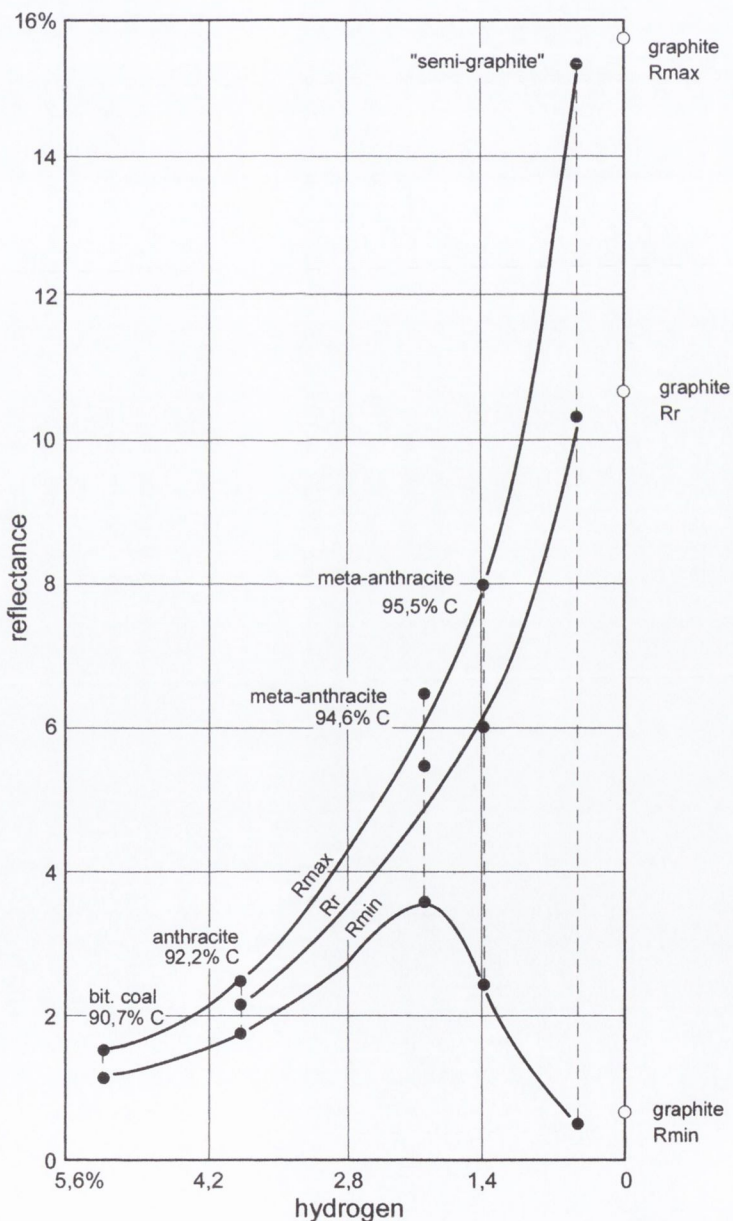


Figure 7.10. Increase of coalification between the stages of bituminous coal and graphite, on the basis of hydrogen content and of optical reflectance of vitrinite (R_{max} , R_r , R_{min}). Note the reversal of the R_{min} curve at the meta-anthracite stage. After Ragot (1977).

Barker and Pawlewicz (1994) identified different vitrinite maturation paths for burial heating and geothermal metamorphism systems (Figure 4.9), and asserted that geothermal-calibrated geothermometers are unsuitable for burial heating systems. These different maturation paths were attributed to physical differences in each environment, such as pressure and the ability of the environment to allow escape or removal of reaction products generated during thermal maturation (Barker and Pawlewicz 1994). For the same reasons, it is also likely that VR-geothermometers, calibrated in both burial and geothermal systems are unsuitable next to thin dykes, where high temperatures are reached very rapidly and are very short-lived. Bostick (1970, 1971) and Bostick and Pawlewicz (1984b) developed a high temperature calibration from laboratory experiments in which lignite in water was heated for up to one month in pressure 'bombs' at various temperatures (Figure 7.11). For samples close to the dyke contact, temperatures estimated from Bostick's calibration curve match well the temperature range of maximum temperature predicted by the Schmidt conductive model (Figure 7.12). For less mature samples at greater distances from the contact, Bostick's calibration overestimates temperatures relative to the conductive model. The heating rates and durations of Bostick's 'bomb' experiments might better simulate conditions closer to the intrusion. At greater distances from the dyke the rates and durations of heating would be greater than those used to calibrate Bostick's VR-temperature curve. Furthermore, the capsules used by Bostick for pyrolysis were foil covered rather than sealed vessels, and are thought to have leaked (Pawlewicz⁶, personal communication). What started out as wet pyrolysis was in fact dry. Dry pyrolysis is not considered a good model of most dyke metamorphism, because in nature it is a wet system.

Conduction may not have been the sole mechanism by which the heat from the intruded magma was transferred to the host sediments. Other heat transfer mechanisms must be considered. Sediments buried only a few thousand metres or less may still retain significant concentrations of pore water. Hence, convection or advection may have a significant effect on the cooling history given adequate porosities and permeabilities (Delaney 1987; Bishop and Abbot 1993; Barker *et al.* 1998). Barker *et al.* (1998) describe four models of heat transfer that commonly operate in a host rock during the cooling of an igneous intrusion: *simple conductive*, *complex conductive*, *incipient convection*, and by *convection cell* (Figure 7.13).

⁶ Mark Pawlewicz, USGS, MS 977, Denver Federal Center, Lakewood, CO 80225

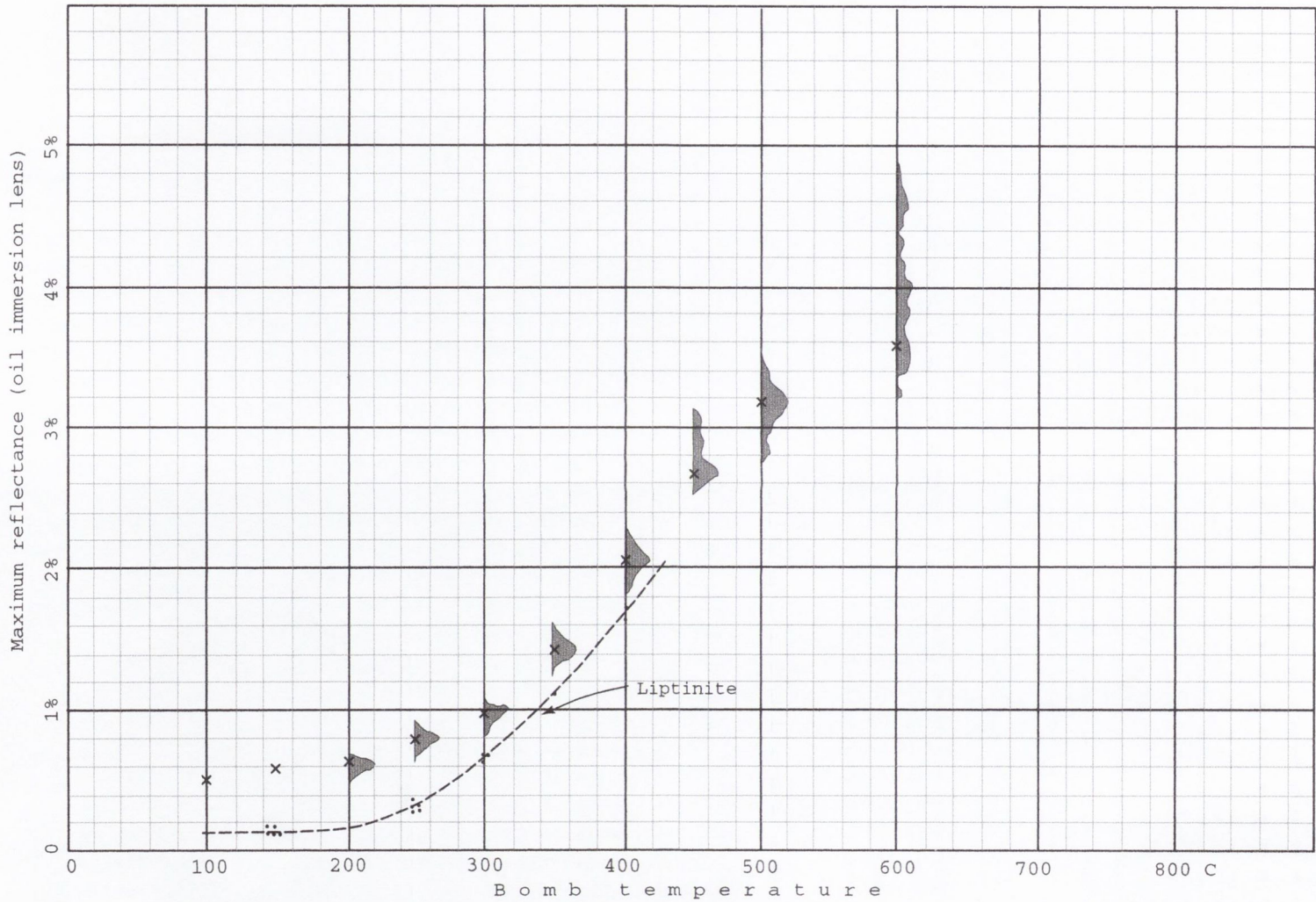


Figure 7.11. Experimentally derived VR-temperature calibration of Bostick (1970, 1971) and Bostick and Pawlewicz (1984). Reflectance of 'low-gray fragments' from 'hydrothermal bomb' samples - shown as approximate plots of frequency of readings with a particular reflectance value. The mean value is marked by an "x". After Bostick (1970).

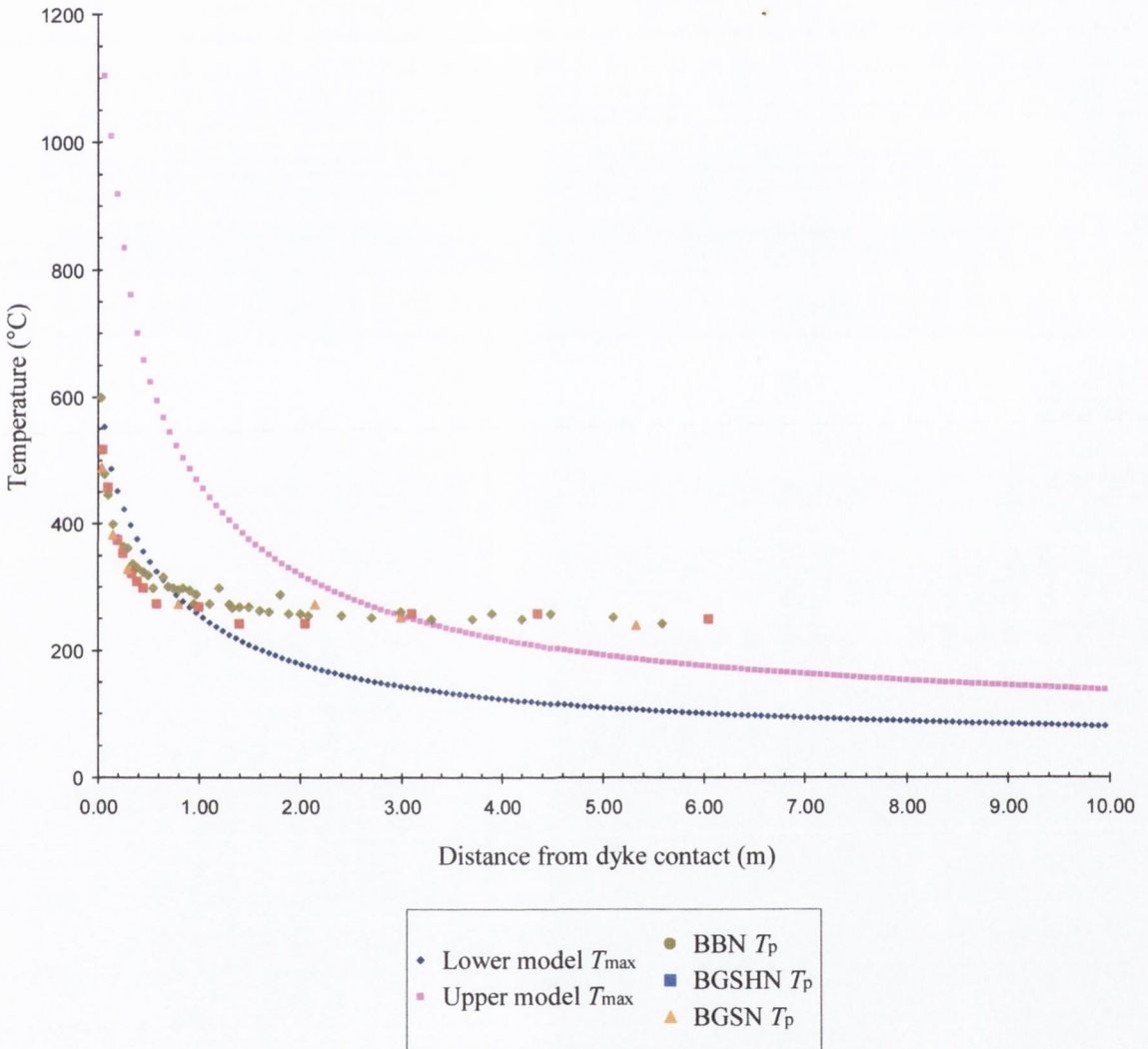


Figure 7.12. Comparison of temperatures, estimated using Bostick's (1970, 1971) experimentally derived calibration curve, and T_{max} range predicted by the Schmidt conductive cooling model, versus distance from the dyke contact.

Barker *et al.* (1998) use the form of % R_r profiles (assuming it sets T_{\max}), described by a normalised distance ratio of the distance from the dyke contact (X) divided by the dyke thickness (D), to identify the likely mechanism of heat transfer operating next to nine basalt dykes, ranging in thickness from 6cm to 40m. Based on empirical observations of natural systems, Barker *et al.* (1998) assert that a contact aureole extending to over $X/D = 2$ and a $T_{\text{contact}} \gg (T_{\text{magma}} + T_{\text{host}})/2$, appears to be a signature of simple conductive cooling. If natural conditions during contact metamorphism diverge much from those assumed in simple conductive cooling models (such as the Schmidt Plot), then the width of the contact aureole, as recorded by the R_r profile, can vary significantly from that predicted by the model (Barker *et al.* 1998).

The *complex conductive* model described in Barker *et al.* (1998) assumes that heat from the cooling magma is partly absorbed by the flash heating and vaporisation of resident pore water in the host rock. The effect of this additional heat sink is to rapidly reduce temperatures in the contact aureole from T_{contact} , restricting the zone of elevated temperatures to a distance approximately equal to that of the dyke thickness ($X/D = 1$).

When water is heated within a contained volume, it pressurises; when uncontained, it expands and flows (Delaney 1982). Dykes may also cool by the advective loss of vapour from the system and the migration of cool groundwater towards the dyke (Jaeger 1959; Delaney 1982; Delaney and Pollard 1982; Delaney 1987; Barker *et al.* 1998). This flow is driven by the thermal expansion of groundwater in the host rock near the dyke and the resulting pressure disparity relative to more distal positions from the intrusion (Delaney 1982). The bouyant rise of heated groundwater, both within and near the dyke, draws cooler pore waters towards the contact, reducing the T_{\max} reached in the host rock. Raymond and Murchison (1988) consider the degree of sediment compaction and the volume of pore water in the sediments at the time of intrusion as the most significant factors in determining the width of the contact aureole adjacent to igneous intrusions. With the exception of thick dykes, the host rock is usually too impermeable and/or cooling is too rapid for a complete convection cell to form (Delaney 1982; Delaney and Pollard 1982; Delaney 1987). The *incipient convection* mechanism of Barker *et al.* (1998) embodies this scenario, where rise of heated fluids near the intrusive contact occurs, without the development of a recharge system.

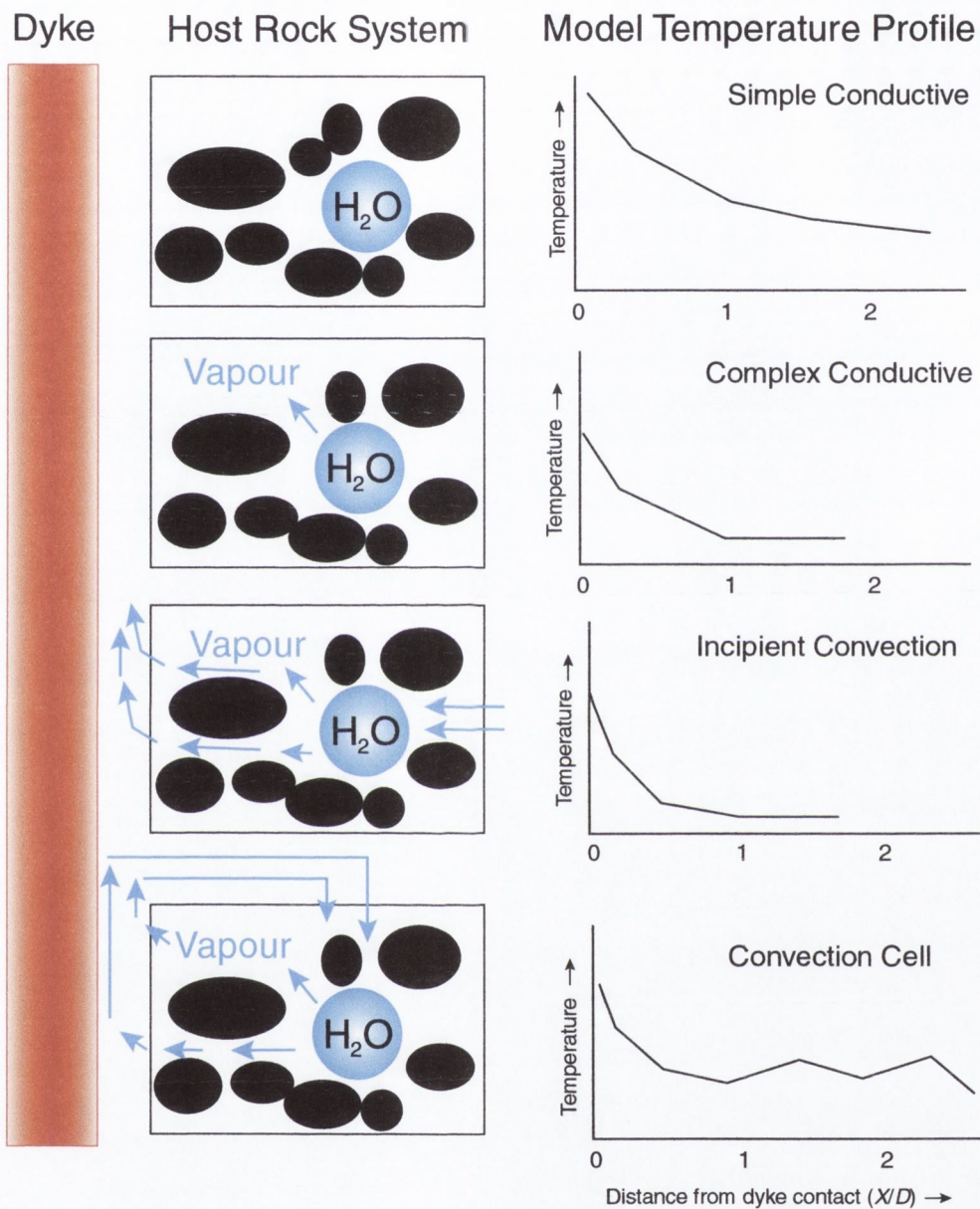


Figure 7.13. Four models of cooling in a host rock after intrusion of an igneous dyke, as described by Barker *et al.* (1998). The host rock system shown initially consists of framework grains (solid spots) with pore water (H_2O). After intrusion, flash vaporisation and/or convection of pore water may occur, forming additional heat sinks. The form of the temperature profile for each mechanism, shown as a function of distance from the dyke contact (X) divided by the dyke thickness (D), indicates the different responses conjectured to result from each cooling mechanism. As T_{max} controls R_r , a similar profile to that shown for temperature is expected for vitrinite reflectance data measured next to a dyke. Modified from Barker *et al.* (1998).

Maximum temperatures next to the dyke can be significantly reduced, generally decreasing VR-derived T_{\max} profiles to 'background' levels at distances corresponding to $X/D < 1$ (Barker *et al.* 1998). A convection cell is indicated by a wave-like reflectance T_p profile and relatively high temperatures that may not decrease to 'background' levels until distances corresponding to $X/D = 1.5$ (Barker *et al.* 1998).

Measured R_r and associated T_p data from the BBN horizon were plotted against distance from the dyke contact, using the normalised distance ratio, X/D (Figure 7.14), and compared with the cooling models depicted by Barker *et al.* (1988). Mean AOM RGB intensity data are also included for comparison. Although the chemical structure of vitrinite is different from that of liptinites, and the kinetics controlling changes in the properties of both are considerably different (Barnard *et al.* 1981), mean RGB intensities of AOM nevertheless define a zone of enhanced thermal alteration, comparable to that of R_r . A 'reflectance-' and 'RGB aureole' extending up to $X/D \approx 1$ is somewhat short of the expected $X/D = 2$ for simple conductive cooling. Based on the models depicted by Barker *et al.* (1988), vaporisation and/or migration of heated pore fluids could be invoked as a possible scenario to explain the cooler than expected temperature profiles.

Major element oxide analysis of the BBN horizon by ICP-OES⁷ was conducted to investigate possible fluctuations in elemental abundances due to migration of heated pore fluids towards the dyke. The results indicate sharp fluctuations in the abundance patterns of several elemental species in the immediate vicinity of the dyke contact (Figure 7.15). This apparent variation of the inorganic component suggests that some hydrothermal alteration may have occurred near the dyke contact. These sharp abundance fluctuations occur within the narrow zone of elevated % R_r , equivalent to $X/D \approx 0.55$. The relatively stable elemental abundance patterns further away from the dyke contact suggests that any hydrothermal convection in the host sediments, associated with dyke intrusion, was confined to a narrow zone immediately adjacent to the contact.

⁷ Analysis performed by OMAC Laboratories Ltd., Athenry Rd., Loughrea, Co. Galway.

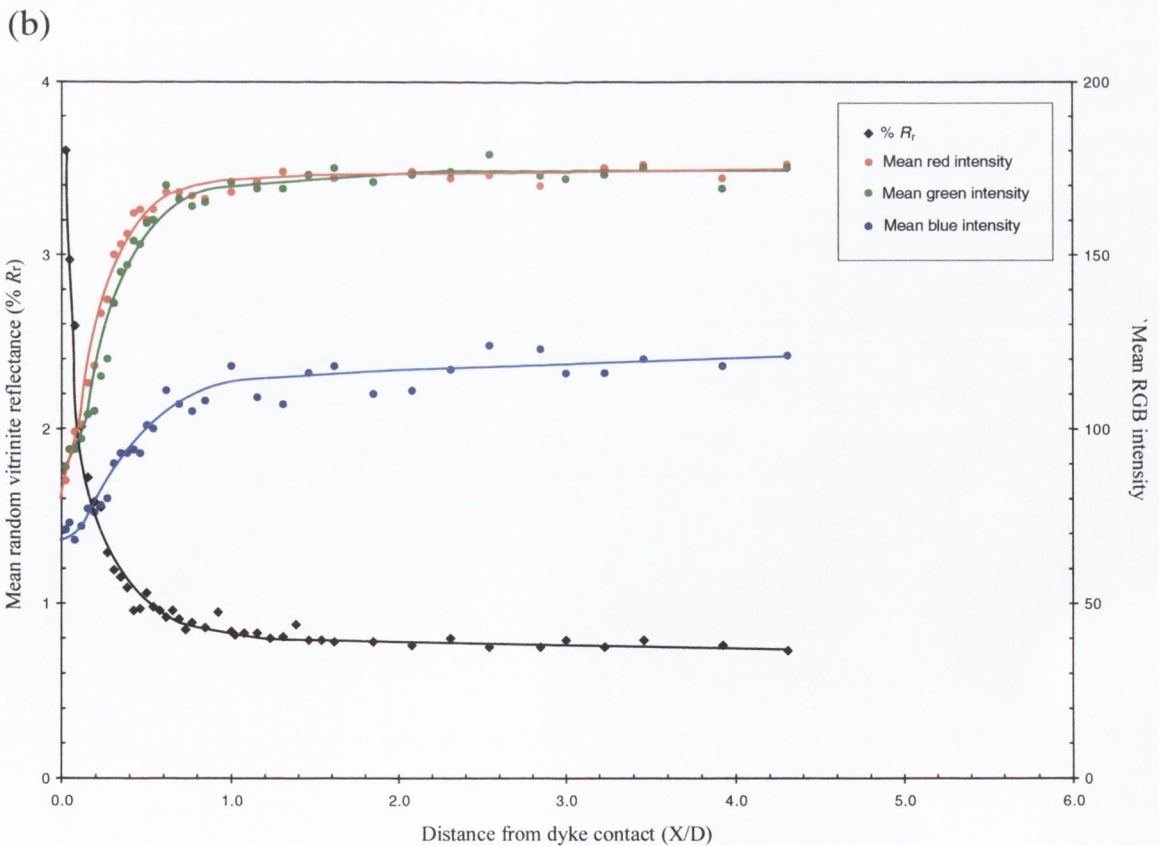
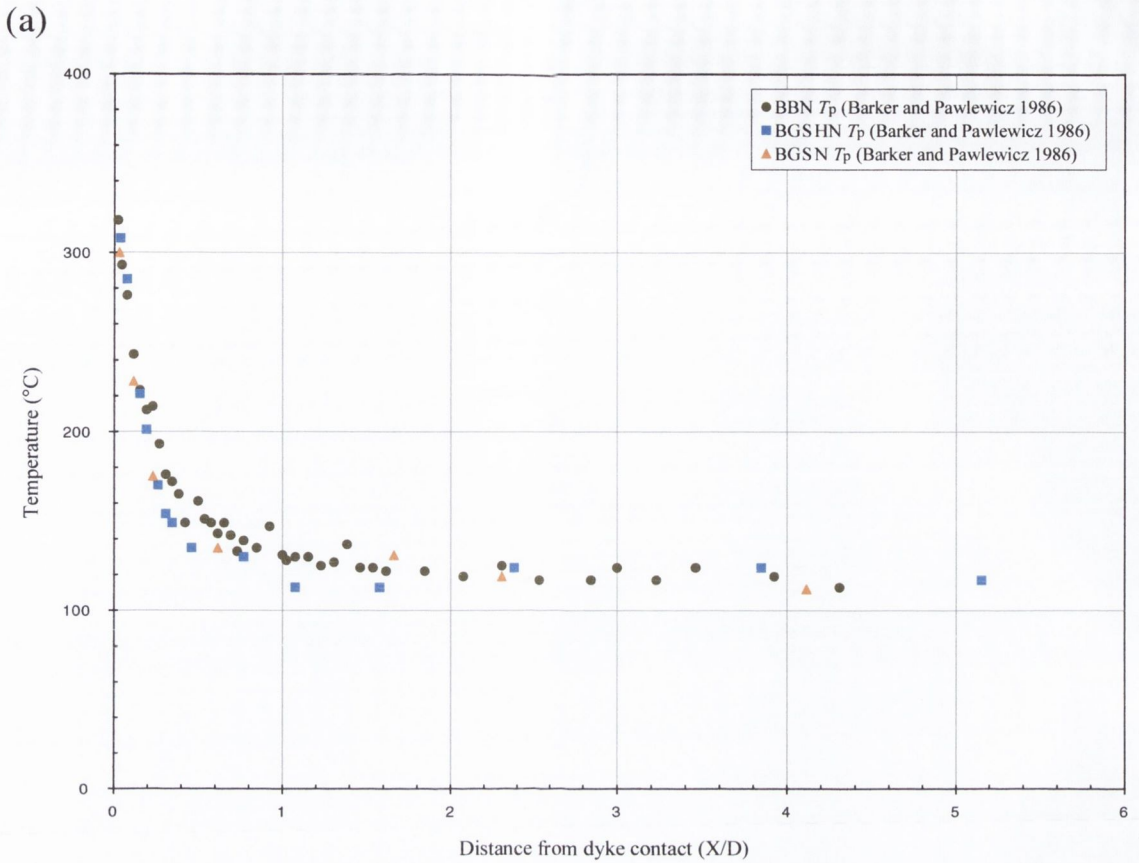


Figure 7.14. (a) Plot of VR-derived temperatures from each of the sample horizons, translated using the geothermal calibration of Barker and Pawlewicz (1994), as a function of normalised distance from the dyke contact (X/D). (b) Plot of R_r and mean AOM RGB colour intensity data from the BBN sample horizon as a function of X/D .

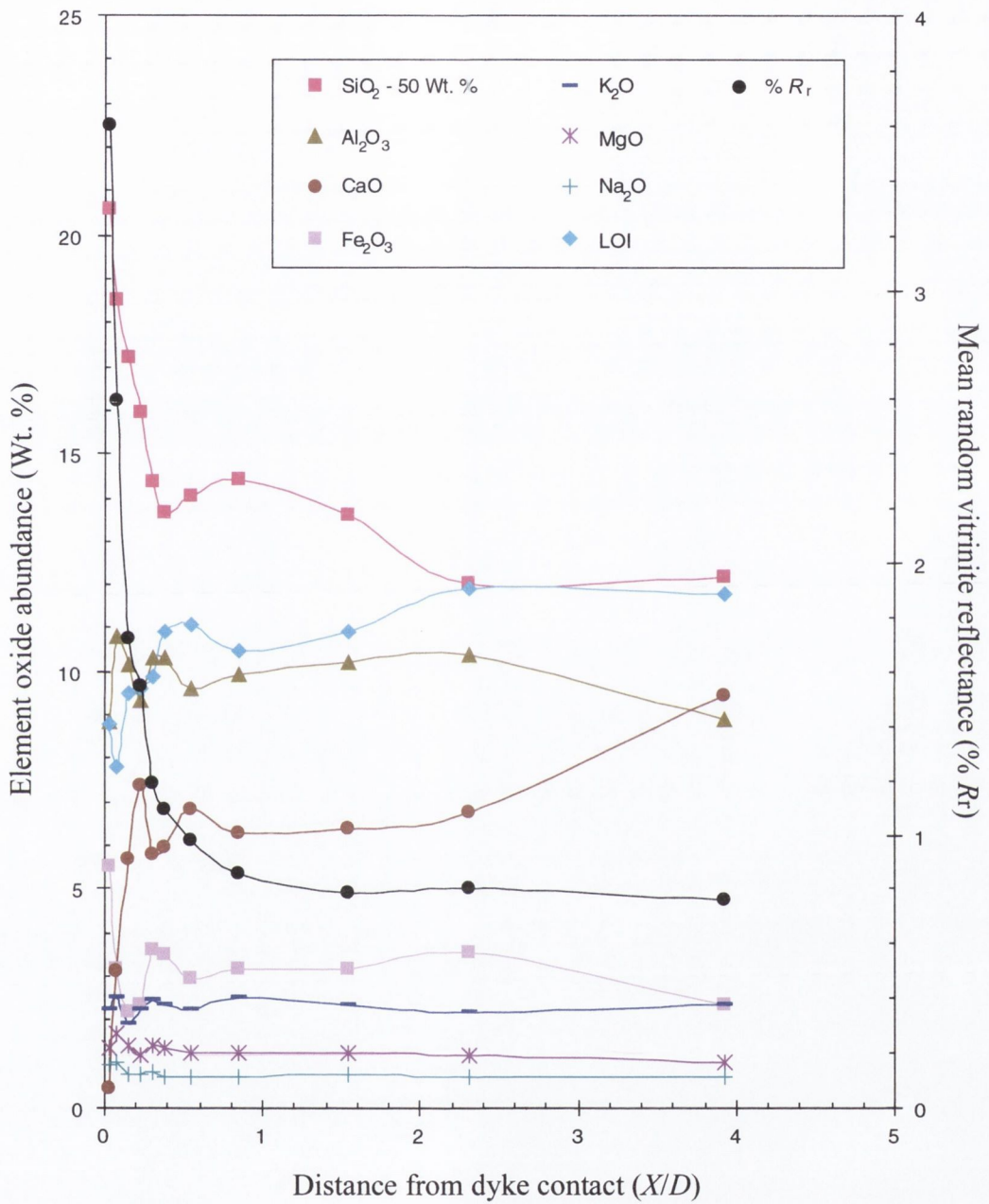


Figure 7.15. Major element oxide abundances (Wt. %) for selected samples from the BBN shale horizon plotted as a function of distance from the dyke contact (X/D). For comparison, % Rr data for the same samples are also plotted on the right hand axis.

Due to the complexities involved in modelling the effects of convection, current mathematical treatments of igneous body cooling models assume that conduction is the sole *modus operandi* by which heat is transferred to the host rocks. No worker has fully treated the early development of hydrothermal circulation along vertical contacts with intrusions, and no worker has coupled this transient process with the cooling of dykes (Delaney 1987). It is deemed beyond the scope of this study to attempt any such modelling. The vaporisation and/or flow of groundwater is simply invoked here as a likely explanation for the apparent lower than expected peak temperatures observed in the vicinity of the dyke.

7.3 SUMMARY

The numerically modelled range of T_{\max} adjacent to the dyke is compared with palaeotemperatures derived from measured vitrinite reflectance data. Good agreement between modelled and apparent peak temperatures is observed at distances greater than 3m from the dyke, suggesting that the apparent 'background' maturity level was achieved in part by heat associated with the intrusion. Close to the dyke, peak palaeotemperatures calculated from measured VR data considerably underestimate those predicted by the model. Accordingly, the width of the contact aureole indicated by the model is greater than that calculated from the vitrinite reflectance data. A number of reasons for this disparity between observed and modelled temperatures are considered.

1. It is likely that the heating episode at peak temperature was too brief for vitrinite in the host rocks adjacent to the dyke to stabilise and record the maximum temperatures achieved. The Schmidt model indicates that samples closest to the dyke were virtually instantaneously heated to peak temperatures. Comparison of modelled temperatures and heating times with VRG derived palaeotemperature data show that, in general, as heating time near measured vitrinite T_p increases, the observed temperature disparity decreases. The results suggest that stabilisation time of vitrinite reflectance near peak temperatures may be less than 10^1 yr.
2. The rate of heating in the host rocks adjacent to the dyke may have been too rapid to facilitate equilibration of complex vitrinite maturation reactions. Under the rapidly

induced high temperature conditions associated with dyke intrusion, the entrapment and immobilisation of the volatile products of maturation reactions within the vitrinite structure may have occurred, suppressing further volatile generation and aromatisation of vitrinite.

3. Standard empirical burial and geothermal calibrations used to translate % R_r data to peak palaeotemperatures (Barker and Pawlewicz 1986; Barker 1988; Barker and Goldstein 1990; Barker and Pawlewicz 1994) are likely to be inappropriate for contact metamorphic systems. Furthermore, the application of R_r as a high temperature geothermometer is limited, due to the anomalous behaviour of R_{min} above the ~meta-anthracite stage of coal rank.
4. Convection and/or advection may have partly contributed as alternative mechanisms of heat transfer during the cooling of the dyke. The cooler than expected temperature profiles, together with fluctuations in the major element abundances close to the dyke contact, suggest that vaporisation and migration of heated pore fluids may have acted as a heat sink, limiting the extent of the temperature aureole.

CHAPTER 8

SUMMARY OF CONCLUSIONS

From a detailed assessment of the thermal response rates of vitrinite reflectance (VR), kerogen colour and fluorescence to the short-lived high temperatures associated with the dyke, the following conclusions are drawn:

Vitrinite reflectance shows a marked reaction to the high temperatures close to the dyke, within a zone of approximately equivalent to *ca.* 50% of the dyke thickness (d.t.).

Peak palaeotemperatures in excess of 300°C, derived from measured VR data, are indicated in the host rocks adjacent to the contact.

Differences in the temperature range predicted by burial and geothermal vitrinite reflectance geothermometers (VRG) indicate that they are sensitive to differing thermal regimes, and selection of VRG should involve consideration of thermal history.

In the absence of adequate numbers of suitable palynomorphs, amorphous organic matter (AOM) is an acceptable alternative to palynomorphs for kerogen colour evaluation and estimation of maturity.

Quantitative measurement of kerogen RGB colour intensities is more sensitive to maturity change, or increasing temperature, than visual TAI estimation. The high temperature zone next to the dyke is manifested by a marked reduction in RGB intensities, and has a width equivalent to *ca.* 50% of the dyke thickness. The position of the break in slope of the mean RGB intensities correlates well with that of the R_r data. The G parameter is the most sensitive parameter in relation to thermal maturation and correlates well with vitrinite reflectance up to *ca.* 1.6% R_r . Plots of the relative percentages of red, green and blue versus VR reveal a unique maturation pathway for each of the three colour parameters, and also suggest a close relationship with fluorescence intensity.

Cessation of organic matter fluorescence is delayed under conditions of rapidly induced high temperature maturation. Slight differences in fluorescence properties between sample horizons may reflect varying diagenetic degradation, or compositional differences in the AOM.

A simple one-dimensional model of transient conductive heat flow, the *Schmidt Plot*, shows that significant cooling of the dyke occurs within days and weeks of its emplacement. Temperatures in the country rocks immediately adjacent to the dyke margin achieve a maximum within hours of intrusion and fall rapidly thereafter. The rate of dyke cooling indicated by the model decreases markedly after 1 year, as the heat from the intrusion is dissipated further away into the host rocks.

Experimentally determined thermal conductivity (k) values from this study fall within the range of published k values for the lithologies investigated. Good agreement of measured k values for the dyke and host lithologies justified the use of a single k value in the model for both dyke and host rocks. The thickness of the dyke and the duration of magma flow have the most significant effect on the width of the contact aureole indicated by the model. The effect of thermal conductivity on T_{\max} is greatest during the early stages of cooling, but its overall effect is limited. T_{magma} and T_{host} control the initial temperature at the contact between dyke and host rocks (T_{contact}). However, as magma flow duration only controls T_{magma} , and is independent of T_{host} , the effect of T_{host} on T_{\max} values close to the dyke is considered relatively minor. Heat flow models which assume immediate arrest of magma flow upon emplacement may be oversimplified, particularly for thicker dykes, where the duration of magma flow can be substantial.

Good agreement between modelled and VRG derived peak palaeotemperatures is observed at distances greater than 3m from the dyke, suggesting that the apparent 'background' maturity level was achieved in part by heat associated with the intrusion. Close to the dyke, peak palaeotemperatures calculated from measured VR data considerably underestimate those predicted by the model. A number of reasons for this disparity between observed and modelled temperatures are considered likely:

1. It is likely that the heating episode at peak temperature was too brief for vitrinite in the host rocks adjacent to the dyke to stabilise and record the maximum temperatures

achieved. Comparison of modelled temperatures and heating times with VRG derived peak palaeotemperature values show that, in general, as heating time near measured vitrinite T_p increases, the observed temperature disparity decreases.

2. The rate of heating in the host rocks adjacent to the dyke may have been too rapid to facilitate complete escape of the volatile products of maturation reactions from the vitrinite structure, suppressing further volatile generation and aromatisation of vitrinite.
3. Standard empirical burial and geothermal calibrations used to translate % R_r data to peak palaeotemperatures are likely to be inappropriate for contact metamorphic systems. The application of R_r as a high temperature geothermometer is limited, due to the anomalous behaviour of R_{min} above the meta-anthracite stage of coal rank.
4. Convective and/or advective heat transfer mechanisms may have contributed during the cooling of the dyke.

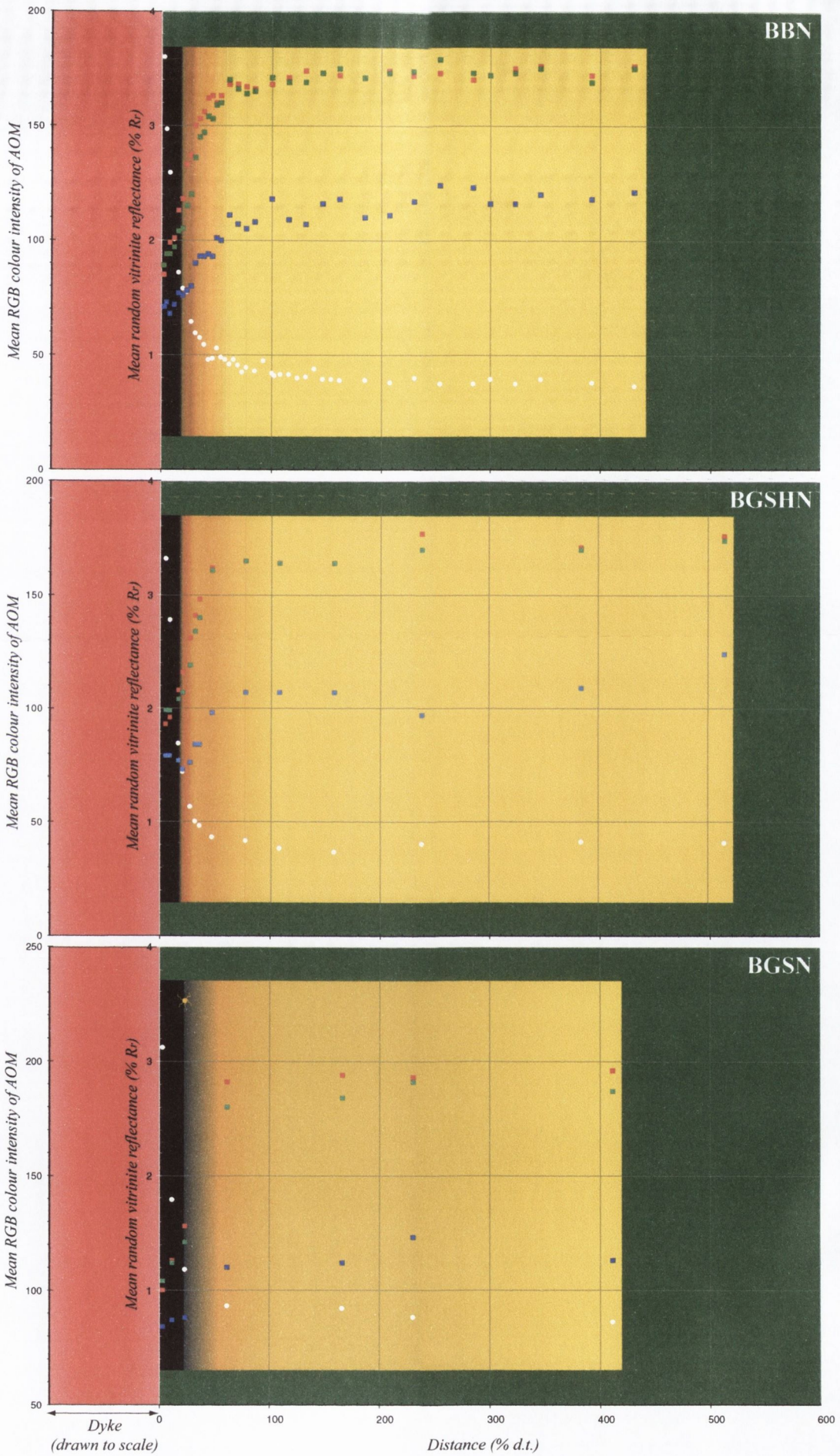
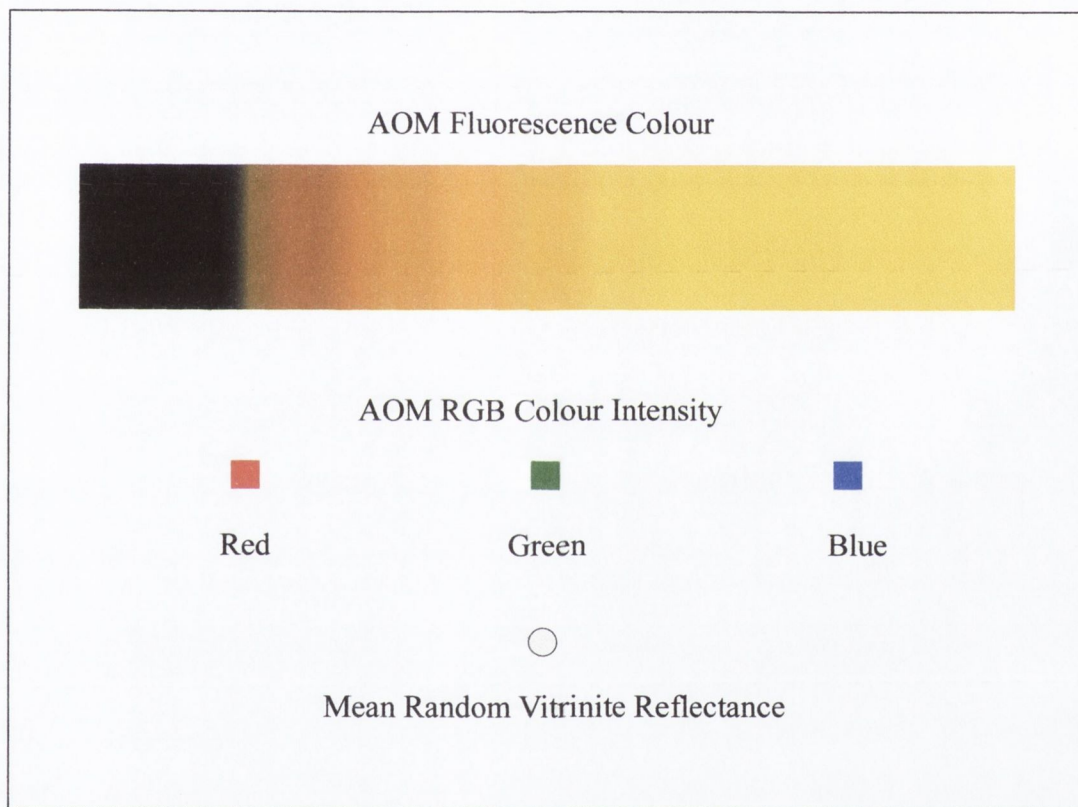


Figure 8.1. Relationships of maturation indices from the studied sample horizons (turn to p195 for key).

Key to Figure 8.1.



REFERENCES

- AIZAWA, J., 1989. Relationship between vitrinite reflectivity and palaeogeotemperature based on fluid inclusions in the south-western coalfields of Japan. *Proceedings, International Conference on Coal Science*. 93-96.
- ANDERSON, F. W. and DUNHAM, K. C., 1966. The Geology of Northern Skye. Explanation of the Portree (80) and parts of the Rubha Hunish (90), Applecross (81) and Gairloch (91) sheets. *Memoirs of the Geological Survey of Great Britain*, 216 pp.
- ANSELMETTI, F. S., LUTHI, S. and EBERLI, G. P., 1998. Quantitative characterization of carbonate pore systems by digital image analysis. *American Association of Petroleum Bulletin*, **82** (10), 1815-1836.
- BARKER, C., 1983. Influence of time on metamorphism of sedimentary organic matter in liquid-dominated geothermal systems, western North America. *Geology*, **11**, 384-388.
- BARKER, C. E. and PAWLEWICZ, M. J., 1986. The correlation of vitrinite reflectance with maximum temperature in humic organic matter. *In*: G. Bunterbarth and L. Stegena (Eds), *Paleogeothermics*. Springer - Verlag, Berlin Heidelberg, 79-93.
- BARKER, C. E., 1988. Geothermics of petroleum systems: implications of the stabilisation of kerogen thermal maturation after a geologically brief heating duration at peak temperature. *In*: L. B. Magoon (Ed), *Petroleum Systems of the United States*. US Geological Survey Bulletin, **1870**, 26-29.
- BARKER, C. E. and GOLDSTEIN, R. H., 1990. Fluid inclusion technique for determining maximum temperature in calcite and its comparison to vitrinite reflectance. *Geology*, **18**, 1003-1006.
- BARKER, C. E., 1991. Implications for organic maturation studies of evidence for a geologically rapid increase and stabilization of vitrinite reflectance at peak temperature:

Cerro Prieto geothermal system, Mexico. *American Association of Petroleum Geologists Bulletin*, **75** (12), 1852-1863.

BARKER, C. E. and PAWLEWICZ, M. J., 1993. An empirical determination of the minimum number of measurements needed to estimate the mean random vitrinite reflectance of disseminated organic matter. *Organic Geochemistry*, **20** (6), 643-651.

BARKER, C. E. and PAWLEWICZ, M. J., 1994. Calculation of vitrinite reflectance from thermal histories and peak temperature: a comparison of methods. In: P. K. Mukhopadhyay and W. G. Dow (Eds), *Vitrinite Reflectance as a Maturity Parameter*. American Chemical Society Symposium series, **570**, 216-229.

BARKER, C. E., BONE, Y. and LEWAN, M. D., 1998. Fluid inclusion and vitrinite-reflectance geothermometry compared to heat-flow models of maximum paleotemperature next to dikes, western onshore Gippsland Basin, Australia. *International Journal of Coal Geology*, **37** (1-2), 73-111.

BARKER, C. E. and LEWAN, M. D., 1999. The effect of supercritical water on vitrinite reflectance as observed in contact metamorphism and pyrolysis experiments. *American Chemical Society 217th National Meeting*, Anaheim, CA, United States, March 21-25, 1999. 411-414.

BARNARD, P. C., COLLINS, A. G. and COOPER, B. S., 1981. Generation of hydrocarbons - time, temperature and source rock quality. In: J. Brooks (Ed), *Organic Maturation Studies and Fossil Fuel Exploration*. Academic Press, 337-342.

BATTEN, D. J., 1980. Use of transmitted light microscopy of sedimentary organic matter for evaluation of hydrocarbon source potential. *Proceedings IV International Palynological Conference, Lucknow, (1976-77)*, **2**, 589-594.

BATTEN, D. J., 1981. Palynofacies, organic maturation and source potential for petroleum. In: J. Brooks (Ed), *Organic maturation studies and fossil fuel exploration*. Academic Press, London, 201-223.

BATTEN, D. J., 1982. Palynofacies, palaeoenvironments and petroleum. *Journal of Micropalaeontology*, **1**, 107-114.

BATTEN, D. J., 1983. Identification of amorphous sedimentary organic matter by transmitted light microscopy. In: J. Brooks (Ed), *Petroleum geochemistry and exploration of Europe*. Geological Society Special Publication. Blackwell Scientific, **12**, 275-287.

BEARDSMORE, G. R. and CULL, J. P., 2001. *Crustal Heat Flow: A Guide to Measurement and Modelling*. Cambridge University Press.

BELL, B. R. and HARRIS, J. W., 1986. *An Excursion Guide to the Geology of the Isle of Skye*. Geological Society of Glasgow, 317pp.

BISHOP, A. N. and ABBOT, G. D., 1993. The interrelationship of biological marker maturity parameters and molecular yields during contact metamorphism. *Geochimica et Cosmochimica Acta*, **57**, 3661-3668.

BISHOP, A. N. and ABBOTT, G. D., 1995. Vitrinite reflectance and molecular geochemistry of Jurassic sediments: the influence of heating by Tertiary dykes (northwest Scotland). *Organic Geochemistry*, **22** (1), 165-177.

BONE, Y. and RUSSELL, N. J., 1988. Correlation of vitrinite reflectivity with fluid inclusion microthermometry: assessment of the technique in the Cooper/Eromanga basins, South Australia. *Australian Journal of Earth Sciences*, **35**, 567-570.

BOSTICK, N. H., 1970. Thermal alteration of clastic organic particles (phytoclads) as an indicator of contact and burial metamorphism in sedimentary rocks. Ph.D. Thesis, Stanford University.

BOSTICK, N. H., 1971. Thermal alteration of clastic organic particles as an indicator of contact and burial metamorphism in sedimentary rocks. *Geoscience and Man*, **3**, 83-93.

BOSTICK, N. H., 1973. Time as a factor in thermal metamorphism of phytoclasts. *Congres International de Stratigraphie et de Geologie du Carbonifere Septieme*, Krefeld. 183-193.

BOSTICK, N. H. and PAWLEWICZ, M. J., 1984a. Regional variation of vitrinite reflectance of the Pierre Shale (Upper Cretaceous) in mountain basins and along the eastern Rocky Mountain front, Colorado. *In: J. Woodward, F. F. Meissner and J. L. Clayton (Eds), Hydrocarbon source rocks of the greater Rocky Mountain region. Rocky Mountain Association of Geologists 1984 symposium*, Denver, CO, United States, 393-399.

BOSTICK, N. H. and PAWLEWICZ, M. J., 1984b. Paleotemperatures based on vitrinite reflectance of shales and limestones in igneous dike aureoles in the Upper Cretaceous Pierre Shale, Walsenburg, Colorado. *In: J. Woodward, F. F. Meissner and J. L. Clayton (Eds), Hydrocarbon source rocks of the Greater Rocky Mountain region. Rocky Mountain Association of Geologists*, Denver, Colorado, 387-392.

BOTT, M. H. P. and TUSON, J., 1973. Deep Structure beneath the Tertiary Volcanic Regions of Skye, Mull and Ardnamurchan, northwest Scotland. *Nature; Physical Science (London)*, **242** (121), 114-116.

BRIGAUD, F., CHAPMAN, D. S. and LE DOUARAN, S., 1990. Estimating thermal conductivity in sedimentary basins using lithological data and geophysical well logs. *American Association of Petroleum Geologists Bulletin*, **74** (1459-1477).

BUI SKOOL TOXOPEUS, J. M. A., 1983. Selection criteria for the use of vitrinite reflectance as a maturity tool. *In: J. Brooks (Ed), Petroleum Geochemistry and Exploration of Europe. Geological Society Special Publication*, **12**, 295-307.

BURGESS, J. D., 1974. Microscopic examination of kerogen (Dispersed Organic Matter) in petroleum exploration. *Geological Society of America. Special Paper 153*, 19-30.

BURNHAM, A. K. and SWEENEY, J. J., 1989. A chemical kinetic model of vitrinite maturation and reflectance. *Geochimica et Cosmochimica Acta*, **53**, 2649-2657.

CARR, A. D., 2000. Suppression and retardation of vitrinite reflectance; Part 2, Derivation and testing of a kinetic model for suppression. *Journal of Petroleum Geology*, **23** (4), 475-496.

CARSLAW, H. S. and JAEGER, J. C., 1959. *Conduction of Heat in Solids*. Oxford University Press, 510 pp.

CECIL, B. C., STANTON, R. W. and ROBBINS, E. I., 1977. Geological factors controlling coalification and hydrocarbon maturation. *American Association of Petroleum Geologists Bulletin*, **61** (5), 775.

CERMAK, V. and RYBACH, L., 1982. Thermal properties. In: K.-H. Hellwege (Ed), *Landolt-Börnstein Numerical Data and Functional Relationships in Science and Technology: Physical Properties of Rocks*. Group V. Geophysics and Space Research. Springer-Verlag, **1a**, Berlin. Heidelberg. New York, 305-371.

CHAO, E. C. T., MINKIN, J. A. and THOMPSON, C. L., 1982. Application of automated image analysis to coal petrography. *International Journal of Coal Geology*, **2** (2), 113-150.

CLAYTON, G., HAUGHEY, N., SEVASTOPULO, G. D. and BURNETT, R., 1989. Thermal maturation levels in the Devonian and Carboniferous of Ireland. ISBN 0951500600, *Geological Survey of Ireland*, 36 pp.

COLLINS, A., 1990. The 1-10 Spore Colour Index (SCI) Scale: a universally applicable colour maturation scale, based on graded, picked palynomorphs. In: W. J. J. Fermont and J. W. Weegink (Eds), *International Symposium on Organic Petrology*. Mededelingen rijks geologische dienst, **45**, 39-47.

COMBAZ, A., 1980. Les kérogènes vus au microscope. In: B. Durand (Ed), *Kerogen: Insoluble Organic Matter from Sedimentary Rocks*. Editions Technip, Paris, 55-111.

CONNOR, C. B., LICHTNER, P. C., CONWAY, F. M., HILL, B. E., OVSYANNIKOV, A. A., FEDERCHENKO, I., DOUBIK, Y., SHAPAR, V. N. and TARAN, Y. A., 1997. Cooling of an igneous dike 20 yr after intrusion. *Geology*, **25** (8), 711-714.

CORCORAN, D. V. and CLAYTON, G., 2001. Interpretation of vitrinite reflectance profiles in sedimentary basins, onshore and offshore Ireland. In: P. M. Shannon, P. D. W. Haughton and D. V. Corcoran (Eds), *The Petroleum Exploration of Ireland's Offshore Basins*. Geological Society, London, Special Publications, **188**, 61-90.

COX, K. G., BELL, J. D. and PANKHURST, R. J., 1979. The Interpretation of Igneous Rocks. Allen and Unwin, 450 pp.

CRELLING, J. C. and DUTCHER, R. R., 1968. A petrologic study of a thermally altered coal from the Purgatoire River Valley of Colorado. *Geological Society of America Bulletin*, **79**, 1375-1386.

DALLA TORRE, M., FERREIRO MÄHLMANN, R. and ERNST, W. G., 1997. Experimental study on the pressure dependence of vitrinite maturation. *Geochimica et Cosmochimica Acta*, **61** (14), 2921-2928.

DAVID, P. and FERMONT, W. J. J., 1993. Advances of colour image analyses of organic matter. *Organic Geochemistry*, **20**, 747-758.

DELANEY, P. T., 1982. Rapid intrusion of magma into wet rock: groundwater flow due to pore pressure increases. *Journal of Geophysical research*, **87** (B9), 7739-7756.

DELANEY, P. T. and POLLARD, D. D., 1982. Solidification of basaltic magma during flow in a dike. *American Journal of Science*, **282**, 856-885.

DELANEY, P. T., 1987. Heat transfer during emplacement and cooling of mafic dykes. In: H. C. Halls and W. F. Fahrig (Eds), *Mafic Dyke Swarms*. Geological Association of Canada Special Paper, **34**, 31-46.

DELANEY, P. T., 1988. FORTRAN 77 programs for conductive cooling of dikes with temperature-dependent thermal properties and heat of crystallization. *Computers and Geosciences*, **14** (2), 181-212.

DEMONGODIN, L., PINOTEAU, B., VASSEUR, G. and GABLE, R., 1991. Thermal conductivity and well logs: a case study in the Paris Basin. *Geophysical Journal International*, **105**, 675-691.

DURAND, B., ALPERN, B., PITTION, J. L. and PRADIER, B., 1985. Reflectance of vitrinite as a control of thermal history of sediments. *1st IFP Exploration Research Conference*, Carcans, France, June 3-7, 1985. 441-474.

EHRlich, R., KENNEDY, S. K., CRABTREE, S. J. and CANNON, R. L., 1984. Petrographic image analysis; I, Analysis of reservoir pore complexes. *Journal of Sedimentary Petrology*, **54** (4), 1365-1378.

EMELEUS, C. H., 1982. The central complexes. In: D. S. Sutherland (Ed), *Igneous Rocks of the British Isles*. John Wiley and Sons, 369-414.

EMELEUS, C. H., 1983. Tertiary igneous activity. In: G. Y. Craig (Ed), *Geology of Scotland*. Scottish Academic Press, 357-397.

EPSTEIN, A. G., EPSTEIN, J. B. and HARRIS, L. D., 1977. Conodont Colour Alteration - an index to organic metamorphism. *U.S. Geological Survey Professional Paper*, **995**, 27 pp.

EVANS, T. R., 1977. Thermal properties of North Sea rocks. *Log Analyst*, **18** (2), 3-12.

FANG, H. and JIANYU, C., 1992. The cause and mechanism of vitrinite reflectance anomalies. *Journal of Petroleum Geology*, **15** (4), 419-434.

FENSTER, D. F., DAVIS, G. H. and KASHATUS, G. P., 1999. Yucca Mountain Site Project: Geology/Hydrology Environmental Baseline File. B00000000-01717-5700-00027

REV 01, DCN 1, *Civilian Radioactive Waste Management System Management and Operating Contractor*, Las Vegas, Nevada, Section 4.4.2.1
<http://www.ymp.gov/documents/geology>.

FISHER, M. J., BARNARD, P. C. and COOPER, B. S., 1980. Organic maturation and hydrocarbon generation in the mesozoic sediments of the Sverdrup Basin, Arctic Canada. *Proceedings IV International Palynological Conference, Lucknow, (1976-77)*, **2**, 581-588.

FITZGERALD, L. G., 1994. Thermal maturation of the Lower Carboniferous sequence in the vicinity of the Navan Zn/Pb Orebody and the Athboy area, Co. Meath, Ireland. Ph.D. Thesis, University of Dublin, Trinity College, 218 pp.

FURLONG, K. P., HANSON, R. B. and BOWERS, J. R., 1991. Modeling Thermal Regimes. In: D. M. Kerrick (Ed), *Contact Metamorphism*. Reviews in Mineralogy. Mineralogical Society of America, **26**, Washington DC, 437-505.

GIBSON, S. A., 1990. The geochemistry of the Trotternish sills, Isle of Skye: crustal contamination in the British Tertiary Volcanic Province. *Journal of the Geological Society*, **147**, 1071-1081.

GILLIAM, T. M. and MORGAN, I. L., 1987. Shale: Measurement of Thermal Properties, *Oak Ridge National Laboratory*, ORNL/TM-10499.

GOODARZI, F., 1987. The use of automated image analysis in coal petrology. *Canadian Journal of Earth Sciences*, **24** (5), 1064-1069.

GOODHUE, R. J. D., 1996. A palynofacies, geochemical and maturation investigation of the Namurian rocks of County Clare. Ph.D. Thesis, University of Dublin, Trinity College, 168 pp.

GRAYSON, J. F., 1975. Relationship of palynomorph translucency to carbon and hydrocarbons in clastic sediments. In: B. Alpern (Ed), *Pétrographie de la Matière*

Organique des Sédiments, Relations avec la Paléotempérature et le Potential Pétrolier.
Editions du Centre National de la Recherche Scientifique, Anatole, 261-273.

GREEN, P. F., DUDDY, I. R., HEGARTY, K. A. and BRAY, R. J., 1999. Early Tertiary heat flow along the UK Atlantic margin and adjacent areas. *In: A. J. Fleet and S. A. R. Boldy (Eds), Petroleum Geology of Northwest Europe: Proceedings of the 5th Conference.* The Geological Society, London, 349-357.

GREGORY, W. A., CHINN, E. W., SASSEN, R. and HART, G. F., 1991. Fluorescent microscopy of particulate organic matter: Sparta Formation and Wilcox Group, South Central Louisiana. *Organic Geochemistry*, **17** (1), 1-9.

GURBA, L. W. and WEBER, C. R., 2001. Effects of igneous intrusions on coalbed methane potential, Gunnedah Basin, Australia. *International Journal of Coal Geology*, **46**, 113-131.

GUTJAHR, C. C. M., 1966. Carbonization of pollen grains and spores and their application. *Leidse Geologische Medelingen*, **38**, 1-30.

GUTJAHR, C. C. M., 1983. Introduction to incident-light microscopy of oil and gas source rocks. *Geologie en Mijnbouw*, **62**, 417-425.

HANLEY, E. J., DEWITT, D. P. and ROY, R. F., 1978. The thermal diffusivity of eight well-characterized rocks for the temperature range 300-1000 K. *Engineering Geology*, **12**, 31-47.

HELSON, S., DAVID, P. and FERMONTE, J. J., 1995. Calibration of conodont color alteration using colour image analysis. *Journal of Geology*, **103**, 257-267.

HÉROUX, Y., CHAGNON, A. and BERTRAND, R., 1979. Compilation and correlation of major thermal maturation indicators. *American Association of Petroleum Geologists Bulletin*, **63**, 2128-2144.

HESSELBO, S. P., OATES, M. J. and JENKYNS, H. C., 1998. The lower Lias Group of the Hebrides Basin. *Scottish Journal of Geology*, **34** (No. 1), 1-38.

HESSELBO, S. P. and COE, A. L., 2000. Jurassic sequences of the Hebrides Basin, Isle of Skye, Scotland. In: J. R. Graham and A. Ryan (Eds), *IAS Dublin September 2000. Field Trip Guidebook*. International Association of Sedimentologists - Enterprise Oil, 41-58.

HILLIER, S. and MARSHALL, J., 1988. A rapid technique to make polished thin sections of sedimentary organic matter concentrates. *Journal of Sedimentary Petrology*, **58**, 754-755.

HOLMAN, J. P., 1990. Heat Transfer. McGraw-Hill Inc., 714 pp.

HOOD, A., GUTJAHR, C. C. M. and HEACOCK, R. L., 1975. Organic metamorphism and the generation of petroleum. *American Association of Petroleum Geologists Bulletin*, **59**, 986-996.

HUDSON, J. D., 1983. Mesozoic sedimentation and sedimentary rocks in the Inner Hebrides. *Proceedings of the Royal Society of Edinburgh*, **83B**, 47-63.

HUGHES, C. J., 1982. Igneous Petrology, Developments in Petrology. Elsevier Scientific Publishing Co., 551 pp.

INTERNATIONAL COMMITTEE FOR COAL PETROLOGY (I.C.C.P.), 1971. Determination of rank by reflectance measurement of vitrinite, *International Handbook of Coal Petrography: supplement to the 2nd edition*. Centre National de la Recherche Scientifique, Paris, 16 pp.

INTERNATIONAL COMMITTEE FOR COAL PETROLOGY (I.C.C.P.), 1998. Vitrinite Classification; ICCP System 1994. *Fuel*, **77** (5), 349-358.

ISHIWATARI, R., ISHIWATARI, M., ROHRBACK, B. G. and KAPLAN, I. R., 1977. Thermal alteration experiments on organic matter from recent marine sediments in relation to petroleum genesis. *Geochimica et Cosmochimica Acta*, **41**, 815-828.

JAEGER, J. C., 1959. Temperatures outside a cooling intrusive sheet. *American Journal of Science*, **257**, 44-54.

JANSONIUS, J. and SCHWAB, K. W., 1996. Appendix to 26B - Palynofacies and Petroleum Potential. In: J. Jansonius and D. C. McGregor (Eds), *Palynology: principles and applications*. American Association of Stratigraphic Palynologists Foundation, **3**, 1075-1084.

JOHNSSON, M. J., HOWELL, D. G. and BIRD, K. J., 1993. Thermal maturity patterns in Alaska: implications for tectonic evolution and hydrocarbon potential. *American Association of Petroleum Geologists Bulletin*, **77** (11), 1874-1903.

KARWEIL, J., 1955. Die Metamorphose der Kohlen vom Standpunkt der physikalischen Chemie. *Deutsche Geologische Gesellschaft Zeitschrift*, **107**, 132-139.

KHORASANI, G. K. and MURCHISON, D. G., 1990. Molecular disordering in natural cokes approaching dyke and sill contacts. *Fuel*, **69**, 1037-1046.

LAW, B. E., NUCCIO, V. F. and BARKER, C. E., 1989. Kinky vitrinite reflectance well profile: evidence of paleopore pressure in low-permeability, gas-bearing sequences in Rocky Mountain Foreland Basins. *The American Association of Petroleum Geologists Bulletin*, **73**, 999-1010.

LEWAN, M. D., 1986. Stable carbon isotopes of amorphous kerogens from Phanerozoic sedimentary rocks. *Geochimica et Cosmochimica Acta*, **50**, 1583-1591.

LEWIS, C. L. E., CARTER, A. and HURFORD, A., 1992. Low-temperature effects of the Skye Tertiary intrusions on Mesozoic sediments in the Sea of the Hebrides basin. In: J.

Parnell (Ed), *Basins on the Atlantic Seaboard: Petroleum Geology, Sedimentology and Basin Evolution*. Geological Society Special Publication, **62**, 175-188.

LIN, R. and DAVIS, A., 1988. A fluorogeochemical model for coal macerals. *Organic Geochemistry*, **12**, 363-374.

LOPATIN, N. V., 1971. Temperature and geological time as factors in coalification. *Akademiya Nauk SSSR Izvestiya, Ser. Geologicheskaya*, **3**, 95-106.

MACDONALD, G. A. and KATSURA, T., 1964. Chemical composition of Hawaiian lavas. *Journal of Petrology*, **5**, 82-133.

MARSHALL, J. E. A., 1991. Quantitative spore colour. *Journal of the Geological Society (London)*, **148**, 223-233.

MARSHALL, J. E. A. and YULE, B. L., 1999. Spore colour measurement. In: T. P. Jones and N. P. Rowe (Eds), *Fossil plants and spores; modern techniques*, 165-168.

MASRAN, T. C. and POCOCK, S. A. J., 1981. The classification of plant-derived particulate organic matter in sedimentary rocks. In: J. Brooks (Ed), *Organic Maturation and Fossil Fuel Exploration*. Academic Press, London, 145-161.

MCCANN, N., 1990. The subsurface geology between Belfast and Larne. *Irish Journal of Earth Sciences*, **10**, 157-173.

MCCANN, N., 1991. Subsurface geology of the Lough Neagh - Larne Basin, Northern Ireland. *Irish Journal of Earth Sciences*, **11** (1), 53-64.

MCCORMACK, N., GOODHUE, R., DOFF, D. and CLAYTON, G., 1997. Response rates of organic maturation indicators in Carboniferous shales intruded by the Tertiary North Star Dyke at Ballycastle, Co. Antrim. *Clay Mineral Evolution, Basin Maturity and Mudrock Properties*, British Geological Survey, Keyworth, Nottingham, U.K. 25.

MCCORMACK, N. J., 1998. The thermal history of the South Portuguese Zone. Ph.D. Thesis, University of Dublin, Trinity College, 179 pp.

MCTAVISH, R. A., 1978. Pressure retardation of vitrinite diagenesis, offshore north-west Europe. *Nature*, **271**, 648-650.

MCTAVISH, R. A., 1998. The role of overpressure in the retardation of organic matter maturation. *Journal of Petroleum Geology*, **21** (2), 153-186.

MELLERE, D. and STEEL, R. J., 1996. Tidal sedimentation in the Inner Hebrides half grabens, Scotland: the Mid-Jurassic Bearerraig Sandstone Formation. *In*: M. De Batist and P. Jacobs (Eds), *Geology of Siliclastic Shelf Seas*. Geological Society Special Publication, **117**, 49-79.

MERRIMAN, R. J. and KEMP, S. J., 1997. Correlating clay mineral reaction progress with organic maturity indicators. *Clay Mineral Evolution, Basin Maturity and Mudrock Properties*, British Geological Survey, Keyworth, Nottingham, U.K. 41-42.

MEYERS, P. A. and SIMONEIT, B. R. T., 1999. Effects of extreme heating on the elemental and isotopic compositions of an Upper Cretaceous coal. *Organic Geochemistry*, **30**, 299-305.

MICHELSSEN, J. K. and KHORASANI, G. K., 1995. The kinetics of thermal degradation of individual oil-generating macerals: calibration with microscopical fluorescence spectrometry and bulk flow pyrolysis. *Organic Geochemistry*, **22** (1), 179-189.

MIDTTØMME, K. and ROALDSET, E., 1999. Thermal conductivity of sedimentary rocks: uncertainties in measurement and modelling. *In*: A. C. Alpin, A. C. Fleet and J. H. S. Macquaker (Eds), *Muds and Mudstones: Physical and Fluid Flow Properties*. Geological Society of London, Special Publications, **158**, 45-60.

MORIN, R. and SILVA, A. J., 1984. The effects of high pressure and high temperature on some physical properties of ocean sediments. *Journal of Geophysical research*, **89** (B1), 511-526.

MORROW, D. W. and ISSLER, D. R., 1993. Calculation of vitrinite reflectance from thermal histories: a comparison of some methods. *American Association of Petroleum Geologists*, **77** (4), 610-624.

MORTON, N., 1987. Jurassic subsidence history in the Hebrides, N.W. Scotland. *Marine and Petroleum Geology*, **4**, 226-242.

MORTON, N. and HUDSON, J. D., 1995. Field Guide to the Jurassic of the Isles of Raasay and Skye, Inner Hebrides, NW Scotland. In: P. Taylor (Ed), *Field Geology of the British Jurassic*. The Geological Society, London, 209-280.

MUSSETT, A. E., DAGLEY, P. and SKELHORN, R. R., 1988. Time and duration of activity in the British Tertiary Igneous Province. In: A. C. Morton and L. M. Parson (Eds), *Early Tertiary Volcanism and the Opening of the NE Atlantic*. Geological Society of London Special Publication, **39**, 337-348.

NAYLOR, D. and SHANNON, P. M., 1982. The Geology of Offshore Ireland and West Britain. Graham and Trotman.

NAYLOR, D., 1992. The post-Variscan history of Ireland. In: J. Parnell (Ed), *Basins on the Atlantic Seaboard: Petroleum Geology, Sedimentology and Basin Evolution*. Geological Society Special Publication, **62**, 255-275.

NUCCIO, V. F., 1985. Comparison between immature vitrinite and solid bitumen, Green River Formation, Piceance Creek Basin, Colorado. AAPG annual convention with divisions SEPM/EMD/DPA. *American Association of Petroleum Geologists Bulletin*, **69** (2), 293 (abstract).

NUSSBAUM, F., 1928. *Zeitschrift für angewandte Mathematik und Mechanik*, **8**, 133-142.

OBERLIN, A., BOULMIER, J. L. and VILLEY, M., 1980. Electron microscopic study of kerogen microtexture. Selected criteria for determining the evolution path and evolution of kerogen. *In: B. Durand (Ed), Kerogen, insoluble organic matter from sedimentary rocks.* Editions Technip, Paris, 191-242.

OXBURGH, E. H. and ANDREWS-SPEED, C. P., 1981. Temperature, thermal gradients and heat flow in southwestern North Sea. *In: L. V. Illing and G. D. Hobson (Eds), Petroleum Geology of the Continental Shelf of Northwest Europe.* Heydon Press, London, 141-151.

PEACOCK, S. M., 1989. Thermal modeling of metamorphic pressure-temperature-time paths: a forward approach. *In: F. S. Spears and S. M. Peacock (Eds), Metamorphic Pressure-Temperature-Time Paths.* American Geophysical Union Short Course in Geology, 7, 57-102.

PEACOCK, S. M., 1990. Numerical simulation of regional and contact metamorphism using the Macintosh microcomputer. *Journal of Geological Education*, 38, 132-137.

PEARCE, J. A. and CANN, J. R., 1973. Tectonic setting of basic volcanic rocks determined using trace element analyses. *Earth and Planetary Science Letters*, 19, 290-300.

PEARSON, D. L., 1982. Approaching a pollen/spore color standard. *Palynology*, 6, 289.

PRICE, L. C., 1983. Geologic time as a parameter in organic metamorphism and vitrinite reflectance as an absolute palaeogeothermometer. *Journal of Petroleum Geology*, 6, 5-38.

PRICE, L. C. and BARKER, C. E., 1985. Suppression of vitrinite reflectance in amorphous-rich kerogen: a major unrecognised problem. *Journal of Petroleum Geology*, 6, 5-38.

RAYMOND, A. C. and MURCHISON, D. G., 1988. Development of organic maturation in the thermal aureoles of sills and its relation to sediment compaction. *Fuel*, **67**, 1599-1608.

RAYMOND, A. C. and MURCHISON, D. G., 1992. Effect of igneous activity on molecular-maturation indices in different types of organic matter. *Organic Geochemistry*, **18**, 725-735.

ROBERT, P., 1980. The Optical evolution and geothermal histories applied to oil and gas exploration. In: B. Durand (Ed), *Kerogen. Insoluble organic matter from sedimentary rocks*. Edition Technip, Paris, 385-414.

ROBERT, P., 1988. Organic Metamorphism and Geothermal History: Microscopic Study of Organic Matter and Thermal Evolution of Sedimentary Basins. Reidel, 311 pp.

ROBISON, C. R., VAN GIJZEL, P. and DARNELL, L. M., 2000. The transmittance color index of amorphous organic matter: a thermal maturity indicator of petroleum source rocks. *International Journal of Coal Geology*, **43** (1-4), 83-103.

ROY, R. F., BECK, A. E. and TOULOUKIAN, Y. S., 1981. Thermophysical Properties of Rocks. In: Y. S. Touloukian, W. R. Judd and R. F. Roy (Eds), *Physical Properties of Rocks and Minerals*. CINDAS Data Series on Material Properties. McGraw-Hill, **II-2**, 409-502.

RUZYLA, K., 1986. Characterization of pore space by quantitative image analysis. *SPE Formation Evaluation*, **1** (4), 389-398.

SANFORD, S. J. and ELDERS, W. A., 1981. Dating thermal events by fission-track annealing in wells M-94 and T-366 at Cerro Prieto. *Third Symposium on the Cerro Prieto geothermal field, Baja California, Mexico*, San Francisco, March 1981. (Abstract).

SCHMIDT, E., 1924. Föppl's Festschrift. Springer.

SCHÖN, J. H., 1996. *Physical Properties of Rocks: Fundamentals and Principles of Petrophysics, Seismic Exploration*. Pergamon, 583 pp.

SCHWAB, K. W., 1990. Visual Kerogen Assessment. *Geo-Strat Inc., Organic Petrology Seminar*, Zeist, Netherlands. 131 pp.

SCHWAB, K. W., SMITH, M. A. and VAN GIJZEL, P., 1995a. Electronic TAI measurements using the ICA/SPD technique; a better method for defining thermal maturity than vitrinite reflectance. *27th annual meeting of the American Association of Stratigraphic Palynologists*, College Station, TX, United States, November 1-5, 1994. 248.

SCHWAB, K. W., SMITH, M. A. and VAN GIJZEL, P., 1995b. Electronic color analysis of Staplin's TAI standards. *27th annual meeting of the American Association of Stratigraphic Palynologists*, College Station, TX, United States, November 1-5, 1994. 248.

SEARL, A., 1994. Diagenetic destruction of reservoir potential in shallow marine sandstones of the Broadford Beds (Lower Jurassic), north-west Scotland: depositional versus burial and thermal history controls on porosity destruction. *Marine and Petroleum Geology*, **11** (No. 2), 131-147.

SIDDER, G. B., 1994. PETRO.CALC.PLOT, Microsoft Excel macros to aid petrologic interpretation. *Computers and Geosciences*, **20** (6), 1041-1061.

SMITH, P. M. R., 1983. Spectral correlation of spore coloration standards. In: J. Brooks (Ed), *Petroleum geochemistry and exploration of Europe*. Geological Society Special Publication. Blackwell Scientific, **12**, 289-294.

SMITH, P. M. R., 1984. The use of fluorescence microscopy in the characterisation of amorphous organic matter. *Organic Geochemistry*, **6**, 839-845.

SPEIGHT, J. M., SKELHORN, R. R., SLOAN, T. and KNAPP, R. J., 1982. The dyke swarms of Scotland. In: D. S. Sutherland (Ed), *Igneous rocks of the British Isles*. Wiley-Interscience, Chichester.

STAPLIN, F. L., 1969. Sedimentary organic matter, organic metamorphism and oil and gas occurrence. *Bulletin Canadian Petroleum Geology*, **17**, 47-66.

STAPLIN, F. L., 1977. Interpretation of thermal history from color of particulate organic matter; a review. *Palynology*, **1**, 9-18.

STOPEs, M. C., 1935. On the petrology of banded bituminous coal. *Fuel*, **14**, 4-13.

SUGGATE, R. P., 1982. Low-rank sequences and scales of organic metamorphism. *Journal of Petroleum Geology*, **4**, 377-392.

SUZUKI, N., MATSUBAYASHI, H. and WAPLES, D. W., 1993. A simpler kinetic model of vitrinite reflectance. *The American Association of Petroleum Geologists Bulletin*, **77**, 1502-1508.

SWAN, A. R. H. and SANDILANDS, M., 1995. Introduction to Geological Data Analysis. Blackwell Science Ltd., 446 pp.

SWARZER, R. R. and ROGERS, J. J. W., 1974. A worldwide comparison of alkali olivine basalts and their differentiation trends. *Earth and Planetary Science Letters*, **23**, 286-296.

SWEENEY, J. J. and BURNHAM, A. K., 1990. Evaluation of a simple model of vitrinite reflectance based on chemical kinetics. *The American Association of Petroleum Geologists Bulletin*, **74** (10), 1559-1570.

SYKES, R. M., 1975. The stratigraphy of the Callovian-Oxfordian (Middle-Upper Jurassic) in northern Scotland. *Scottish Journal of Geology*, **11**, 51-78.

TAYLOR, G. H., TEICHMULLER, M., DAVIS, A., DIESSEL, C. F. K., LITCKE, R. and ROBERT, P., 1998. Organic Petrology, a new handbook incorporating some revised parts of Stach's Textbook of Coal Petrology. Borntraeger, 704 pp.

TAYLOR, H. P. and FORESTER, R. W., 1977. $^{18}\text{O}/^{16}\text{O}$, D/H and $^{13}\text{C}/^{12}\text{C}$ studies of the Tertiary igneous complex of Skye, Scotland. *American Journal of Science*, **277**, 136-177.

TEICHMÜLLER, M. and TEICHMÜLLER, R., 1968. Geological aspects of coal metamorphism. In: D. G. Murchison and T. S. Westoll (Eds), *Coal and Coal-Bearing Strata*. Oliver and Boyd, Edinburgh, 233-267.

TEICHMÜLLER, M., 1974. Generation of petroleum-like substances in coal seams as seen under the microscope. In: B. Tissot and K. Bennier (Eds), *Advances in Organic Geochemistry 1973*. Technip, Paris, 321-348.

TEICHMÜLLER, M. and WOLF, M., 1977. Application of fluorescence microscopy in coal petrology and oil exploration. *Journal of Microscopy*, **109** (1), 49.

TEICHMÜLLER, M. and TEICHMÜLLER, R., 1979. Diagenesis of coal (coalification). In: G. Larsen and G. V. Chilingar (Eds), *Diagenesis in Sediments and Sedimentary Rocks*. Elsevier, Amsterdam, 207-24

TEICHMÜLLER, M., 1980. A coalification section along a geotraverse west of the Rhine between Schleiden and Aachen. In: Closs (Ed), *Mobile Earth*. International Geodynamics Project, Boldt: Boppard, 204-206.

TEICHMÜLLER, M., 1982. Origin of the petrographic constituents of coal. In: E. Stach, M.-T. Mackowsky, M. Taylor, D. Chandra and R. Teichmuller (Eds), *Stach's Textbook of Coal Petrology*. Gebruder Borntraeger, Berlin/Stuttgart, 219-294.

TEICHMÜLLER, M., 1987. Recent advances in coalification studies and their application to geology. In: A. C. Scott (Ed), *Coal and Coal-Bearing Strata: Recent Advances*. Blackwell Scientific, **32**, Oxford, 127-170.

THOMPSON, R. N., ESSON, J. and DUNHAM, A. C., 1972. Major element chemical variation in the Eocene lavas of the Isle of Skye, Scotland. *Journal of Petrology*, **13**, 219-253.

THRASHER, J., 1992. Thermal effect of the Tertiary Cullins intrusive complex in the Jurassic of the Hebrides: an organic geochemical study. *In: J. Parnell (Ed), Basins on the Atlantic Seaboard: Petroleum Geology, Sedimentology, and Basin Evolution*. Geological Society of London Special Publication, **62**, 35-49.

TING, F. T. C., 1991. Review of vitrinite reflectance techniques and applications. *Organic Geochemistry*, **17** (2), 269-270.

TISSOT, B. P. and WELTE, D. H., 1978. Petroleum formation and occurrence. Springer-Verlag-Berlin, 538 pp.

TOBIN, R. C. and CLAXTON, B. L., 2000. Multidisciplinary thermal maturity studies using vitrinite reflectance and fluid inclusion microthermometry: A new calibration of old techniques. *American Association of Petroleum Geologists Bulletin*, **84** (10), 1647-1665.

TRAVERSE, A., 1988. Palaeopalynology. Unwin Hyman, 600 pp.

TURCOTTE, D. L. and SCHUBERT, G., 2002. Geodynamics. Cambridge University Press.

TYSON, R. V., 1984. Palynofacies investigation of Callovian (Middle Jurassic) sediments from DSDP site 534, Blake-Bahama Basin, western central Atlantic. *Marine and Petroleum Geology*, **1**, 3-13.

TYSON, R. V., 1989. Late Jurassic palynofacies trends, Piper and Kimmeridge Clay Formations, UK onshore and northern North Sea. *In: D. J. Batten and M. Keen (Eds), Northwest European Micropalaeontology and Palynology*. British Micropalaeontological Society Series. British Micropalaeontological Society Series, Ellis Horwood, Chichester, 135-172.

TYSON, R. V., 1990. Automated transmitted light kerogen typing by image analysis: 1. General aspects and program description. *Proceedings 1st Symposium in Organic Petrology*, Zeist, January 1990. 139-150.

TYSON, R. V., 1995. *Sedimentary Organic Matter: Organic Facies and Palynofacies*. Chapman and Hall, 615.

VAN DE LAAR, J. G. M. and DAVID, P., 1998. Determination of spore colour alteration by means of colour image analysis. *Review of Palaeobotany and Palynology*, **103** (1-2), 41-44 (extended abstract).

VAN GIJZEL, P., 1989. Transmittance color index (TCI) of amorphous organic matter; new thermal maturity indicator for hydrocarbon source rocks, correlation with mean vitrinite reflectance and thermal alteration index (TAI). *American Association of Petroleum Geologists Bulletin*, **73** (9), 1177.

VENKATACHALA, B. S., 1981. Differentiation of amorphous organic matter types in sediments. In: J. Brooks (Ed), *Organic Maturation and Fossil Fuel Exploration*. Academic Press, London, 177-200.

WAPLES, D. W., 1980. Time and temperature in petroleum formation. *American Association of Petroleum Geologists Bulletin*, **64**, 916-926.

WAPLES, D. W., KAMATA, H. and SUIZU, M., 1992a. The art of maturity modelling. Part 1: Finding a satisfactory geological model. *American Association of Petroleum Geologists Bulletin*, **76**, 31-46.

WAPLES, D. W., SUIZU, M. and KAMATA, H., 1992b. The art of maturity modelling. Part 2: Alternative models and sensitivity analysis. *American Association of Petroleum Geologists Bulletin*, **76**, 47-66.

WILSON, H. E., 1972. *Regional Geology of Northern Ireland*. Geological Survey of Northern Ireland, 115 pp.

YULE, B., ROBERTS, S., MARSHALL, J. E. A. and MILTON, J. A., 1998. Quantitative spore colour measurement using colour image analysis. *Organic Geochemistry*, **28** (3/4), 139-149.

YULE, B., CARR, A. D., MARSHALL, J. E. A. and ROBERTS, S., 1999. Spore transmittance (%St): a quantitative method for spore colour analysis. *Organic Geochemistry*, **30**, 567-581.

YULE, B. L., ROBERTS, S. and MARSHALL, J. E. A., 2000. The thermal evolution of sporopollenin. *Organic Geochemistry*, **31** (9), 859-870.

ZIEGLER, P. A., 1990. Geological atlas of western and central Europe. Shell International Petroleum Maatschappij BV, 239 pp.

APPENDICES

APPENDIX I

SAMPLE CATALOGUE

Sample data for the BBN horizon, Bearreraig Bay, Trotternish, northeast Skye.

TCD No.	Sample no.	VR Code	Details	Rock Sample	A. Organic Residue	B. Palynology Thin Section	C. Vitrinite Thin Section	D. Vitrinite Block	E. Petrological Thin Section	F. Conductivity Sample Discs
56151	BB01N	Mags 05	Dark grey shale, 0.00-0.03m from dyke	X	X	X	X	X		
56152	BB02N	Mags 16	Dark grey shale, 0.03-0.06m from dyke	X	X	X	X	X		
56153	BB03N	Mags 20	Dark grey shale, 0.06-0.10m from dyke	X	X	X	-	X		
56154	BB04N	Mags 08	Dark grey shale, 0.10-0.15m from dyke	X	X	X	-	X		
56155	BB05N	Mags 09	Dark grey shale, 0.15-0.20m from dyke	X	X	X	X	X		
56156	BB06N	Mags 17	Dark grey shale, 0.20-0.25m from dyke	X	X	X	X	-		
56157	BB07N	Mags 23	Dark grey shale, 0.25-0.30m from dyke	X	X	X	X	-		
56158	BB08N	Mags 39	Dark grey shale, 0.30-0.35m from dyke	X	X	X	X	X		
56159	BB09N	Mags 32	Dark grey shale, 0.35-0.40m from dyke	X	X	X	-	X		
56160	BB10N	Mags 25	Dark grey shale, 0.40-0.45m from dyke	X	X	X	X	X		
56161	BB11N	Mags 10	Dark grey shale, 0.45-0.50m from dyke	X	X	X	X	X		
56162	BB12N	Mags 03	Dark grey shale, 0.50-0.55m from dyke	X	X	X	X	-		
56163	BB13N	Mags 21	Dark grey shale, 0.55-0.60m from dyke	X	X	X	-	X		
56164	BB14N	Mags 43	Dark grey shale, 0.60-0.65m from dyke	X	X	X	X	-		
56165	BB15N	Mags 31	Dark grey shale, 0.65-0.70m from dyke	X	X	X	X	X		
56166	BB16N	Mags 38	Dark grey shale, 0.70-0.75m from dyke	X	X	X	X	X		
56167	BB17N	Mags 11	Dark grey shale, 0.75-0.80m from dyke	X	X	X	X	X		
56168	BB18N	Mags 15	Dark grey shale, 0.80-0.85m from dyke	X	X	X	X	X		X
56169	BB19N	Mags 22	Dark grey shale, 0.85-0.90m from dyke	X	X	X	X	-		
56170	BB20N	Mags 01	Dark grey shale, 0.90-0.95m from dyke	X	X	X	X	-		
56171	BB21N	Mags 04	Dark grey shale, 0.95-1.00m from dyke	X	X	X	X	X		
56172	BB22N	Mags 35	Dark grey shale, 1.00-1.10m from dyke	X	X	X	X	-		
56173	BB23N	Mags 24	Dark grey shale, 1.10-1.20m from dyke	X	X	X	-	X		
56174	BB24N	Mags 14	Dark grey shale, 1.20-1.30m from dyke	X	X	X	X	-		
56175	BB25N	Mags 07	Dark grey shale, 1.30-1.40m from dyke	X	X	X	X	-		
56176	BB26N	Mags 30	Dark grey shale, 1.35-1.40m from dyke	X	X	X	X	-		
56177	BB27N	Mags 40	Dark grey shale, 1.40-1.50m from dyke	X	X	X	X	-		
56178	BB28N	Mags 28	Dark grey shale, 1.60-1.70m from dyke	X	X	X	X	-		
56179	BB29N	Mags 37	Dark grey shale, 1.50-1.60m from dyke	X	X	X	X	-		
56180	BB30N	Mags 13	Dark grey shale, 1.70-1.80m from dyke	X	X	X	X	X		
56181	BB31N	Mags 44	Dark grey shale, 1.80-1.90m from dyke	X	X	X	X	-		
56182	BB32N	Mags 33	Dark grey shale, 1.90-2.00m from dyke	X	X	X	X	-		
56183	BB33N	Mags 26	Dark grey shale, 2.00-2.10m from dyke	X	X	X	X	-		
56184	BB34N	Mags 02	Dark grey shale, 2.30-2.40m from dyke	X	X	X	X	-		
56185	BB35N	Mags 36	Dark grey shale, 2.60-2.70m from dyke	X	X	X	X	X		
56186	BB36N	Mags 29	Dark grey shale, 2.90-3.00m from dyke	X	X	X	X	X		
56187	BB37N	Mags 19	Dark grey shale, 3.20-3.30m from dyke	X	X	X	X	-		
56188	BB38N	Mags 42	Dark grey shale, 3.50-3.70m from dyke	X	X	X	X	X		
56189	BB39N	Mags 34	SAMPLE LOST							
56190	BB40N	Mags 18	Dark grey shale, 3.80-3.90m from dyke	X	X	X	X	X		
56191	BB41N	Mags 41	Dark grey shale, 4.10-4.20m from dyke	X	X	X	X	X		
56192	BB42N	Mags 27	Dark grey shale, 4.40-4.50m from dyke	X	X	X	X	-		
56193	BB43N	Mags 12	Dark grey shale, 5.00-5.10m from dyke	X	X	X	X	-		
56194	BB44N	Mags 06	Dark grey shale, 5.50-5.60m from dyke	X	X	X	X	-		

Sample data for the BGSNN horizon, Bearreraig Bay, Trotternish, northeast Skye.

TCD No.	Sample no.	VR Code	Details	Rock Sample	A. Organic Residue	B. Palynology Thin Section	C. Vitrinite Thin Section	D. Vitrinite Block	E Petrological Thin Section	F. Conductivity Sample Discs
56195	BGSH01N		Dark grey shale, 0.00-0.05m from dyke	X	X	X	-	X		
56196	BGSH02N		Dark grey shale, 0.05-0.10m from dyke	X	X	X	-	X		X
56197	BGSH03N		Dark grey shale, 0.15-0.20m from dyke	X	X	X	-	X		
56198	BGSH04N		Dark grey shale, 0.20-0.25m from dyke	X	X	X	-	X		
56199	BGSH05N		Dark grey shale, 0.32-0.34m from dyke	X	X	X	-	X		
56200	BGSH06N		Dark grey shale, 0.35-0.40m from dyke	X	X	X	-	X		
56201	BGSH07N		Dark grey shale, 0.40-0.45m from dyke	X	X	X	-	X		
56202	BGSH08N		Dark grey shale, 0.50-0.60m from dyke	X	X	X	-	X		
56203	BGSH09N		Dark grey shale, 0.96-1.00m from dyke	X	X	X	-	X		
56204	BGSH10N		Dark grey shale, 1.30-1.40m from dyke	X	X	X	-	X		
56205	BGSH11N		Dark grey shale, 1.95-2.05m from dyke	X	X	X	-	X		
56206	BGSH12N		Dark grey shale, 3.00-3.10m from dyke	X	X	X	-	X		
56207	BGSH13N		Dark grey shale, 4.90-5.00m from dyke	X	X	X	-	X		
56208	BGSH14N		Dark grey shale, 6.70m from dyke	X	X	X	-	X		

Sample data for the BGSN horizon, Bearreraig Bay, Trotternish, northeast Skye.

TCD No.	Sample no.	VR Code	Details	Rock Sample	A. Organic Residue	B. Palynology Thin Section	C. Vitrinite Thin Section	D. Vitrinite Block	E Petrological Thin Section	F. Conductivity Sample Discs
56209	BGS01N		Sandy limestone concretionary horizon, 0.00-0.04m from dyke	X	X	X	-	X		
56210	BGS02N		Sandy limestone concretionary horizon, 0.10-0.15m from dyke	X	X	X	-	X		
56211	BGS03N		Sandy limestone concretionary horizon, 0.23-0.30m from dyke	X	X	X	-	X		
56212	BGS04N		Sandy limestone concretionary horizon, 0.70-0.80m from dyke	X	X	X	-	X		X
56213	BGS05N		Sandy limestone concretionary horizon, 2.06-2.16m from dyke	X	X	X	-	X		
56214	BGS06N		Sandy limestone concretionary horizon, 2.90-3.00m from dyke	X	X	X	-	X	X	
56215	BGS07N		Sandy limestone concretionary horizon, 5.25-5.35m from dyke	X	X	X	-	X		

Sample data for the Bearreraig Bay dyke, Trotternish, northeast Skye.

TCD No.	Sample no.	VR Code	Details	Rock Sample	A. Organic Residue	B. Palynology Thin	C. Vitrinite Thin	D. Vitrinite Block	E Petrological Thin	F. Sample Discs
56216	BBD01		Dyke centre	X	-	-	-	-	X	X
56217	BBD02		Dyke margin (north side)	X	-	-	-	-	X	
56218	BBD03		Altered dyke margin (north side)	X	-	-	-	-		

Other sample information

TCD No.	Sample no.	VR Code	Details	Rock Sample	A. Organic Residue	B. Palynology Thin Section	C. Vitrinite Thin Section	D. Vitrinite Block	E Petrological Thin Section	F. Conductivity Sample Discs
56219	WH03		Island Magee, Larne. Dark grey mudrock, 4.0m from dyke	X	X	X	-	X		
56220	CDE26		Carn Dearg, Eishort. Dark grey micaceous shale, 18.0m E of dyke	X	X	X	X	X		
56221	CDW25		Carn Dearg, Eishort. Dark grey micaceous shale, 5.70m W of dyke	X	X	X	X	X		
56222	WO24E		Broadford Bay. Dark grey micaceous shale, 14.3m E of dyke	X	-	X	-	X		
56223	WO23W		Broadford Bay. Dark grey micaceous shale, 15.5m W of dyke	X	-	X	-	X		
56224	MD01	G10	Prolabo Microdigest Experiments, 90%/30min	-	-	X	-	X		
56225	MD02	G01	Prolabo Microdigest Experiments, 50%/30min	-	-	X	-	X		
56226	MD03	G05	Prolabo Microdigest Experiments, 45%/30min	-	-	X	-	X		
56227	MD04	G09	Prolabo Microdigest Experiments, 40%/30min	-	-	X	-	X		
56228	MD05	G03	Prolabo Microdigest Experiments, 35%/30min	-	-	X	-	X		
56229	MD06	G08	Prolabo Microdigest Experiments, 30%/30min	-	-	X	-	X		
56230	MD07	G04	Prolabo Microdigest Experiments, 25%/30min	-	-	X	-	X		
56231	MD08	G02	Prolabo Microdigest Experiments, 50%/60min	-	-	X	-	X		
56232	MD09	G06	Prolabo Microdigest Experiments, 50%/45min	-	-	X	-	X		
56233	MD10	G07	Prolabo Microdigest Experiments, Cold Digestion (standard)	-	-	X	-	X		
56234	RGB Std		RGB colour standard. <i>Punctatisporites Solidus</i> , E.F. L32/1	-	-	X	-	-		

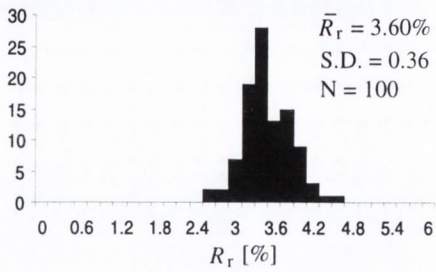
APPENDIX II

VITRINITE REFLECTANCE HISTOGRAMS

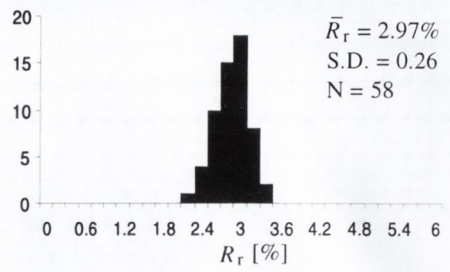
&

CALIBRATION REFLECTANCE PROFILES

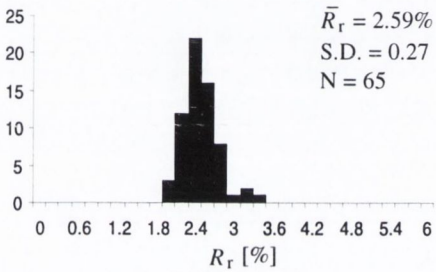
BB01N



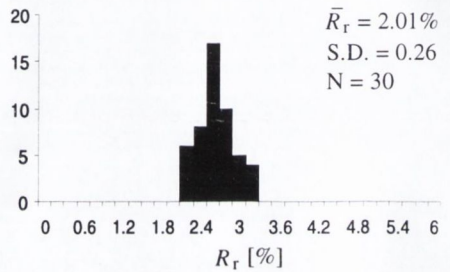
BB02N



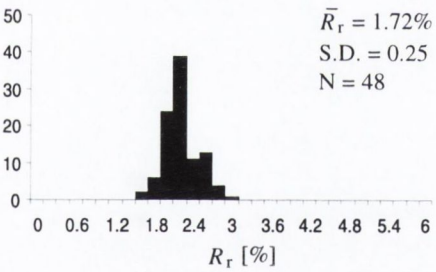
BB03N



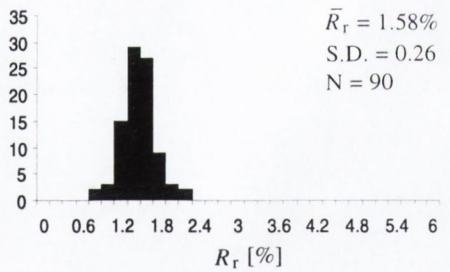
BB04N



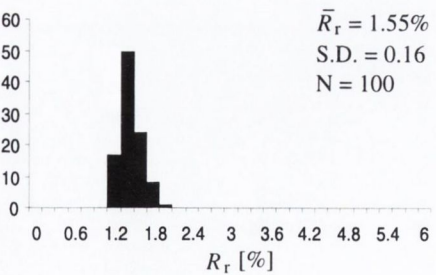
BB05N



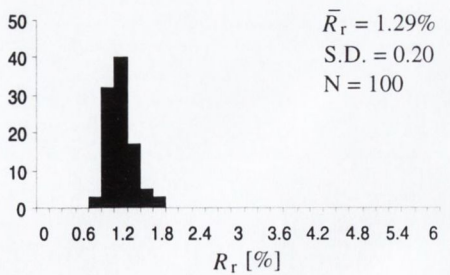
BB06N



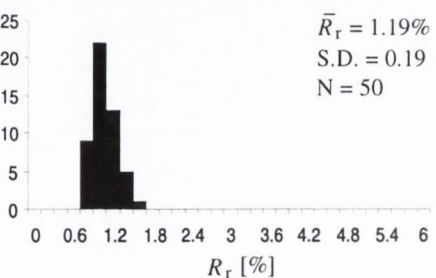
BB07N



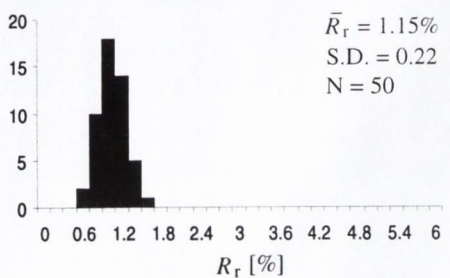
BB08N



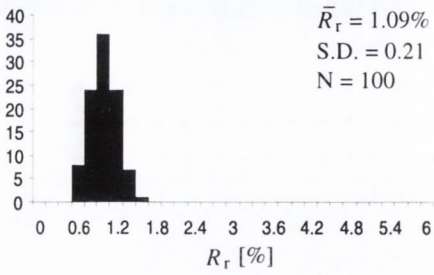
BB09N



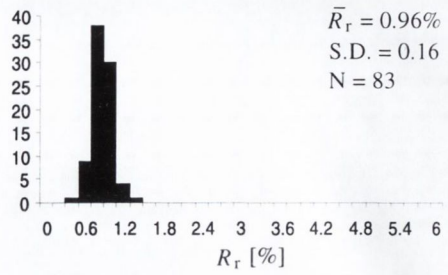
BB10N



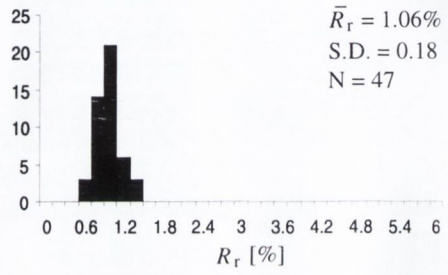
BB11N



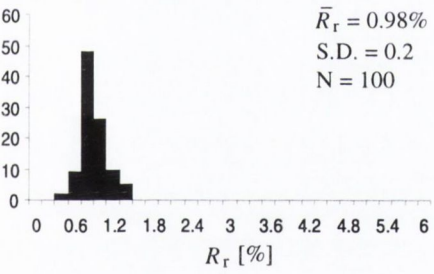
BB12N



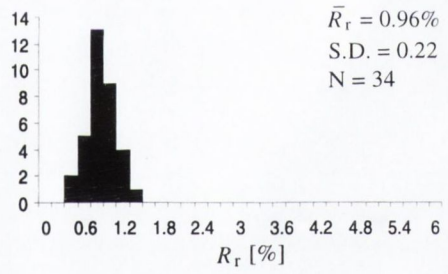
BB14N



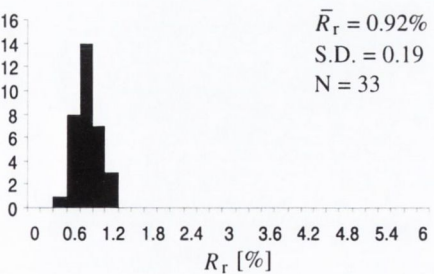
BB15N



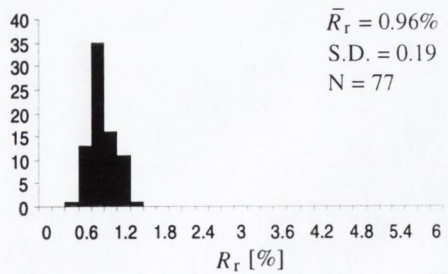
BB16N



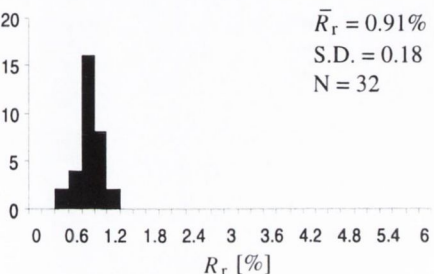
BB17N



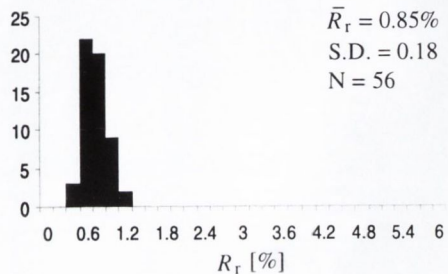
BB18N



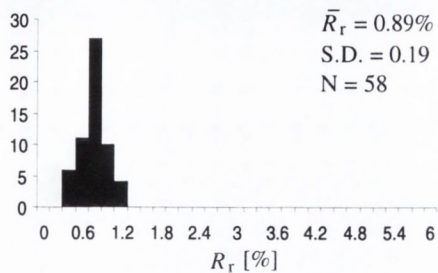
BB19N



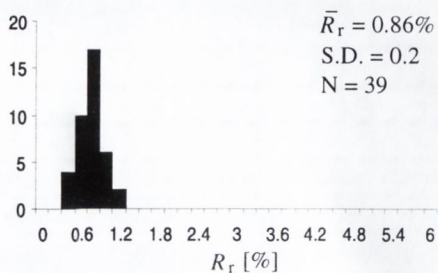
BB20N



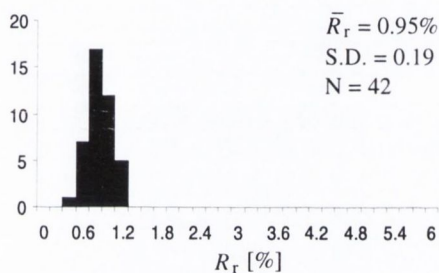
BB21N



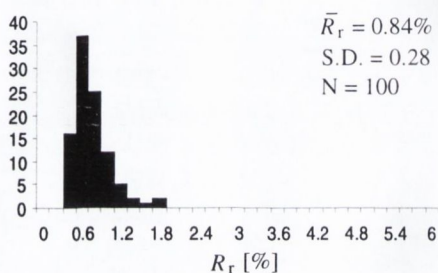
BB22N



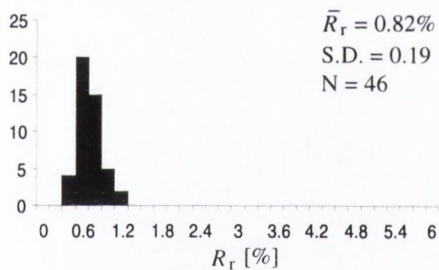
BB23N



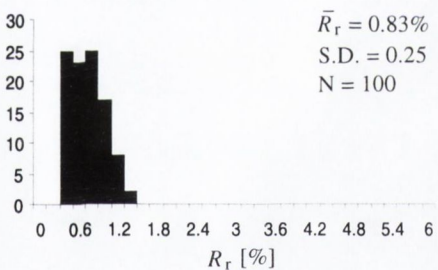
BB24N



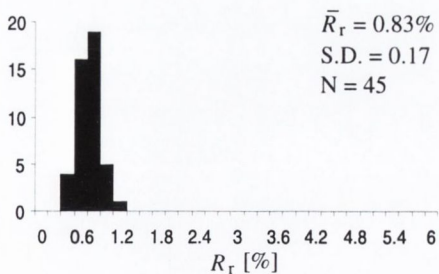
BB25N



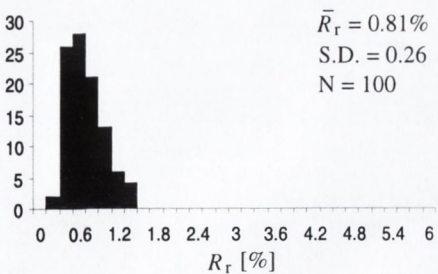
BB26N



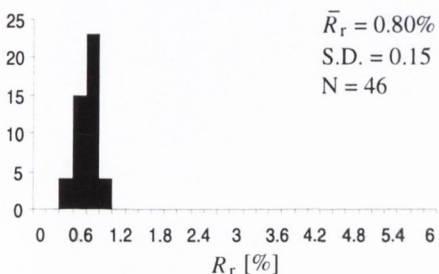
BB27N



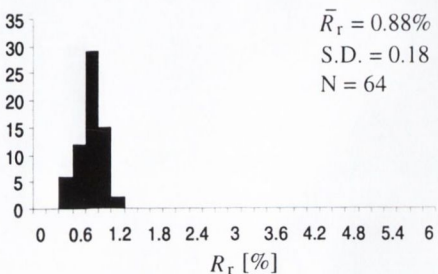
BB28N



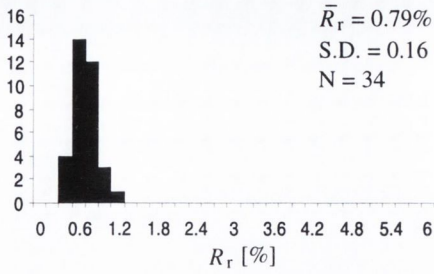
BB29N



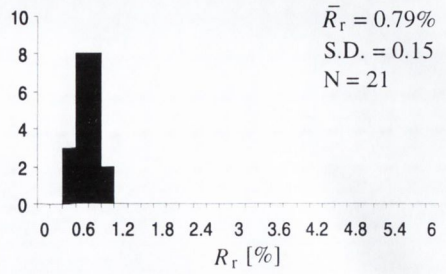
BB30N



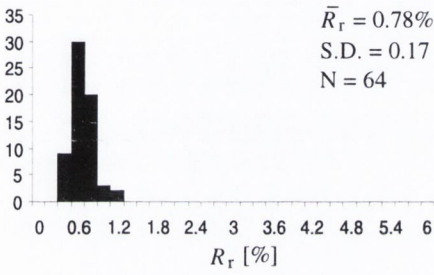
BB31N



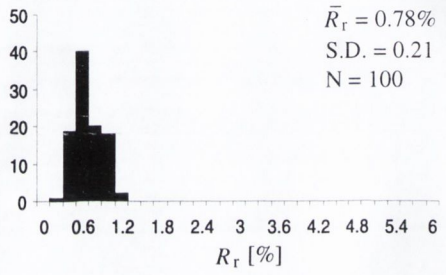
BB32N



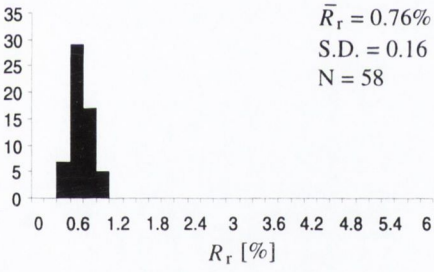
BB33N



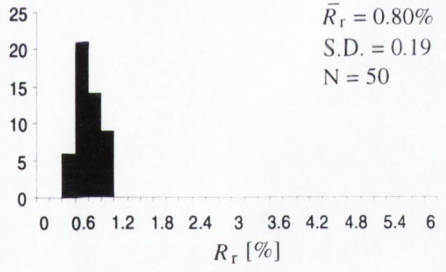
BB34N



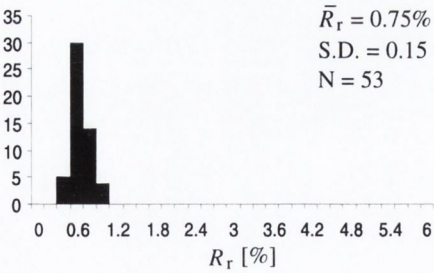
BB35N



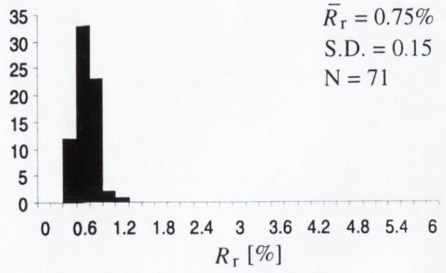
BB36N



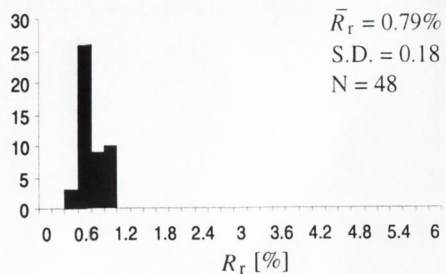
BB37N



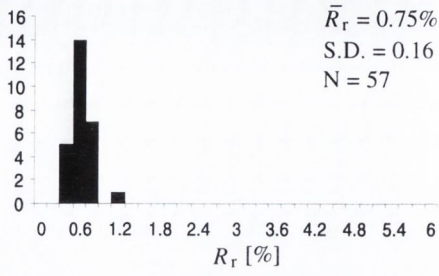
BB38N



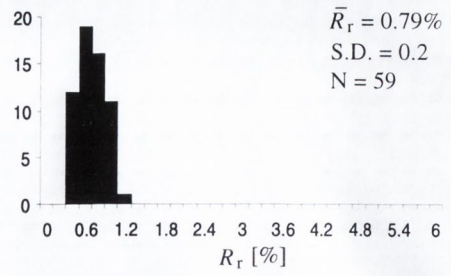
BB40N



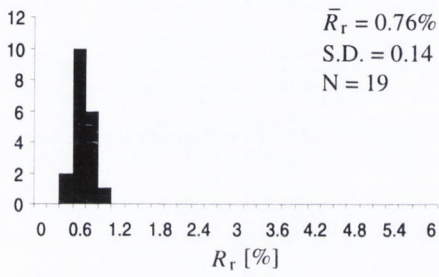
BB41N



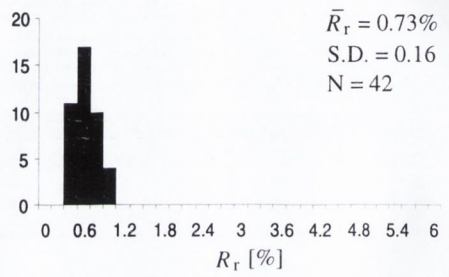
BB42N



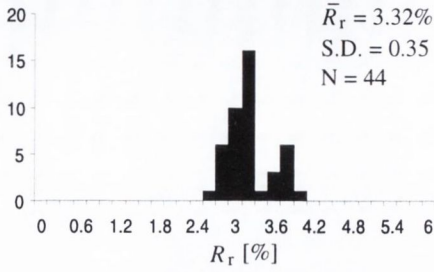
BB43N



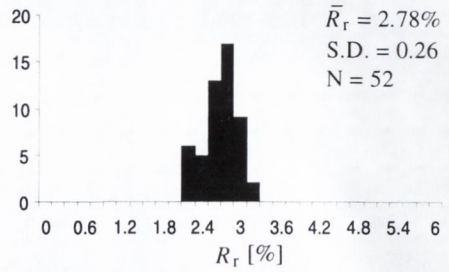
BB44N



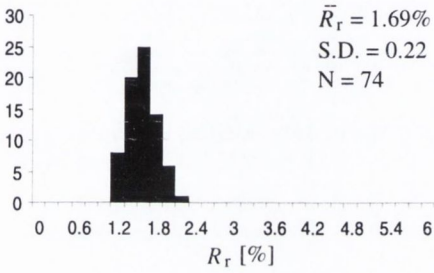
BGSH01N



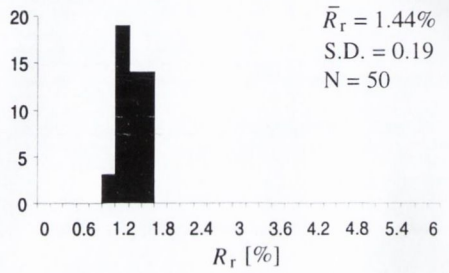
BGSH02N



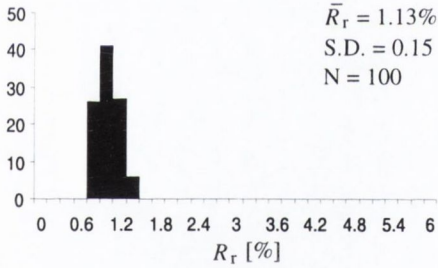
BGSH03N



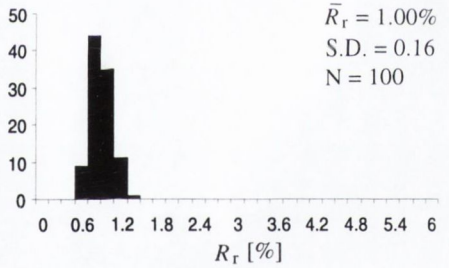
BGSH04N



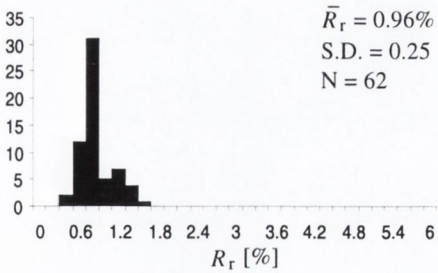
BGSH05N



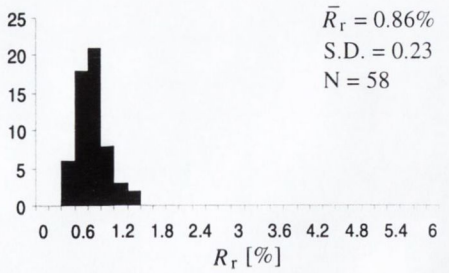
BGSH06N



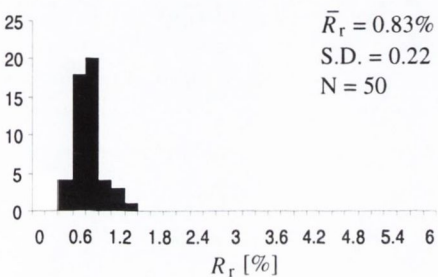
BGSH07N



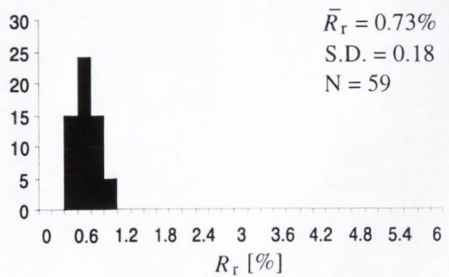
BGSH08N



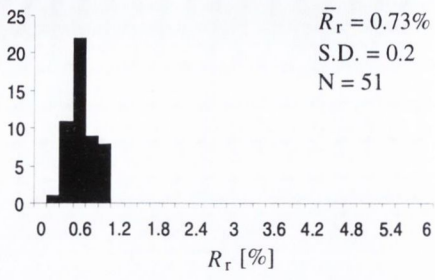
BGSH09N



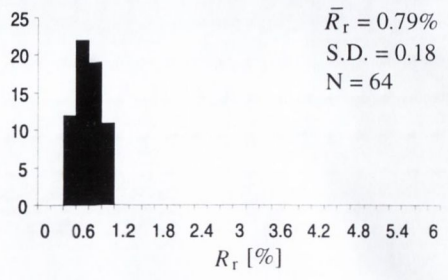
BGSH10N



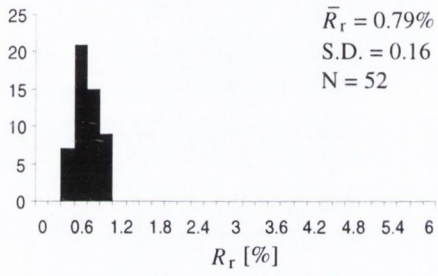
BGSH11N



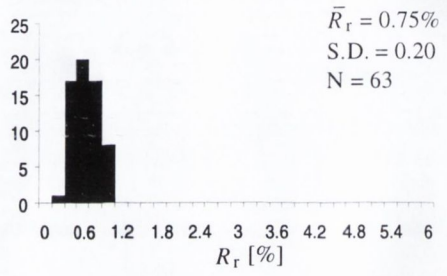
BGSH12N



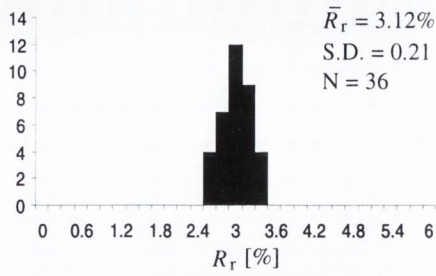
BGSH13N



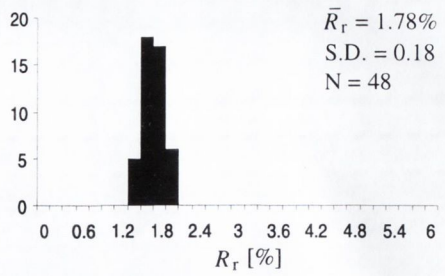
BGSH14N



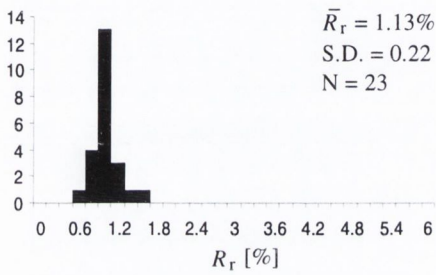
BGS01N



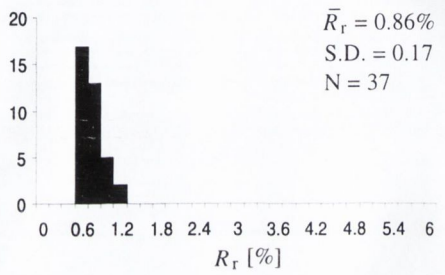
BGS02N



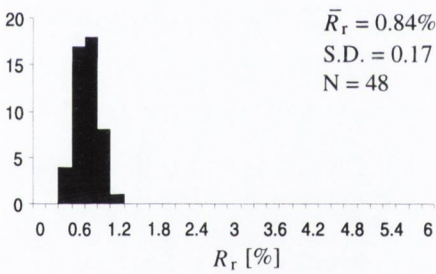
BGS03N



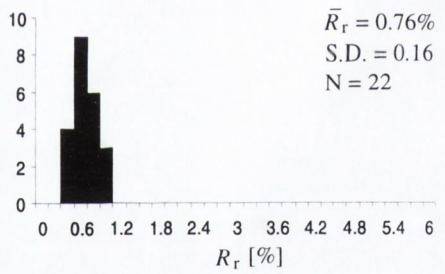
BGS04N



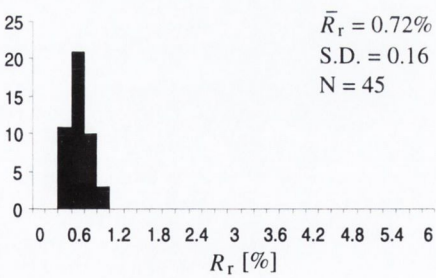
BGS05N



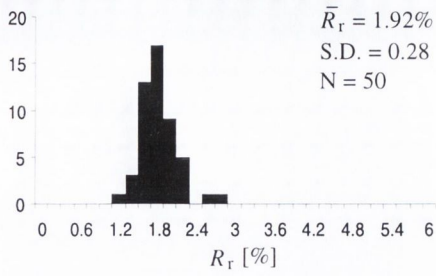
BGS06N



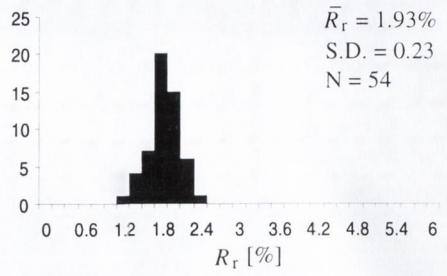
BGS07N



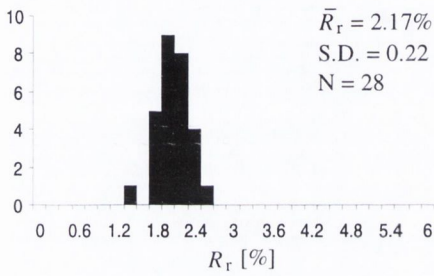
WO24E (14.3m east of dyke contact)



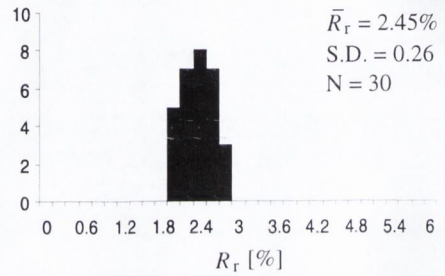
WO23W (15.5m west of dyke contact)



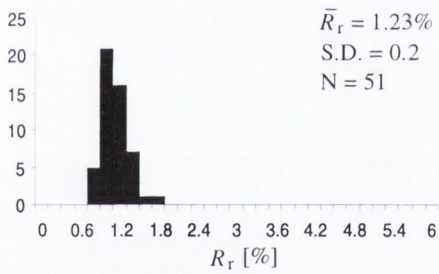
CD26E (18m east of dyke contact)



CD25E (5.7m west of dyke contact)



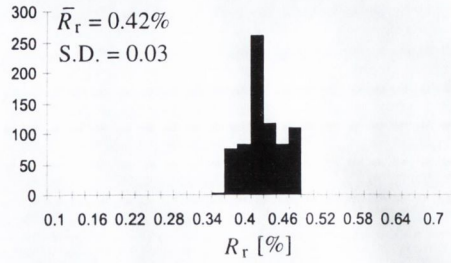
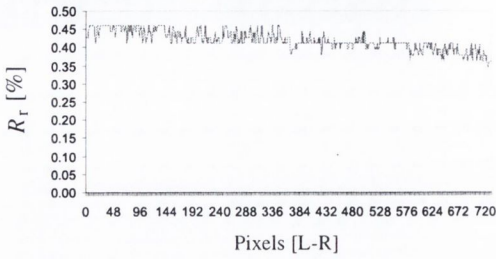
WH03 (White House, western foreshore, Island Magee)



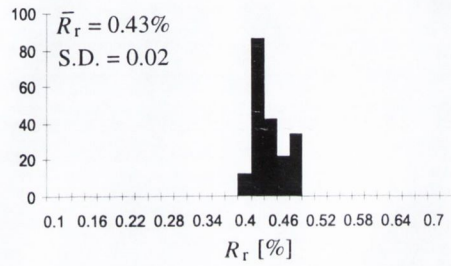
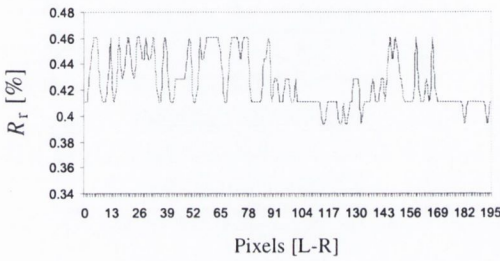
LOWREFLECTANCE.Q5R CALIBRATION STANDARD

REFLECTANCE PROFILES AND HISTOGRAMS

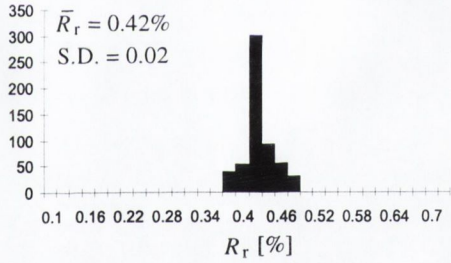
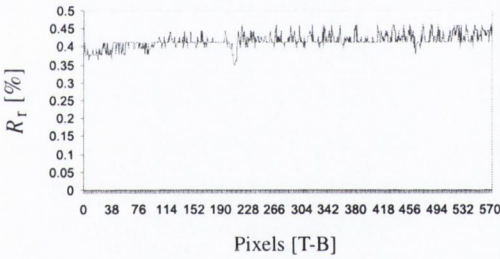
0.42% Standard field of view: horizontal profile



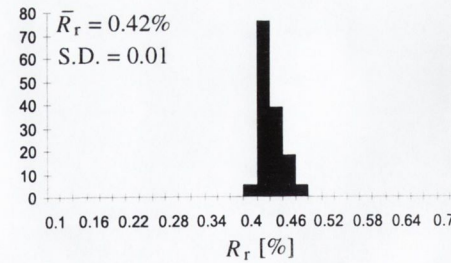
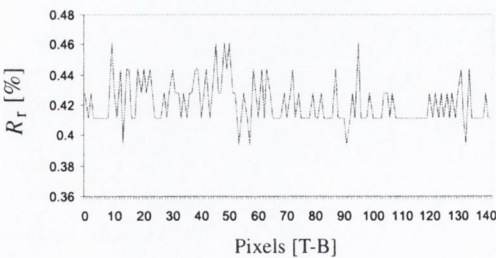
0.42% Standard limiting frame: horizontal profile



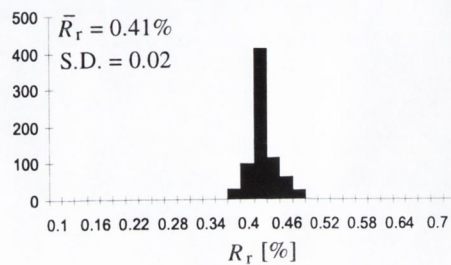
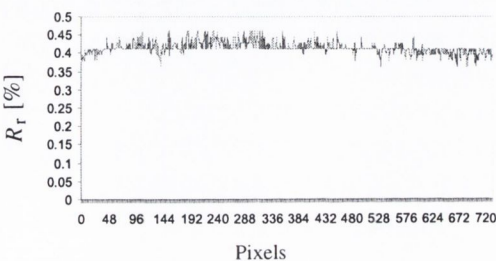
0.42% Standard field of view: vertical profile



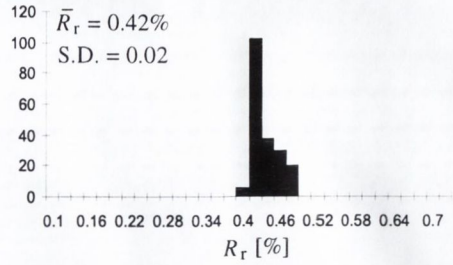
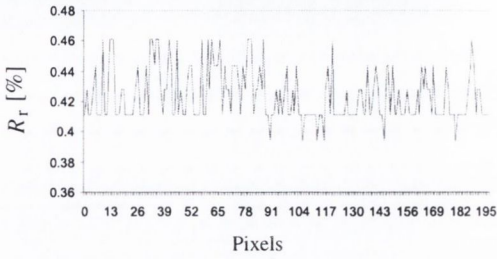
0.42% Standard limiting frame: vertical profile



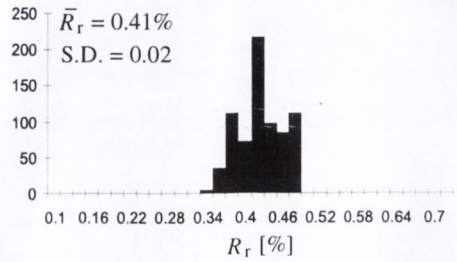
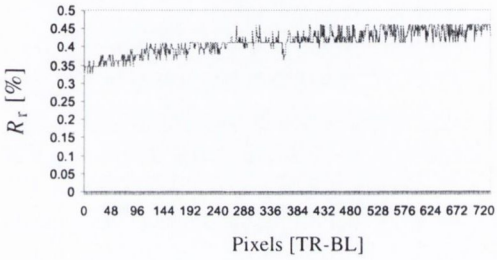
0.42% Standard field of view: diagonal [\N] profile



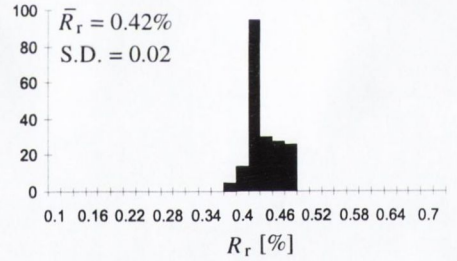
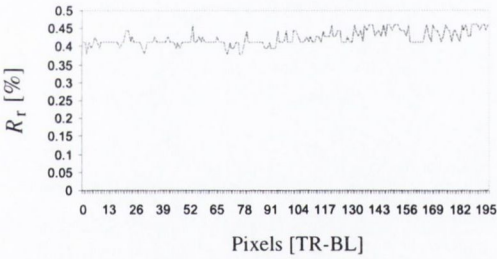
0.42% Standard limiting frame: diagonal [\] profile



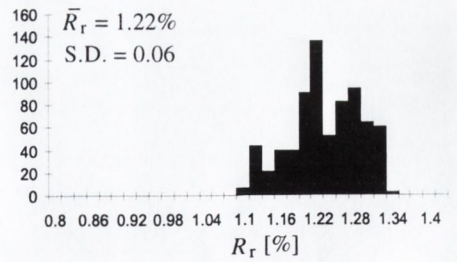
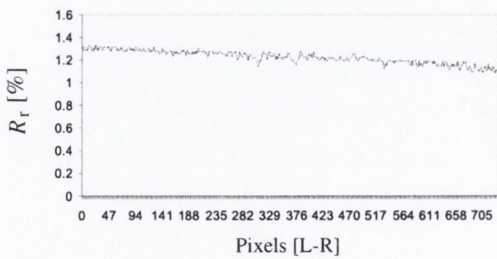
0.42% Standard field of view: diagonal [/] profile



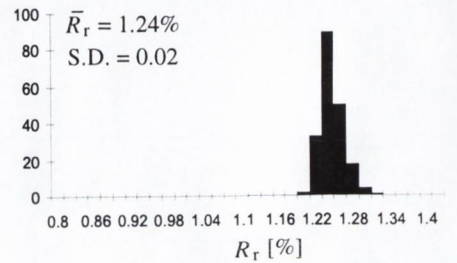
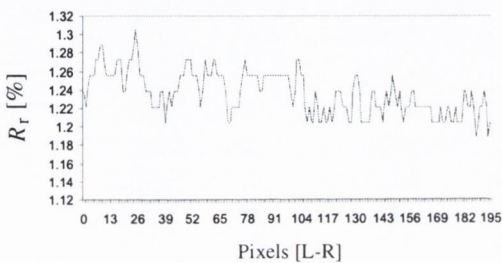
0.42% Standard limiting frame: diagonal [/] profile



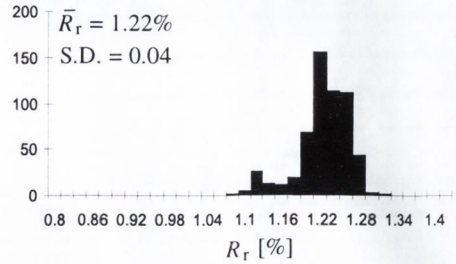
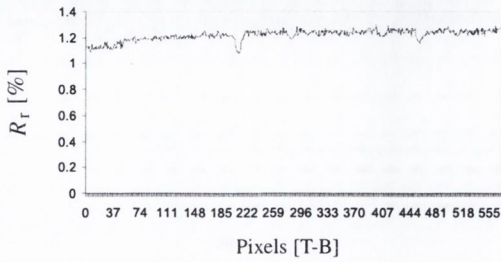
1.23% Standard field of view: horizontal profile



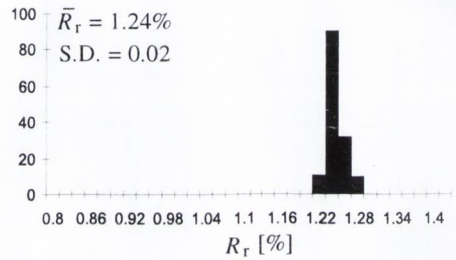
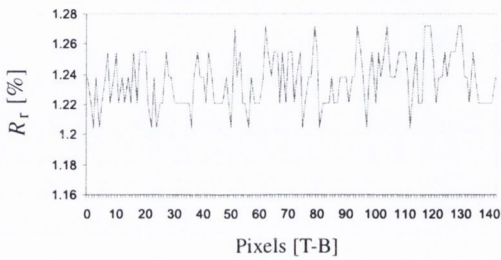
1.23% Standard limiting frame: horizontal profile



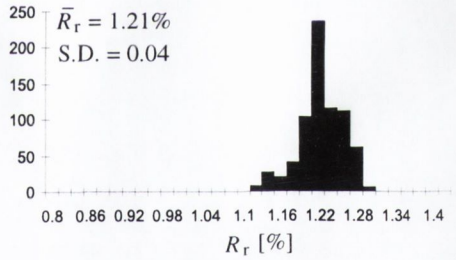
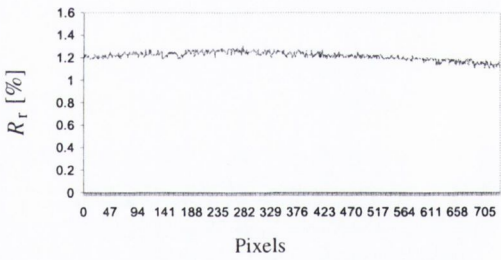
1.23% Standard field of view: vertical profile



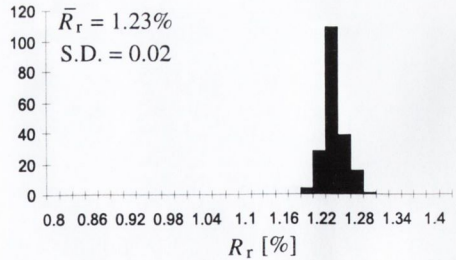
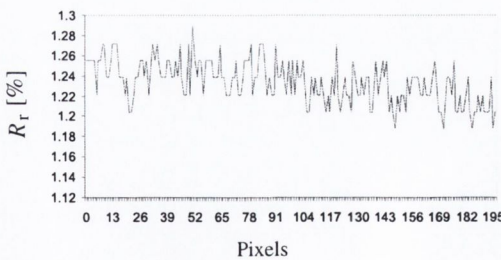
1.23% Standard limiting frame: vertical profile



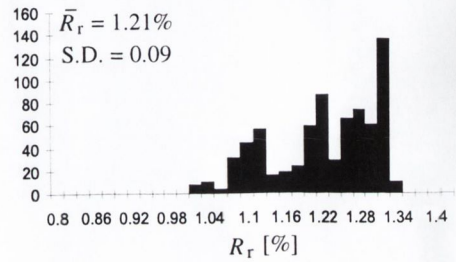
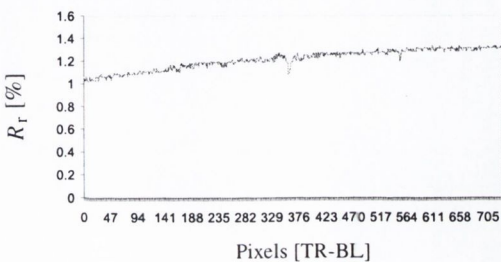
1.23% Standard field of view: diagonal [\] profile



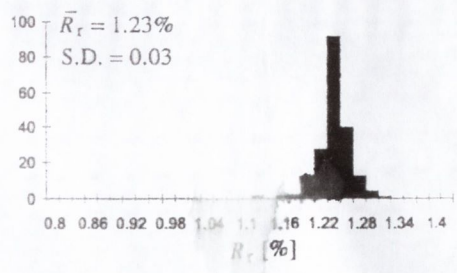
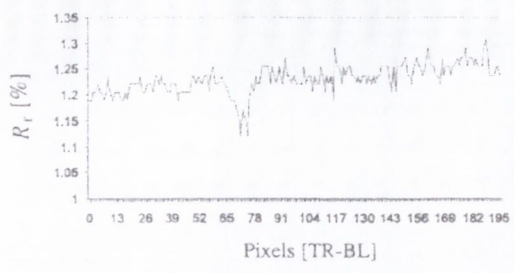
1.23% Standard limiting frame: diagonal [\] profile



1.23% Standard field of view: diagonal [/] profile



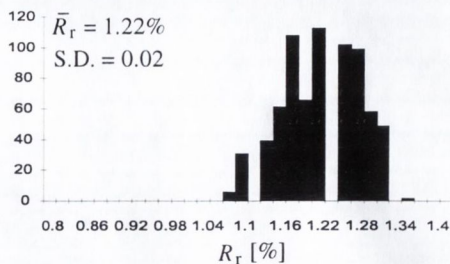
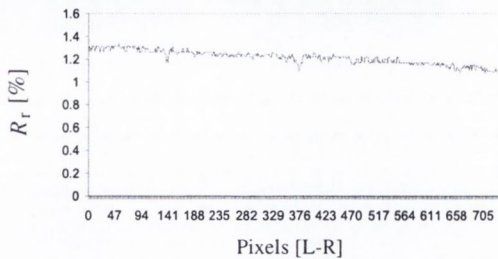
1.23% Standard limiting frame: diagonal [7] profile



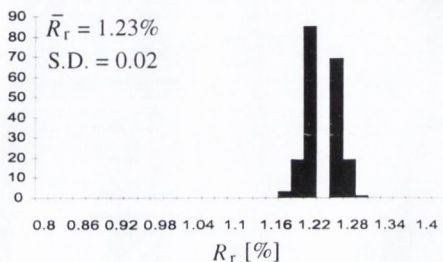
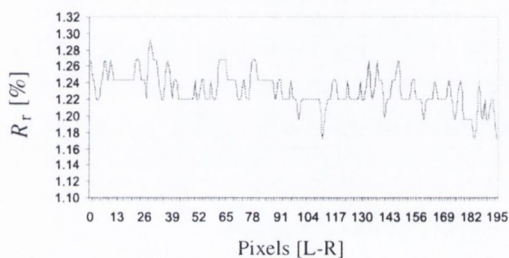
MEDREFLECTANCE.Q5R CALIBRATION STANDARD

REFLECTANCE PROFILES AND HISTOGRAMS

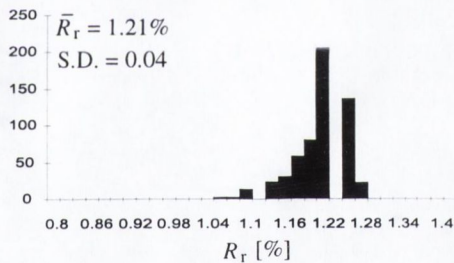
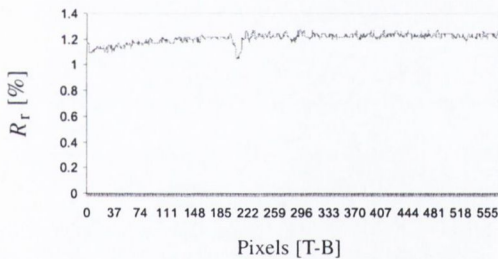
1.23% Standard field of view: horizontal profile



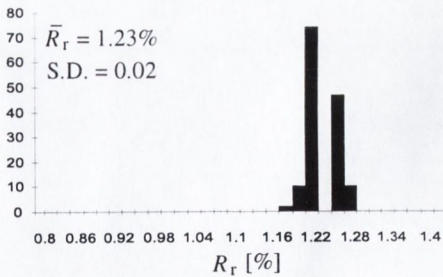
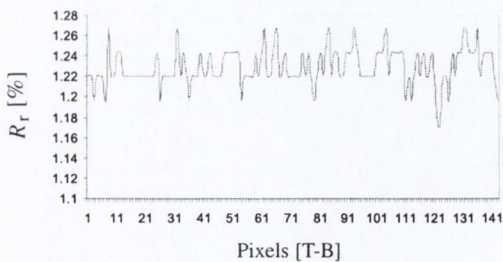
1.23% Standard limiting frame: horizontal profile



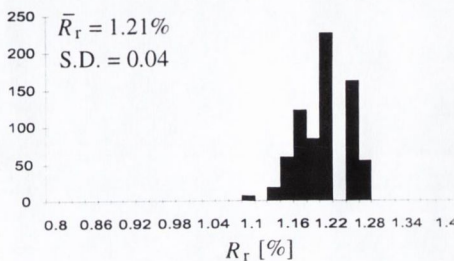
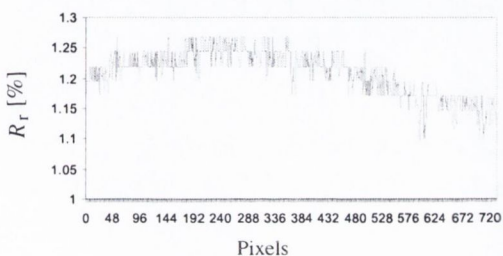
1.23% Standard field of view: vertical profile



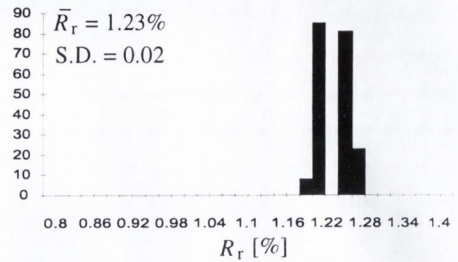
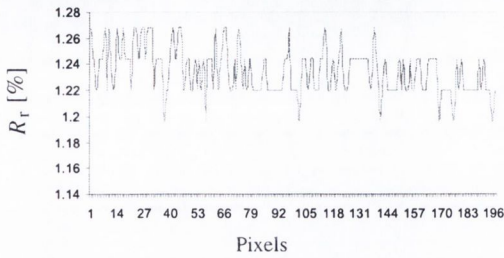
1.23% Standard limiting frame: vertical profile



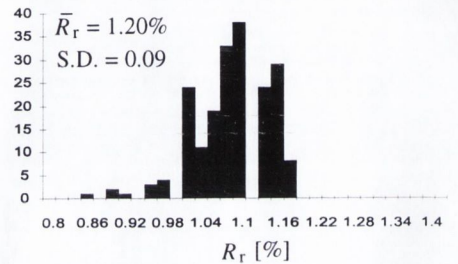
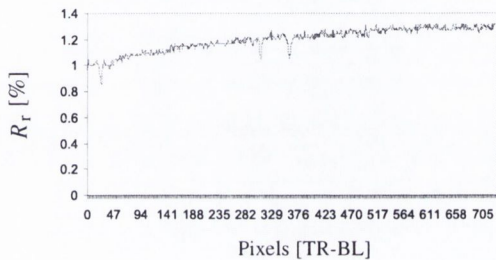
1.23% Standard field of view: diagonal [\] profile



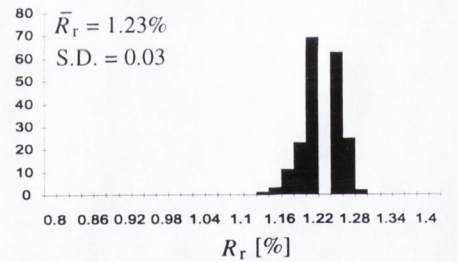
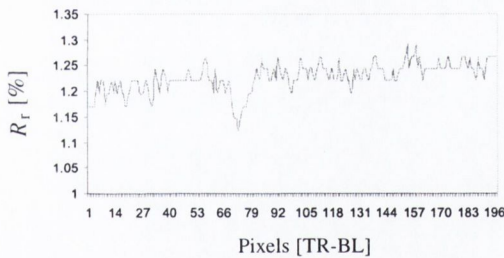
1.23% Standard limiting frame: diagonal [\] profile



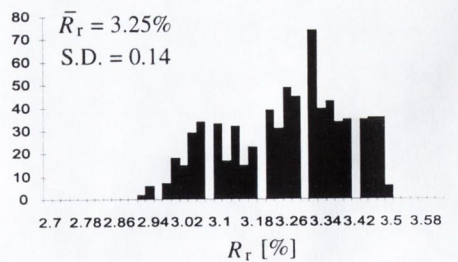
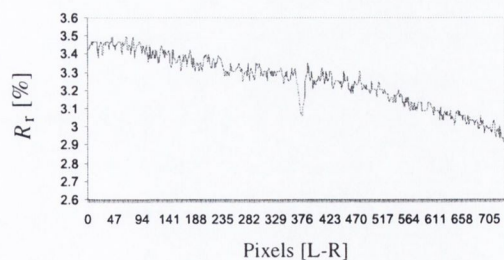
1.23% Standard field of view: diagonal [/] profile



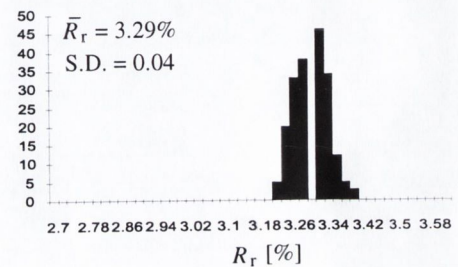
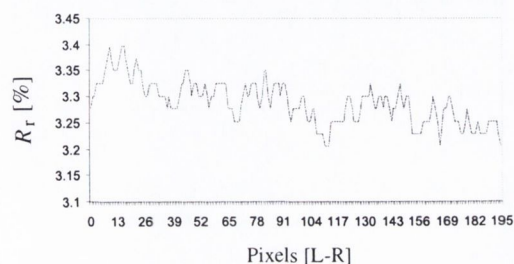
1.23% Standard limiting frame: diagonal [/] profile



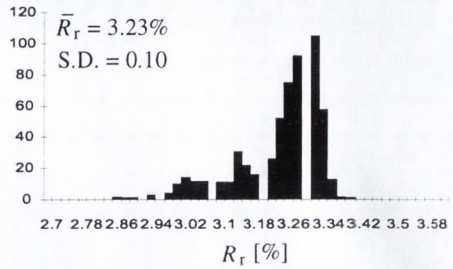
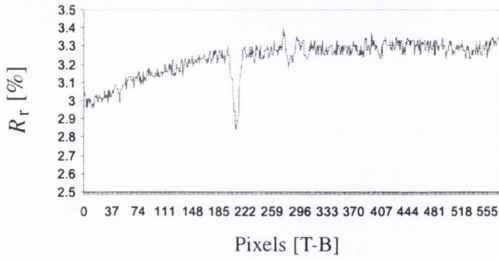
3.28% Standard field of view: horizontal profile



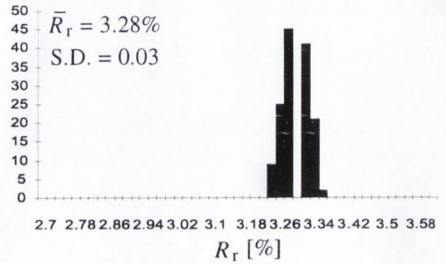
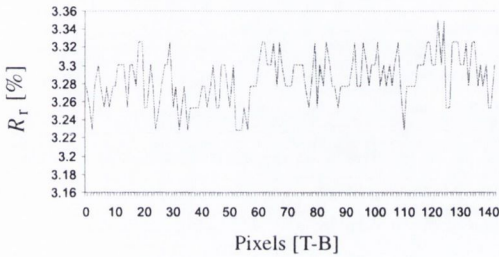
3.28% Standard limiting frame: horizontal profile



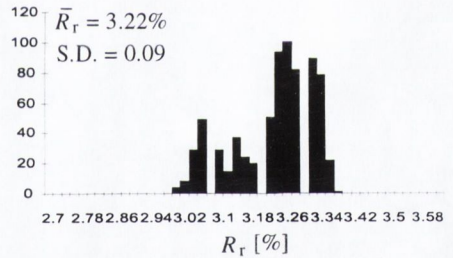
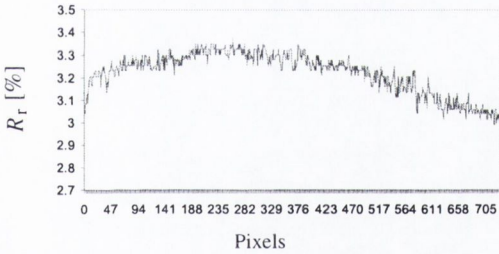
3.28% Standard field of view: vertical profile



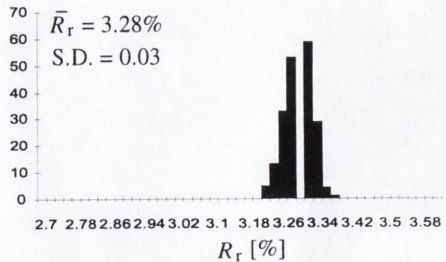
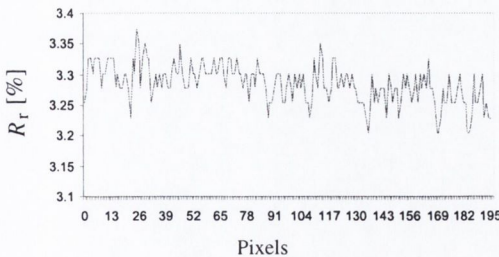
3.28% Standard limiting frame: vertical profile



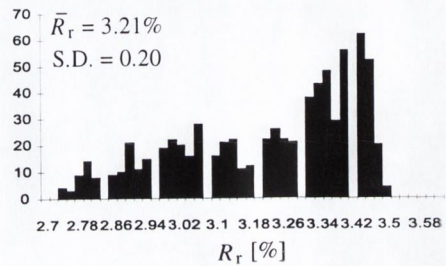
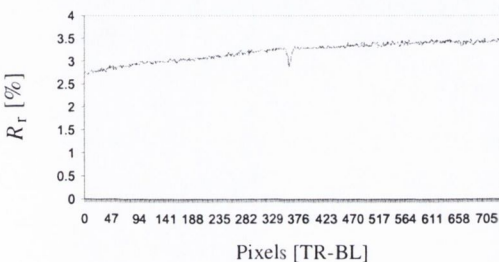
3.28% Standard field of view: diagonal [V] profile



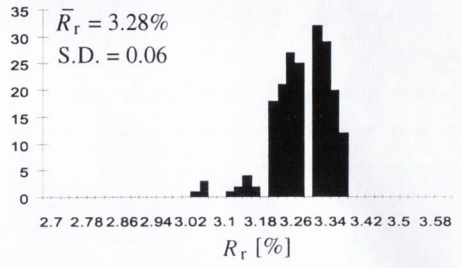
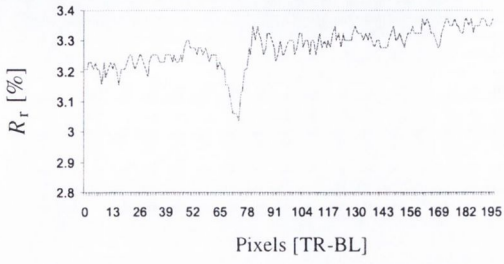
3.28% Standard limiting frame: diagonal [V] profile



3.28% Standard field of view: diagonal [/] profile

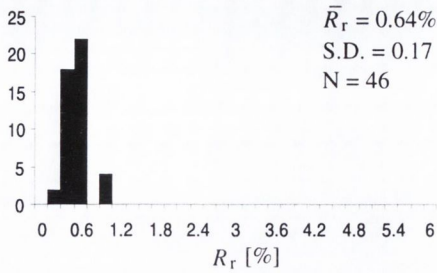


3.28% Standard limiting frame: diagonal [I] profile

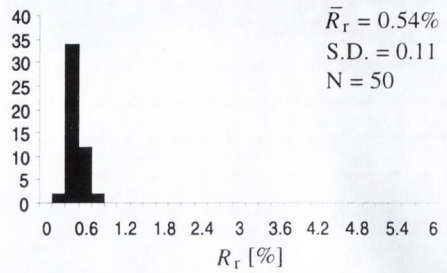


MICRODIGEST CALIBRATION (MD) R_r HISTOGRAMS

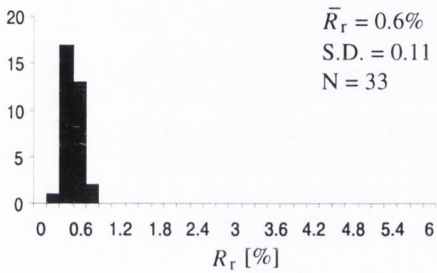
MD01 (90%/30 min)



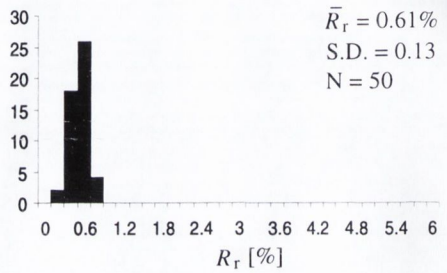
MD02 (50%/30 min)



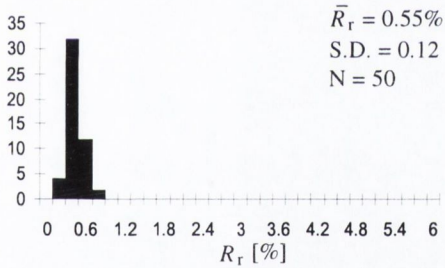
MD03 (45%/30 min)



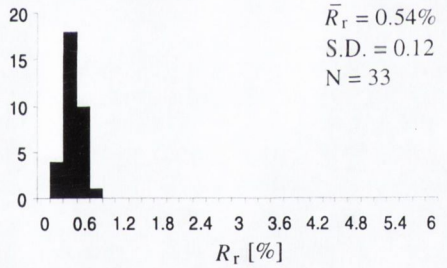
MD04 (40%/30 min)



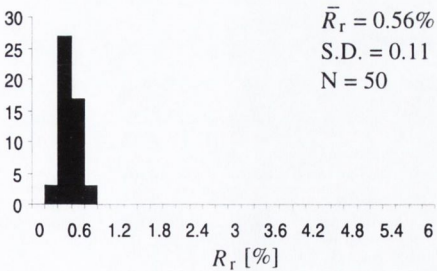
MD05 (35%/30 min)



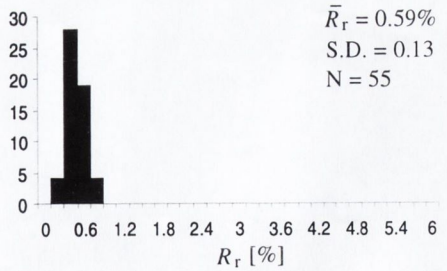
MD06 (30%/30 min)



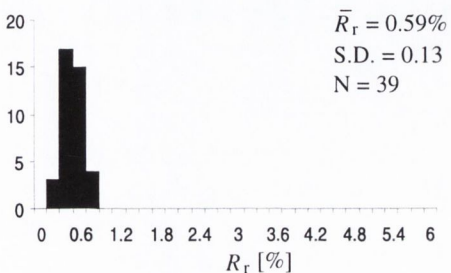
MD07 (25%/30 min)



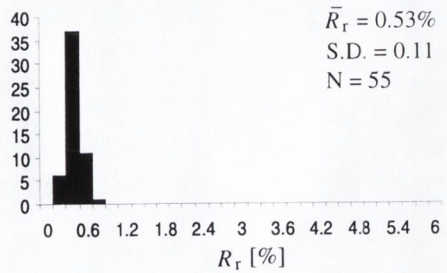
MD08 (50%/60 min)



MD09 (50%/45 min)



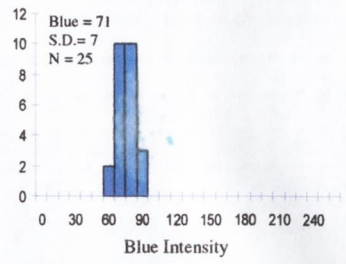
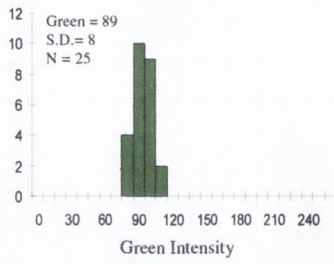
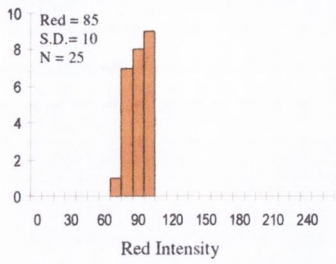
MD10 (unheated standard)



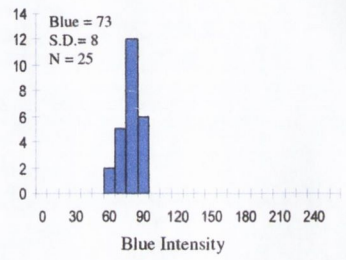
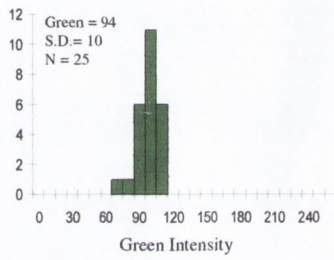
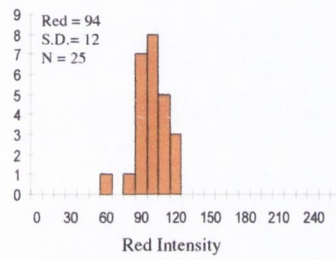
APPENDIX III

RGB HISTOGRAMS

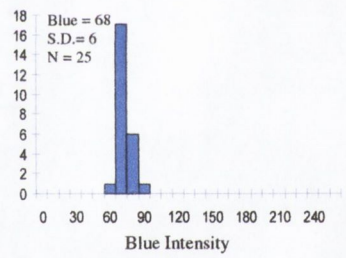
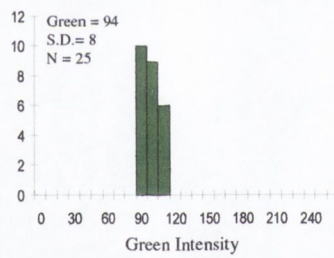
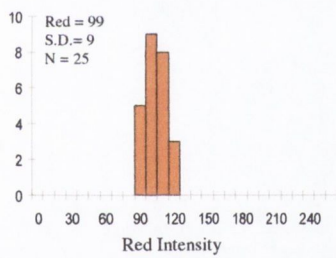
BB01N



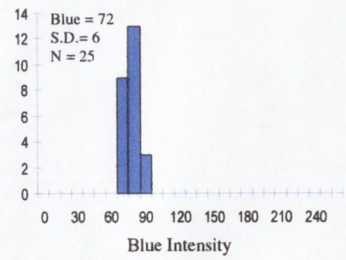
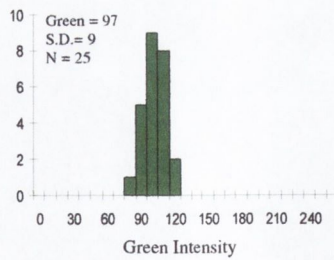
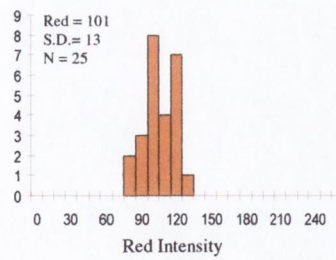
BB02N



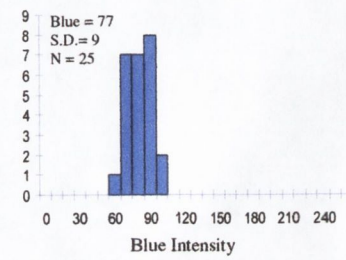
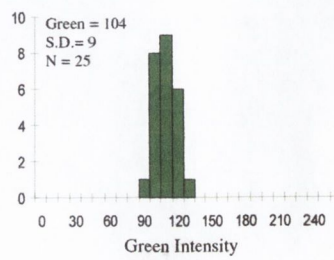
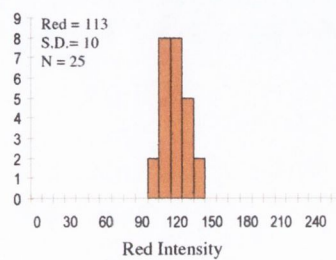
BB03N



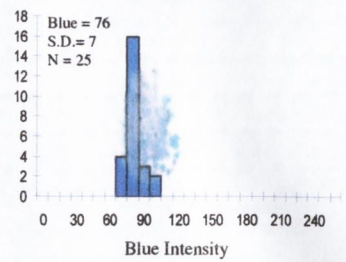
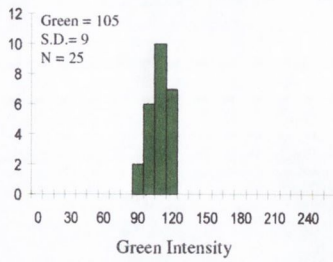
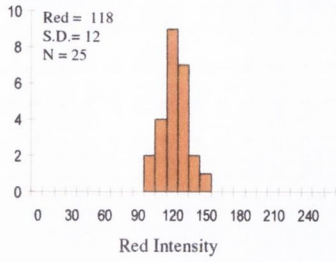
BB04N



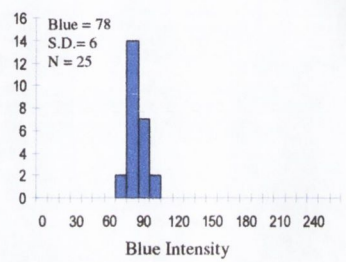
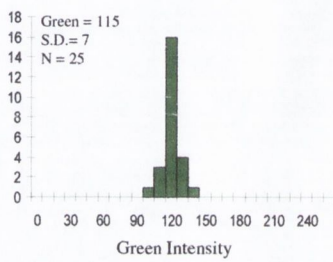
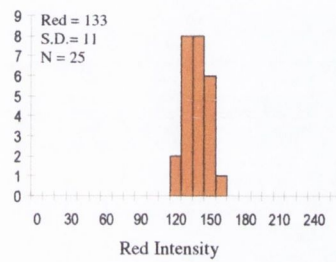
BB05N



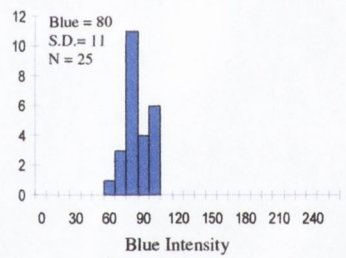
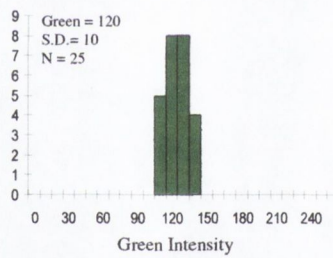
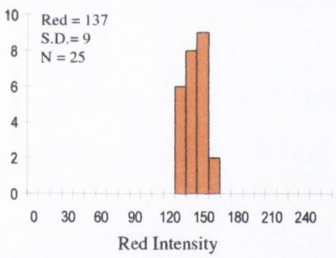
BB06N



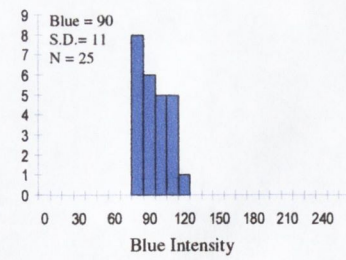
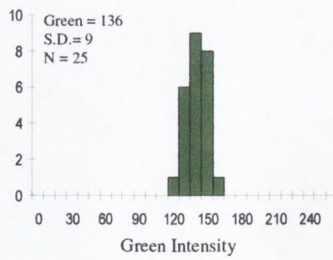
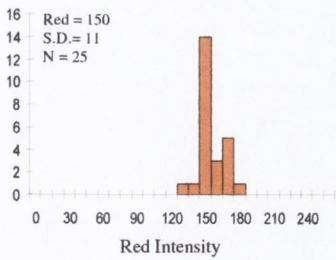
BB07N



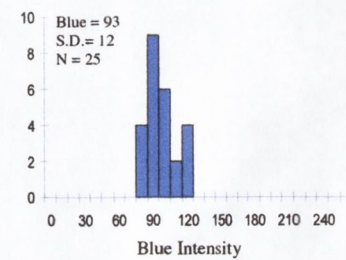
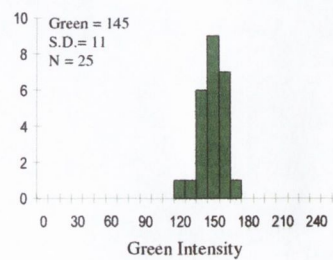
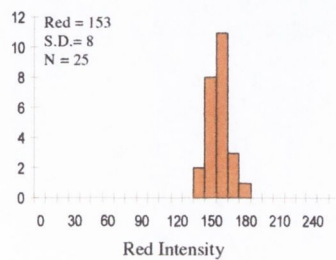
BB08N



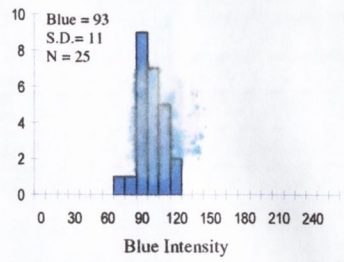
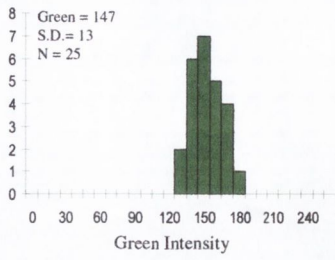
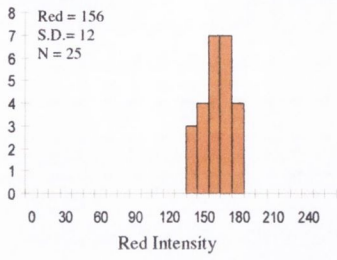
BB09N



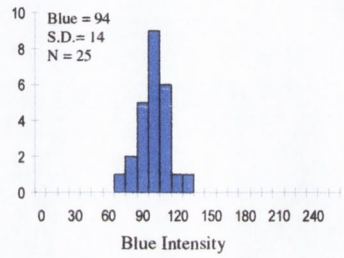
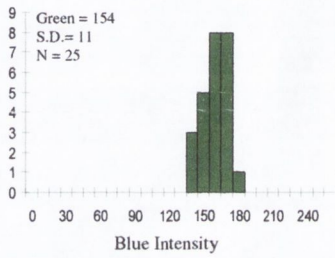
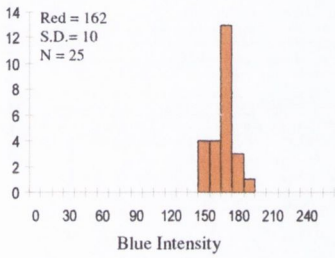
BB10N



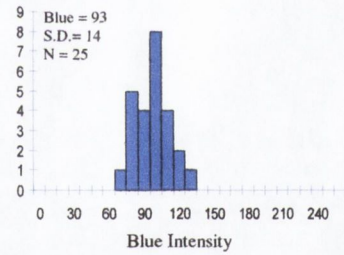
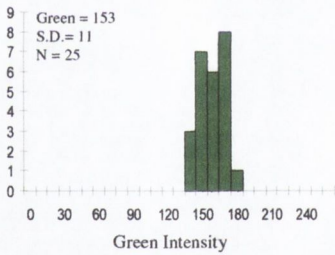
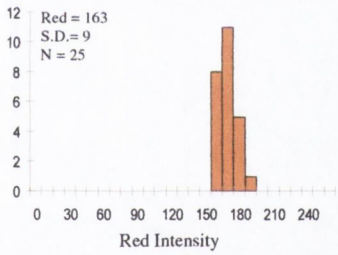
BB11N



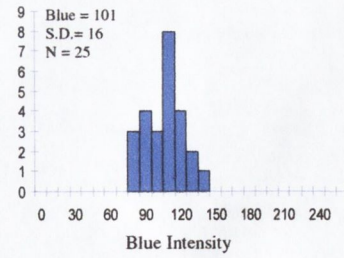
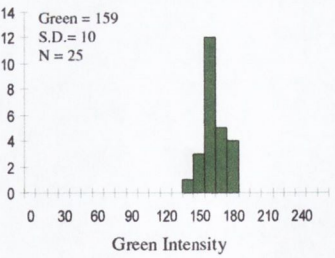
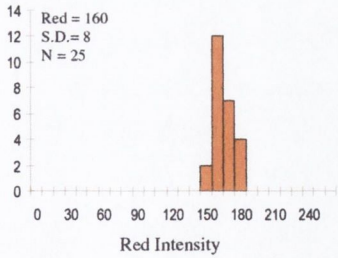
BB12N



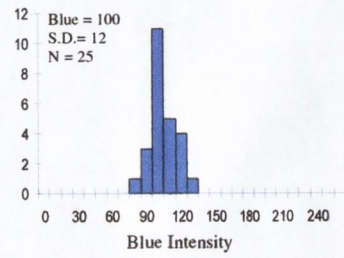
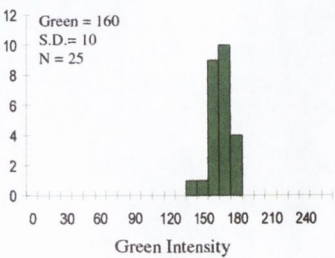
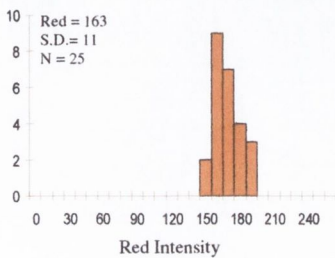
BB13N



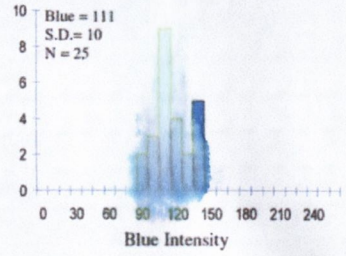
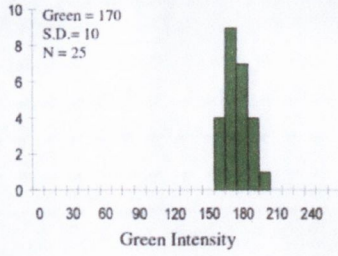
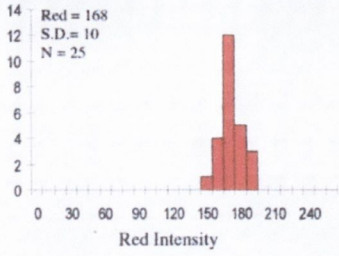
BB14N



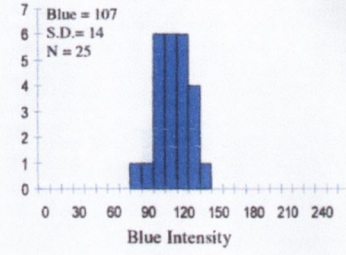
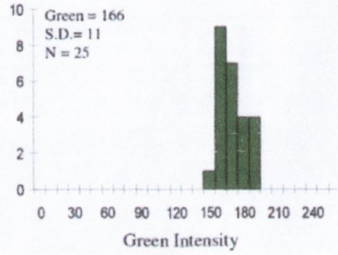
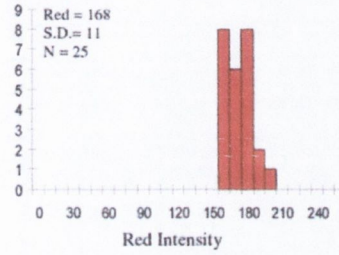
BB15N



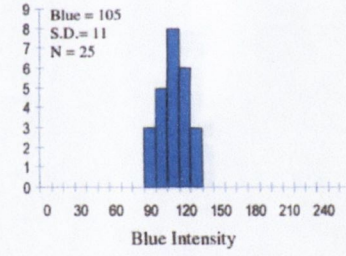
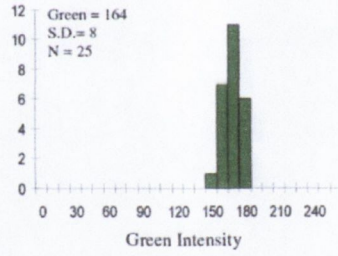
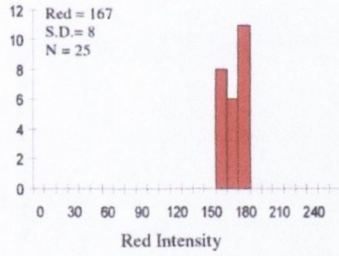
BB17N



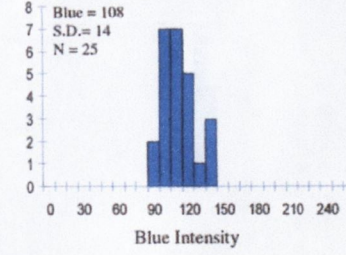
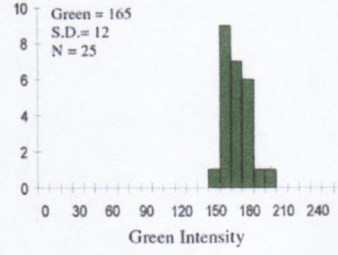
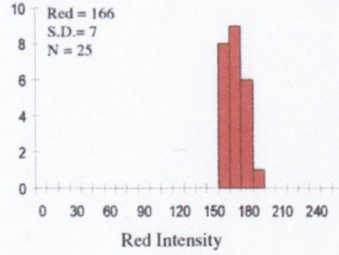
BB19N



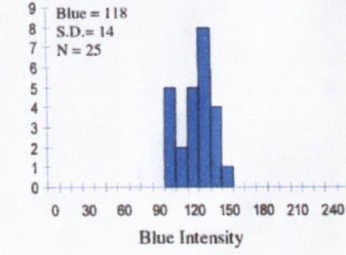
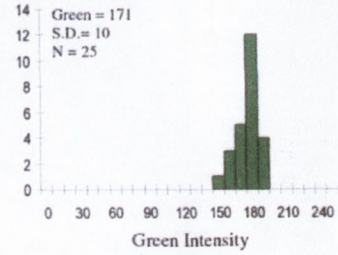
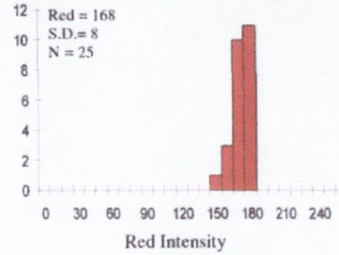
BB21N



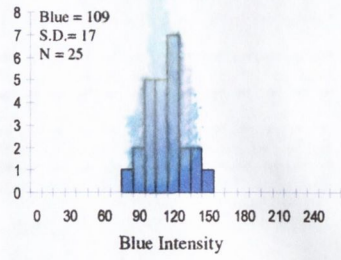
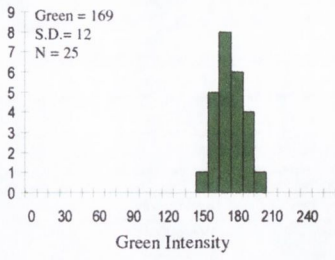
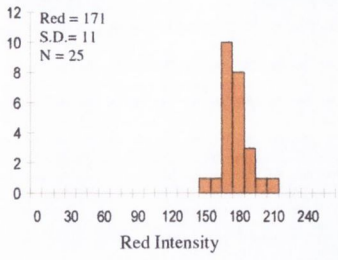
BB22N



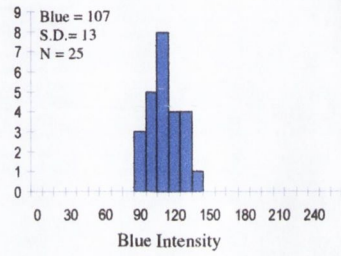
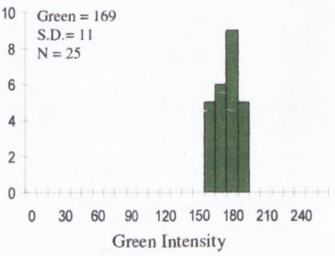
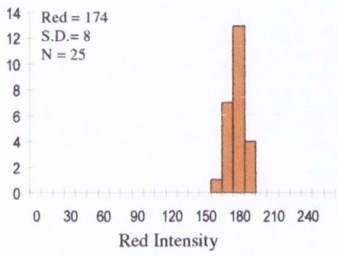
BB24N



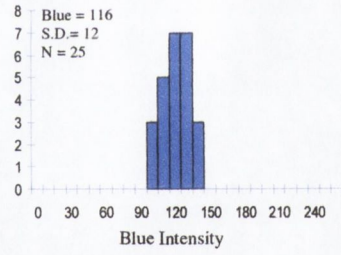
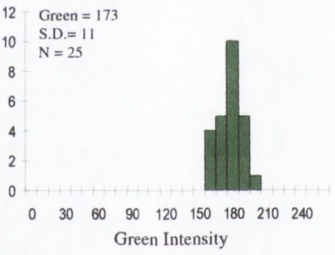
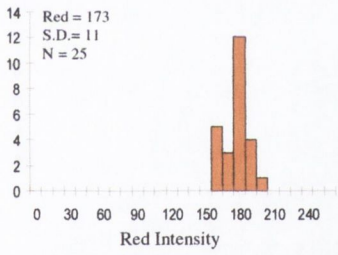
BB27N



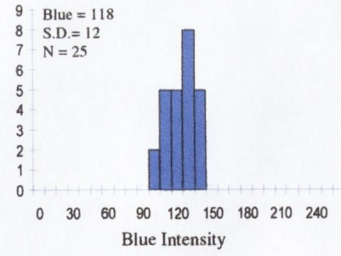
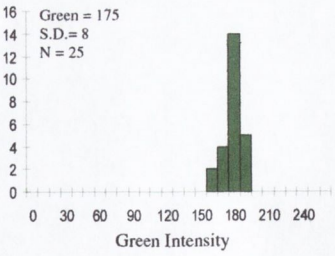
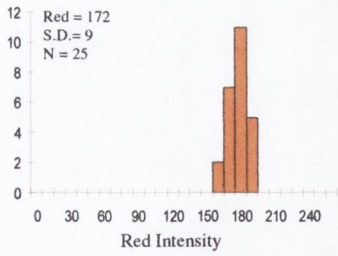
BB29N



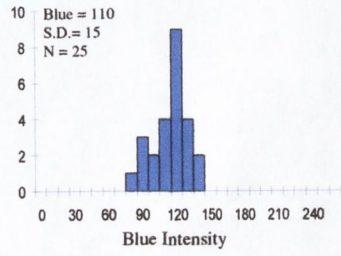
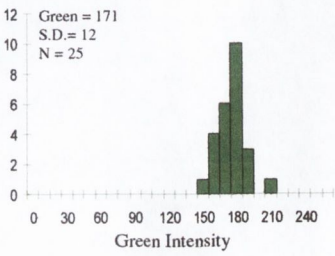
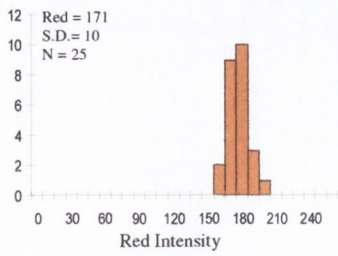
BB31N



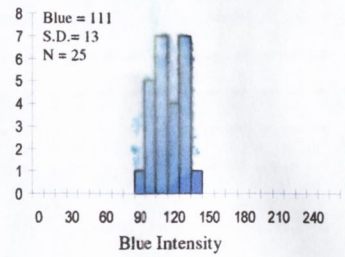
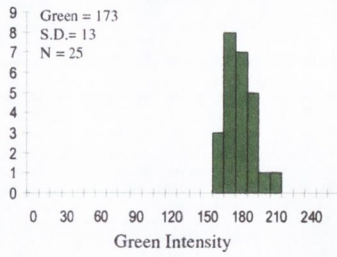
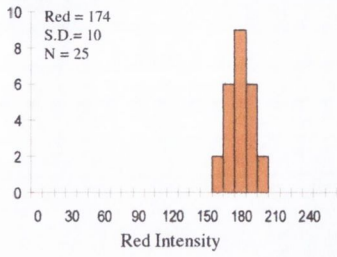
BB33N



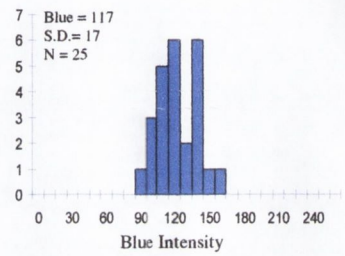
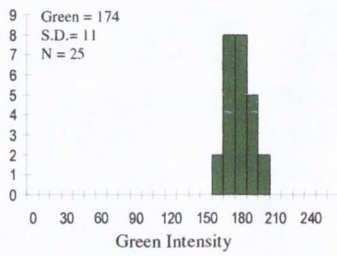
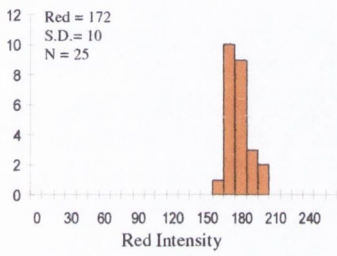
BB34N



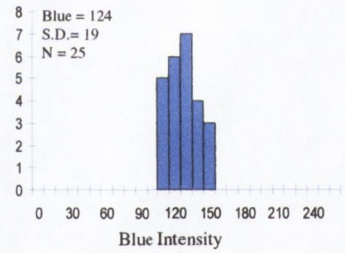
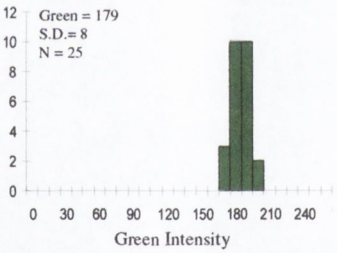
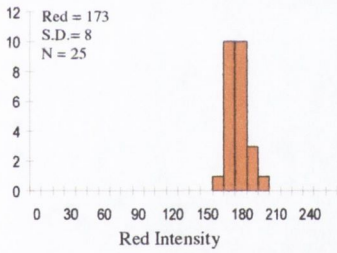
BB35N



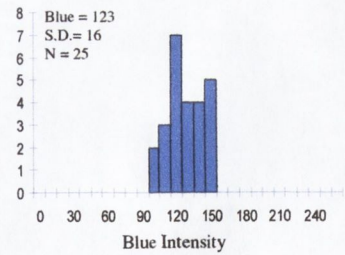
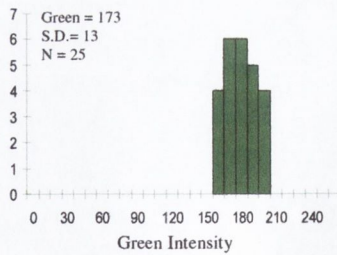
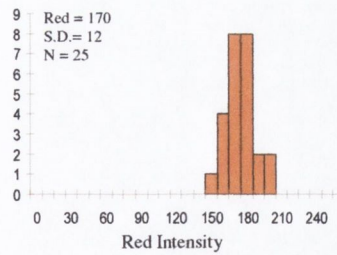
BB36N



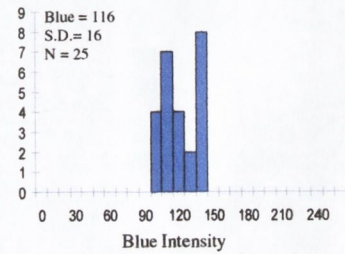
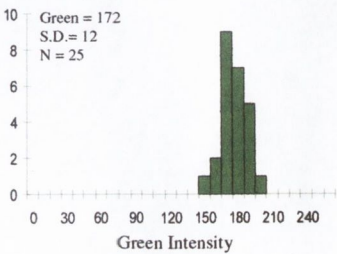
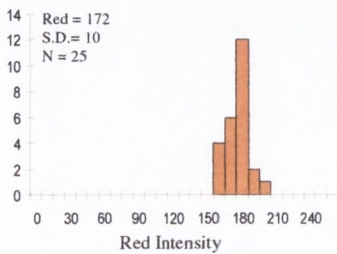
BB37N



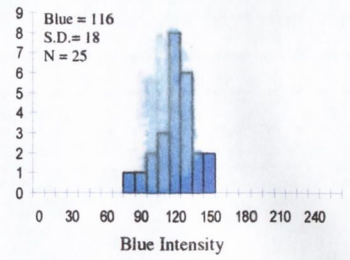
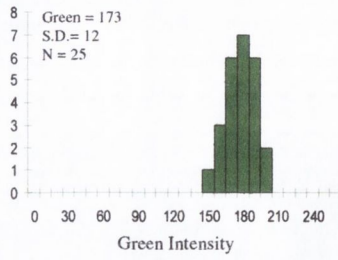
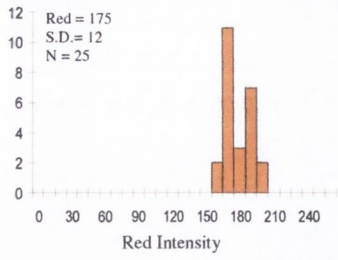
BB38N



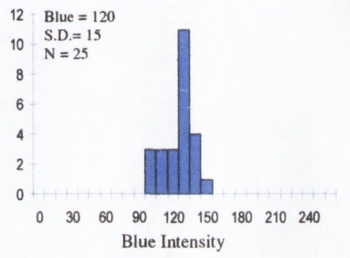
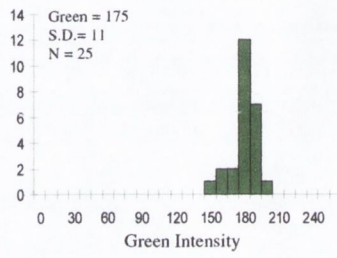
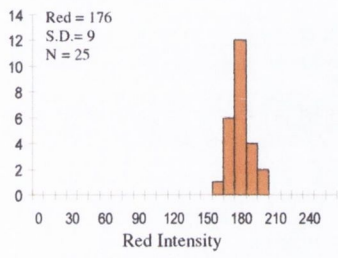
BB40N



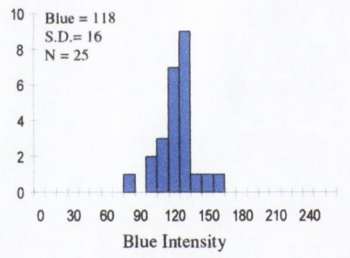
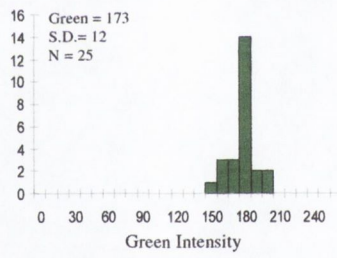
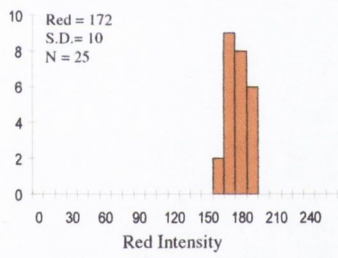
BB41N



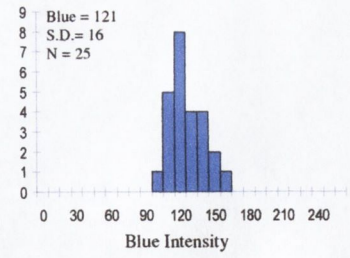
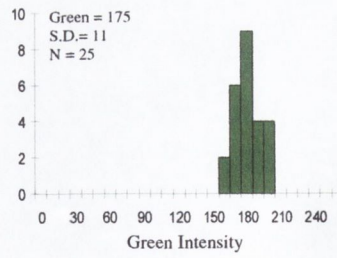
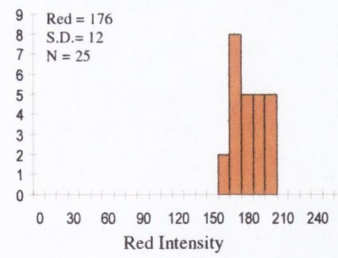
BB42N



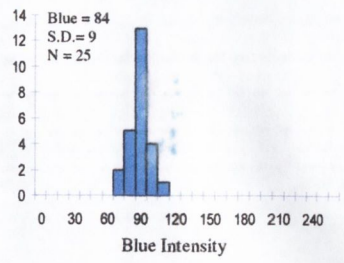
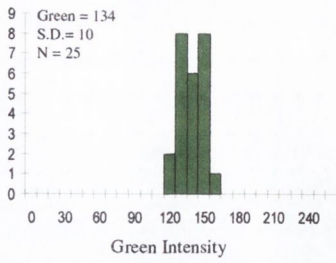
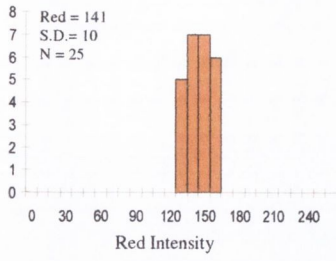
BB43N



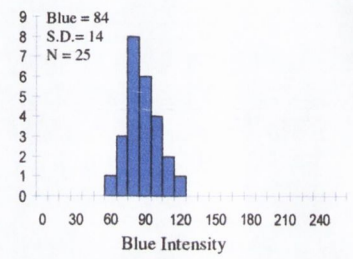
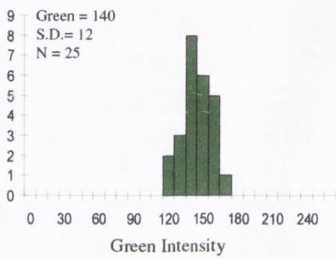
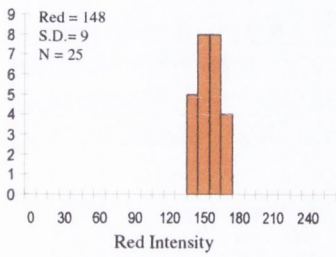
BB44N



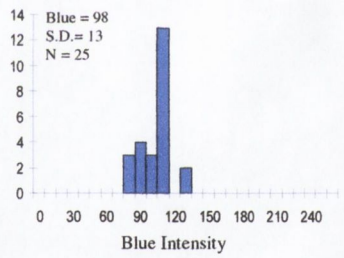
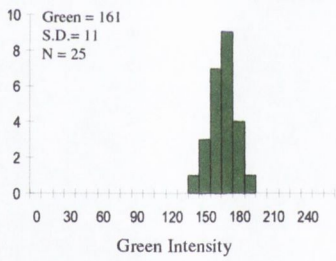
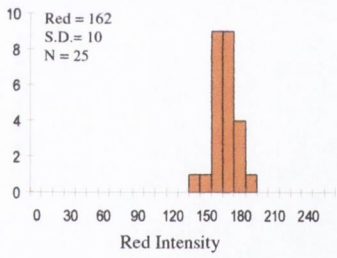
BGSH06N



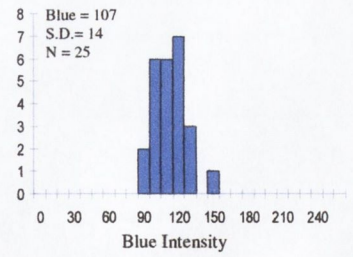
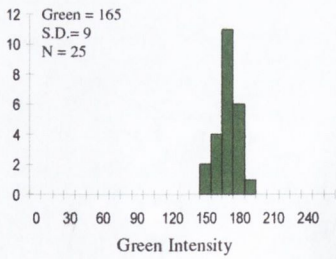
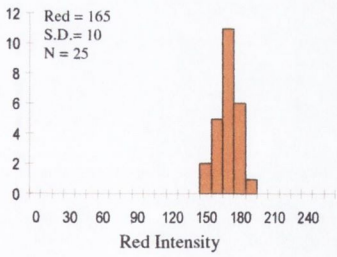
BGSH07N



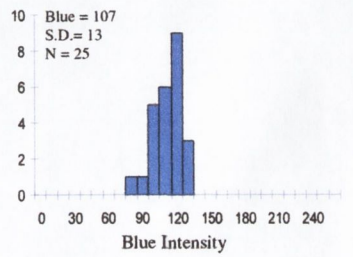
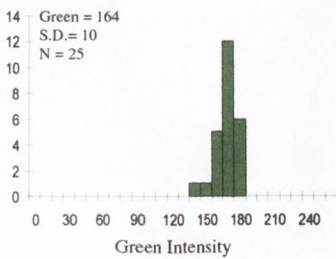
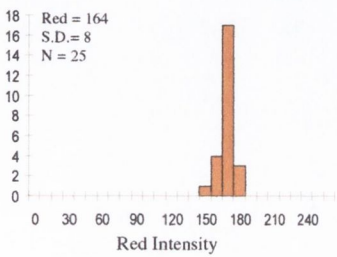
BGSH08N



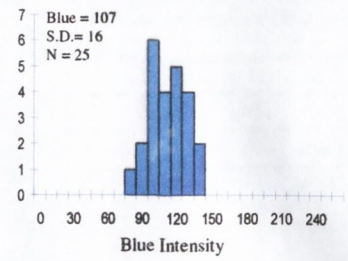
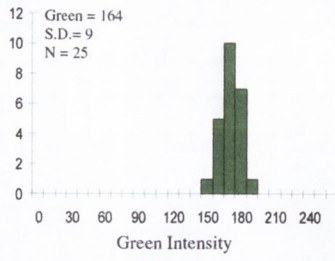
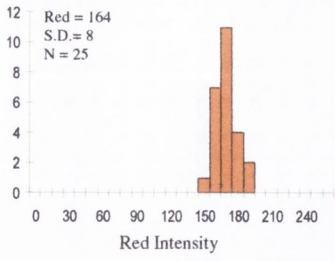
BGSH09N



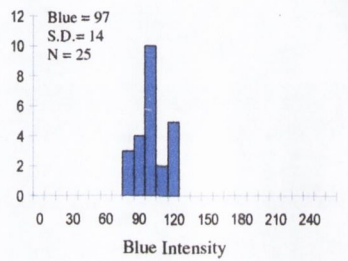
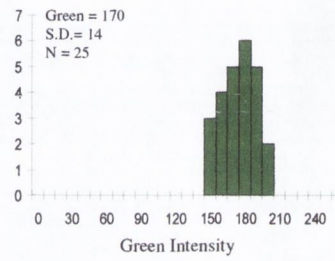
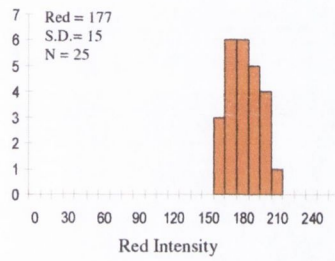
BGSH10N



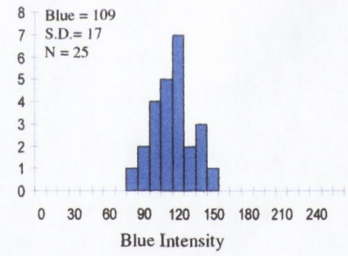
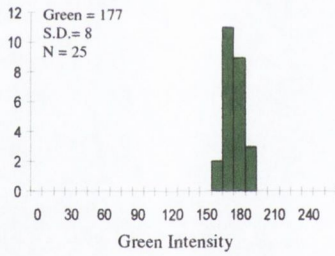
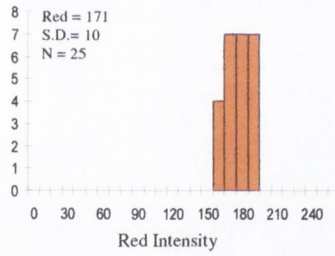
BGSH11N



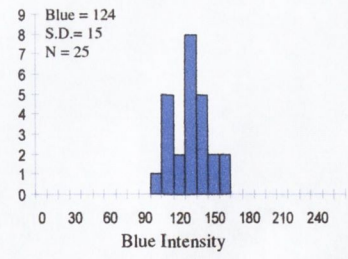
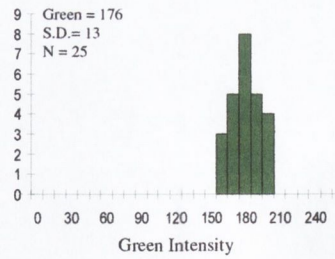
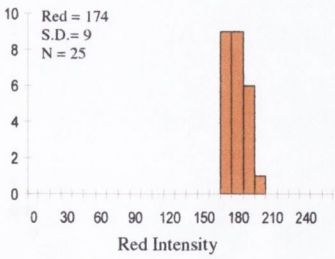
BGSH12N



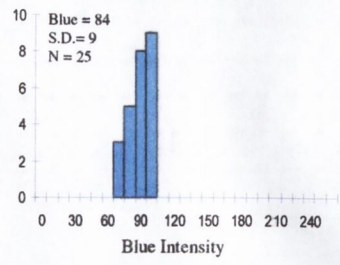
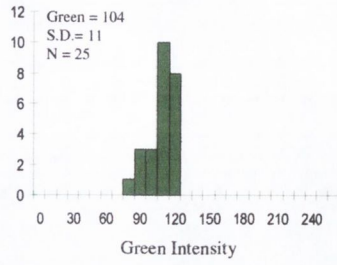
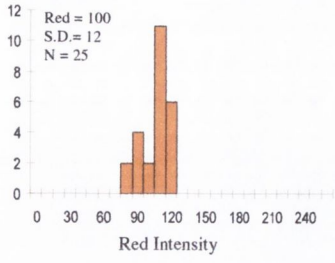
BGSH13N



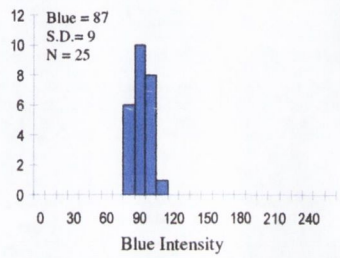
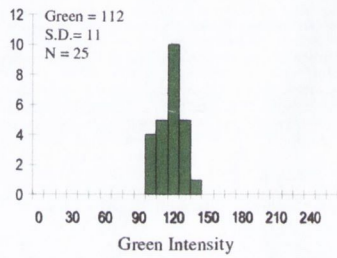
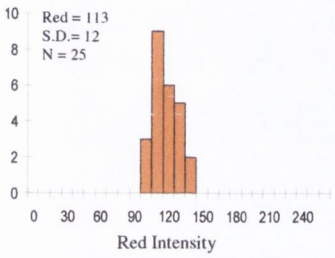
BGSH14N



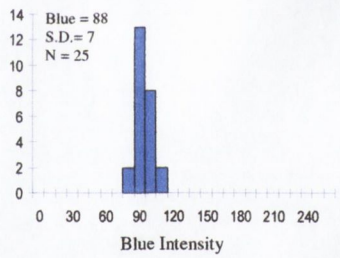
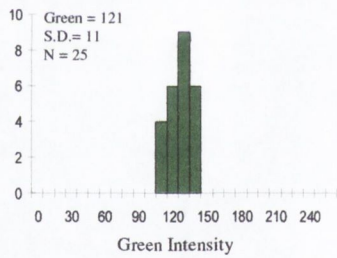
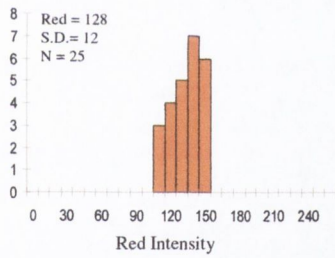
BGS01N



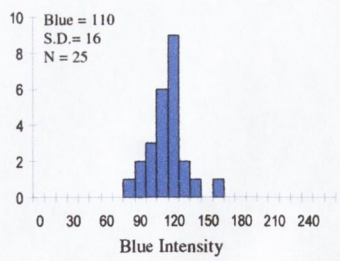
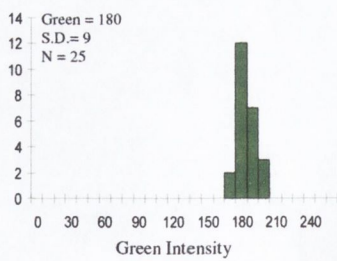
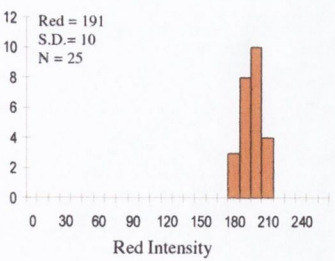
BGS02N



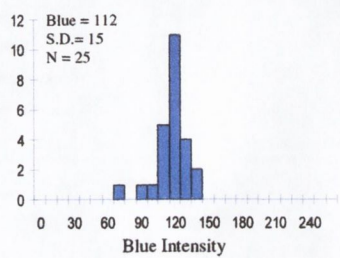
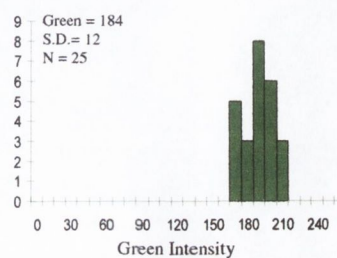
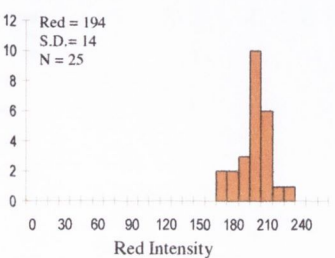
BGS03N



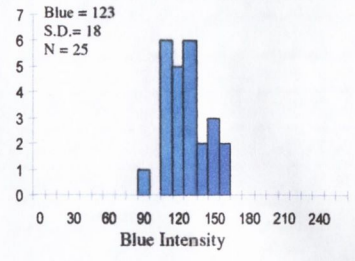
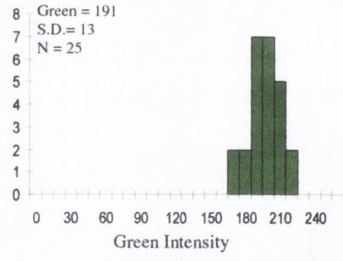
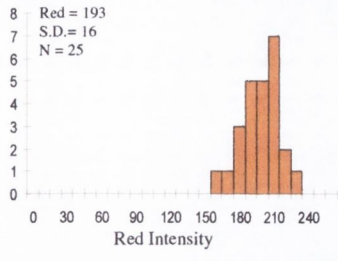
BGS04N



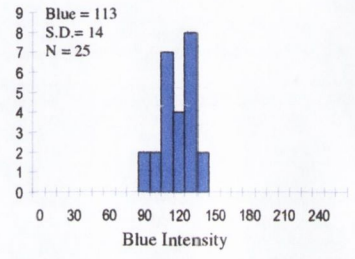
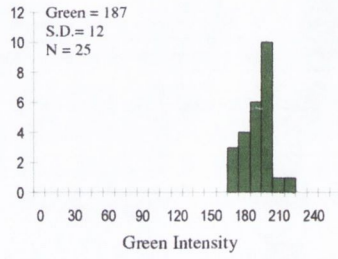
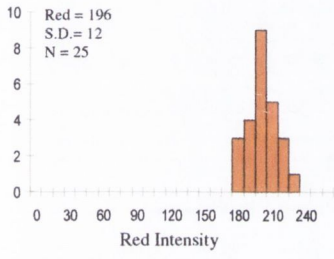
BGS05N



BGS06N



BGS07N



APPENDIX IV

MATURITY DATA

Maturity data for all sampled horizons, Berreraig Bay, Trotternish, northeast Skye.

Sample	Distance from Dyke Contact (m)	Vitrinite Reflectance			AOM Colour by RGB Intensity (n = 25)						TAI (Staplin)	Fluorescence		
		n	% Rr	S.D.	mean R	mean G	mean B	S.D. R	S.D. G	S.D. B		AOM	Tasmanites	Acritarch
BB01N	0.00-0.03	100	3.60	0.36	85	89	71	10	8	7	4-/4			
BB02N	0.03-0.06	58	2.97	0.26	94	94	73	12	10	8	4-/4			
BB03N	0.06-0.10	65	2.59	0.27	99	94	68	9	8	6	4-			
BB04N	0.10-0.15	30	2.01	0.26	101	97	72	13	9	6	4-			
BB05N	0.15-0.20	48	1.72	0.25	113	104	77	10	9	9	3+			
BB06N	0.20-0.25	90	1.58	0.26	118	105	76	12	9	7	3+	Some B	-	-
BB07N	0.25-0.30	100	1.55	0.16	133	115	78	11	7	6	3/3+	CB	-	-
BB08N	0.30-0.35	100	1.29	0.20	137	120	80	9	10	11	3/3+	O	-	-
BB09N	0.35-0.40	50	1.19	0.19	150	136	90	11	9	11	3/3+	O	-	-
BB10N	0.40-0.45	50	1.15	0.22	153	145	93	8	11	12	3	O	-	-
BB11N	0.45-0.50	100	1.09	0.21	156	147	93	12	13	11	3	O	-	-
BB12N	0.50-0.55	83	0.96	0.16	162	154	94	10	11	14	3-	O	-	-
BB13N	0.55-0.60				163	153	93	9	11	14	3-	YO	-	-
BB14N	0.60-0.65	47	1.06	0.18	160	159	101	8	10	16	3-	YO	-	-
BB15N	0.65-0.70	100	0.98	0.20	163	160	100	11	10	12	3-	YO	-	-
BB16N	0.70-0.75	34	0.96	0.22							3-	YO	-	-
BB17N	0.75-0.80	33	0.92	0.19	168	170	111	10	10	16	3-	YO	-	Y
BB18N	0.80-0.85	77	0.96	0.19							3-	DY	-	-
BB19N	0.85-0.90	32	0.91	0.18	168	166	107	11	11	14	3-	DY	-	-
BB20N	0.90-0.95	56	0.85	0.18							2+/3-	DY	-	-
BB21N	0.95-1.00	58	0.89	0.19	167	164	105	8	8	11	2+/3-	DY	-	Y
BB22N	1.00-1.10	39	0.86	0.20	166	165	108	9	12	14	3-	DY	-	Y-BY
BB23N	1.10-1.20	42	0.95	0.19							2+	DY	-	-
BB24N	1.20-1.30	100	0.84	0.28	168	171	118	8	10	14	2+	DY	-	-
BB25N	1.30-1.40	46	0.82	0.19							2/2+	DY	-	-
BB26N	1.35-1.40	100	0.83	0.25							2/2+	DY	-	Y-BY
BB27N	1.40-1.50	45	0.83	0.17	171	169	109	11	12	17	2-/2	DY	-	-
BB28N	1.60-1.70	100	0.81	0.26							2+	DY	BY	-
BB29N	1.50-1.60	46	0.80	0.15	174	169	107	8	11	13	2	DY	-	-
BB30N	1.70-1.80	64	0.88	0.18							2	DY	Y	-
BB31N	1.80-1.90	34	0.79	0.16	173	173	116	11	11	12	2-	DY	-	-
BB32N	1.90-2.00	21	0.79	0.15							2-	DY	-	-
BB33N	2.00-2.10	64	0.78	0.17	172	175	118	9	8	12	2-	DY	-	-
BB34N	2.30-2.40	100	0.78	0.21	171	171	110	10	12	15	2-	DY	BY	-
BB35N	2.60-2.70	58	0.76	0.16	174	173	111	10	13	13	2-	DY	-	-
BB36N	2.90-3.00	50	0.80	0.19	172	174	117	10	11	17	2-/2	Y	-	-
BB37N	3.20-3.30	53	0.75	0.15	173	179	124	8	8	19	2-	Y	BY	-
BB38N	3.50-3.70	71	0.75	0.15	170	173	123	12	13	16	2-	Y	-	-
BB40N	3.80-3.90	48	0.79	0.18	172	172	116	10	12	16	2-	Y	-	-
BB41N	4.10-4.20	57	0.75	0.16	175	173	116	12	12	18	2-/2	Y	-	-
BB42N	4.40-4.50	59	0.79	0.20	176	175	120	9	11	15	2-	Y	-	-
BB43N	5.00-5.10	19	0.76	0.14	172	169	118	10	22	16	2-/2	Y	Y	-
BB44N	5.50-5.60	42	0.73	0.18	176	175	121	12	11	16	2-	Y	Y	BY
BGSH01N	0.00-0.05	44	3.32	0.35	93	99	79	11	9	6	4-/4			
BGSH02N	0.05-0.10	52	2.78	0.26	96	99	79	15	12	8	4-/4			
BGSH03N	0.15-0.20	74	1.69	0.22	108	104	77	12	11	7	3+			
BGSH04N	0.20-0.25	50	1.44	0.19	116	107	73	14	14	11	3	Some B	-	-
BGSH05N	0.32-0.34	100	1.13	0.15	131	119	76	14	14	11	3-/3	CB	-	-
BGSH06N	0.35-0.40	100	1.00	0.16	141	134	84	10	10	9	3-	CB	YO	-
BGSH07N	0.40-0.45	60	0.96	0.25	148	140	84	9	12	14	2+	O	YO	-
BGSH08N	0.50-0.60	58	0.86	0.23	162	161	98	10	11	13	2+	YO	Y	-
BGSH09N	0.96-1.00	50	0.83	0.22	165	165	107	10	9	14	2	DY	BY	-
BGSH10N	1.30-1.40	59	0.73	0.18	164	164	107	8	10	13	2	DY	BY	-
BGSH11N	1.95-2.05	51	0.73	0.20	164	164	107	8	9	16	2	DY	BY	-
BGSH12N	3.00-3.10	64	0.79	0.18	177	170	97	15	14	14	2-/2	Y	-	-
BGSH13N	4.90-5.00	52	0.79	0.16	171	170	109	10	8	17	2-	Y	BY	-
BGSH14N	6.70	63	0.75	0.20	176	174	124	9	13	15	2-/2	Y	-	-
BGS01N	0.00-0.04	36	3.12	0.21	100	104	84	12	11	9	4-/4			
BGS02N	0.10-0.15	46	1.79	0.18	113	112	87	12	11	9	4-/4			
BGS03N	0.23-0.30	27	1.18	0.21	128	121	88	12	11	7	3+			Y
BGS04N	0.70-0.80	37	0.86	0.17	191	180	110	10	9	16	2/2+	O	BY	Y
BGS05N	2.06-2.16	48	0.84	0.17	194	184	112	14	12	15	2	DY	BY	Y
BGS06N	2.90-3.00	22	0.76	0.16	193	191	123	16	13	18	2-	DY	Y - BY	BY
BGS07N	5.25-5.35	45	0.72	0.16	196	187	113	12	12	14	2-	Y	BY	BY

BY	Bright Yellow
Y	Yellow
DY	Dull Yellow
YO	Yellow-Orange
O	Orange
CB	Orange-Brown
B	Brown
	No Fluorescence

Quantitative AOM colour data for all sampled horizons, Berreraig Bay, Trotternish, northeast Skye.

Sample	Distance from Dyke Contact (m)	RGB Intensity (N = 25)						Relative RGB percent			Hue-Saturation-Brightness		
		mean R	mean G	mean B	S.D. R	S.D. G	S.D. B	%R	%G	%B	H	S	B
BB01N	0.00-0.03	85	89	71	10	8	7	35	36	29	73	20	35
BB02N	0.03-0.06	94	94	73	12	10	8	36	36	28	60	22	37
BB03N	0.06-0.10	99	94	68	9	8	6	38	36	26	50	31	39
BB04N	0.10-0.15	101	97	72	13	9	6	37	36	27	52	29	40
BB05N	0.15-0.20	113	104	77	10	9	9	38	35	26	45	32	44
BB06N	0.20-0.25	118	105	76	12	9	7	39	35	25	41	36	46
BB07N	0.25-0.30	133	115	78	11	7	6	41	35	24	40	41	52
BB08N	0.30-0.35	137	120	80	9	10	11	41	36	24	42	42	54
BB09N	0.35-0.40	150	136	90	11	9	11	40	36	24	46	40	59
BB10N	0.40-0.45	153	145	93	8	11	12	39	37	24	52	39	60
BB11N	0.45-0.50	156	147	93	12	13	11	39	37	23	51	40	61
BB12N	0.50-0.55	162	154	94	10	11	14	40	38	23	53	42	64
BB13N	0.55-0.60	163	153	93	9	11	14	40	37	23	51	43	64
BB14N	0.60-0.65	160	159	101	8	10	16	38	38	24	59	37	63
BB15N	0.65-0.70	163	160	100	11	10	12	39	38	24	57	39	64
BB16N	0.70-0.75												
BB17N	0.75-0.80	168	170	111	10	10	16	37	38	25	62	35	67
BB18N	0.80-0.85												
BB19N	0.85-0.90	168	166	107	11	11	14	38	38	24	58	36	66
BB20N	0.90-0.95												
BB21N	0.95-1.00	167	164	105	8	8	11	38	38	24	57	37	66
BB22N	1.00-1.10	166	165	108	9	12	14	38	38	25	59	35	65
BB23N	1.10-1.20												
BB24N	1.20-1.30	168	171	118	8	10	14	37	37	26	63	31	67
BB25N	1.30-1.40												
BB26N	1.35-1.40												
BB27N	1.40-1.50	171	169	109	11	12	17	38	38	24	58	36	67
BB28N	1.60-1.70												
BB29N	1.50-1.60	174	169	107	8	11	13	39	38	24	56	39	68
BB30N	1.70-1.80												
BB31N	1.80-1.90	173	173	116	11	11	12	37	37	25	60	33	68
BB32N	1.90-2.00												
BB33N	2.00-2.10	172	175	118	9	8	12	37	38	25	63	33	69
BB34N	2.30-2.40	171	171	110	10	12	15	38	38	24	60	36	67
BB35N	2.60-2.70	174	173	111	10	13	13	38	38	24	59	36	68
BB36N	2.90-3.00	172	174	117	10	11	17	37	38	25	62	33	68
BB37N	3.20-3.30	173	179	124	8	8	19	36	38	26	67	31	70
BB38N	3.50-3.70	170	173	123	12	13	16	36	37	26	64	29	68
BB40N	3.80-3.90	172	172	116	10	12	16	37	37	25	60	33	68
BB41N	4.10-4.20	175	173	116	12	12	18	38	37	25	58	34	69
BB42N	4.40-4.50	176	175	120	9	11	15	37	37	25	59	32	69
BB43N	5.00-5.10	172	169	118	10	22	16	37	37	26	57	31	68
BB44N	5.50-5.60	176	175	121	12	11	16	37	37	26	53	31	69
BGSH01N	0.00-0.05	93	99	79	11	9	6	34	37	29	78	20	39
BGSH02N	0.05-0.10	96	99	79	15	12	8	35	36	29	69	20	39
BGSH03N	0.15-0.20	108	104	77	12	11	7	37	36	27	52	29	42
BGSH04N	0.20-0.25	116	107	73	14	14	11	39	36	25	47	37	45
BGSH05N	0.32-0.34	131	119	76	14	14	11	40	37	23	47	42	51
BGSH06N	0.35-0.40	141	134	84	10	10	9	39	37	23	53	40	55
BGSH07N	0.40-0.45	148	140	84	9	12	14	40	38	23	52	43	58
BGSH08N	0.50-0.60	162	161	98	10	11	13	38	38	23	59	40	64
BGSH09N	0.96-1.00	165	165	107	10	9	14	38	38	24	60	35	65
BGSH10N	1.30-1.40	164	164	107	8	10	13	38	38	25	60	35	64
BGSH11N	1.95-2.05	164	164	107	8	9	16	38	38	25	60	35	64
BGSH12N	3.00-3.10	177	170	97	15	14	14	40	38	22	55	45	69
BGSH13N	4.90-5.00	171	170	109	10	8	17	38	38	24	59	36	67
BGSH14N	6.70	176	174	124	9	13	15	37	37	26	58	30	69
BGS01N	0.00-0.04	100	104	84	12	11	9	35	36	29	72	19	41
BGS02N	0.10-0.15	113	112	87	12	11	9	36	36	28	58	23	41
BGS03N	0.23-0.30	128	121	88	12	11	7	38	36	26	49	31	50
BGS04N	0.70-0.80	191	180	110	10	9	16	40	37	23	52	42	75
BGS05N	2.06-2.16	194	184	112	14	12	15	40	38	23	53	42	76
BGS06N	2.90-3.00	193	191	123	16	13	18	38	38	24	58	36	76
BGS07N	5.25-5.35	196	187	113	12	12	14	40	38	23	53	42	77

RGB AOM colour data for BBN sample horizon, Berreraig Bay, Trotternish, northeast Skye

	N	1	2	3	4	5	6	7	8	9	10	11	12	13	14	15	16	17	18	19	20	21	22	23	24	25	Mean
BB01N	R	61.72	73.11	82.67	93.86	76.97	97.13	72.08	92.53	80.92	87.85	74.03	81.45	87.33	83.96	76.34	74.59	97.19	91.63	91.97	95.93	98.47	75.64	83.00	86.57	96.52	84.54
	G	71.93	80.58	88.67	95.35	82.66	99.62	82.53	96.67	83.56	89.17	77.62	79.85	90.40	87.34	79.32	82.46	100.46	98.25	93.32	99.25	100.95	82.43	89.08	91.08	96.22	88.75
	B	62.53	67.63	69.50	75.22	64.87	84.35	69.70	77.64	62.65	70.82	59.55	56.36	66.49	74.76	60.48	68.62	76.23	80.09	70.17	77.05	83.07	68.22	74.47	71.50	75.65	70.71
BB02N	R	88.10	93.60	110.63	101.33	58.17	82.42	103.91	86.61	98.72	106.47	85.84	110.89	87.87	72.18	99.86	104.11	99.45	89.99	104.64	110.55	90.10	90.94	98.48	86.67	95.86	94.30
	G	86.26	97.92	109.87	98.54	67.39	84.66	102.63	88.23	94.23	104.78	89.24	108.86	84.81	77.20	95.66	97.09	102.24	89.70	98.05	107.32	91.82	92.63	99.37	90.22	97.14	94.23
	B	63.23	75.79	88.16	72.59	54.82	64.41	84.10	70.19	72.18	81.52	67.05	79.71	60.80	57.96	74.65	70.07	82.03	69.12	74.46	80.26	75.92	75.76	82.27	73.77	75.42	73.05
BB03N	R	91.67	86.58	91.23	108.18	95.37	89.91	106.56	108.15	96.16	94.93	86.89	109.19	103.28	90.58	96.55	101.77	93.57	113.22	103.42	111.67	88.54	108.80	110.04	91.89	85.24	98.54
	G	90.81	86.92	87.55	107.05	92.43	89.13	104.56	97.37	92.09	89.68	86.70	98.38	94.88	87.29	92.84	94.45	87.67	108.32	92.75	105.01	85.31	101.71	104.78	89.52	80.12	93.89
	B	65.71	62.59	63.95	79.48	66.27	66.97	75.65	71.69	67.32	61.69	67.18	72.87	64.68	64.38	69.11	68.15	63.21	81.12	69.98	67.72	63.44	74.17	77.91	64.73	59.20	68.37
BB04N	R	93.46	83.41	86.96	114.97	114.77	110.17	115.15	97.47	77.38	96.58	91.96	101.31	78.37	109.95	89.44	116.02	98.37	113.02	109.72	94.96	115.86	121.55	101.26	90.08	92.02	100.57
	G	95.20	79.84	89.10	105.42	108.16	100.20	107.41	97.94	81.64	97.89	92.79	95.66	83.12	102.85	88.75	106.17	91.08	104.20	103.05	92.26	110.30	111.92	99.44	89.14	94.83	97.13
	B	76.43	65.69	65.72	76.58	78.08	64.42	76.77	81.53	63.83	76.32	71.61	73.10	66.43	69.79	62.37	71.24	64.06	71.99	72.37	68.46	81.53	77.39	80.51	70.62	73.66	72.02
BB05N	R	100.49	124.62	111.69	132.40	122.76	123.29	113.23	103.79	132.44	119.21	108.41	113.50	106.42	109.39	109.65	102.61	100.72	96.43	120.73	112.60	97.02	111.52	121.15	116.12	118.57	113.15
	G	89.98	117.88	100.51	122.30	113.18	117.38	105.26	100.24	116.43	109.48	99.52	107.33	98.98	97.21	91.28	98.80	90.27	96.05	111.98	107.37	103.27	94.73	110.12	103.33	104.16	104.28
	B	64.17	88.75	66.05	86.52	88.27	90.48	83.74	75.58	80.26	77.36	73.61	83.88	70.00	67.66	59.94	66.53	66.12	72.60	91.17	85.07	86.66	64.83	77.37	72.43	76.72	76.63
BB06N	R	107.89	128.45	126.69	123.33	108.30	113.91	102.05	116.15	118.26	113.85	99.04	114.61	124.02	125.35	132.51	142.39	111.59	126.08	106.28	113.60	128.49	136.58	94.82	117.65	116.24	117.93
	G	96.85	110.59	109.13	105.61	97.81	106.84	92.72	104.12	114.37	98.07	89.48	100.60	108.41	109.92	117.61	115.96	101.23	113.03	97.77	96.97	118.51	116.54	87.29	106.79	102.43	104.75
	B	70.68	71.09	74.15	74.79	72.56	74.48	73.65	75.71	96.31	69.71	66.29	70.14	76.26	81.06	79.63	76.50	67.94	81.87	74.53	68.50	90.36	85.03	70.66	76.09	76.09	75.76
BB07N	R	142.06	142.69	127.74	130.77	122.28	126.67	132.81	138.04	115.15	120.86	146.81	133.91	144.97	131.01	120.89	137.83	129.99	112.23	139.49	141.32	121.80	153.98	132.00	144.10	125.47	132.59
	G	124.51	118.83	105.02	111.37	100.55	112.50	111.29	111.55	113.29	112.36	126.48	115.10	130.95	115.76	118.01	115.29	114.46	99.53	114.33	114.23	114.55	122.05	117.41	123.23	107.38	114.80
	B	91.83	73.35	76.18	81.94	67.57	81.27	72.30	72.06	84.02	83.31	79.77	78.52	90.97	79.81	83.35	77.21	82.16	71.07	76.99	73.87	83.89	72.61	76.04	72.61	66.18	77.96
BB08N	R	122.88	136.23	137.59	130.53	144.35	140.09	125.24	123.91	125.74	149.13	146.34	151.56	140.70	134.80	136.82	135.43	140.15	154.53	135.90	130.09	140.29	144.93	126.30	126.84	149.55	137.20
	G	106.93	116.54	129.54	127.46	133.45	129.79	107.41	110.01	110.40	126.80	133.14	128.58	114.14	115.65	108.28	116.07	131.39	137.76	127.61	111.46	117.45	124.28	108.72	109.20	128.91	120.44
	B	73.90	84.82	91.51	96.15	93.14	72.18	59.09	78.08	78.35	82.86	88.07	80.92	75.99	73.78	68.27	74.29	90.19	98.39	99.26	75.63	72.39	73.18	72.21	69.26	66.98	79.56
BB09N	R	147.40	145.42	171.95	156.85	142.64	149.53	144.09	151.98	144.83	144.33	162.45	129.47	148.70	160.65	142.38	162.12	157.47	142.03	163.35	143.65	140.28	169.32	147.50	133.02	142.03	149.74
	G	141.98	128.38	149.42	134.56	138.53	140.19	135.18	144.62	131.27	128.23	147.42	115.09	131.20	137.09	129.92	142.70	143.30	132.16	148.54	134.21	128.33	152.37	139.36	121.87	122.38	135.93
	B	111.49	78.90	95.57	95.05	104.12	90.59	84.22	102.24	78.66	70.67	90.72	75.99	66.29	77.05	78.47	89.68	89.65	89.61	104.94	90.43	78.48	105.78	102.66	88.07	78.93	89.53
BB10N	R	155.87	146.43	149.98	151.81	138.67	154.16	149.40	147.87	151.15	148.06	145.57	148.18	158.96	160.36	153.94	155.82	156.00	164.97	155.07	146.01	171.08	137.12	160.85	158.96	155.87	152.89
	G	147.63	149.02	152.40	152.29	115.35	148.67	136.66	127.08	145.75	139.53	132.82	132.27	147.82	163.26	145.76	149.06	155.94	154.83	154.33	133.71	150.65	130.99	153.23	147.82	147.63	144.58
	B	87.67	110.33	98.30	110.74	72.23	107.00	82.97	77.68	83.79	91.03	87.62	79.15	87.75	116.91	92.73	94.01	107.70	95.86	112.96	79.34	88.09	87.08	95.47	87.75	87.67	92.87
BB11N	R	152.59	163.49	138.28	165.51	176.07	152.67	147.20	156.33	135.49	132.30	149.05	151.94	166.66	141.08	153.79	157.37	164.29	161.24	170.05	172.90	145.72	161.35	171.51	152.53	168.04	156.30
	G	147.17	154.89	127.24	160.95	170.89	147.30	137.72	142.23	131.87	126.96	132.85	144.70	152.07	135.23	145.16	135.22	156.12	145.43	169.62	155.93	133.50	163.02	161.85	142.22	154.86	147.00
	B	102.94	105.08	82.03	103.01	112.93	83.22	86.85	95.79	86.05	76.00	81.55	95.05	84.42	96.36	98.66	81.99	97.77	89.12	111.48	99.99	69.44	105.77	103.29	95.93	86.80	93.26
BB12N	R	151.02	166.40	162.35	142.85	164.20	168.10	178.08	167.33	169.09	149.98	166.43	165.53	156.53	176.33	167.39	167.69	152.56	164.79	143.73	152.89	182.36	162.87	162.30	149.12	171.34	162.45
	G	150.43	163.25	154.05	130.25	166.98	154.08	163.47	164.01	170.68	136.02	147.46	148.33	154.72	169.51	160.35	149.16	141.74	150.12	132.28	142.89	162.19	161.78	154.99	151.44	157.79	153.52
	B	78.88	90.85	92.19	72.78	126.07	80.83	96.86	104.77	109.40	63.90	87.23	93.68	105.73	100.66	94.22	98.73	92.49	83.17	80.11	82.84	101.09	107.90	98.21	117.04	93.66	94.13
BB13N	R	163.51	166.64	160.05	170.11	150.09	152.11	170.80	165.81	159.03	174.84	152.37	178.02	162.95	152.12	154.70	175.54	181.62	160.29	163.77	168.59	154.23	167.70	153.20	160.67	162.96	163.27
	G	160.80	163.35	153.04	175.07	138.27	151.45	153.45	145.01	137.36	168.22	130.43	162.89	162.28	145.41	141.04	164.69	169.50	146.76	150.05	152.82	148.28	145.72	140.39	156.35	161.56	152.97
	B	99.48	93.71	95.47	120.85	95.29	103.12	87.71	78.56	73.33	112.33	78.32	93.11	96.50	100.59	88.35	98.90	103.23	77.64	82.36	91.90	87.05	79.21	63.05	113.48	106.00	92.78
BB14N	R	172.17	152.28	156.14	155.00	143.17	154.23	163.48	173.43	166.93	155.63	163.98	163.25	158.07	165.73	157.22	153.68	159.37	172.52	159.15	148.36	155.07	176.37	162.06	159.66	161.68	160.35
	G	172.28	152.06	149.96	149.07	137.61	152.27	168.02	177.91	164.32	158.50	161.61	159.35	162.75	159.46	151.27	154.63	158.97	174.57	150.90	145.32	151.45	174.84	166.41	155.40	158.76	158.71
	B	117.94	97.48	86.08	77.62	76.98																					

RGB AOM colour data for BBN sample horizon, Berreraig Bay, Trotternish, northeast Skye

	N	1	2	3	4	5	6	7	8	9	10	11	12	13	14	15	16	17	18	19	20	21	22	23	24	25	Mean
BB01N	R	61.72	73.11	82.67	93.86	76.97	97.13	72.08	92.53	80.92	87.85	74.03	81.45	87.33	83.96	76.34	74.59	97.19	91.63	91.97	95.93	98.47	75.64	83.00	86.57	96.52	84.54
	G	71.93	80.58	88.67	95.35	82.66	99.62	82.53	96.67	83.56	89.17	77.62	79.85	90.40	87.34	79.32	82.46	100.46	98.25	93.32	99.25	100.95	82.43	89.08	91.08	96.22	88.75
	B	62.53	67.63	69.50	75.22	64.87	84.65	69.70	77.64	62.65	70.82	59.55	56.36	66.69	74.76	60.48	68.62	76.23	80.09	70.17	77.05	83.07	68.22	74.47	71.50	75.65	70.71
BB02N	R	88.10	93.60	110.63	101.33	58.17	82.42	103.91	86.61	98.72	106.47	85.84	110.89	87.87	72.18	99.86	104.11	99.45	89.99	104.64	110.55	90.10	90.94	98.48	86.67	95.86	94.30
	G	86.26	97.92	109.87	98.54	67.39	84.66	102.63	88.23	94.23	104.78	89.24	108.86	84.81	77.20	95.66	97.09	102.24	89.70	98.05	107.32	91.82	92.63	99.37	90.22	97.14	94.23
	B	63.23	75.79	88.16	72.59	54.82	64.41	84.10	70.19	72.18	81.52	67.05	79.71	60.80	57.96	74.65	70.07	82.03	69.12	74.46	80.26	75.92	75.76	82.27	73.77	75.42	73.05
BB03N	R	91.67	86.58	91.23	108.18	95.37	89.91	106.56	108.15	96.16	94.93	86.89	109.19	103.28	90.58	96.55	101.77	93.57	113.22	103.42	111.67	88.54	108.80	110.04	91.89	85.24	98.54
	G	90.81	86.92	87.55	107.05	92.43	89.13	104.56	97.37	92.09	89.68	86.70	98.38	94.88	87.29	92.84	94.45	87.67	108.32	92.75	105.01	85.31	101.71	104.78	89.52	80.12	93.89
	B	65.71	62.59	63.95	79.48	66.27	66.97	75.65	71.69	67.32	61.69	67.18	72.87	64.68	64.38	69.11	68.15	63.21	81.12	69.98	67.72	63.44	74.17	77.91	64.73	59.20	68.37
BB04N	R	93.46	83.41	86.96	114.97	114.77	110.17	115.15	97.47	77.38	96.58	91.96	101.31	78.37	109.95	89.44	116.02	98.37	113.02	109.72	94.96	115.86	121.55	101.26	90.08	92.02	100.57
	G	95.20	79.84	89.10	105.42	108.16	100.20	107.41	97.94	81.64	97.89	92.79	95.66	83.12	102.85	88.75	106.17	91.08	104.20	103.05	92.26	110.30	111.92	99.44	89.14	94.83	97.13
	B	76.43	65.69	65.72	76.58	78.08	64.42	76.77	81.53	63.83	76.32	71.61	73.10	66.43	69.79	62.37	71.24	64.06	71.99	72.37	68.46	81.53	77.39	80.51	70.62	73.66	72.02
BB05N	R	100.49	124.62	111.69	132.40	122.76	123.29	113.23	103.79	132.44	119.21	108.41	113.50	106.42	109.39	109.65	102.61	100.72	96.43	120.73	112.60	97.02	111.52	121.15	116.12	118.57	113.15
	G	89.98	117.88	100.51	122.30	113.18	117.38	105.26	100.24	116.43	109.48	99.52	107.33	98.98	97.21	91.28	98.80	90.27	96.05	111.98	107.37	103.27	94.73	110.12	103.33	104.16	104.28
	B	64.17	88.75	66.05	86.52	88.27	90.48	83.74	75.58	80.26	77.36	73.61	83.88	70.00	67.66	59.94	66.53	66.12	72.60	91.17	85.07	86.66	64.83	77.37	72.43	76.72	76.63
BB06N	R	107.89	128.45	126.69	123.33	108.30	113.91	102.05	116.15	118.26	113.85	99.04	114.61	124.02	125.35	132.51	142.39	111.59	126.08	106.28	113.60	128.49	136.58	94.82	117.65	116.24	117.93
	G	96.85	110.59	109.13	105.61	97.81	106.84	92.72	104.12	114.37	98.07	89.48	100.60	108.41	109.92	117.61	115.96	101.23	113.03	97.77	96.97	118.51	116.54	87.29	106.79	102.43	104.75
	B	70.68	71.09	74.15	74.79	72.56	74.48	73.65	75.71	96.31	69.71	66.29	70.14	76.26	81.06	79.63	76.50	67.94	81.87	74.53	68.50	90.36	85.03	70.66	76.09	76.09	75.76
BB07N	R	142.06	142.69	127.74	130.77	122.28	126.67	132.81	138.04	115.15	120.86	146.81	133.91	144.97	131.01	120.89	137.83	129.99	112.23	139.49	141.32	121.80	153.98	132.00	144.10	125.47	132.59
	G	124.51	118.83	105.02	111.37	100.55	112.50	111.29	111.55	113.29	112.36	126.48	115.10	130.95	115.76	118.01	115.29	114.46	99.53	114.33	114.23	114.55	122.05	117.41	123.23	107.38	114.80
	B	91.83	73.35	76.18	81.94	67.57	81.27	72.30	72.06	84.02	83.31	79.77	78.52	90.97	79.81	83.35	77.21	82.16	71.07	76.99	73.87	83.89	72.61	76.04	72.61	66.18	77.96
BB08N	R	122.88	136.23	137.59	130.53	144.35	140.09	125.24	123.91	125.74	149.13	146.34	151.56	140.70	134.80	136.82	135.43	140.15	154.53	135.90	130.09	140.29	144.93	126.30	126.84	149.55	137.20
	G	106.93	116.54	129.54	127.46	133.45	129.79	107.41	110.01	110.40	126.80	133.14	128.58	114.14	115.65	108.28	116.07	131.39	137.76	127.61	111.46	117.45	124.28	108.72	109.20	128.91	120.44
	B	73.90	84.82	91.51	96.15	93.14	72.18	59.09	78.08	78.35	82.86	88.07	80.92	75.99	73.78	68.27	74.29	90.19	98.39	99.26	75.63	72.39	73.18	72.21	69.26	66.98	79.56
BB09N	R	147.40	145.42	171.95	156.85	142.64	149.53	144.09	151.98	144.83	144.33	162.45	129.47	148.70	160.65	142.38	162.12	157.47	142.03	163.35	143.65	140.28	169.32	147.50	133.02	142.03	149.74
	G	141.98	128.38	149.42	134.56	138.53	140.19	135.18	144.62	131.27	128.23	147.42	115.09	131.20	137.09	129.92	142.70	143.30	132.16	148.54	134.21	128.33	152.37	139.36	121.87	122.38	135.93
	B	111.49	78.90	95.57	95.05	104.12	90.59	84.22	102.24	78.66	70.67	90.72	75.99	86.29	77.05	78.47	89.68	89.65	89.61	104.94	90.43	78.48	105.78	102.66	88.07	78.93	89.53
BB10N	R	155.87	146.43	149.98	151.81	138.67	154.16	149.40	147.87	151.15	148.06	145.57	148.18	158.96	160.36	153.94	155.82	156.00	164.97	155.07	146.01	171.08	137.12	160.85	158.96	155.87	152.89
	G	147.63	149.02	152.40	152.29	115.35	148.67	136.66	127.08	145.75	139.53	132.82	132.27	147.82	163.26	145.76	149.06	155.94	154.83	154.33	133.71	150.65	130.99	153.23	147.82	147.63	144.58
	B	87.67	110.33	98.30	110.74	72.23	107.00	82.97	77.68	83.79	91.03	87.62	79.15	87.75	116.91	92.73	94.01	107.70	95.86	112.96	79.34	88.09	87.08	95.47	87.75	87.67	92.87
BB11N	R	152.59	163.49	138.28	165.51	176.07	152.67	147.20	156.33	135.49	132.30	149.05	151.94	166.66	141.08	153.79	157.37	164.29	161.24	170.05	172.90	145.72	161.35	171.51	152.53	168.04	156.30
	G	147.17	154.89	127.24	160.95	170.89	147.30	137.72	142.23	131.87	126.96	132.85	144.70	152.07	135.23	145.16	135.22	156.12	145.43	169.62	155.93	133.50	163.02	161.85	142.22	154.86	147.00
	B	102.94	105.08	82.03	103.01	112.93	83.22	86.85	95.79	86.05	76.00	81.55	95.05	84.42	96.36	98.66	81.99	97.77	89.12	111.48	99.99	69.44	105.77	103.29	95.93	86.80	93.26
BB12N	R	151.02	166.40	162.35	142.85	164.20	168.10	178.08	167.33	169.09	149.98	166.43	165.53	156.53	176.33	167.39	167.69	152.56	164.79	143.73	152.89	182.36	162.87	162.30	149.12	171.34	162.45
	G	150.43	163.25	154.05	130.25	166.98	154.08	163.47	164.01	170.68	136.02	147.46	148.33	154.72	169.51	160.35	149.16	141.74	150.12	132.28	142.89	162.19	161.78	154.99	151.44	157.79	153.52
	B	78.88	90.85	92.19	72.78	126.07	80.83	96.86	104.77	109.40	63.90	87.23	93.68	105.73	100.66	94.22	98.73	92.49	83.17	80.11	82.84	101.09	107.90	98.21	117.04	93.66	94.13
BB13N	R	163.51	166.64	160.05	170.11	150.09	152.11	170.80	165.81	159.03	174.84	152.37	178.02	162.95	152.12	154.70	175.54	181.62	160.29	163.77	168.59	154.23	167.70	153.20	160.67	162.96	163.27
	G	160.80	163.35	153.04	175.07	138.27	151.45	153.45	145.01	137.36	168.22	130.43	162.89	162.28	145.41	141.04	164.69	169.50	146.76	150.05	152.82	148.28	145.72	140.39	156.35	161.56	152.97

RGB AOM colour data for BBN sample horizon, Berreraig Bay, Trotternish, northeast Skye

	N	1	2	3	4	5	6	7	8	9	10	11	12	13	14	15	16	17	18	19	20	21	22	23	24	25	Mean
BB17N	R	183.65	167.92	166.52	153.47	165.95	167.54	141.18	170.00	159.61	173.28	179.81	168.25	178.95	165.15	175.40	171.74	165.42	166.49	184.49	162.38	159.10	166.06	186.13	163.70	158.54	168.03
	G	191.10	171.58	172.68	155.51	167.93	172.42	151.02	161.01	167.52	167.85	181.51	174.17	187.58	166.41	179.26	170.75	167.66	168.30	184.97	165.90	153.93	157.79	183.29	171.74	163.39	170.21
	B	134.16	117.53	129.72	91.42	112.46	132.23	100.87	91.96	119.74	88.83	105.69	130.25	137.14	104.37	126.55	102.76	110.96	103.33	101.70	106.61	92.09	89.71	135.62	106.41	106.06	111.13
BB19N	R	156.46	154.83	171.26	178.57	158.27	170.37	196.15	165.63	177.66	157.99	163.92	172.18	185.80	175.15	158.58	176.34	154.86	164.49	167.27	181.38	157.87	167.83	163.71	152.52	179.01	168.32
	G	157.08	150.25	167.58	181.08	154.50	171.34	188.79	158.48	182.34	167.11	167.51	165.31	184.62	178.13	163.56	166.99	158.08	156.53	152.57	174.85	148.37	154.25	160.92	156.12	172.88	165.57
	B	107.06	96.26	111.13	128.82	111.85	121.71	123.83	94.90	132.09	124.57	106.09	107.44	112.87	118.08	110.78	98.66	100.19	91.04	79.03	110.80	96.01	101.03	100.26	96.26	81.56	106.65
BB21N	R	154.81	167.36	161.90	150.95	176.28	175.64	175.62	177.79	159.18	154.06	175.55	161.64	158.95	169.73	173.84	171.79	177.04	170.89	169.38	159.71	166.12	173.68	159.30	159.79	178.62	167.18
	G	145.31	170.79	166.86	150.59	170.68	176.86	160.01	175.03	164.66	154.35	169.40	153.91	159.11	169.49	177.09	158.87	161.89	168.52	165.86	160.39	154.50	164.32	158.90	160.25	170.60	163.53
	B	94.22	115.56	109.21	107.97	103.12	111.67	94.62	122.16	124.62	87.61	104.92	108.46	99.33	117.31	124.32	87.10	103.43	103.35	110.17	96.85	86.05	101.49	116.65	112.71	91.77	105.39
BB22N	R	159.84	187.20	152.36	170.53	169.14	156.87	155.13	156.46	174.46	178.87	179.13	161.94	163.24	163.17	173.61	167.58	165.43	164.27	168.84	152.44	156.11	179.03	165.29	159.05	168.47	165.94
	G	146.03	190.71	151.91	176.90	168.39	156.79	151.06	153.39	173.70	185.09	174.72	169.90	159.45	175.95	168.60	168.81	175.84	170.90	167.22	152.37	155.70	165.85	168.55	152.52	155.57	165.44
	B	85.65	118.85	97.12	134.62	108.72	95.43	94.36	101.32	117.07	125.11	111.22	115.37	94.66	134.12	108.92	116.61	132.92	109.33	107.24	101.92	97.64	92.35	109.93	98.01	85.02	107.74
BB24N	R	171.58	168.74	178.36	170.14	171.43	162.65	158.48	175.25	168.07	157.61	163.66	173.26	175.68	162.67	176.60	168.71	161.66	163.80	171.07	164.17	178.10	167.05	156.03	176.32	148.29	167.58
	G	181.20	172.16	174.92	171.99	174.33	157.48	159.84	178.22	171.10	166.24	179.25	181.19	178.97	165.55	182.42	168.42	174.82	166.43	177.49	157.13	175.57	173.53	161.69	184.12	144.50	171.14
	B	141.05	112.37	95.34	114.54	119.26	98.24	94.65	130.66	103.68	124.61	127.83	122.94	133.70	114.68	122.32	105.47	127.11	120.71	129.08	99.25	120.80	137.56	112.52	134.28	97.28	117.80
BB27N	R	170.38	167.96	166.32	176.14	162.40	161.63	172.80	172.37	164.33	171.09	177.10	182.80	172.96	169.28	168.26	180.43	154.11	148.82	182.55	190.70	162.51	176.43	164.43	204.69	166.97	171.50
	G	166.00	161.89	159.34	179.84	155.78	163.38	168.44	160.67	153.27	178.16	182.66	182.32	180.27	164.71	163.67	177.08	158.37	153.09	179.20	188.20	168.99	172.64	170.31	190.17	145.36	168.95
	B	110.76	111.21	101.76	133.39	99.42	103.67	108.52	95.69	81.89	129.85	142.87	118.48	133.19	100.06	87.48	97.22	94.55	104.06	116.40	117.83	116.56	113.56	127.13	97.50	74.87	108.72
BB29N	R	175.98	179.44	179.65	167.65	165.69	171.53	170.56	187.90	185.69	177.92	168.20	167.58	173.16	175.56	189.69	184.90	166.76	172.96	165.13	172.92	176.94	157.88	164.27	176.69	176.55	174.05
	G	155.04	175.34	182.21	157.77	162.32	152.94	160.53	181.11	189.49	181.69	163.92	162.82	165.02	175.46	179.00	170.47	175.80	170.75	163.87	180.96	177.18	152.40	152.97	170.66	175.27	169.40
	B	98.63	107.10	122.49	108.40	108.79	89.35	97.78	95.30	112.97	136.12	97.43	109.32	100.28	121.92	109.86	106.95	126.36	104.01	87.70	126.42	115.91	84.79	90.91	115.24	112.20	107.45
BB31N	R	160.86	159.33	165.83	157.11	159.54	159.24	178.10	171.67	163.00	186.95	174.65	195.05	176.20	176.26	183.16	178.84	186.83	177.13	185.54	156.36	176.73	178.09	175.70	179.78	171.48	173.34
	G	166.47	150.51	167.50	160.93	151.31	169.09	188.21	174.54	155.87	178.50	181.88	194.07	172.20	178.78	179.69	179.84	184.34	175.63	179.11	157.03	171.88	181.18	185.60	177.39	165.83	173.10
	B	109.67	92.58	124.56	112.50	93.76	126.17	123.10	117.17	101.60	110.19	117.79	132.47	102.07	124.12	108.80	137.20	127.71	123.46	116.07	123.89	95.19	117.70	131.55	119.55	105.84	115.79
BB33N	R	172.17	170.45	164.43	184.18	171.55	180.78	172.67	175.42	162.97	154.56	176.45	182.59	173.46	175.81	167.48	186.20	173.60	164.11	169.64	179.55	164.32	152.38	183.93	170.33	163.53	171.70
	G	175.22	170.19	168.69	185.46	173.66	184.10	175.38	177.66	165.81	159.96	171.76	187.78	177.64	177.48	166.31	186.06	178.78	175.17	178.43	173.92	174.37	157.04	189.14	173.68	163.27	174.68
	B	130.80	117.01	113.97	127.84	132.39	132.65	121.60	122.37	120.46	101.76	100.47	122.94	117.57	126.76	96.67	107.85	103.21	128.52	119.67	116.66	130.92	99.22	139.21	123.72	103.87	118.32
BB34N	R	176.12	176.04	161.32	174.89	197.70	166.22	160.89	159.04	174.12	161.45	176.02	165.11	168.22	171.72	176.24	154.02	175.86	165.69	170.03	167.25	181.00	163.53	188.88	183.43	171.72	171.46
	G	177.51	169.27	152.98	164.54	200.79	151.88	159.32	155.05	183.27	171.64	178.92	166.34	177.75	168.31	175.44	148.71	175.18	160.72	175.09	170.58	175.15	170.77	186.61	182.46	168.31	170.66
	B	128.38	104.95	80.43	106.35	110.24	75.97	110.53	95.27	137.72	113.51	119.30	101.08	121.53	88.99	116.62	94.97	124.22	112.01	123.58	116.24	115.77	108.29	130.91	111.73	88.99	109.50
BB35N	R	197.44	172.90	182.20	172.72	181.44	157.84	184.25	180.74	168.25	162.96	174.60	174.88	190.03	174.47	171.10	162.71	173.01	162.36	181.30	152.37	174.09	168.30	188.36	169.37	175.25	174.12
	G	200.43	172.80	178.13	177.50	187.88	162.96	192.07	165.58	160.79	161.50	173.91	182.03	186.61	174.17	179.09	165.25	164.35	157.08	182.82	151.97	176.33	162.10	187.10	163.50	154.99	172.84
	B	130.21	108.53	122.09	106.20	126.39	117.20	129.48	90.46	104.46	94.94	122.69	116.08	124.29	109.37	123.44	114.45	94.64	96.47	110.67	99.80	105.93	101.22	126.40	102.87	89.59	110.71
BB36N	R	165.26	161.42	158.85	163.26	170.52	176.32	176.90	195.32	169.16	171.37	170.95	167.30	172.37	185.04	179.65	166.92	171.73	163.59	181.71	191.50	170.75	161.19	165.12	183.10	161.55	172.03
	G	178.92	163.55	160.63	174.94	175.39	169.09	171.95	196.95	180.06	166.19	174.10	154.94	186.18	185.00	181.53	155.22	168.85	166.89	179.08	182.99	173.39	170.20	168.05	192.25	165.08	173.66
	B	138.03	110.77	105.24	112.38	121.93	110.38	133.35	139.49	127.03	107.64	135.96	96.71	151.92	142.15	133.57	89.58	96.69	103.49	109.10	91.99	110.91	106.78	110.04	133.57	117.12	117.43
BB37N	R	181.81	172.04	175.78	172.95	165.94	193.65	163.74	179.08	166.68	168.94	169.13	183.32	169.95	168.52	184.63	176.01	179.82	169.99	176.05	160.62	177.51	156.				

RGB AOM colour data for BBN sample horizon, Bearreraig Bay, Trotternish, northeast Skye

	N	1	2	3	4	5	6	7	8	9	10	11	12	13	14	15	16	17	18	19	20	21	22	23	24	25	Mean
BB41N	R	196.58	159.17	174.94	167.11	165.86	158.72	169.19	168.21	188.77	174.64	168.18	162.39	176.81	187.02	169.19	184.78	186.85	160.08	181.71	188.18	180.86	166.46	165.06	199.14	162.68	174.50
	G	183.28	159.17	176.94	158.30	149.26	166.01	170.48	171.23	195.56	188.66	162.46	166.81	167.27	194.18	172.73	185.28	182.58	162.54	186.75	180.88	177.62	172.58	175.78	156.54	166.20	173.16
	B	129.03	90.18	136.35	95.61	85.47	128.20	109.43	125.79	147.18	149.90	105.48	123.03	111.44	116.29	127.08	113.65	114.56	104.71	137.22	112.23	112.52	114.79	129.77	73.69	118.50	116.48
BB42N	R	170.17	175.03	166.98	186.83	170.84	175.48	178.96	190.78	189.47	177.37	177.26	179.76	167.65	172.72	164.29	167.45	181.69	184.61	163.69	159.06	163.56	194.93	177.92	174.59	179.18	175.61
	G	174.69	170.65	174.77	177.00	156.24	181.69	173.63	188.80	187.10	177.65	180.64	170.36	172.09	179.05	171.46	174.17	189.21	187.14	149.26	168.67	168.75	193.19	184.21	157.44	171.44	175.17
	B	132.65	116.11	129.77	95.52	90.07	132.16	106.21	126.79	129.42	121.15	121.77	100.17	117.91	149.68	139.79	126.46	131.21	121.07	96.48	127.51	128.74	123.24	121.02	102.31	110.84	119.92
BB43N	R	170.13	180.26	170.72	168.85	168.47	169.96	188.71	189.11	183.50	189.90	165.21	170.97	169.27	177.12	164.34	156.34	178.01	173.08	151.35	175.76	174.47	185.70	162.37	160.33	165.93	172.39
	G	179.19	178.18	174.31	178.70	164.17	154.69	188.91	196.96	175.43	193.32	169.44	177.20	165.95	181.46	172.40	146.84	179.31	179.48	151.03	177.58	172.56	179.64	172.64	155.41	172.47	173.49
	B	118.88	120.05	116.15	118.86	113.13	92.15	142.78	150.32	126.27	137.58	123.27	129.87	107.18	125.54	125.77	78.20	102.91	128.77	93.87	117.02	116.14	110.64	125.29	100.64	126.05	117.89
BB44N	R	169.31	166.95	195.08	186.40	156.31	164.45	183.16	192.22	161.19	190.75	188.77	169.18	181.23	192.13	157.08	162.24	171.08	196.88	174.51	164.72	168.36	174.56	180.33	171.93	173.94	175.71
	G	174.61	175.98	194.16	196.56	165.01	150.63	178.02	191.38	159.55	180.17	189.99	169.52	182.33	190.91	162.57	169.04	171.20	165.05	173.92	162.91	173.08	176.24	180.84	173.32	173.58	175.22
	B	120.91	117.68	136.03	149.50	105.49	101.92	116.65	143.77	116.14	113.98	157.45	123.14	127.37	116.78	104.66	111.74	100.58	90.10	117.27	110.27	105.52	128.82	132.08	130.35	135.45	120.55

RGB AOM colour data for BGSHN sample horizon, Bearreraig Bay, Trotternish, northeast Skye

	N	1	2	3	4	5	6	7	8	9	10	11	12	13	14	15	16	17	18	19	20	21	22	23	24	25	Mean
BGS01N	R	100.35	91.40	80.04	96.97	103.66	91.46	84.97	97.24	104.99	107.22	103.67	65.37	75.70	106.83	93.32	101.90	90.68	97.09	88.63	82.08	76.79	92.39	91.18	101.75	92.18	92.71
	G	105.27	98.34	92.33	101.01	113.96	100.83	91.25	100.72	111.19	112.60	108.10	80.87	82.67	112.25	96.22	101.09	97.86	104.16	92.31	90.53	86.25	93.75	94.41	103.11	92.76	98.55
	B	82.77	77.78	75.34	76.23	90.66	77.22	69.83	77.97	83.97	86.34	86.51	71.13	68.56	85.95	83.10	82.27	83.86	84.37	74.44	76.67	72.34	73.83	77.36	83.99	67.01	78.78
BGS02N	R	98.99	78.54	94.20	95.98	131.62	95.47	92.29	98.29	98.22	84.62	66.09	98.64	90.27	71.12	86.97	99.14	96.40	112.97	113.35	100.60	116.98	118.42	73.90	93.28	90.03	95.86
	G	107.54	78.54	99.00	103.38	115.26	99.02	91.98	100.45	101.79	87.44	76.07	102.70	93.51	78.57	95.23	100.64	98.13	112.14	115.19	107.27	117.58	116.91	79.84	93.83	101.15	98.93
	B	83.17	61.79	80.75	89.02	83.38	79.99	65.91	78.79	83.34	68.32	68.74	84.13	74.24	65.39	77.17	77.19	81.25	83.01	93.83	84.05	87.98	87.21	68.85	73.27	86.18	78.68
BGS03N	R	97.31	118.15	124.95	123.67	97.58	96.70	104.17	103.46	126.02	76.85	113.26	92.53	97.20	103.68	107.46	128.42	118.07	106.95	105.98	105.26	114.66	101.82	123.14	99.35	104.98	107.66
	G	91.17	110.22	123.25	117.01	92.40	98.34	102.84	97.86	121.49	76.90	109.18	85.74	97.96	99.37	101.99	119.71	117.86	102.71	103.38	108.16	115.31	101.45	112.08	98.59	100.74	104.23
	B	69.55	77.76	91.55	89.50	62.08	75.62	72.06	67.44	90.35	66.26	77.78	67.01	75.44	74.90	76.30	77.89	84.44	72.46	76.81	76.53	85.33	77.90	76.45	81.12	74.42	76.68
BGS04N	R	128.53	141.24	122.57	116.33	86.27	91.92	108.23	130.84	116.68	119.36	116.57	104.31	136.25	117.98	99.17	133.31	116.28	126.61	112.50	128.64	102.68	109.68	125.37	110.97	103.37	116.23
	G	123.40	123.98	116.96	112.41	90.26	85.93	103.61	119.52	118.59	114.39	112.14	97.67	124.55	102.53	80.91	129.39	106.13	119.82	102.06	112.66	94.40	97.57	108.41	101.49	84.94	107.35
	B	82.00	75.67	83.78	74.01	75.34	65.39	82.20	75.46	89.27	82.40	80.95	70.99	83.24	54.44	51.98	94.40	66.88	76.46	60.83	72.36	62.78	63.89	73.31	73.73	56.16	73.12
BGS05N	R	121.71	118.98	151.13	123.66	128.94	156.88	139.05	105.84	140.52	139.98	117.64	147.75	133.36	118.96	103.38	132.39	134.23	134.29	110.13	132.05	131.16	146.22	140.65	125.59	133.93	130.74
	G	111.88	106.87	139.64	109.99	117.61	142.62	127.96	92.61	132.67	118.20	109.10	141.85	119.09	106.37	93.32	114.00	116.21	122.24	98.74	111.70	127.81	140.42	129.38	119.91	127.45	119.11
	B	72.15	80.55	86.93	73.83	88.24	92.81	74.16	48.55	93.30	72.47	65.55	98.36	74.30	65.31	63.77	73.32	66.93	76.40	70.66	73.29	79.79	86.52	75.48	64.68	76.98	75.77
BGS06N	R	155.77	127.13	146.16	150.23	125.97	155.43	143.18	143.56	152.59	134.76	128.78	137.60	148.24	128.36	147.91	135.82	134.74	151.74	140.58	152.38	136.89	138.37	134.39	147.58	126.35	140.98
	G	145.62	117.44	134.58	142.70	122.81	148.38	137.86	142.80	151.37	120.45	115.65	127.57	141.02	122.54	140.46	135.83	120.24	144.86	132.96	146.87	131.12	129.40	128.71	136.69	126.27	133.77
	B	81.70	82.78	77.70	81.86	81.89	91.83	95.75	98.44	106.02	64.55	68.58	80.89	82.59	80.53	79.95	79.87	73.91	85.50	84.45	95.77	85.99	80.25	77.52	88.25	88.66	83.81
BGS07N	R	160.02	134.70	142.04	166.29	150.97	138.62	153.75	150.06	140.25	148.14	144.16	141.25	147.21	156.24	141.04	134.85	143.17	136.63	160.21	138.95	160.18	156.49	150.15	150.53	159.34	148.21
	G	150.40	117.68	127.26	160.07	143.19	115.04	141.98	138.50	134.09	151.58	139.06	133.17	137.29	158.98	131.30	126.52	144.89	122.05	146.22	136.19	152.51	156.47	147.11	138.45	140.12	139.60
	B	94.50	70.97	89.43	106.28	77.48	68.68	72.98	69.40	83.40	110.91	79.72	77.24	83.03	99.88	70.62	59.04	89.74	75.32	79.04	83.22	98.00	108.54	95.46	83.68	67.03	83.74
BGS08N	R	187.12	150.91	162.21	164.59	164.01	158.24	179.28	173.82	159.74	170.29	155.17	165.37	162.61	165.53	159.29	157.93	138.26	157.77	148.10	175.34	161.93	163.96	160.38	151.48	152.48	161.83
	G	176.62	133.32	163.33	145.58	163.02	150.37	186.07	174.42	162.15	170.49	157.93	167.64	156.52	164.29	159.34	154.79	151.44	159.63	164.80	170.94	168.89	167.80	164.98	149.12	148.87	161.29
	B	102.78	85.24	74.77	71.78	93.89	76.13	120.02	108.86	100.79	121.64	107.71	103.95	95.53	104.53	103.71	87.30	100.64	100.00	106.00	101.90	109.18	103.54	108.78	85.92	80.88	98.22
BGS09N	R	187.27	165.38	143.23	154.43	162.93	161.62	157.95	167.97	169.65	157.52	175.53	171.40	153.63	161.74	169.81	159.10	179.53	165.04	148.53	170.20	164.25	166.12	165.92	174.17	170.78	164.95
	G	185.90	167.52	140.13	163.25	163.62	168.90	170.49	164.21	162.65	147.64	166.40	164.02	152.39	162.37	176.03	158.53	172.21	170.91	154.82	174.96	162.58	159.04	172.36	165.51	170.56	164.68
	B	127.75	115.16	89.04	111.59	105.00	117.38	108.25	92.99	99.56	91.17	90.48	95.44	91.54	100.02	148.72	112.63	112.77	121.81	104.25	106.50	116.88	110.21	121.45	87.87	103.01	107.26
BGS10N	R	170.05	160.98	151.26	141.61	169.11	167.85	167.23	154.87	166.82	163.71	169.57	161.44	168.48	167.80	162.63	169.76	154.37	159.14	169.42	161.95	163.65	160.85	172.99	166.77	179.53	164.07
	G	168.78	156.18	157.50	130.71	155.11	164.86	169.07	148.48	170.15	165.40	172.47	164.51	166.67	162.18	172.69	173.28	158.03	155.19	177.01	166.30	168.49	169.30	168.60	164.62	175.30	164.04
	B	111.49	90.86	99.21	78.00	80.06	99.53	108.18	104.87	125.09	114.78	117.87	108.80	108.32	91.26	128.42	107.61	110.88	112.99	119.78	125.37	111.33	114.58	110.36	92.04	107.66	107.17
BGS11N	R	161.60	182.32	153.42	166.77	152.85	163.68	165.71	170.31	166.04	167.88	171.70	155.97	158.94	166.55	160.20	172.20	159.77	182.97	156.37	163.10	164.82	148.96	163.68	171.74	156.80	164.17
	G	154.63	161.27	151.64	170.44	162.05	169.83	171.51	178.18	159.08	170.63	180.15	157.29	170.27	163.62	152.13	165.76	161.36	178.71	161.12	161.80	168.05	140.67	163.40	172.35	158.75	164.19
	B	99.02	79.23	85.09	129.93	103.17	118.34	115.38	137.24	107.72	121.70	126.22	96.98	134.08	113.73	95.84	95.88	92.69	118.72	112.85	93.22	104.66	80.69	101.92	122.46	97.67	107.38
BGS12N	R	203.89	170.14	164.51	199.63	174.39	172.14	158.95	199.11	185.24	168.24	161.46	161.33	153.73	158.99	188.65	197.25	170.63	189.10	178.69	184.21	163.42	167.06	196.55	175.67	188.03	177.24
	G	177.55	180.66	149.97	187.33	171.66	170.12	155.33	191.69	187.41	156.17	149.55	159.23	146.12	156.11	165.96	198.10	161.48	181.23	176.12	176.12	163.56	166.80	179.79	162.56	189.11	170.39
	B	81.88	141.82	73.89	118.56	95.96	118.47	83.86	98.18	119.89	93.77	99.98	100.11	75.46	93.26	85.93	114.33	85.15	98.49	91.56	91.56	97.09	102.56	95.34	74.41	119.15	98.03
BGS13N	R	181.08	175.17	163.96	175.54	174.40	170.78	159.79	164.11	162.36	183.12	163.35	173.23	179.84	181.00	167.24	156.19	151.30	162.66	182.79	184.87	188.57	182.17	154.89	168.32	172.34	171.16
	G	181.40	168.82	174.39	187.82	174.68	176.58	166.04	161.01	166.55	179.54	164.31	167.86	179.90	165.71	17											

RGB AOM colour data for BGSN sample horizon, Berreraig Bay, Trotternish, northeast Skye

	N	1	2	3	4	5	6	7	8	9	10	11	12	13	14	15	16	17	18	19	20	21	22	23	24	25	Mean
BGS01N	R	74.60	109.19	102.04	109.77	93.25	100.23	103.56	75.16	100.08	105.91	87.99	105.62	110.90	110.52	105.65	113.32	113.92	102.64	86.22	88.95	91.56	111.85	102.69	114.27	85.28	100.21
	G	79.62	106.25	107.85	108.76	95.63	101.89	112.91	91.28	107.04	111.37	93.08	111.45	113.19	109.37	106.05	118.70	116.54	106.49	89.41	89.71	101.43	114.59	106.69	116.24	86.62	104.09
	B	65.52	77.26	91.48	85.29	79.44	84.13	90.94	82.55	84.36	95.78	75.81	93.80	90.83	76.51	80.48	94.18	94.09	82.35	68.71	68.32	85.85	92.29	88.54	91.84	73.23	83.74
BGS02N	R	103.70	104.16	134.00	103.88	115.11	93.35	104.19	114.45	127.92	123.64	123.98	119.82	125.20	112.12	119.51	133.63	118.36	109.50	98.03	92.35	106.18	100.75	108.44	101.71	123.64	112.70
	G	95.62	102.70	125.26	107.63	116.73	92.72	104.25	117.79	124.90	120.61	113.33	119.83	125.77	115.09	122.33	131.72	118.13	111.44	93.07	94.04	115.50	103.92	112.77	103.24	119.00	112.30
	B	74.00	86.57	89.98	84.85	89.76	71.80	84.13	90.32	85.21	94.93	77.14	101.03	96.18	94.13	97.67	95.38	92.82	89.21	71.22	74.85	97.16	83.56	87.52	75.07	88.62	86.92
BGS03N	R	114.54	133.38	141.66	115.07	137.60	122.88	132.74	135.32	108.44	121.66	125.35	116.57	109.99	125.18	141.03	119.50	131.97	107.72	134.66	141.90	140.83	141.19	124.20	134.78	143.22	128.06
	G	106.42	129.78	137.38	114.05	131.99	111.86	121.44	130.61	107.54	117.21	131.19	112.63	104.18	121.32	121.59	110.64	126.12	100.64	124.12	126.29	135.97	127.80	117.28	127.69	134.81	121.22
	B	81.40	94.18	100.47	88.50	91.01	75.18	87.65	99.68	83.99	82.92	102.46	85.12	80.64	90.17	86.68	81.67	91.51	74.35	91.36	82.45	99.16	85.54	83.66	87.46	95.13	88.09
BGS04N	R	199.71	197.37	193.84	189.11	191.31	179.92	193.41	194.71	170.55	191.17	185.64	183.31	207.12	202.91	183.70	199.57	184.75	183.50	208.02	185.54	175.70	203.39	190.78	184.45	198.23	191.11
	G	180.59	174.40	173.71	177.18	185.31	169.73	172.82	179.84	160.85	186.31	177.70	173.47	181.08	196.99	177.73	184.58	175.46	183.35	196.72	180.97	170.75	197.35	179.30	178.54	196.96	180.47
	B	99.16	86.97	107.54	106.40	119.27	109.44	78.85	101.05	88.44	113.98	116.16	96.23	111.10	119.49	105.57	111.89	125.60	114.00	122.31	112.48	118.84	151.56	105.13	92.81	137.27	110.06
BGS05N	R	205.19	208.15	227.68	201.05	203.25	172.20	167.34	192.97	183.05	195.67	168.98	204.87	194.77	193.77	178.84	198.25	193.98	194.63	190.57	207.39	214.82	187.52	182.96	195.41	191.14	194.18
	G	202.82	189.29	209.70	184.07	189.83	173.00	169.21	185.17	178.50	192.54	164.60	190.70	180.90	184.76	166.54	191.82	195.97	179.07	169.84	201.68	195.71	160.84	180.67	191.88	182.11	184.45
	B	124.13	106.45	123.47	101.88	113.69	117.23	111.74	102.32	119.25	133.23	119.81	114.91	117.17	115.60	107.68	104.25	131.97	81.54	91.15	115.71	122.13	68.22	116.10	124.21	116.22	112.00
BGS06N	R	173.01	176.04	188.56	197.20	193.86	191.79	159.61	161.61	174.26	200.77	204.38	186.81	205.81	202.08	188.52	191.82	188.17	186.47	217.48	204.61	200.36	190.77	203.52	213.86	224.78	193.05
	G	176.92	169.94	192.72	187.85	203.10	193.22	171.15	160.22	185.47	205.15	202.11	198.13	200.54	182.03	191.77	192.18	181.09	186.80	210.89	205.29	183.73	196.14	196.05	180.58	212.61	190.63
	B	101.03	126.37	135.13	112.18	158.00	113.54	106.10	106.14	149.15	155.31	112.20	147.17	126.99	109.12	130.96	129.38	111.99	108.93	140.65	126.85	127.12	106.76	110.77	88.52	124.57	122.60
BGS07N	R	185.12	215.56	179.19	200.84	191.16	202.47	178.74	192.55	211.16	175.57	190.68	221.21	190.31	196.70	191.47	205.17	216.11	185.63	207.43	197.01	190.09	200.66	186.75	188.24	196.05	195.83
	G	173.94	195.36	177.39	193.98	197.96	191.72	167.12	194.21	183.75	169.09	184.79	194.05	172.72	187.27	192.22	204.20	217.17	191.31	198.27	172.36	184.17	191.43	186.82	166.36	189.46	187.08
	B	120.67	110.45	126.30	131.11	125.75	118.42	108.85	111.76	95.60	105.46	102.04	94.16	88.78	105.28	101.77	124.97	137.72	127.60	121.63	100.46	108.36	122.37	117.33	86.43	121.97	112.61

APPENDIX V

VR-TRANSLATED PEAK TEMPERATURE DATA

KEY TO APPENDIX V

1. BARKER & PAWLEWICZ (1986)

$$\ln(R_r) = 0.0078(T_p) - 1.2$$

2. BARKER (1988)

$$T_p = (\ln R_r \times 104) + 148$$

3. BARKER & GOLDSTEIN (1990)

$$\ln(R_r) = 0.00811(T_h) + 1.26$$

4. BARKER & GOLDSTEIN (1990)

$$T_p = 12.1 + 0.965(T_h)$$

5. BARKER & PAWLEWICZ (1994) (BURIAL HEATING)

$$T_p = (\ln R_r + 1.68) / 0.0124$$

6. BARKER & PAWLEWICZ (1994) (GEOTHERMAL METAMORPHISM)

$$T_p = (\ln R_r + 1.19) / 0.00782$$

7. BOSTICK (1970, 1971) PYROLYSIS GEOTHERMOMETER

Sample	Distance from Dyke Contact (m)	n	% Rr	S.D.	1	2	3	4	5	6	7
					Tp (°C)	Tp (°C)	Th (°C)	Tp (°C)	Tp (°C)	Tp (°C)	T (°C)
BB01N	0.00-0.03	100	3.60	0.36	318	281	313	314	239	316	600
BB02N	0.03-0.06	58	2.97	0.26	293	261	290	292	223	291	480
BB03N	0.06-0.10	65	2.59	0.27	276	247	273	275	212	274	447
BB04N	0.10-0.15	30	2.01	0.26	243	221	241	245	192	241	400
BB05N	0.15-0.20	48	1.72	0.25	223	204	222	227	179	222	377
BB06N	0.20-0.25	90	1.58	0.26	212	196	212	216	172	211	365
BB07N	0.25-0.30	100	1.55	0.16	214	194	209	210	171	208	363
BB08N	0.30-0.35	100	1.29	0.20	193	174	187	186	156	185	338
BB09N	0.35-0.40	50	1.19	0.19	176	166	177	183	150	174	332
BB10N	0.40-0.45	50	1.15	0.22	172	163	173	179	147	170	325
BB11N	0.45-0.50	100	1.09	0.21	165	157	166	172	142	163	320
BB12N	0.50-0.55	83	0.96	0.16	149	144	150	157	132	147	300
BB13N	0.55-0.60										
BB14N	0.60-0.65	47	1.06	0.18	161	154	163	169	140	160	317
BB15N	0.65-0.70	100	0.98	0.20	151	146	153	160	134	150	302
BB16N	0.70-0.75	34	0.96	0.22	149	144	150	157	132	147	300
BB17N	0.75-0.80	33	0.92	0.19	143	139	145	152	129	142	297
BB18N	0.80-0.85	77	0.96	0.19	149	144	150	157	132	147	300
BB19N	0.85-0.90	32	0.91	0.18	142	138	144	151	128	140	296
BB20N	0.90-0.95	56	0.85	0.18	133	131	135	143	122	131	275
BB21N	0.95-1.00	58	0.89	0.19	139	136	141	148	126	137	290
BB22N	1.00-1.10	39	0.86	0.20	135	132	137	144	123	133	275
BB23N	1.10-1.20	42	0.95	0.19	147	143	149	156	131	146	300
BB24N	1.20-1.30	100	0.84	0.28	131	130	134	141	121	130	274
BB25N	1.30-1.40	46	0.82	0.19	128	127	131	138	119	127	268
BB26N	1.35-1.40	100	0.83	0.25	130	129	132	140	120	128	270
BB27N	1.40-1.50	45	0.83	0.17	130	129	132	140	120	128	270
BB28N	1.60-1.70	100	0.81	0.26	127	126	129	137	118	125	264
BB29N	1.50-1.60	46	0.80	0.15	125	125	128	135	117	124	262
BB30N	1.70-1.80	64	0.88	0.18	137	135	140	147	125	136	289
BB31N	1.80-1.90	34	0.79	0.16	124	123	126	134	116	122	259
BB32N	1.90-2.00	21	0.79	0.15	124	123	126	134	116	122	259
BB33N	2.00-2.10	64	0.78	0.17	122	122	125	132	115	120	256
BB34N	2.30-2.40	100	0.78	0.21	122	122	125	132	115	120	256
BB35N	2.60-2.70	58	0.76	0.16	119	119	122	129	113	117	253
BB36N	2.90-3.00	50	0.80	0.19	125	125	128	135	117	124	262
BB37N	3.20-3.30	53	0.75	0.15	117	118	120	128	112	115	250
BB38N	3.50-3.70	71	0.75	0.15	117	118	120	128	112	115	250
BB40N	3.80-3.90	48	0.79	0.18	124	123	126	134	116	122	259
BB41N	4.10-4.20	57	0.75	0.16	117	118	120	128	112	115	250
BB42N	4.40-4.50	59	0.79	0.20	124	123	126	134	116	122	259
BB43N	5.00-5.10	19	0.76	0.14	119	119	122	129	113	117	253
BB44N	5.50-5.60	42	0.73	0.18	113	115	117	125	110	112	243
BGSH01N	0.00-0.05	44	3.32	0.35	308	273	303	305	232	306	518
BGSH02N	0.05-0.10	52	2.78	0.26	285	254	281	284	218	283	458
BGSH03N	0.15-0.20	74	1.69	0.22	221	203	220	224	178	219	375
BGSH04N	0.20-0.25	50	1.44	0.19	201	186	200	205	165	199	355
BGSH05N	0.32-0.34	100	1.13	0.15	170	161	170	177	145	168	323
BGSH06N	0.35-0.40	100	1.00	0.16	154	148	155	162	135	152	310
BGSH07N	0.40-0.45	60	0.96	0.25	149	144	150	157	132	147	300
BGSH08N	0.50-0.60	58	0.86	0.23	135	132	137	144	123	133	275
BGSH09N	0.96-1.00	50	0.83	0.22	130	129	132	140	120	128	270
BGSH10N	1.30-1.40	59	0.73	0.18	113	115	117	125	110	112	243
BGSH11N	1.95-2.05	51	0.73	0.20	113	115	117	125	110	112	243
BGSH12N	3.00-3.10	64	0.79	0.18	124	123	126	134	116	122	259
BGSH13N	4.90-5.00	52	0.79	0.16	124	123	126	134	116	122	259
BGSH14N	6.70	63	0.75	0.20	117	118	120	128	112	115	250
BGS01N	0.00-0.04	36	3.12	0.21	300	266	296	297	227	298	490
BGS02N	0.10-0.15	46	1.79	0.18	228	209	227	231	182	227	384
BGS03N	0.23-0.30	27	1.18	0.21	175	165	176	182	149	173	330
BGS04N	0.70-0.80	37	0.86	0.17	135	132	137	144	123	133	275
BGS05N	2.06-2.16	48	0.84	0.17	131	130	134	141	121	130	274
BGS06N	2.90-3.00	22	0.76	0.16	119	119	122	129	113	117	253
BGS07N	5.25-5.35	45	0.72	0.16	112	114	117	123	110	112	241

APPENDIX VI

GEOCHEMICAL DATA

Geochemical data from the BBN sample horizon, Berreraig Bay, Trotternish, NE Skye.

Sample	Distance from Dyke Contact (m)	Major Element Oxide Abundance (Wt. %)												
		SiO ₂	Al ₂ O ₃	Fe ₂ O _{3t}	MgO	CaO	Na ₂ O	K ₂ O	TiO ₂	P ₂ O ₅	MnO	Cr ₂ O ₃	LOI	Total
		BB01N	0.00-0.03	70.59	8.85	5.49	1.36	0.46	0.99	2.26	0.64	0.36	0.02	0.022
BB03N	0.06-0.10	68.53	10.82	3.14	1.71	3.13	1.01	2.53	0.67	0.40	0.02	0.022	7.8	99.78
BB05N	0.15-0.20	67.17	10.15	2.18	1.44	5.66	0.78	1.93	0.60	0.36	0.03	0.020	9.5	99.82
BB07N	0.25-0.30	65.96	9.34	2.34	1.21	7.36	0.79	2.24	0.55	0.36	0.04	0.016	9.6	99.81
BB09N	0.35-0.40	64.33	10.34	3.62	1.42	5.80	0.84	2.43	0.63	0.41	0.03	0.022	9.9	99.77
BB11N	0.45-0.50	63.67	10.31	3.52	1.34	5.93	0.71	2.35	0.61	0.39	0.03	0.019	10.9	99.78
BB15N	0.65-0.70	64.01	9.62	2.97	1.27	6.82	0.71	2.23	0.58	0.34	0.03	0.015	11.1	99.70
BB22N	1.00-1.10	64.41	9.91	3.16	1.24	6.28	0.73	2.51	0.59	0.39	0.03	0.019	10.5	99.77
BB32N	1.90-2.00	63.61	10.21	3.19	1.24	6.40	0.78	2.35	0.60	0.35	0.03	0.017	10.9	99.68
BB36N	2.90-3.00	62.02	10.37	3.54	1.18	6.77	0.73	2.19	0.65	0.41	0.03	0.020	11.9	99.81
BB43N	5.00-5.10	62.17	8.92	2.37	1.01	9.43	0.70	2.34	0.51	0.37	0.03	0.018	11.8	99.67

Fe₂O_{3t}: Total iron as Fe₂O₃

LOI: Loss on Ignition

n/a: Data not available

Analysis type: WR/ICP-AES

OMAC Laboratories Ltd., Atherry Rd., Loughrea, Co. Galway

Geochemical data from the studied dyke at Berreraig Bay, Trotternish, NE Skye.

Sample	Distance from Dyke Contact (m)	Major Element Oxide Abundance (Wt. %)																	Minor and Trace Element Abundance (ppm)														
		SiO ₂	Al ₂ O ₃	Fe ₂ O ₃	MgO	CaO	Na ₂ O	K ₂ O	TiO ₂	P ₂ O ₅	MnO	Cr ₂ O ₃	LOI	H ₂ O	CO ₂	Total	Co	Cr	Ni	V	Zn	Ce	La	Nb	Ga	Pb	Pr	Pb	Ba	Sr	Th	Y	Zr
		BBD01a*	Dyke centre	44.86	17.39	12.95	4.09	6.64	4.23	0.65	3.43	0.44	0.13	n/a	n/a	2.48	2.46	99.75	45	<18	29	201	85	73	<14	17	13	7	<4	16	178	807	<4
BBD01b	Dyke centre	45.91	16.10	12.39	4.66	5.15	4.59	0.64	3.45	0.39	0.10	0.012	6.4	n/a	n/a	99.8	n/a	n/a	n/a	n/a	n/a	n/a	n/a	n/a	n/a	n/a	n/a	n/a	n/a	n/a	n/a	n/a	n/a
BBD02	Dyke margin (N)	46.20	16.05	10.18	3.45	7.42	4.15	1.13	3.13	0.47	0.08	0.008	7.4	n/a	n/a	99.7	n/a	n/a	n/a	n/a	n/a	n/a	n/a	n/a	n/a	n/a	n/a	n/a	n/a	n/a	n/a	n/a	n/a
BBD03	Altered dyke margin (N)	45.56	13.70	11.40	3.33	6.96	3.40	1.59	2.70	0.34	0.15	0.012	10.5	n/a	n/a	99.6	n/a	n/a	n/a	n/a	n/a	n/a	n/a	n/a	n/a	n/a	n/a	n/a	n/a	n/a	n/a	n/a	n/a

Fe₂O₃: Total iron as Fe₂O₃
 LOI: Loss on Ignition
 n/a: Data not available

Analysis type: WRC/CP-OES
 OMAC Laboratories Ltd., Athlery Rd., Loughrea, Co. Galway

except

*XRF analysis: Sequential X-Ray Spectrometer, X'Unique, Rh-Tube
 Forschungszentrum GEDOMAR-Wischhofstr. D-24148 Kiel, Germany.

Wt %/Sample No.	BBD01a	BBD01b	BBD02	BBD03
SiO ₂	44.86	45.91	46.20	45.56
Al ₂ O ₃	17.39	16.10	16.05	13.70
Fe ₂ O ₃				
FeO				
MgO	4.09	4.66	3.45	3.33
CaO	6.64	5.15	7.42	6.96
Na ₂ O	4.23	4.59	4.15	3.40
K ₂ O	0.65	0.64	1.13	1.59
TiO ₂	3.43	3.45	3.13	2.70
P ₂ O ₅	0.44	0.39	0.47	0.34
MnO	0.13	0.10	0.08	0.15
LOI	4.94	6.40	7.40	10.50
FeTO ₃	12.95	12.39	10.18	11.40
Fe ₂ O ₃ /FeO	0.20	0.20	0.20	0.20
TOTAL (w/ Fe ₂ O ₃ & FeO, or FeO*)	98.65	98.73	98.80	98.66
TOTAL (w/ FeTO ₃ or FeO*)	99.75	99.78	99.66	99.63
Normalized %	BBD01a	BBD01b	BBD02	BBD03
SiO ₂	47.87	49.72	50.55	51.68
Al ₂ O ₃	18.56	17.44	17.56	15.54
Fe ₂ O ₃	2.11	2.05	1.70	1.97
FeO	10.54	10.23	8.49	9.86
MgO	4.36	5.05	3.77	3.78
CaO	7.09	5.58	8.12	7.89
Na ₂ O	4.51	4.97	4.54	3.86
K ₂ O	0.69	0.69	1.24	1.80
TiO ₂	3.66	3.74	3.42	3.06
P ₂ O ₅	0.47	0.42	0.51	0.39
MnO	0.14	0.11	0.09	0.17
Total	100.00	100.00	100.00	100.00
Na ₂ O _n + K ₂ O _n	5.21	5.66	5.78	5.66
Na ₂ O _n /K ₂ O _n	6.51	7.17	3.67	2.14
K ₂ O _n /Na ₂ O _n	0.15	0.14	0.27	0.47
FeTO _{3n}	13.82	13.42	11.14	12.93
FeO _n	12.43	12.07	10.02	11.64
FeO _n /MgO _n	2.85	2.39	2.66	3.08
FeO _n /(FeO _n +MgO _n)	0.74	0.71	0.73	0.75
Mg #	42.47	46.78	44.20	40.57
Fe ₂ O _{3n} /FeO _n	0.20	0.20	0.20	0.20
A	23.66	24.86	29.51	26.86
F	56.50	52.99	51.20	55.22
M	19.83	22.15	19.28	17.92
Total	100.00	100.00	100.00	100.00
Ti/100 [(ppm * 0.5995)/100]	205.63			
Y * 3	102.00			
Zr	272.00			

APPENDIX VII

THERMAL CONDUCTIVITY DATA

BBD01^a

Test sample diameter	D [m]	0.022741
Test sample cross-section area	$\pi D^2/4$ [m ²]	0.000406
Test sample thickness	Δx [m]	0.003336
Heat transfer rate	Q [W]	16.0
Temperature difference	$\Delta T = T_4 - T_5$ [°C]	62.5

Node	X _{hot} [mm]	Temperature [°C]	Node	X _{cold} [mm]	Temperature [°C]
1	4.93	87.5	5	4.93	22.3
2	14.93	86.4	6	14.93	21.9
3	24.93	85.4	7	24.93	21.0
4	29.96	84.8	8	29.96	20.1

BBD01^b

Test sample diameter	D [m]	0.022741
Test sample cross-section area	$\pi D^2/4$ [m ²]	0.000406
Test sample thickness	Δx [m]	0.003336
Heat transfer rate	Q [W]	16.0
Temperature difference	$\Delta T = T_4 - T_5$ [°C]	48.7

Node	X _{hot} [mm]	Temperature [°C]	Node	X _{cold} [mm]	Temperature [°C]
1	4.93	75.5	5	4.93	24.0
2	14.93	74.3	6	14.93	23.4
3	24.93	73.2	7	24.93	22.3
4	29.96	72.7	8	29.96	21.2

BBD01^c

Test sample diameter	D [m]	0.022742
Test sample cross-section area	$\pi D^2/4$ [m ²]	0.000406
Test sample thickness	Δx [m]	0.003237
Heat transfer rate	Q [W]	16.5
Temperature difference	$\Delta T = T_4 - T_5$ [°C]	49.7

Node	X _{hot} [mm]	Temperature [°C]	Node	X _{cold} [mm]	Temperature [°C]
1	4.93	76.3	5	4.93	23.9
2	14.93	75.2	6	14.93	23.3
3	24.93	74.1	7	24.93	22.2
4	29.96	73.6	8	29.96	21.2

BGSH02N^a

Test sample diameter	D [m]	0.022753
Test sample cross-section area	$\pi D^2/4$ [m ²]	0.000407
Test sample thickness	Δx [m]	0.003722
Heat transfer rate	Q [W]	16.0
Temperature difference	$\Delta T = T_4 - T_5$ [°C]	49.8

Node	X _{hot} [mm]	Temperature [°C]	Node	X _{cold} [mm]	Temperature [°C]
1	4.93	76.6	5	4.93	24.1
2	14.93	75.4	6	14.93	23.6
3	24.93	74.4	7	24.93	22.6
4	29.96	73.9	8	29.96	21.5

BGSH02^b

Test sample diameter	D [m]	0.022721
Test sample cross-section area	$\pi D^2/4$ [m ²]	0.000405
Test sample thickness	Δx [m]	0.003722
Heat transfer rate	Q [W]	15.5
Temperature difference	$\Delta T = T_4 - T_5$ [°C]	49.6

Node	X _{hot} [mm]	Temperature [°C]	Node	X _{cold} [mm]	Temperature [°C]
1	4.93	76.0	5	4.93	23.7
2	14.93	74.9	6	14.93	23.2
3	24.93	73.9	7	24.93	22.2
4	29.96	73.3	8	29.96	21.3

BGS04N^a

Test sample diameter	D [m]	0.022733
Test sample cross-section area	$\pi D^2/4$ [m ²]	0.000406
Test sample thickness	Δx [m]	0.00291
Heat transfer rate	Q [W]	15.0
Temperature difference	$\Delta T = T_4 - T_5$ [°C]	41.9

Node	X _{hot} [mm]	Temperature [°C]	Node	X _{cold} [mm]	Temperature [°C]
1	4.93	66.9	5	4.93	22.9
2	14.93	65.9	6	14.93	22.4
3	24.93	65.1	7	24.93	21.5
4	29.96	64.8	8	29.96	20.6

BGS04N^b

Test sample diameter	D [m]	0.022733
Test sample cross-section area	$\pi D^2/4$ [m ²]	0.000406
Test sample thickness	Δx [m]	0.00291
Heat transfer rate	Q [W]	15.9
Temperature difference	$\Delta T = T_4 - T_5$ [°C]	46.3

Node	X _{hot} [mm]	Temperature [°C]	Node	X _{cold} [mm]	Temperature [°C]
1	4.93	73.6	5	4.93	24.9
2	14.93	72.6	6	14.93	24.4
3	24.93	71.5	7	24.93	23.4
4	29.96	71.2	8	29.96	22.4

APPENDIX VIII

QUIPS ROUTINES

&

SCHMIDT MODEL VBA SOURCE CODE

LowReflectance.Q5R

Routine Header

Number of fields: 200

Standard frames

Configure (Image Store 736 x 574, Grey Images 6, Binaries 8)

PauseText ("IMAGE SETUP - Set white level using Gain & Offset controls - then press OK")

Image Setup [PAUSE] (Camera 0, Upper 70.00, Lower 77.48, Lamp 0.00)

Acquire (into Image0)

PauseText ("CALIBRATION - Load Calibration file - then press OK")

Measure Frame [x379, y298, Width 15, Height 15]

Grey Calibrate [PAUSE] (Reflectance, Load from file

C:\QPCMC\Calibration\Reflectance\0.42-1.23%.Q5C)

PauseText ("Choose size and position of measuring frame - then press MEASURE. Press OK when done.")

Image frame (x256, y233, Width 196, Height 143)

Measure Grey [PAUSE] (Plane Image0, Mask Off)

Selected parameters: MeanGrey

END

MedReflectance.Q5R

Routine Header

Number of fields: 200

Standard frames

Configure (Image Store 736 x 574, Grey Images 6, Binaries 8)

PauseText ("IMAGE SETUP - Set white level using Gain & Offset controls - then press OK")

Image Setup [PAUSE] (Camera 0, Upper 51.16, Lower 48.84, Lamp 0.00)

Acquire (into Image0)

PauseText ("CALIBRATION - Load Calibration file - then press OK")

Measure Frame [x379, y298, Width 15, Height 15]

Grey Calibrate [PAUSE] (Reflectance, Load from file

C:\QPCMC\Calibration\Reflectance\1.23-3.28%.Q5C)

PauseText ("Choose size and position of measuring frame - then press MEASURE. Press OK when done.")

Image frame (x256, y233, Width 196, Height 143)

Measure Grey [PAUSE] (Plane Image0, Mask Off)

Selected parameters: MeanGrey

END

EasyColour.Q5R

Routine Header

Number of fields: 50

Standard frames

Setup Results Window (Move Feature Results to x12, y535, w662, h193)

Image Setup [PAUSE] (Camera 1, Upper 50.00, Lower 50.00, Lamp 0.00)

Acquire (into Colour0)

Colour Detect [PAUSE] (RGB: 250-255, 255-255, 0-255, from Colour0 into Binary0)

Binary Edit [PAUSE] (Keep from Binary0 to Binary1, nib Fill, width 5)

Measure Feature [PAUSE] (plane Binary1, 8 ferets, minimum area: 4, grey image: Colour0)

Selected parameters: Mean Red, Mean Green, Mean Blue

Display Field Results (x48, y462, w665, h211)

END

Schmidt Plot (300 nodes)

```
Private Sub cmdExit_Click()  
    End  
End Sub
```

```
Private Sub cmdRun_Click()
```

```
'Define Constants
```

```
    Const n As Integer = 303
```

```
'Declare variables
```

```
    Dim T(n + 1)
```

```
    Dim newT(n + 1)
```

```
    Dim AvT(n + 1)
```

```
    Dim maxT(n + 1)
```

```
    Dim X As Single, D As Single
```

```
    Dim Tm As Single, Th As Single
```

```
    Dim alpha As Double
```

```
    Dim flow As Double
```

```
    Dim FlowSec As Double
```

```
    Dim Iterations2 As Integer
```

```
    Dim duration As Double
```

```
    Dim time As Double
```

```
    Dim dx, nd, dt
```

```
    Dim i As Integer, j As Integer
```

```
    Dim k As Double, g As Double
```

```
    Dim c As Single
```

```
    Dim TimeSec As Double
```

```
    Dim Columns As String
```

```
    Dim Width As Double
```

```
    Dim Heading As String
```

```
    Dim TimeStepCol As Single
```

```
    Dim colHeadings As String
```

```
    Dim clipTimeStepCol As String
```

```
    Dim colIncrement As Single
```

```
    Dim Iterations As Integer 'No. of calculations
```

```
    Dim OutputStep As Integer
```

```
    Dim counter As Integer, counter2 As Integer, ct As Integer, ct2  
    AsInteger
```

```
    Dim ctIncrement As Boolean
```

```
    Dim OutputStep2 As Integer
```

```
'Assign variables
```

```
    X = CSng(txtX)
```

```
    D = CSng(txtD)
```

```
    Tm = CSng(txtTm)
```

```
    Th = CSng(txtTh)
```

```
    alpha = CDBl(txtAlpha)
```

```
    flow = CSng(txtFlow)
```

```
    duration = CDBl(txtRuntime)
```

```
    time = 0
```

```
'Convert years to seconds
```

```
    TimeSec = YearsToSec(duration)
```

```
    FlowSec = HoursToSec(flow)
```

```
    dx = X / (n - 3)
```

```
'Assign distance increments
```

```

nd = Int((n - 3) * D / X)      'Assign dyke elements

'Set "Distance" name for total element values in excel spreadsheet
Range("A1").Select
ActiveCell.FormulaR1C1 = "Distance from Dyke Centre"
Range("A3").Select 'Set 'initial value of Cell A2 to 0
ActiveCell.FormulaR1C1 = 0

'Populate cells with distance increments
c = 0 'Set initial distance at dyke origin

For i = 1 To n - 3
    c = c + dx 'Increments distance to populate spreadsheet.
    Cells(i + 3, "A").Value = c
Next i

'*****

'Sets initial magma and host rock temperatures

For i = 3 To nd + 3
    T(i) = Tm 'Initial Magma temp for dyke elements
    Cells(i, "B").Value = T(i) 'Writes Tm to worksheet
Next i

For i = (nd + 4) To n
    T(i) = Th 'Host rock temp
    Cells(i, "B").Value = T(i) 'Writes intial Th to worksheet
Next i

'*****

'User input's no. of inerpolated columns to be outputted to spreadsheet
Columns = InputBox("Please enter no. of columns between 100 and
200!", "No. of Columns", "240")
If Columns = "" Then
    MsgBox "Bye bye"
    End
End If

Width = Int(Columns) 'Sets no. of columns to populate in
spreadsheet.

'Select case checks that user has entered correct numbers between 100-300
Select Case Width 'Forces max. and min. no. of columns.
    Case Is > 200
        Width = 200
    Case Is < 100
        Width = 100
End Select

Range("B1").Select 'Sets initial value of Cell B1 to 0
ActiveCell.FormulaR1C1 = "T(0Yr)"

Range("C1").Select 'Writes "Tmax" to Cell C1
ActiveCell.FormulaR1C1 = "Tmax"

For i = 0 To Width 'Set's up the loop for creating the correct
amount of column Headings

```

```

TimeStepCol = duration / Width 'Calculates time increment
colIncrement = colIncrement + TimeStepCol 'Increments time
interval

clipTimeStepCol = Left(colIncrement, 6) 'Extract first 6
characters of time increment
colHeadings = "T(" + clipTimeStepCol + "Yr)" 'Concatenates column
headings

Cells(1, i + 4).Value = colHeadings 'Writes headings to
spreadsheet

```

```
Next i
```

```
*****
```

```

dt = (dx ^ 2) / (2 * alpha): 'Timestep calculation

Iterations = Cdbl(TimeSec) / dt 'Calculates no. of computations

OutputStep = Iterations / Width 'Increments for extracting data and
writing to spreadsheet

'Initialise counters
counter = 0 'For extracting temperatures
k = 1 'Ratio to increment excel column by 1
ct = 1
g = 0

```

```

OutputStep2 = OutputStep 'Outputstep2 is used for extracting time
period of temperature to spreadsheet.
k = k / OutputStep 'Ratio to increment excel column by 1

Iterations2 = Iterations - (OutputStep * 1)

```

```
*****
```

```

For j = 0 To Iterations 'No. of computations to perform
ctIncrement = True 'Sets up a boolean expression for extracting
the appropriate computation to spreadsheet.

```

```

For i = 3 To n
    If counter = Int(Iterations) Then
        MsgBox "Finished", vbInformation, "Plot"
    End
    End If
Next i

```

```

For i = 3 To n
    If newT(i) < Th Then newT(i) = Th
    If T(i + 1) = "" Then T(i + 1) = T(i) 'Set's boundary
    condition for country rock temperature
    newT(i) = (T(i + 1) + T(i - 1)) / 2 'Schmidt Plot
Next i

```

```

'Smoothes plot
For i = 3 To n
    AvT(i) = (T(i) + T(i + 1)) / 2
Next i

```

```

counter = counter + 1
ct = ct + 1
g = g + k

ct2 = ((ct - OutputStep2) + (g)) + 2 'Variable used for writing T
values to spreadsheet

If counter = OutputStep2 Then ctIncrement = False

For i = 3 To n
    T(i) = newT(i)
    If ctIncrement = False Then
        Cells(i, ct2).Value = AvT(i)
    End If
Next i

'Reset Maximum Temperature
For i = 3 To n
    If AvT(i) > maxT(i) Then maxT(i) = AvT(i)
    If ctIncrement = False Then
        Cells(i, "C").Value = maxT(i)
    End If
Next i

time = time + dt 'Resets time

'Holds half-dyke at initial Tm until magma flow complete
If time < FlowSec Then
    For i = 3 To (nd + 3)
        T(i) = Tm
    Next i
End If

For i = 2 To n
    If T(2) < T(4) Then T(2) = T(4)
Next i

T(2) = T(4) 'Dyke symmetry - boundary condition of dyke's
initial temperature at each time slice

If ctIncrement = False Then OutputStep2 = OutputStep2 +
OutputStep

Next j

End Sub

*****

Private Sub txtFlow_Change()

End Sub

*****

Private Sub UserForm_Click()

End Sub

```

```

'*****
Public Function YearsToSec(Value As Double) As Double
Const YearToSec As Double = 31557600
YearsToSec = Value * YearToSec
End Function

'*****
Public Function HoursToSec(Value As Double) As Double
Const HourToSec As Double = 3600
HoursToSec = Value * HourToSec
End Function

'*****
Public Function SecToYears(Value As Double) As Double
    Const SecToYear As Double = 3.16880878140289E-08
    SecToYears = Value * SecToYear
End Function

'*****
Sub CreateCustomMenus()

'Create custom menu on worksheets menu bar if not
already present. Use control's tag property to identify it.

Dim cbcpop As CommandBarControl

Set cbcpop = Application.CommandBars("Worksheet menu bar").FindControl( _
Type:=msoControlPopup, Tag:="SchmidtPlotCustomMenu")

If Not cbcpop Is Nothing Then Exit Sub

Set cbcpop = Application.CommandBars("Worksheet menu bar").Controls.Add(
Type:=msoControlPopup, Temporary:=True)
cbcpop.Caption = "&Schmidt Plot"

'Set tag property to find it later for deletion
cbcpop.Tag = "SchmidtPlotCustomMenu"

'Add menu item to popup menu
With cbcpop.Controls.Add(Type:=msoControlButton, Temporary:=True)
    .Caption = "&Set Parameters"
    .OnAction = "SchmidtPlot"
End With

End Sub
Sub DeleteCustomMenuItem()
Dim cbcpop As CommandBarControl

```

```
Set cbcpop = Application.CommandBars("Worksheet Menu Bar").  
FindControl(Type:=msoControlPopup, Tag:="SchmidtPlotCustomMenu")  
If Not cbcpop Is Nothing Then cbcpop.Delete  
End Sub
```

```
Public Sub SchmidtPlot()  
frmParameters.Show  
1. End Sub
```

APPENDIX IX

RGB STATISTICS DATA

Red	% R _r	Group	Count	Sum	Average	Variance
	3.60	BB01N	25	2113.46	84.5384	96.3995
	2.97	BB02N	25	2357.39	94.2956	152.0159
	2.59	BB03N	25	2463.39	98.5356	80.8713
	2.01	BB04N	25	2514.21	100.5684	164.9157
	1.72	BB05N	25	2828.76	113.1504	100.7651
	1.58	BB06N	25	2948.13	117.9252	134.4443
	1.55	BB07N	25	3314.87	132.5948	110.7507
	1.29	BB08N	25	3429.92	137.1968	84.3214
	1.19	BB09N	25	3743.44	149.7376	115.2963
	1.15	BB10N	25	3822.16	152.8864	58.4269
	1.09	BB11N	25	3907.45	156.2980	144.2744
	0.96	BB12N	25	4061.26	162.4504	105.6850
	0.91	BB19N	25	4208.10	168.3240	121.8752
	0.84	BB24N	25	4189.38	167.5752	58.6036
	0.79	BB40N	25	4289.99	171.5996	94.2604

Green	% R _r	Group	Count	Sum	Average	Variance
	3.60	BB01N	25	2218.77	88.7508	67.57985767
	2.97	BB02N	25	2355.86	94.2344	97.001309
	2.59	BB03N	25	2347.32	93.8928	58.12130433
	2.01	BB04N	25	2428.36	97.1344	80.323434
	1.72	BB05N	25	2607.04	104.2816	80.84622233
	1.58	BB06N	25	2618.65	104.7460	77.73975
	1.55	BB07N	25	2870.03	114.8012	53.566686
	1.29	BB08N	25	3010.97	120.4388	98.938461
	1.19	BB09N	25	3398.3	135.9320	86.79315833
	1.15	BB10N	25	3614.5	144.5800	118.7835417
	1.09	BB11N	25	3675	147.0000	162.1061167
	0.96	BB12N	25	3837.97	153.5188	121.0940027
	0.91	BB19N	25	4139.24	165.5696	128.8370373
	0.84	BB24N	25	4278.56	171.1424	90.623394
	0.79	BB40N	25	4296.8	171.8720	132.7482167

Blue	% R _r	Group	Count	Sum	Average	Variance
	3.60	BB01N	25	1767.82	70.7128	52.562821
	2.97	BB02N	25	1826.24	73.0496	69.523954
	2.59	BB03N	25	1709.17	68.3668	32.91099767
	2.01	BB04N	25	1800.5	72.0200	34.021025
	1.72	BB05N	25	1915.77	76.6308	89.109191
	1.58	BB06N	25	1894.08	75.7632	48.73089767
	1.55	BB07N	25	1948.88	77.9552	41.969576
	1.29	BB08N	25	1988.89	79.5556	112.8092673
	1.19	BB09N	25	2238.31	89.5324	121.8089773
	1.15	BB10N	25	2321.83	92.8732	144.755781
	1.09	BB11N	25	2331.52	93.2608	125.5013743
	0.96	BB12N	25	2353.29	94.1316	193.3523307
	0.91	BB19N	25	2666.32	106.6528	190.2776127
	0.84	BB24N	25	2944.93	117.7972	197.317096
	0.79	BB40N	25	2909.85	116.3940	256.8066667

PLATES

PLATE 1

A

Sampled locality below Carn Dearg on the northern shore of Loch Eishort, central Skye.



B

Sampled locality at Waterloo, Broadford Bay, central Skye.



PLATE 1

A



B



PLATE 2

A

Sampled locality at Berreraig, Trotternish, north-east Skye.



B

Sampled horizons adjacent to the 1.3m thick dyke at Berreraig, north-east Skye.
1 = BGSNH sample horizon, 2 = BGSN sample horizon, 3 = BBN sample horizon.



PLATE 2

A



B

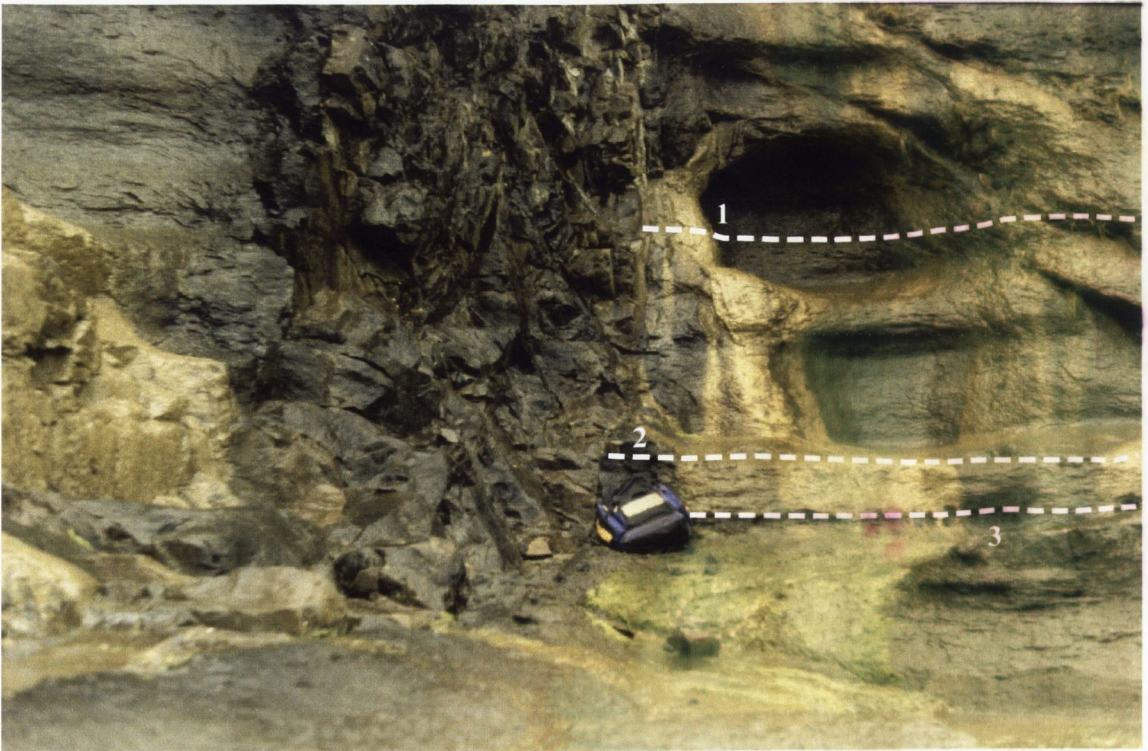


PLATE 3

A

Baked zone in the country rocks adjacent to the northern contact of the 1.3m thick dyke at Berreraig, north-east Skye.



B

'Divided-bar' apparatus used in this study for rock thermal conductivity determinations. 1 = insulated brass cylinders and rock sample, 2 = heater coil, 3 = power supply (car battery), 4 = voltmeter, 5 = ammeter, 6 = rheostat variable resistor, 7 = thermocouple.



PLATE 3

A



B

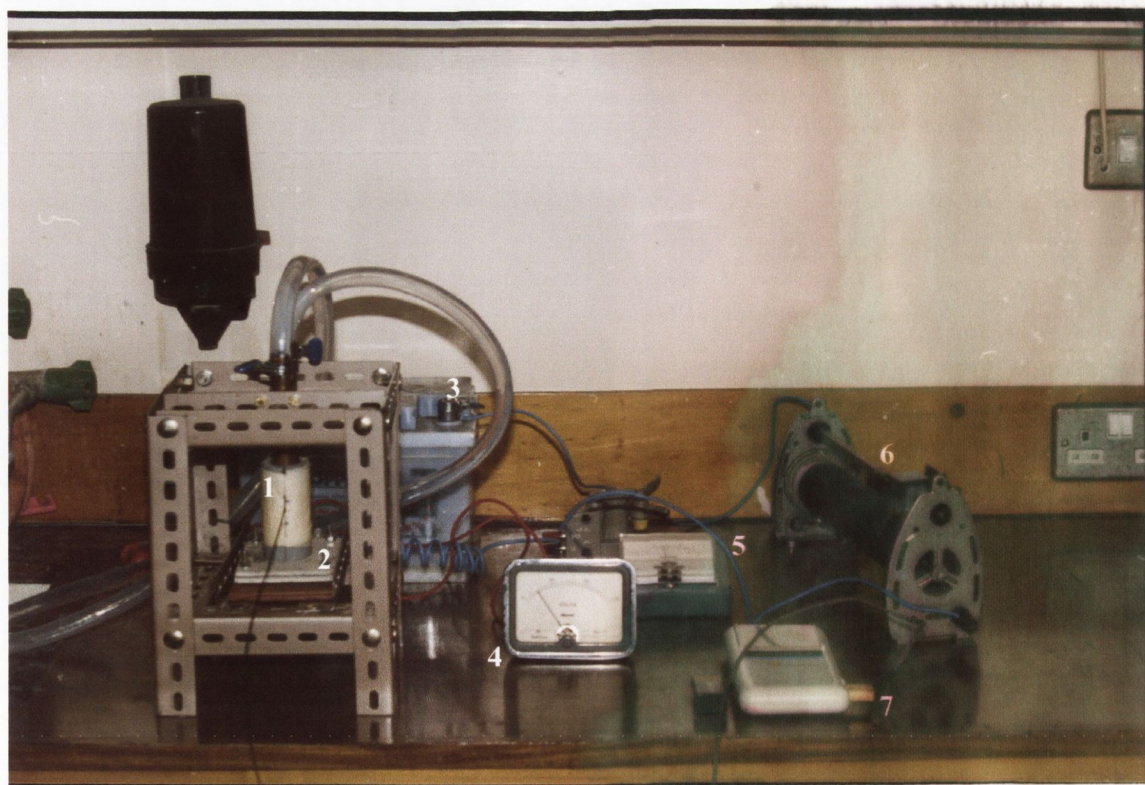


PLATE 4

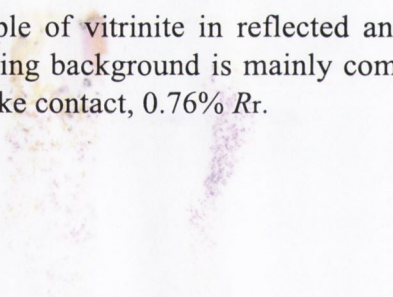
A

Maceral examples from the BBN sample horizon: vit = vitrinite, inert = inertinite (pyr = fromboidal pyrite. BB41N, 4.1-4.2m from the dyke contact, 0.75% *Rr*.



B

Example of vitrinite in reflected and transmitted light under oil immersion. The low reflecting background is mainly composed of 'AOM' macerals. BB43N, 5.0-5.1m from the dyke contact, 0.76% *Rr*.



C

Example of solid bitumen in reflected and transmitted light under oil immersion.

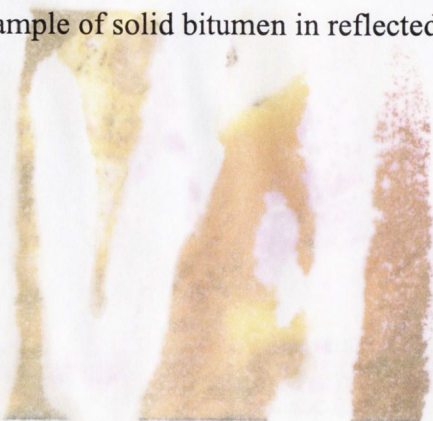
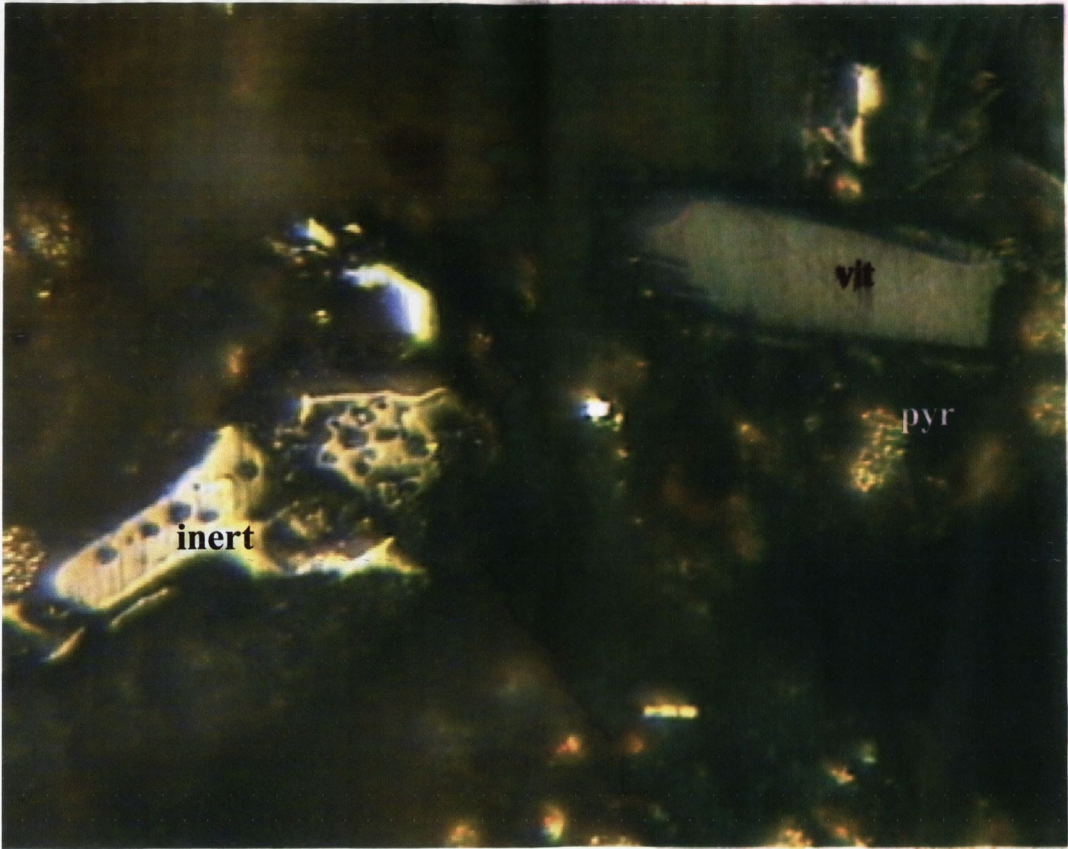
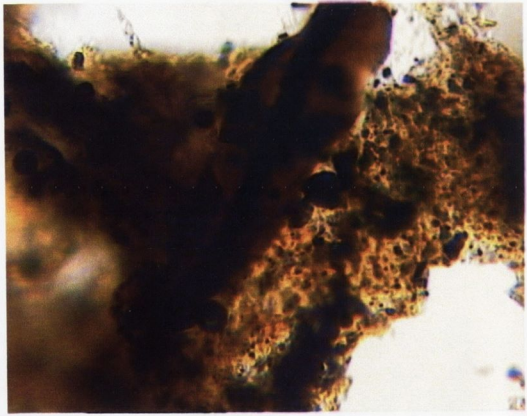
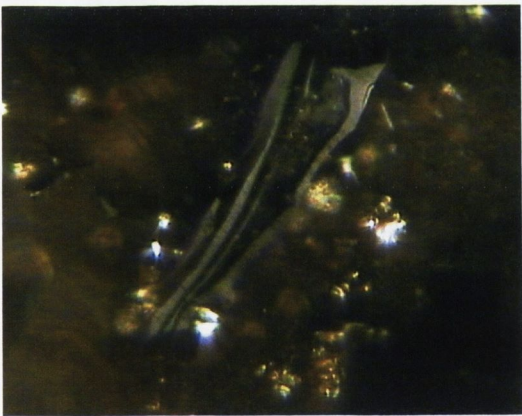


PLATE 4

A



B



C

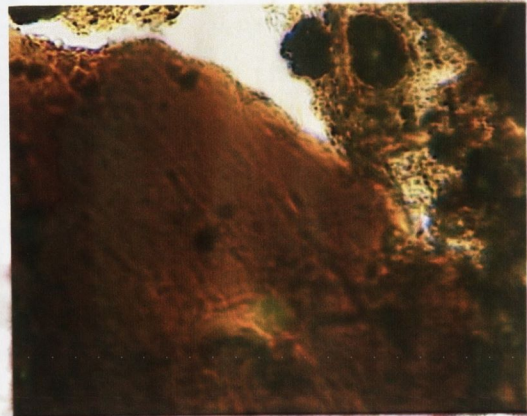
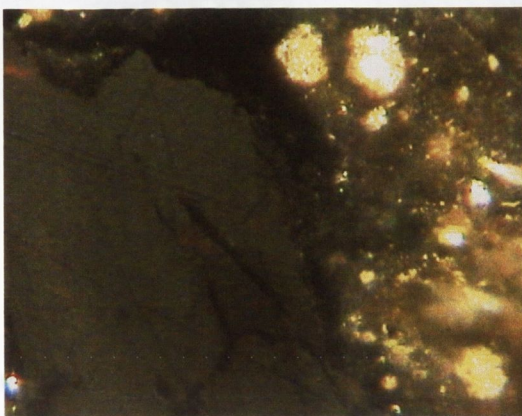


PLATE 5

1. Typical AOM from the BBN sample horizon. BB44N, 5.6m from the dyke contact, 0.73% *Rr*.
2. Typical AOM from the BBN sample horizon. BB44N, 5.6m from the dyke contact, 0.73% *Rr*.
3. Typical AOM from the BBN sample horizon. BB43N, 5.0-5.1m from the dyke contact, 0.76% *Rr*.
4. Tasmanitid. BB41N, 4.1-4.2m from the dyke contact, 0.75% *Rr*.
5. Typical AOM from the BBN sample horizon. BB07N, 0.25-0.3m from the dyke contact, 1.55% *Rr*.
6. Typical AOM from the BBN sample horizon. BB05N, 0.15-0.2m from the dyke contact, 1.72% *Rr*.
7. Carbonised AOM from the BBN sample horizon. BB01N, 0-0.03m from the dyke contact, 3.6% *Rr*.
8. Carbonised AOM from the BBN sample horizon. BB01N, 0-0.03m from the dyke contact, 3.6% *Rr*.

PLATE 5

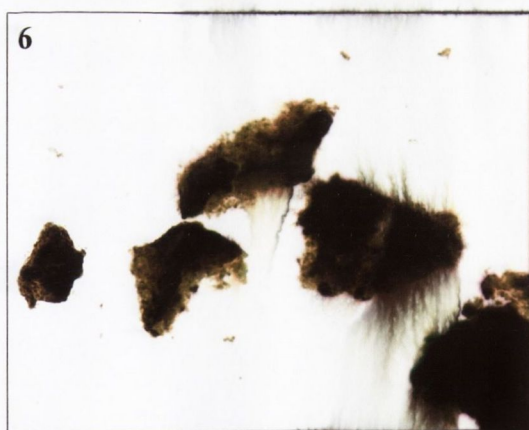
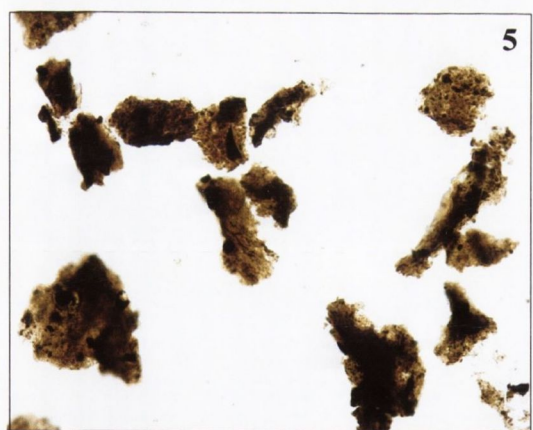
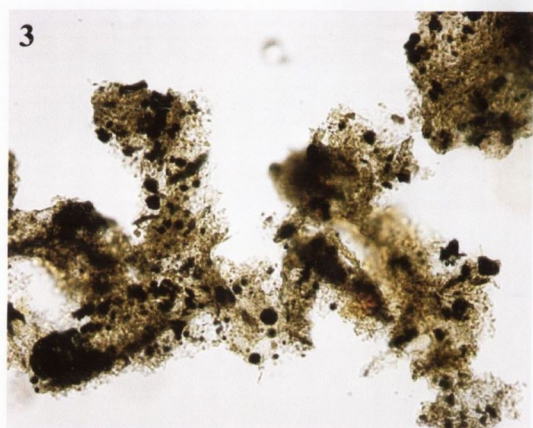
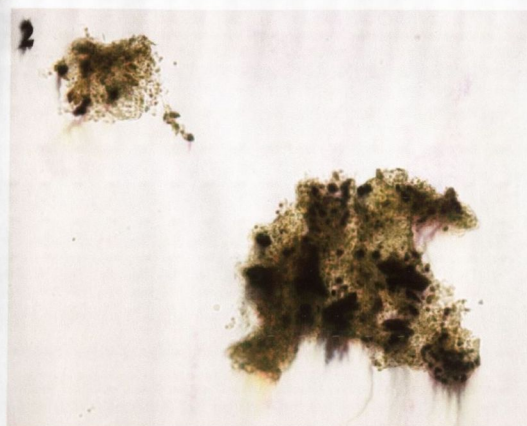
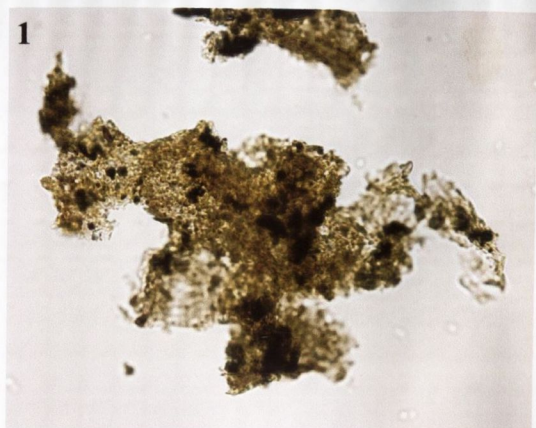


PLATE 6

1. Typical AOM from the BGSHN sample horizon. BGSH14N, 6.7m from the dyke contact, 0.75% Rr.
2. Typical AOM from the BGSHN sample horizon. BGSH13N, 4.9-5.0m from the dyke contact, 0.79% Rr.
3. Typical AOM and translucent woody phytoclast from the BGSHN sample horizon. BGSH12N, 3.0-3.1m from the dyke contact, 0.79% Rr.
4. Typical AOM from the BGSHN sample horizon, BGSH12N, 3.0-3.1m from the dyke contact, 0.79% Rr.
5. Typical AOM from the BGSHN sample horizon. BGSH08N, 0.5-0.6m from the dyke contact, 0.86% Rr.
6. Typical AOM from the BGSHN sample horizon. BGSH07N, 0.4-0.45m from the dyke contact, 0.96% Rr.
7. Thermally altered 'brittle' AOM from the BGSHN sample horizon. BGSH05N, 0.32-0.34m from the dyke contact, 1.13% Rr.
8. Carbonised AOM from the BGSHN sample horizon. BGSH01N, 0-0.05m from the dyke contact, 3.32% Rr.

PLATE 6

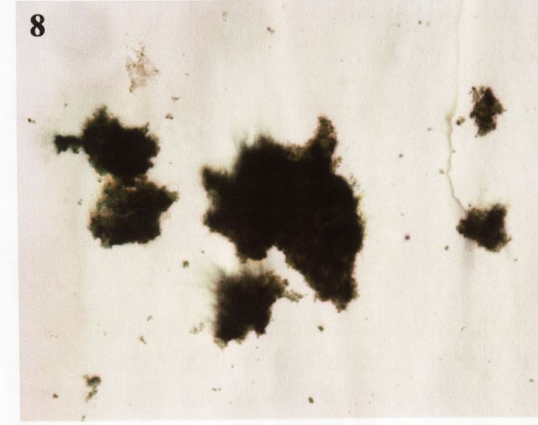
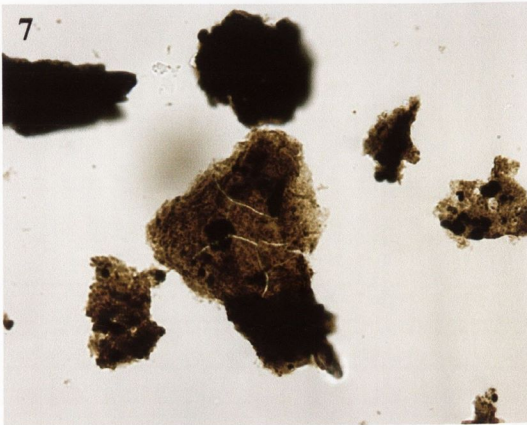
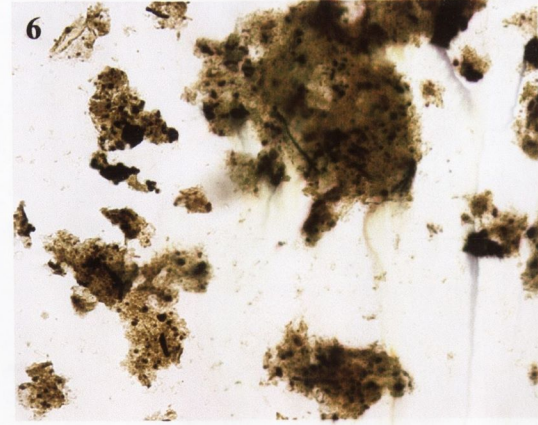
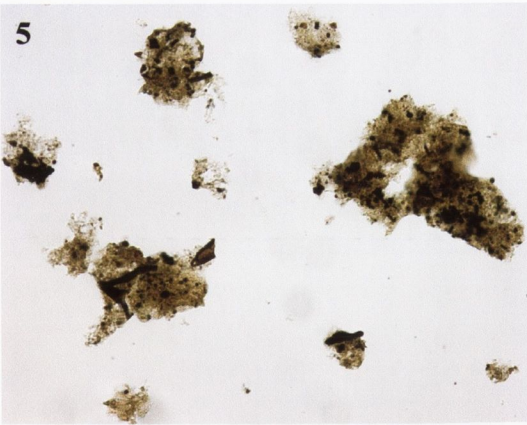
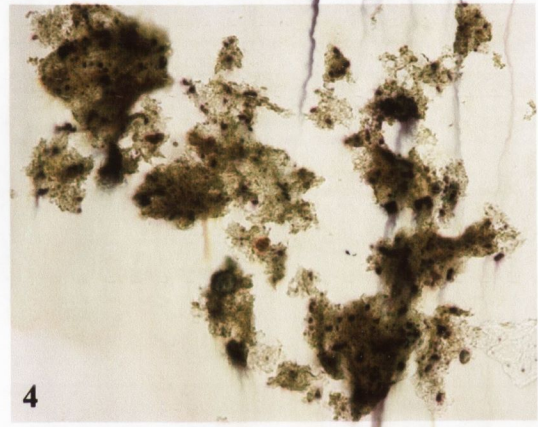
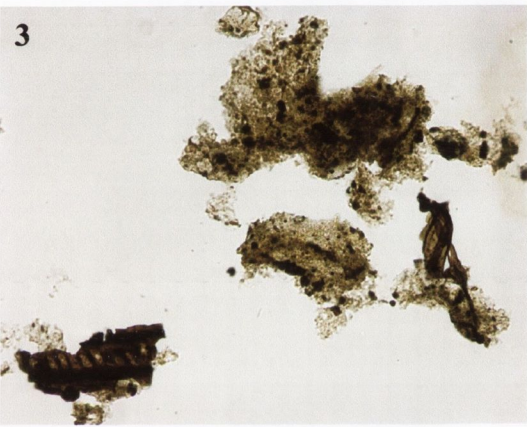
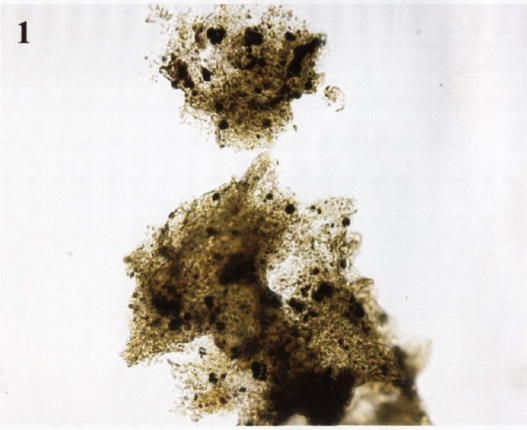


PLATE 7

1. Typical AOM from the BGSN sample horizon. BGS07N, 5.25-5.35m from the dyke contact, 0.72% Rr.
2. Partly sapropelized algal filaments from the BGSN sample horizon. BGS07N, 5.25-5.35m from the dyke contact, 0.72% Rr.
3. Typical AOM from the BGSN sample horizon. BGS06N, 2.9-3.0m from the dyke contact, 0.76% Rr.
4. Palynomorph with relict crystal imprints and typical AOM from the BGSN sample horizon, BGS06N, 2.9-3.0m from the dyke contact, 0.76% Rr.
5. Typical AOM from the BGSN sample horizon. BGS06N, 2.9-3.0m from the dyke contact, 0.76% Rr.
6. Coiled foraminiferal lining, 'woody' phytoclasts, and AOM from the BGSN sample horizon. BGS04N, 0.7-0.8m from the dyke contact, 0.86% Rr.
7. Opaque 'woody' phytoclasts and degraded tasmanitid (?) from a thermally altered BGSN sample. BGS03N, 0.23-0.3m from the dyke contact, 1.18% Rr.
8. Thermally altered AOM from the BGSN sample horizon. BGS02N, 0.1-0.15m from the dyke contact, 1.79% Rr.

PLATE 7

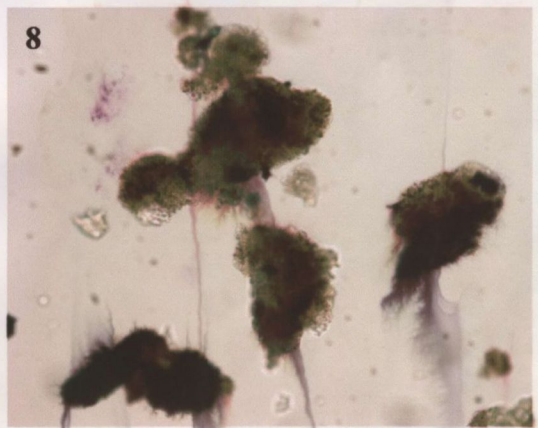
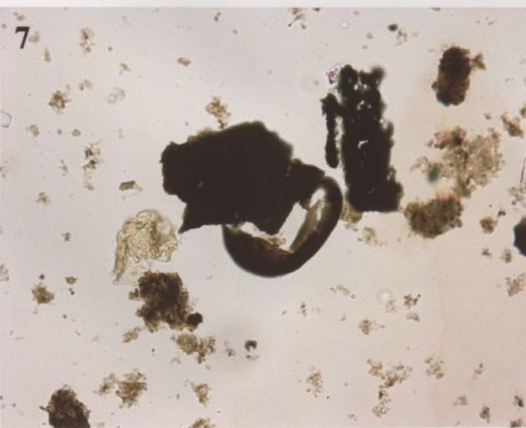
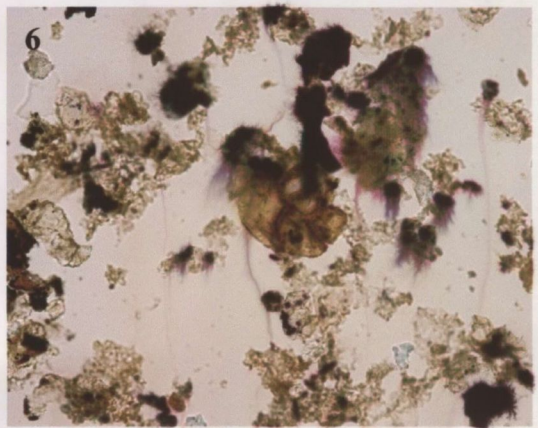
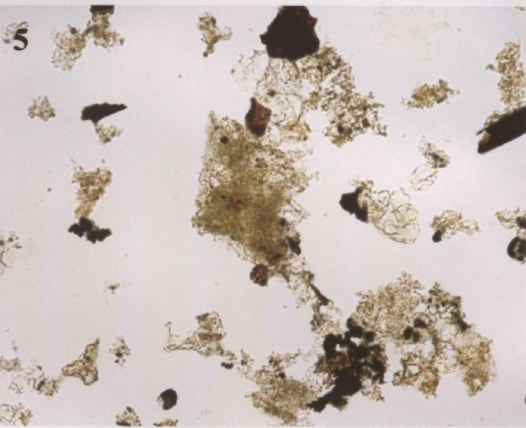
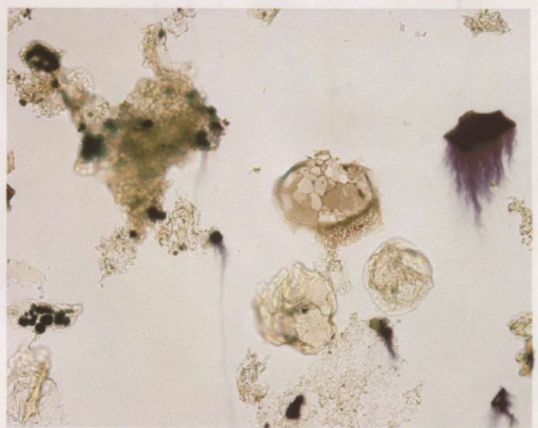
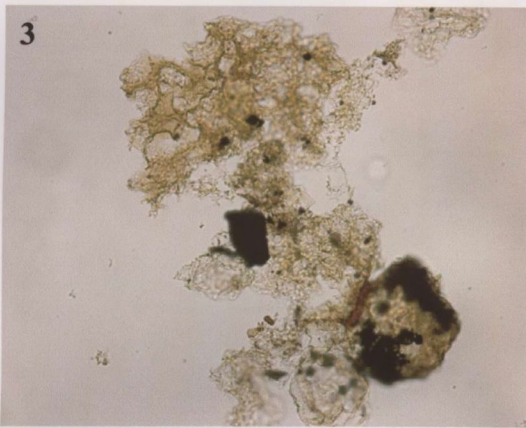
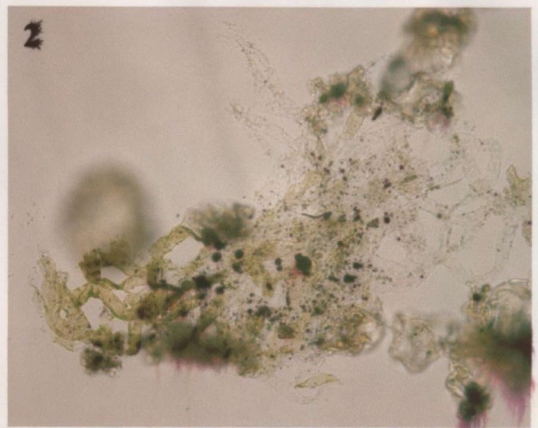
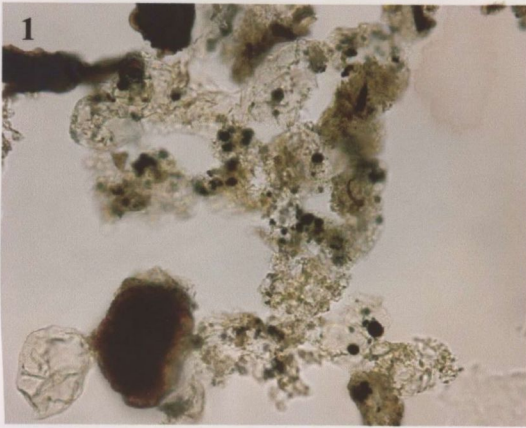


PLATE 8

A

Photomicrographs of a thin section of the studied basaltic dyke at Berreraig, showing plagioclase laths in groundmass.

B

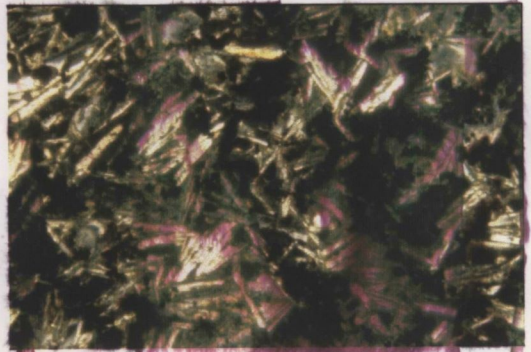
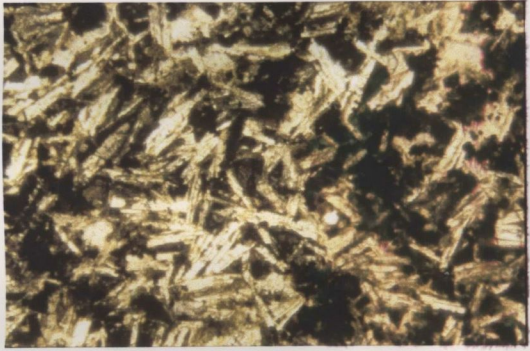
Photomicrographs of a thin section of the studied basaltic dyke at Berreraig, showing a plagioclase phenocryst with substantial alteration rim.

C

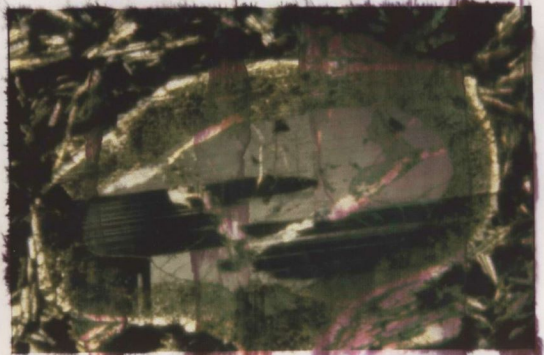
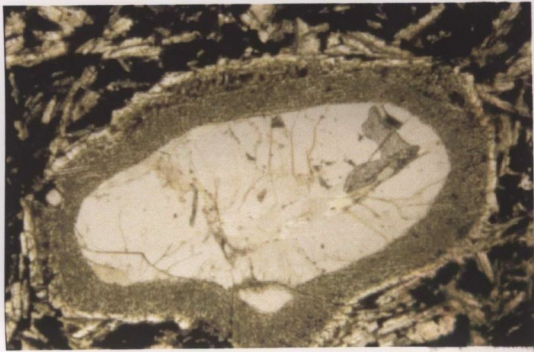
Crystal alignment suggestive of magma flow direction from a thin section of the dyke margin.

PLATE 8

A



B



C

